The Development of a Stochastic Solar Radiation Model and its Application in Estimating Evaporation

Natalie A. Lockart

BE (Hons)

A thesis submitted for the degree of Doctor of Philosophy

THE UNIVERSITY OF NEWCASTLE AUSTRALIA

May 2013

The thesis contains no material which has been accepted for the award of any other degree or diploma in any university or other tertiary institution and, to the best of my knowledge and belief, contains no material previously published or written by another person, except where due reference has been made in the text. I give consent to the final version of my thesis being made available worldwide when deposited in the University's Digital Repository, subject to the provisions of the Copyright Act 1968.

_____

Natalie A. Lockart

I hereby certify that the work embodied in this thesis contains published paper/s/scholarly work of which I am a joint author. I have included as part of the thesis a written statement, endorsed by my supervisor, attesting to my contribution to the joint publication/s/scholarly work.

Prof. Stewart W. Franks
Supervisor

.

Acknowledgements

This thesis has only been made possible with the support and advice from my family, friends and colleagues.

To my supervisors, Stewart Franks and Dmitri Kavetski, thank you for all your help, support and guidance. You made this a very enjoyable project to work on. Thanks also for all the tea.

To my fellow PhD students, thank you for your friendship, support, advice and the many fun distractions. A particular thank you to Amanda for all your programming assistance. Thank you also to all the administrative staff of the School of Engineering.

To my parents, Grant and Sue, and family, David and Bek, Ian and Kate, thank you for always being interested in my work and for your constant encouragement and support from afar. A special thanks to my amazing sister, Alison. You have kept me sane since day one.

And finally, Jonathan, thank you for your love, patience, understanding and encouragement during the past four years. I could not have done this without you.

Table of Contents

List of Figures

List of Tables

List of Symbols and Notation

The following is a description of the symbols and notation commonly used in this thesis.

Evaporation Notation

Symbol	Explanation	Units
ET_o	Reference evapotranspiration	mm d^{-1}
G_h	Ground heat flux	MJ m^{-2} d^{-1}
P	Atmospheric pressure	kPa
R_A	Extra-terrestrial radiation received on a horizontal plane	MJ m^{-2} d^{-1}
R_n	Net radiation	MJ m^{-2} d^{-1}
R_{nl}	Net longwave radiation	MJ m^{-2} d^{-1}
R_{ns}	Net shortwave radiation	MJ m^{-2} d^{-1}
R_s	Solar radiation received on a horizontal plane	MJ m^{-2} d^{-1}
R_{so}	Solar radiation on a cloudless day	MJ m^{-2} d^{-1}
RH	Relative humidity	percentage
T	Air temperature	°C
T_d	Dry bulb temperature	°C
T_w	Wet bulb temperature	°C
U_d	Mean daytime wind speed	m s^{-1}
a,b	Constants	see usage
c_p	Specific heat of air at constant pressure	KJ kg^{-1} °C $^{-1}$
d_z	Zero plane displacement	m
e	Water vapour pressure in air	kPa
e_a	Actual vapour pressure	kPa
e_s	Saturation vapour pressure	kPa
k	von Karman's constant	-
n/N	Daily sunshine hour fraction	-
r_a	Aerodynamic resistance	s m^{-1}
r_s	Surface resistance	s m^{-1}
u_2	Wind speed at height 2m	m s^{-1}
z	Elevation	m
z_a	Reference height of anemometer	m
z_0	Roughness length	m

α	Albedo	-
α_{PT}	Coefficient for the Priestley-Taylor model	-
γ	Psychrometric constant	kPa °C $^{-1}$
Δ	Slope of the saturated specific humidity temperature curve	kPa °C $^{-1}$
λ	Latent heat of vaporization	MJ kg^{-1}
ρ	Air density	kg m^{-3}
σ	Stefan-Boltzmann constant	MJ K^{-4} m^{-2} d^{-1}

PBL Model Notation

Symbol	Explanation	Units
E_i	Water vapour flux at inversion	kg m^{-2} s^{-1}
E_S	Water vapour flux at land surface	kg m^{-2} s^{-1}
H_i	Sensible heat flux at inversion	W m^{-2}
H_s	Sensible heat flux at land surface	W m^{-2}
c_e	Coefficient of entrainment	-
h	Height	m
q	Specific humidity of PBL	-
t	Time	s
γ_q	Lapse rate of specific humidity	kg kg^{-1} m^{-1}
γ_θ	Lapse rate of potential temperature	K m^{-1}
Θ	PBL temperature	K

Solar Radiation Notation

Symbol	Explanation	Units
A,B,C,D	Radiation model parameters	-
G	Global radiation on a horizontal surface	MJ m^{-2} d^{-1}
G_b	Direct radiation on a horizontal surface	MJ m^{-2} d^{-1}
G_{clear}	Clear sky global radiation	MJ m^{-2} d^{-1}
G_d	Diffuse radiation on a horizontal surface	MJ m^{-2} d^{-1}
G_0	Extra-terrestrial radiation	MJ m^{-2} d^{-1}
G_{sc}	Solar constant	MJ m^{-2} min^{-1}
N	Day length (maximum possible sunshine hours)	h
N'	Maximum potential sunshine hours, above threshold	h
R	Radiation	MJ m^{-2} d^{-1}
$R_{diffuse}$	Diffuse radiation component of radiation model	MJ m^{-2} d^{-1}

R_{direct}	Direct radiation component of radiation model	MJ m^{-2} d^{-1}
R_T	Direct radiation threshold for the CS recorder	W m^{-2}
a,b,c,d	Coefficients of radiation equations	-
d_r	Inverse relative sun-earth distance	-
e_t	Residual error	-
h	Altitude	m
i	Number of iterations	-
k_t	Clearness index	-
m	Air mass	-
n	Actual measured sunshine hours	h
n_d	Number of dull periods	h
secz	Secant of the solar zenith angle	rad
t	Time	h
δ	Declination of the sun	rad
φ	Latitude	rad
ω	Sun hour angle	rad
ω_s	Sunset hour angle	rad

Main Subscripts

diff	Diffuse radiation
dir	Direct radiation
Obs	Observed
Sim	Simulated
var	Variance
h	‘Bright’ period
t	Time

Abbreviations

BoM	Bureau of Meteorology
CS	Campbell-Stokes
DP	Doorenbos-Pruitt model
ET	Evapotranspiration (potential, unless otherwise stated)
ETR	Extra-terrestrial radiation
FAO	Food and Agriculture Organisation of the United Nations
FAO-24-BC	FAO-24 version of the Blaney-Criddle model

FAO-56-PM	FAO-56 version of the Penman-Monteith model
GCM	General circulation model
HS	Hargreaves-Samani model
LE	Latent energy
Mod-JH	Modified Jensen-Haise model
PBL	Planetary boundary layer
PDSI	Palmer drought severity index
PM	Penman-Monteith
PT	Priestley-Taylor model
QQ	Quantile-quantile
RMSE	Root-mean-square-error
SimRad	Simulated radiation
SSH	Sunshine hours
VPD	Vapour pressure deficit

Abstract

Global radiation is an important input for evaporation calculations; however, limited measurements exist. Current models for estimating global radiation are deterministic and do not give an estimate of the errors associated with the predicted radiation amounts. In this thesis, five stochastic models are developed to estimate the mean amount and associated uncertainty of global, direct and diffuse radiation from sunshine duration data. The modelled global radiation is used to estimate evaporation amounts using a variety of models, including the Penman-Monteith model, radiation-based models, and temperature-based models. Evaporation estimates are compared to determine the influence of uncertainty in the global radiation estimate on evaporation amounts. The second part of this thesis deals with the relationship between temperature and evaporation, with implications for anthropogenic climate change studies. The influence of temperature on evaporation amounts is analysed using a combination of empirical evaporation models and a more physically-based planetary boundary layer model.

The results indicate that global radiation can be accurately estimated using all of the developed radiation models (average error = 9%), when compared with measured data. The variance of the errors is greater for cloudy days compared with clear days. The diffuse radiation component is best modelled using a quadratic model (average error = 22%). The direct radiation component is best modelled using a linear model (average error = 23%). Two types of regional models are also developed to calculate radiation amounts at any location. These models have only a small loss of accuracy compared to the locally calibrated models. While the variance of the errors for the locally calibrated models is shown to be location dependent, these regional models allow for the model parameters and the error variance to be estimated at any location, as there is a statistically significant relationship between the model and error parameters and latitude. The regional models are also comparable in accuracy to satellite estimates of global radiation.

It is also found that the uncertainty in global radiation leads to considerable uncertainty in evaporation rates, up to ±31% for the radiation-based models. The locations with greater uncertainty in the radiation estimate have an associated greater uncertainty in the evaporation estimate.

Temperature increases are shown to have minor influences on evaporation rates. Soil moisture is the most dominant influence. Consequently, temperature-based models are shown to lead to unreasonable estimates of evaporation when temperatures are increased.

Chapter 1 - Introduction

1.1 General Background

Knowledge of evaporation amounts is necessary for many agricultural and hydrological applications; however, measurements of evaporation are limited. Further, there is a question about how anthropogenic climate change may affect evaporation, which requires a fundamental understanding of the interaction between temperature and evaporation. Many models, such as the Penman-Monteith model (Monteith, 1965, 1981), have been developed to address the first issue and estimate evaporation. One of the dominant drivers of evaporation and a common input into evaporation models is global radiation. However, measured amounts of global radiation are often not available or have only recently become available. While more complex theoretical models for estimating global radiation are now more useable and satellite estimates are becoming more common, the data and technology has only recently become available. Therefore, empirical methods are still needed for historical analysis of climate states and trends, and for locations with no measured data.

The simple and empirical Angstrom-Prescott equation is commonly used for calculating global radiation, for example in the Food and Agriculture Organisation of the United Nations Irrigation and Drainage Paper 56 (Allen et al., 1998). This equation, and other common empirical methods, calculates radiation amounts from sunshine hours data. These methods are deterministic and give no indication of the amount or nature of the uncertainty associated with radiation estimates. In this thesis, a stochastic model is developed to provide an estimate, and associated uncertainty, of global, direct, and diffuse radiation. While only global radiation amounts are necessary for estimating evaporation, estimates of direct and diffuse radiation are important for calculating radiation on sloped surfaces and for ecosystem modelling.

The second part of this thesis examines the relationship between evaporation, soil moisture and temperature using well-known evaporation models and a more complex planetary boundary layer model. The fundamentals and causality of this relationship

have important implications in the context of anthropogenic climate change studies that investigate the impact of increased temperatures on evaporation.

1.2 Objectives and Scope

The thesis has two main foci, reflecting distinct research directions in the published literature. The first focus is on the development of a stochastic model to estimate global radiation and its components from sunshine hours data. Current models for estimating global radiation do not provide an estimate of the uncertainty in radiation estimates. The second focus is on the interaction between evaporation, temperature and soil moisture.

The objectives of this thesis are to:

- Develop a novel stochastic sunshine hour based model for estimating global, direct, and diffuse radiation, explicitly accounting for the uncertainty in the radiation estimates;
- Apply the global radiation amounts to a variety of well-known evaporation models to determine the influence of the uncertainty in the global radiation estimate on evaporation estimates;
- Examine the relationship and interaction between evaporation and temperature; and,
- Examine the influence of soil moisture on the evolution of daytime temperatures.

1.3 Overview

A flow chart of the main thesis components is given in Figure 1.1. The above objectives are presented in the following manner. First, previous empirical approaches for calculating global, direct, and diffuse radiation, along with the models for evaporation and their uses, are critically reviewed in Chapter 2. This provides a rationale for developing a stochastic radiation model that explicitly accounts for the uncertainty in the radiation estimate and for assessing the interaction between evaporation, temperature, and soil moisture.

The stochastic radiation models are developed using measured sunshine hour and radiation data from a variety of locations around Australia. A description of the locations and their climatology is given in Chapter 3. Chapter 3 also details the development of the stochastic radiation models for estimating global, direct and diffuse radiation amounts, as well as the uncertainty in the estimates due to the timing of the bright hours and external influences. In Chapter 4 the stochastic models are used to estimate global, direct and diffuse radiation amounts. In Chapter 4 the stochastic models are calibrated at each of nine locations; however, local data often does not exist for calibration. Therefore, in Chapter 5 two different types of regional models are developed to calculate global, direct and diffuse radiation at any location in Australia. In Chapter 6 the global radiation estimates are used to determine the influence of the uncertainty in the radiation amounts on evaporation rates.

The following two chapters focus on the interaction between evaporation, temperature, and soil moisture. Previous studies into the Murray-Darling Basin drought noted that temperatures were 2°C higher than average. These studies then erroneously suggested that this increase in temperature led to increased evaporation rates. In Chapter 7 the influence of a 2°C increase in temperature on evaporation rates is analysed using a selection of empirical evaporation models. However, the interaction between evaporation and temperature is complex and is influenced by feedback between the land-surface and the atmosphere. Therefore, in Chapter 8 a planetary boundary layer model, which accounts for land-surface-atmosphere interactions, is used to study the interaction between evaporation, temperature, and soil moisture.

To conclude, the major findings of this thesis are summarized in Chapter 9.

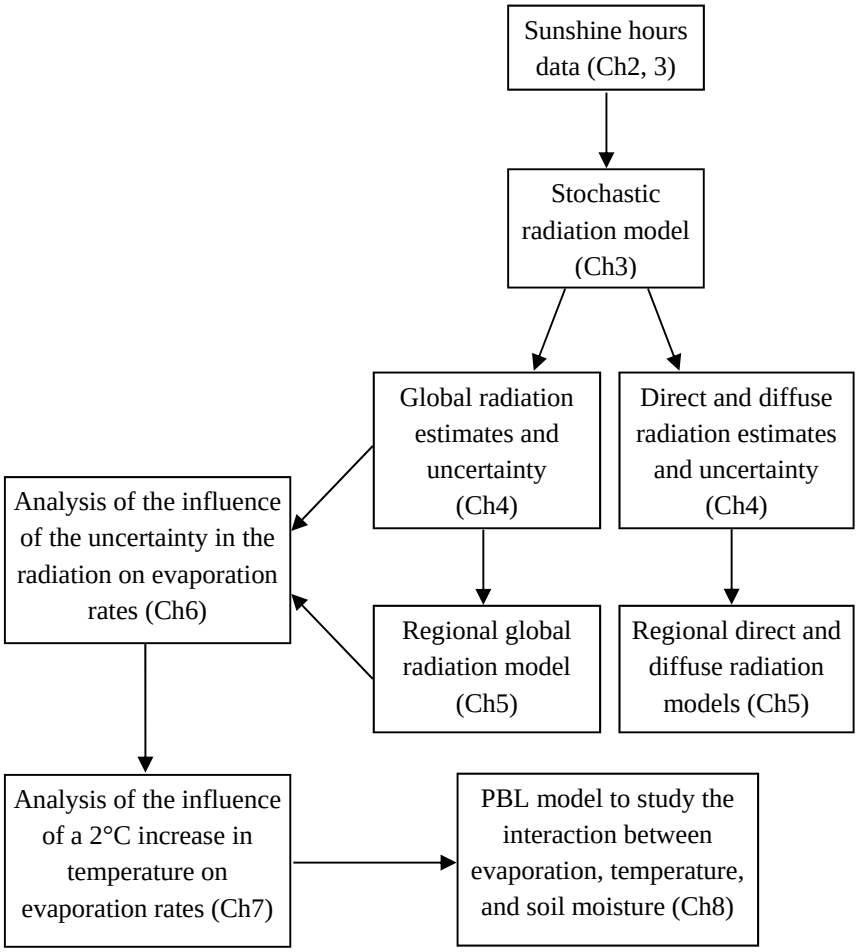

Figure 1.1 Summary of thesis components

As a result of the research work undertaken during the course of this thesis, four journal articles and conference papers have been published.

Lockart, N., D. Kavetski, and S. W. Franks (2009), On the recent warming in the Murray-Darling Basin: Land surface interactions misunderstood. *Geophysical Research Letters*, 36, *L24405, doi:10.1029/2009GL040598.*

Lockart, N., D. Kavetski and S. W. Franks (2009), Misattribution of Climate Trends in the Murray Darling Basin. *H2009: 32nd Hydrology and Water Resources Symposium, Newcastle: Adapting to Change*. Institution of Engineers Australia, 1332-1340.

Lockart, N., D. Kavetski, and S. W. Franks (2011), Hydro-climatological variability in the Murray-Darling Basin. *Hydro-Climatology: Variability and Change*, S. W. Franks, E. Boegh, E. Blyth, D. M. Hannah, and K. K. Yilmaz, Eds., 344:105-111.

Lockart, N., D. Kavetski and S. W. Franks (2012), On the role of soil moisture in daytime evolution of temperatures. *Hydrological Processes*, doi: 10.1002/hyp.9525

Chapter 2 - Background

Overview

Models of evaporation and global radiation, and uncertainty estimates in their predictions, are of significant importance for agricultural applications such as irrigation scheduling and reservoir design. The following is a review of the current literature surrounding methods for estimating evaporation and approaches for estimating global radiation. This review supports the need to develop a stochastic model for estimating global radiation from sunshine hours, for application to evaporation modelling. This review also clarifies important aspects of the interaction and causality of temperature and evaporation.

2.1 Evaporation

Evapotranspiration is an important component of the hydrologic cycle and measurements are needed for water balance modelling, rainfall-runoff models, agricultural and urban planning, irrigation scheduling and reservoir design.

Evaporation occurs when water in the liquid state gains sufficient energy (usually from solar radiation) to pass into the gaseous state (Allen et al., 1998). Water will evaporate from bare and vegetated soil, trees, impervious surfaces, open water, and flowing streams and rivers. Transpiration is the process where water is used by vegetation to support growth. In this process, water moves from the ground, through the roots to the stem or trunk of a plant, and to the leafy part where it is transpired into the atmosphere (Jensen et al., 1990). In field conditions it is hard to differentiate between evaporation and transpiration, so they are commonly linked together as evapotranspiration (ET).

Factors affecting ET include solar radiation, wind, relative humidity, and temperature. Solar radiation provides the energy necessary for water molecules to move from liquid to vapour. Clouds reduce the amount of solar radiation and slow ET. ET requires a vapour-pressure gradient between the evaporating surface and the surrounding air. Wind is necessary to ensure the saturated air at the boundary between the water surface and

the atmosphere is replaced by drier air, allowing ET to proceed. Relative humidity determines the ability of air to absorb more water vapour, affecting the rate of ET. And finally, temperature affects the water holding capacity of air. As air temperature increases so does the capacity of air to absorb water vapour. Temperature can also provide the heat energy required for ET. ET is also influenced by topography, soil properties, irrigation, precipitation, and available soil and subsoil moisture.

Solar radiation is considered the primary climatic factor controlling ET when water is not limiting (Jensen et al., 1990). Solar radiation is the primary source of heat energy for ET. It is the most significant parameter for all combination and radiation–based ET models (Amatya et al., 1995). According to Samani (2000) the most important variables for estimating reference crop ET are temperature and solar radiation, although Hargreaves (1974) found relative humidity to be an important factor for ET in areas of high relative humidity.

Xu and Singh (1998) evaluated the role of solar radiation, vapour pressure deficit, relative humidity, wind speed, and air temperatures in controlling ET at hourly, daily, ten-day, and monthly timescales. Using data from one location in Switzerland, the variables were compared with measured pan ET. They found that the influence of the variables on ET varied with the time-scale used. At all timescales the vapour pressure deficit was best correlated with the pan ET. The wind speed was found to be a controlling factor for the hourly data, but the degree of dependence of ET on wind speed decreased with the increase in time interval. For time steps longer than a day the wind speed was not a significant influence on ET. Relative humidity was found to be well correlated with ET in general; however the importance of the variable decreased with increasing time-scale. Radiation was also found to compare well with ET on all timescales, though the daily timescale had the best agreement. Temperature was found to have a good agreement at the hourly and daily timescales, but at the monthly timescale there was a lag between the temperature and ET.

Pan ET has declined in many regions over the last several decades. Roderick et al. (2007) used a physical model to attribute the changes in pan ET at 41 sites in Australia to changes in radiation, temperature, humidity and wind speed. The decrease in pan ET

was attributed mainly to decreasing wind speed with some regional contributions from decreasing solar irradiance. Air temperature, as well as the vapour pressure deficit, was found to play only a minor role in the changes in pan ET. The trend in the vapour pressure deficit, as assessed at 41 sites from 1975-2004 was only -0.2Pa a^{-1} compared to a background average of 1205Pa (less than 1% over the 30 years).

2.1.1 Evapotranspiration measurements

There are two ET measurements: potential and actual. ET rates are influenced by the amount of water available. Therefore, potential ET is different to the actual ET that takes place. Potential ET is "the rate at which water, if available, would be removed from wet soil and plant surfaces expressed as the rate of latent heat transfer per unit area, or as a depth of water per unit time" (Jensen et al., 1990, p. 42). The amount of actual ET is determined by the available moisture supply, which in turn varies with rainfall and soil characteristics.

To provide a standard potential ET, reference crop ET has been established. Reference crop ET (ET_0) is "the rate of evapotranspiration from an extensive surface of 8 to 15cm tall, green grass cover of uniform height, actively growing, completely shading the ground and not short of water" (Doorenbos & Pruitt, 1977, p. 1). The reference crop is often alfalfa or grass (Jensen et al., 1990).

Evapotranspiration can be measured using a lysimeter, although measurements are very difficult and, therefore, not very common. However, a multitude of models exist for estimating potential ET from a range of meteorological variables. These models have been developed by relating ET to climatological data, based on experimental data. Some models relate ET to just one meteorological variable, such as temperature (e.g., Thornthwaite, 1948), while other models use a combination of some or all of the driving variables. These models fall into several categories such as combination; mass transfer; radiation; temperature; and water budget. Most of these models were developed for use in specific climates and land use conditions.

The Penman-Monteith (PM) model is recommended by many authors as the best performing model for estimating ET (e.g., Jensen et al., 1990; McKenney & Rosenberg,

1993; Allen et al., 1998). This is because it is physically derived, incorporates all the driving variables, and has been shown to perform well in a variety of climates. The Food and Agriculture Organisation of the United Nations (FAO) (Allen et al., 1998) have proposed using the FAO-56-PM model as the standard model for estimating reference ET. However, when there is insufficient weather data for the application of the PM model, models based on temperature or radiation are often used to estimate reference ET. The choice of model is usually based on the time step required, the type and accuracy of climatic data available, the aridity of the area, and the accuracy required (Hargreaves & Allen, 2003).

McMahon et al. (2013) present a comprehensive summary of the different techniques for estimating actual and potential ET, reference crop ET and pan evaporation, and detail the more common potential ET equations and their data requirements. Their paper also outlines the estimation of ET for non-vegetated crop areas such as bare soil, groundwater, shallow and deep lakes, which is not considered in this study. Wang and Dickinson (2012) also summarise different methods for estimating or measuring ET, such as the Bowen ratio and Eddy covariance methods and remote sensing methods, which are beyond the scope of this study. They also summarise the different factors influencing ET for different land cover types (e.g. forests and wetlands).

2.1.2 Potential evapotranspiration models

The PM model is generally considered as the most physically realistic model, and is the recommended method by the FAO, as well as Shuttleworth (1992) and Hargreaves and Allen (2003). The following section details the PM model as well as common radiation-based models, as solar radiation is one of the dominant drivers of ET. Six temperature-based models are also presented as these are also commonly used due to their simplicity and the ready availability of temperature data.

2.1.2.1 Combination models

2.1.2.1.1 Penman-Monteith model

The PM model (Monteith, 1965, 1981) is:

$$\lambda ET = \frac{\Delta(R_n - G_h) + \rho c_p \left(\frac{e_s - e_a}{r_a} \right)}{\Delta + \gamma \left(1 + \frac{r_s}{r_a} \right)} \tag{2.1}$$

where λ is the latent heat of vaporization (MJ kg^{-1}), R_n is the net radiation (MJ m^{-2} d^{-1}), G_h is the soil heat flux (MJ m^{-2} d^{-1}), Δ is the slope of the saturated specific humidity temperature curve (kPa °C $^{-1}$), ($e_s - e_a$) is the specific humidity deficit (kPa), ρ is the density of air (kg m^{-3}), c_p is the specific heat of air at constant pressure (KJ kg^{-1} °C $^{-1}$), γ is the psychrometric constant (kPa °C^{-1}), r_s is the surface resistance (s m^{-1}) and r_a is the aerodynamic resistance (s m^{-1}). The surface resistance parameter is a function of soil moisture availability, solar radiation, temperature, CO_2 etc. This parameter deals with the physiological resistance that crops impose on water transfer from within to their outer surfaces. These estimates can be used on a daily scale (Jensen et al. 1990).

2.1.2.1.2 FAO-56-PM model for reference crop evapotranspiration

The FAO propose the adoption of the FAO-56-PM combination model as the sole method for determining reference ET (Allen et al., 1998). The equation was derived with the reference crop defined as a hypothetical crop with a height of 0.12m, a surface resistance of 70 sm^{-1}, and an albedo of 0.23, which resembles ET from green grass with a uniform height, actively growing, and adequately watered. The FAO-56 formulation of the PM equation for a reference crop is:

$$ET_0 = \frac{0.408\Delta(R_n - G) + \gamma \frac{900}{T + 273} u_2 (e_s - e_a)}{\Delta + \gamma(1 + 0.34 u_2)} \tag{2.2}$$

where u_2 is the wind speed (m s^{-1}) at height 2m.

2.1.2.1.3 Penman model

The Penman model (Penman, 1948), also known as the Penman combination equation, can be considered an implementation of the Penman-Monteith model with specific values of surface resistance (set to zero) and aerodynamic resistance (Shuttleworth, 2012):

$$ET = \frac{\Delta}{\Delta + \gamma}\frac{R_n - G}{\lambda} + \frac{\gamma}{\Delta + \gamma}\frac{6.43(1 + 0.536u_2)(e_s - e_a)}{\lambda} \tag{2.3}$$

where ET is in mm day^{-1}.

2.1.2.2 Radiation-based models

2.1.2.2.1 Makkink (1957)

Makkink (1957) developed a method for estimating ET (mm day^{-1}) for grassed lands under cool climatic conditions in the Netherlands for ten-day periods:

$$ET_0 = 0.61\frac{\Delta}{\Delta + \gamma}\frac{R_S}{\lambda} - 0.12 \tag{2.4}$$

where R_s is the solar radiation in MJ m^{-2} d^{-1}.

2.1.2.2.2 Turc (1961)

Turc (1961) developed a simplified estimate of ET_0 for Western Europe for ten-day periods:

$$ET_0 = 0.0133\frac{T}{T + 15}\left(23.8856\,R_S + 50\right) \qquad \text{For RH} \geq 50 \tag{2.5}$$

$$ET_0 = 0.0133\frac{T}{T + 15}\left(23.8856\,R_S + 50\right)\left(1 + \frac{50 - RH}{70}\right) \qquad \text{For RH} < 50 \tag{2.6}$$

where T is the air temperature (°C) and RH is the daily mean relative humidity (%).

2.1.2.2.3 Jensen-Haise (1963)

Jensen and Haise (1963) evaluated 3000 observations of ET and proposed for a crop like alfalfa:

$$ET_0 = C_T (T - T_x) \frac{R_s}{\lambda} \tag{2.7}$$

where C_T and T_x are coefficients. Jensen (1966) later defined C_T as:

$$C_T = \frac{1}{C_1 + C_2 C_H} \tag{2.8}$$

where

$$C_H = \frac{5.0kPh}{e_2 - e_1} \tag{2.9}$$

where e_2 and e_1 are the saturation vapour pressures in kPa at the mean maximum and mean minimum temperatures, respectively, for the warmest month of the year, and T_x, C_1 and C_2 are constants (C_2 = 7.3°C).

Jensen et al. (1970) further defined:

$$C_1 = 38 - (2z / 305) \tag{2.10}$$

$$T_X = -2.5 - 1.4(e_2 - e_1) - z / 550 \tag{2.11}$$

where z is the elevation in m. The recommended minimum time period for use as given by Jensen et al. (1990) is five days.

2.1.2.2.4 Priestley-Taylor (1972)

Priestley and Taylor (1972) developed a simplified version of the Penman combination equation (Penman, 1948) for estimating potential evaporation, where the mass transfer effects are represented by a constant value:

$$ET = \alpha_{PT} \frac{\Delta}{\Delta + \gamma} \frac{R_n}{\lambda} \tag{2.12}$$

where α_{PT} = 1.26 for humid conditions (RH>60) and α_{PT} = 1.74 for arid conditions (RH<60) (Shuttleworth, 1992).

The model was developed for saturated land surfaces (α_{PT} = 1.26). However, α_{PT} is known to vary with climate. Jensen et al. (1990) recommend using the higher α_{PT} value for arid locations to account for the advection of sensible heat energy to an irrigated crop. The recommended minimum time period for use as given by Jensen et al. (1990) is ten days, although it has been used for daily estimates.

2.1.2.2.5 Hargreaves (1975)

Hargreaves (1975) formed an equation for estimating grass related reference crop ET. This was derived from eight years of cool season Alta fescue grass lysimeter data. The Hargreaves equation was developed primarily for the purposes of irrigation planning and design (Hargreaves and Allen, 2003). This method was developed for the dry California climate. For a five-day time step:

$$ET_0 = 0.0135 R_S (T + 17.8) \tag{2.13}$$

where ET_o and R_s are in the same units of water evaporation.

2.1.2.2.6 Doorenbos and Pruitt (1977)

The method developed by Doorenbos and Pruitt (1977) is an adaptation of the Makkink (1957) method. It is recommended over the Penman method when wind and humidity data are not available (Jensen et al., 1990):

$$ET_0 = a + b \frac{\Delta}{\Delta + \gamma} \frac{R_s}{\lambda} \tag{2.14}$$

where a is a constant equal to -0.3 and b is given by:

$$b = 1.066 - 0.0013RH + 0.045U_d - 0.0002RH\,U_d - 0.0000315RH^2 - 0.0011U_d^2 \tag{2.15}$$

where U_d is the mean daytime wind speed (m s^{-1}). The recommended minimum time period for use as given by Jensen et al. (1990) is five days.

2.1.2.2.7 Abtew (1996)

Abtew (1996), using data from three lysimeters, derived a simple model based solely on solar radiation data:

$$ET = 0.53\frac{R_s}{\lambda} \tag{2.16}$$

2.1.2.3 Temperature-based models

2.1.2.3.1 Thornthwaite (1948)

Many empirical formulae relate ET to temperature. Thornthwaite (1948) devised the following formula for calculating ET on a monthly basis:

$$ET_m = 16N_m\left(\frac{10\overline{T}_m}{I}\right)^a \tag{2.17}$$

where m is the months (1…12), N_m is the monthly adjustment factor related to the hours of daylight, T_m is the monthly mean temperature (°C), I is the heat index for the year:

$$I = \Sigma im = \Sigma\left(\frac{\overline{T}_m}{5}\right)^{1.5}_{m=1...12} \tag{2.18}$$

and a (to 2 significant figures) is:

$$a = 6.7\times10^{-7}I^3 - 7.7\times10^{-5}I^2 + 1.8\times10^{-2}I + 0.49 \tag{2.19}$$

The unadjusted monthly ET values are adjusted depending on the number of days (N_d) in a month ($1\leq N_d\leq 31$) and the duration of average monthly or daily daylight (d, in hours), which is a function of season and latitude:

$$N_m = \left(\frac{d}{12}\right)\left(\frac{N_d}{30}\right) \tag{2.20}$$

This model has been widely used throughout the world (Shaw, 1994), but is strictly only valid for climates similar to the area for which it was developed (eastern USA), which is a humid environment. When compared with estimates from the Penman formula, the Thornthwaite model tends to exaggerate the ET, particularly in summer months when the high temperatures have a dominant effect in the Thornthwaite computation, whereas the Penman model considers other meteorological factors (Shaw, 1994).

This model should not be used in arid and semiarid areas. However, because of its limited data needs, Jensen et al. (1990) report that this model has been one of the most misused empirical equations in arid and semiarid irrigated regions.

The Thornthwaite model is used in the traditional calculation of the Palmer Drought Severity Index (PDSI) (Palmer, 1965). The PDSI is a measure of dryness based on precipitation and temperature and is routinely used in the US to assess developing drought conditions.

2.1.2.3.2 Blaney-Criddle (1950)

One of the most well-known and widely-used of the temperature-based models is the Blaney-Criddle model (Jensen et al., 1990). This model was developed by Blaney and Criddle (1950) and utilises temperature and day length data. The model was designed to provide daily estimates of evaporation averaged over a period. The usual form, converted to metric units is:

$$ET_0 = kp(0.46T + 8.13) \tag{2.21}$$

where p is the mean daily percentage of total annual daytime hours for a given month and altitude, and k is a monthly consumptive use factor, depending on relative humidity, sunshine duration, and day time wind.

Doorenbos and Pruitt (1977) recommend the Blaney-Criddle model only be used for periods of one month or longer.

The Blaney-Criddle model has been considerably modified over the years. The FAO-24 version (Doorenbos & Pruitt, 1977) is a major modification as it includes climatic information in addition to air temperature data (Jensen et al., 1990). The climatic information includes minimum humidity, sunshine, and daytime wind movement, which can be gained from subjective knowledge rather than actual measurements. However, if there are actual measurements, a combination model such as the Penman model is usually regarded as being superior. The FAO-24 model is only recommended for use when air temperature is the only climatic data available (Doorenbos & Pruitt, 1977).

The FAO-24 Blaney-Criddle model is (mm d^{-1}):

$$ET_0 = a + bf \tag{2.22}$$

$$f = p(0.46T + 8.13) \tag{2.23}$$

$$a = 0.0043RH - \frac{n}{N} - 1.41 \tag{2.24}$$

$$b = 0.82 - 0.0041RH + 1.07\frac{n}{N} + 0.066u_2 - 0.006RH\frac{n}{N} - 0.0006RH \times u_2 \tag{2.25}$$

where *n/N* is the ratio of actual to possible sunshine hours. The recommended minimum time period for use as given by Jensen et al. (1990) is five days.

2.1.2.3.3 Hamon (1961)

Hamon (1961) derived the following equation (as given in Federer et al., 1996):

$$ET_0 = 715.5D\frac{e_s}{T + 273.2} \tag{2.26}$$

where *D* is the hours of daylight for a given day (in units of 12 h).

2.1.2.3.4 Romanenko (1961)

Romanenko (1961) derived the following equation using mean temperature and relative humidity:

$$ET = 0.0018(25 + T)^2(100 - RH) \tag{2.27}$$

This model has also been considered a humidity-based model (Xu & Singh, 1998).

2.1.2.3.5 Hargreaves and Samani (1982, 1985)

The original Hargreaves model is considered a radiation model. However, due to the lack of readily available solar radiation data, the model was subsequently modified by Hargreaves and Samani (1982, 1985). Hargreaves and Samani (1982, 1985) recommended estimating ET from extraterrestrial radiation, R_A, and the difference between mean monthly maximum and minimum temperatures, TD (°C). This form of the equation is:

$$ET = 0.0023R_A TD^{1/2}(T + 17.8) \tag{2.28}$$

where R_A is expressed in equivalent evaporation units. As the only variable for a given location and time period is air temperature, the Hargreaves method has become a temperature-based method (Jensen et al., 1990).

This method implicitly accounts for relative humidity through the difference between the maximum and minimum temperature, as the temperature difference is linearly related to relative humidity (Hargreaves & Samani, 1982; Hargreaves & Allen, 2003). The temperature difference also implicitly accounts for the effects of cloudiness as the temperature range generally decreases with increasing cloudiness (Hargreaves & Allen, 2003).

The Hargreaves model is only recommended for use for five-day or longer time intervals (Hargreaves & Allen, 2003). This is because the influence of the temperature range, caused by the movement of weather fronts and by large variations in wind speed or cloud cover, causes errors for daily estimates.

According to Hargreaves and Allen (2003), the 1985 method has often been used to provide reference crop ET predictions for weekly or longer periods for many uses, including regional planning; reservoir operation studies; regional requirements for irrigation; and canal design capacities. The simplicity, reliability, minimum data requirements, and ease of computation make it an attractive method.

2.1.2.3.6 Kharrufa (1985)

Kharrufa (1985) derived an equation through correlation of ET/*p* and T:

$$ET = 0.34\,pT^{1.3} \tag{2.29}$$

where *ET* is in mm month^{-1}, and *p* is the percentage of total daytime hours for the period used (daily or monthly) out of the total daytime hours of the year (365×12).

2.1.3 Use and comparison of models in evapotranspiration investigations

Many authors have compared the performance of the different ET models. Some authors compared the ET estimates against measured ET values, while others compared the models using the PM ET as a benchmark. A review of these comparison studies has led to two main conclusions: (1) the PM model is generally accepted as a benchmark for comparing ET estimates from the different models, and, (2) when calibrated to local conditions, all models perform reasonably well, although the combination and radiation-based models tend to perform better than the temperature-based models.

The PM model, in either its original form or the FAO-56 reference form, is commonly used and accepted as a benchmark for comparing ET_0 models (Jensen et al., 1990; Amatya et al., 1995; Hargreaves & Allen, 2003). It is generally considered to be one of the more physically sound methods. Doorenbos and Pruitt (1977) recommend using combination models when measurements of humidity, temperature, wind, and radiation are available. Where data quality issues prevent the use of the full PM model, Hargreaves and Allen (2003) recommend using the FAO-56-PM model or the 1985 Hargreaves model. These two models have been shown to perform similarly over a wide range of climates.

Jensen et al. (1990) state that models that only use temperature as an input are generally inadequate for arid or semi-arid regions. They also reiterate that all existing models for estimating crop ET from climatic data involve some empiricism and, therefore, some validation or calibration to local or regional conditions is advisable with any selected model. This should be done using simultaneous measurements of crop ET and corresponding climatic data. However, where local crop ET measurements do not exist for calibration or validation, many authors use either pan evaporation or the FAO-56-PM model as the reference ET.

Jensen et al. (1990) compared nineteen models for evaluating ET on a monthly basis and thirteen models for evaluating ET on a daily basis, for a variety of locations and climates. These models included the PM model, Jensen-Haise, Doorenbos and Pruitt,

Priestley-Taylor, Turc, FAO-24 Blaney-Criddle, Hargreaves, Thornthwaite and pan models. The models were compared with lysimeter data. They were also adjusted using a coefficient based on a linear regression, between the estimated and measured data, though the origin. The radiation-based models were found to perform well in the humid locations but tended to underestimate the peak and seasonal ET in the arid climates. The air temperature models tended not to perform as well as the other methods. However, the Hargreaves and FAO-24 Blaney-Criddle models performed better than the Thornthwaite model due to the addition of other parameters such as solar radiation. The Thornthwaite model also had a lag in the peak ET estimate, as temperature tends to lag seasonally behind solar radiation.

On a monthly basis for arid locations, Jensen et al. (1990) found that the combination models performed the best, followed by the Doorenbos and Pruitt model. The FAO-24 Blaney-Criddle model ranked the highest of the temperature models. The Turc, Priestley-Taylor, and Thornthwaite models ranked the lowest. For humid locations the Turc and the Priestley-Taylor models compared very favourably with the combination models. For all locations the PM model ranked the highest. Following the combination models the Doorenbos and Pruitt, the FAO-24 Blaney-Criddle and the Jensen-Haise models ranked the next highest. The worst performing model was the Thornthwaite model, followed by the Priestley-Taylor and the Turc models. For the daily ET estimates, for all locations, the PM model ranked the highest, followed by the FAO-24 Blaney-Criddle model. The Priestley-Taylor model had the worst performance, followed by the Hargreaves and the Jensen-Haise models.

Amatya et al. (1995) compared the PM, Makkink, Priestley-Taylor, Turc, Hargreaves-Samani, and Thornthwaite models for estimating daily reference ET at three sites in eastern North Carolina. The PM model was used as the standard of comparison for evaluating the other models. A good correlation was found with all the models. In general, they found that the daily and mean monthly radiation-based models correlated well with the PM ET at all three locations. Overall the Turc model had the greatest comparison with the monthly and annual PM ET. All the other models were found to under predict the annual ET by as much as 16%, except the Hargreaves model, which

over predicted by an average of 15%. Their recommendation was to calibrate the models for each location.

Federer et al. (1996) compared a selection of temperature- and radiation-based models with combination ET models. Results were compared in terms of annual potential ET amounts. Similar to Jensen et al. (1990), they found the Hamon and Thornthwaite models exhibited a lag in ET as temperature lags seasonally behind solar radiation. In general all models were found to compare reasonably well, however, at a given location the differences in annual ET between the models were frequently hundreds of millimetres.

Following Federer et al. (1996), Vorosmarty et al. (1998) compared eleven ET estimates in a global-scale water balance model. The range in ET over all models varied considerably. They showed that the water balance model used was sensitive to the ET estimates and this affected the estimated actual ET and streamflow. Due to the influence of soil-moisture, the variation in actual ET was not as great as that in the potential ET.

Xu and Singh (1998) compared a temperature-based model (Thornthwaite), a humidity-based model (Romanenko), a radiation-based model (Turc) and a mass transfer model (Penman) to investigate their suitability for estimating ET. Monthly estimates were compared with monthly corrected pan evaporation values. The Penman model gave the best mean annual, seasonal and monthly ET estimates, while the Thornthwaite model followed by the Turc model gave the worst.

In a further study, Xu and Singh (2000) compared eight radiation-based models for estimating ET. The models were compared with pan evaporation, which was only measured at one location in Switzerland. Large errors resulted when using the original model constant values, but, when the recalibrated constants were used, all models performed well for determining the mean annual ET. The more physically based Makkink and modified Priestley-Taylor models compared most favourably with the pan data on a monthly scale.

Xu and Singh (2001) then compared seven temperature-based models for estimating ET. The models were compared with measured pan data. The models performed better when the constants of the models were recalibrated for the local conditions. All the models were found to produce reasonable mean seasonal values. For monthly ET values, the Blaney-Criddle, Hargreaves, and Thornthwaite models produced the least error for all months, with the Blaney-Criddle model having the best performance. This study again showed that using the original constant values of the models for other climatic areas led to large biases in estimating monthly evaporation.

Lu et al. (2005) compared three temperature-based ET models (Thornthwaite, Hamon, and Hargreaves-Samani) and three radiation-based models (Turc, Makkink, and Priestley-Taylor) using a monthly time step. The ET estimates were more variable among the temperature-based models than the radiation-based models. The ET estimates from the different models were highly correlated. Similar to Federer et al. (1996), they found that the magnitude of the ET estimates by the different models could vary by as much as 500mm/yr. In general, the Priestley-Taylor, Turc, and Hamon models performed better than the other ET models.

Trajkovic and Kolakovic (2009) compared the Hargreaves, Thornthwaite, Turc, Priestley–Taylor, and Jensen–Haise ET models against the FAO-56-PM model for seven humid locations using average monthly data. The Turc model was found to perform the best at the humid locations followed by the Priestley–Taylor, Jensen–Haise, Thornthwaite, and Hargreaves models. These results are similar to those reported by Jensen et al. (1990) and Lu et al. (2005).

Tabari et al. (2011) evaluated thirty-one reference ET models against the FAO-56-PM model in the humid climate of Iran. The radiation models all performed well with coefficients of determination all above 0.93. Of the temperature-based models the Blaney-Criddle model performed the best. The Blaney-Criddle, Jensen-Haise and Hargreaves models slightly overestimated the FAO-56-PM ET, while the Thornthwaite model underestimated it.

2.1.4 Evapotranspiration models and climate change

Several authors have compared the estimates of ET given by different models in response to climate change. The main conclusion of these studies is that different ET models can produce vastly different responses to climate change. The models that incorporate a greater number of the driving variables give the most realistic estimates of ET (e.g., McKenney & Rosenberg, 1993; Kingston et al., 2009; Donohue et al., 2010). Additionally, the differences in the ET estimated by different models can lead to large uncertainty in future water projections under climate change, and the different ET models can produce different climate change signals (e.g., Kay & Davies, 2008; Hobbins et al., 2008).

In an early study, McKenney and Rosenberg (1993) investigated the sensitivity of eight ET models to an increase in temperature of 2, 4 and 6°C. They found the Blaney-Criddle, Jensen-Haise, and Thornthwaite models to be most sensitive to an increase in temperature. The Hargreaves-Samani, Priestley-Taylor, PM and Penman models all had similar and mostly linear responses to an increase in temperature. In contrast the Thornthwaite model had a non-linear response with a greater rate of change at higher temperatures. They also concluded that the different ET models and the locations used lead to very different conclusions regarding the effect of a temperature increase on ET. The input data type for the models was also found to not be consistent with the trends in ET. The Blaney-Criddle model (temperature) and Jensen-Haise model (radiation) were both relatively sensitive to temperature change while the Hargreaves-Samani model (temperature) and combination models had a similar temperature response. They also examined the response of the ET models to general circulation model (GCM) derived scenarios of climate change using the change in temperature only, and also the change in all variables. For the temperature-based models, the ET always increased. However, for the PM model, when only temperature was changed the ET increased, but when the change in all variables was considered the ET decreased. They concluded that temperature models, which do not account for the influence of climate change on other climate elements, may give unreliable estimates of ET.

Kay and Davies (2008) compared the PM model against a temperature-based model for calculating ET from climate model data in Britain. The two models gave very different

ET estimates, which affect the modelled hydrological impacts. The GCM outputs always led to an increase in annual ET, which tended to be larger with the temperature-based ET. The PM ET was sometimes negative throughout the year. For the regional climate model output, the annual change in temperature-based ET was always positive but the PM ET was sometimes negative throughout the year. For some catchments the annual change in ET was of a different sign for the two ET estimates.

Hobbins et al. (2008) examined how two different parameterisations for ET influence long-term trends in soil moisture, evaporative flux, and runoff simulated by the water balance model which underlies the PDSI. The first parameterisation was based solely on air temperature, while the second was derived from observations of ET from class-A pans. The two different parameterisations led to trends in ET of opposite sign in almost half the locations tested in Australia and New Zealand. The choice of parameterisation was found to be most influential in energy-limited regions.

Kingston et al. (2009) investigated the response of six ET models to a 2°C increase in global mean temperature simulated using five different GCMs. The ET models used were the PM, Hamon, Hargreaves, Priestley-Taylor, Blaney-Criddle and Jensen-Haise models and the ET was calculated on a monthly basis. They assessed the impacts of the ET models using an aridity index (precipitation/ET) and regional precipitation minus ET water surplus. With the increase in temperature the ET increased at all latitudes for all models and all GCMs. However, the magnitude of the ET differed greatly between the models. At most latitudes the Hamon model produced the largest climate change signal followed by the Jensen-Haise model. The Hargreaves, PM and Priestley-Taylor models had similar responses. They found that the different ET models led to both positive and negative projections of future water resources. The change in aridity was also very different between the models. It was clearly shown that the choice of ET model leads to considerable uncertainty in the climate change signal.

Donohue et al. (2010) examined the Penman, Priestley-Taylor, Morton point, Morton areal and Thornthwaite ET models to assess their ability to capture the dynamics in evaporative demand in a changing climate in Australia. The ET dynamics were assessed by comparing the long-term trends against trends in precipitation, as ET and

precipitation are inversely related. The Penman model was found to be the most suitable model. An attribution analysis, using the Penman model, was performed to assess how each input variable contributed to the overall trend in ET. Temperature was found to lead to a large increase in ET, but this influence was outweighed and compensated for by the change in the other variables, which led to an overall decrease in ET. Changes in wind speed and albedo also played important roles in the dynamics of Penman ET. They concluded that under conditions of climate change all four variables may have different, even opposing, trends on ET. Therefore, ET models that only use one variable could give quite misleading results.

Liu and McVicar (2012) further showed for the Yellow River Basin, China, that the four driving meteorological variables could have different influences on ET and, therefore, fully physically-based ET formulations should be used as these account for the combined influence of all four key meteorological variables.

2.1.5 Interaction of evapotranspiration, soil moisture and temperature

The relationship between soil moisture, temperature, and precipitation has been well studied using both observational analysis (e.g., Vautard et al., 2007; Hirschi et al., 2011) and coupled land surface atmosphere models (e.g., Manabe, 1969; D'Andrea et al., 2006; van Heerwaarden et al., 2010). The relationship between temperature and evaporation is driven by interactions between the land surface and the lowest part of the atmosphere, known as the planetary boundary layer (PBL). It is well established that soil moisture can have a strong influence on the surrounding air temperature (e.g., Manabe, 1969; Durre et al., 2000; Vautard et al., 2007; Zhang et al., 2009; Seneviratne et al., 2010; Hirschi et al., 2011; Alexander, 2011). The land surface and PBL are a tightly coupled system (Santanello et al., 2005). The characteristics of the landscape (predominantly soil moisture) influence the atmosphere by controlling the division of net radiation into latent and sensible heat fluxes (Stensrud, 2007). Conversely, the atmosphere forces the land surface through precipitation, radiative, and momentum fluxes.

The relationships and feedbacks between temperature and evaporation are increasingly forming the basis of climatological analyses and projections (Milly and Dunne, 2011).

For example, several recent studies of the drought in the Murray-Darling basin (MDB) in Australia have linearly correlated maximum temperatures with rainfall and examined the residual temperature time series (e.g., Nicholls, 2004). The 2002 MDB drought had higher temperatures than expected from the fitted linear trend alone, which was interpreted as increased temperatures leading to increased evaporation and an exacerbation of the 2002 drought. In particular, Karoly et al. (2003) noted that whilst monthly rainfall totals were at extreme lows during the 2002 drought, the monthly average maximum temperatures were much higher than in previous droughts. This led the authors to state that "…the higher temperatures caused a marked increase in evaporation rates, which sped up the loss of soil moisture and the drying of vegetation and watercourses. This is the first drought in Australia where the impact of human-induced global warming can be clearly observed…" (p. 1).

Similarly, Nicholls (2004) investigated the anomalously high air temperatures that occurred during the 2002 cool season (May-October) in the MDB. This was achieved through a comparison to an identified negative correlation between average monthly temperature and average monthly rainfall between 1952 and 2002. Nicholls (2004) then examined the residual timeseries of the correlation, which demonstrated a statistically significant monotonic increase toward higher air temperatures over the period of the regression data. It was speculated that this was due to the increasing trend in atmospheric carbon dioxide and other greenhouse gases, and that "the warming has meant that the severity and impacts of the most recent drought have been exacerbated by enhanced evaporation and evapotranspiration" (p. 334).

Further studies have proposed that increased temperatures are the cause of reduced inflows into the MDB (Cai & Cowan, 2008), and that increased temperatures have led to decreased soil moisture in the MDB (Cai et al., 2009). These propositions would imply that increased evaporation is primarily a consequence of higher temperatures. However, in terms of physical mechanisms, it is the amount of evaporation that plays a major role in controlling the temperatures reached in the daytime, rather than vice versa (e.g., Dai et al., 1999; Lockart et al., 2009). The advantages of physically-based energy balance models have been noted by many authors, including Milly and Dunne (2011).

More precisely, the evolution of daytime temperatures are affected by numerous processes, including clouds, soil moisture, and land surface characteristics. Soil moisture is important as it controls the division of net radiation into latent and sensible heat. Clouds can also greatly reduce the diurnal temperature range by decreasing surface solar radiation. Passing synoptic systems can rapidly change surface air temperatures, although this generally only occurs on small timescales (days). Diurnal variations in surface wind direction can also influence the diurnal temperature range through advection of air mass with different humidity and temperatures (Dai et al., 1999).

Seneviratne et al. (2010) presented a comprehensive review of the interactions between soil moisture and climate. Soil moisture has its strongest influence on ET and temperature in soil-moisture limited environments, between a dry and a wet climate. Dry soil leads to less ET, which results in more sensible heat and higher temperatures. D'Andrea et al. (2006) used a coupled surface-PBL model to show that initial soil moisture conditions play a key role in determining if European summers will be dry or wet. Similarly, Hirschi et al. (2011), using observational analysis in Europe, showed that for locations where ET is limited by soil moisture, drier surface conditions led to hot extremes, particularly a higher number of hot days and longer heat wave durations. For the contiguous United States, Durre et al. (2000) showed that the distribution of summertime daily maximum temperatures, particularly near-record high temperatures, was shifted toward higher temperatures when the soil was dry.

2.1.6 Evapotranspiration summary

Evapotranspiration is an important component of many hydrological studies and is becoming increasingly important for estimates of future climate states. The drivers of ET include solar radiation, humidity, wind speed, soil moisture, and temperature. ET has a complex interaction with soil moisture and temperature. This interaction is often misunderstood, leading to potentially erroneous conclusions regarding the influence of temperatures on ET during drought conditions.

Whilst clearly important for climate studies, ET is very difficult to measure directly. There are, however, numerous models for estimating potential ET rates. These models vary in complexity and data requirements. In studies comparing the different models,

the combination and radiation-based models tend to perform better than the temperature-based models. The models also perform better when calibrated to local conditions. In studies investigating the influence of increased temperatures on ET, a common finding is that the different empirical models give vastly different changes in ET, even of different sign.

An important data requirement of the radiation-based ET models and the more physically based combination models is solar radiation. However, solar radiation measurements are also quite scarce. Methods for estimating solar radiation and its components is the focus of the next section of this review.

2.2 Solar Radiation

The sun is the primary source of energy for most natural processes, such as photosynthesis and evaporation. Knowledge of the radiation amounts reaching the earth's surface is therefore important for many applications such as hydrological modelling and agricultural management. The amount of radiation reaching the earth's surface is influenced by latitude and time of year, as well as the atmospheric properties of the region including absorption and scattering by gases, aerosols, and clouds.

The radiation from the sun has several components as shown in Figure 2.1.

Extra-terrestrial radiation (ETR) is the radiation from the sun before losses by atmospheric absorption. It is the radiation onto a horizontal plane, parallel to the ground, at the top of the atmosphere. It depends on the solar constant, the time of year and latitude (i.e., the orientation of the ground to the sun).

Net radiation is important for ET calculations. It is the balance between incoming and outgoing shortwave and longwave radiation. Net radiation is influenced by the sun's elevation, cloudiness, turbidity, albedo, temperature, the dryness of the atmosphere and altitude (Allen et al., 1998).

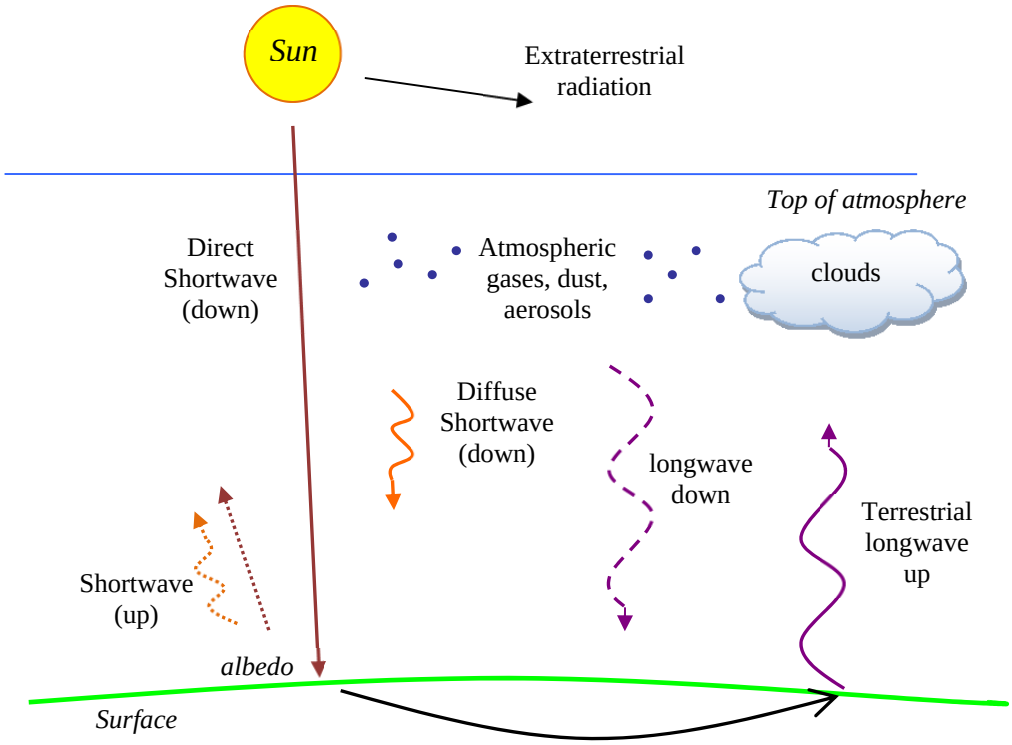

Figure 2.1 Components of solar radiation

Shortwave radiation, also known as solar radiation or global radiation, is the total incoming radiation and is composed of direct and diffuse radiation. The direct radiation, also known as beam radiation, is the unaffected shortwave radiation reaching the land surface. Interception of direct radiation is indicated by shadows on the ground. The diffuse radiation is the scattered shortwave radiation, for example radiation intercepted and scattered by aerosols, dust, or clouds. Diffuse radiation provides whatever illumination is present in a shadow. The outgoing shortwave radiation is that part reflected by the earth's surface and is dependent on the surface albedo.

Part of the energy absorbed by the earth's surface is radiated from the surface as terrestrial longwave radiation. This longwave radiation can subsequently be absorbed by atmospheric gases and emitted in all directions. The component that is emitted back to the surface is known as the downward longwave radiation.

Of all the radiation components, the direct shortwave is the main contributor to net radiation.

2.2.1 Global radiation

Direct measurements of global radiation exist, but these records are limited and in some countries have only recently begun. In contrast, many indirect methods are available that can be used to estimate global radiation, using readily accessible data such as temperature, humidity, and sunshine hours (SSH) data (Bristow & Campbell, 1984; Bakirci, 2009). Global radiation can be estimated by models that have a strong theoretical basis, by models based on empirical relationships, or a mix of the two. Often the approach used is dependent on data availability and computational requirements (Hay, 1993a).

Along with SSH, global radiation can be estimated from many climatic parameters including mean temperature, maximum temperature, relative humidity, number of rainy days, altitude, latitude, total precipitation, cloudiness, and evaporation. However, SSH is the most commonly used parameter for estimating global radiation, as SSH can be easily measured and data are widely available (Jain, 1990; Bakirci, 2009).

2.2.1.1 Theoretical/physical models

Theoretical approaches account for the physical influence of atmospheric components such as molecular gases, aerosols, and water vapour on the incoming global radiation. These generally include terms for the scattering of radiation by gases and aerosols, absorption by gases, and the scattering and absorption by clouds and the underlying surface.

The theoretical approach uses measurable atmospheric parameters such as optical density, surface reflectivity, amount of ozone and precipitable water (e.g., Hay, 1993a), type of cloud, cloud amount, thickness and number of cloud layers (Wong & Chow, 2001). This data is used in physically derived equations for scattering (e.g., Rayleigh and Mie scattering), transmission, and absorption by ozone and aerosols.

The most dominant influence on the intensity of global radiation at the earth's surface is the seasonal and diurnal variations in the ETR, which can be calculated using latitude, time of year, and time of day. In contrast, the processes of scattering and absorption in the atmosphere are not easily calculated and require some approximation due to the

uncertainty of the influence of clouds and the composition of the atmosphere (Hay, 1993a).

The processes of scattering and absorption of radiation in the atmosphere are explicitly treated in the radiative transfer equation, as given by Hay (1993a):

$$\frac{\mu dI_\lambda}{d\tau_\lambda} = -I_\lambda + \frac{\omega_0}{4\pi}\int_\omega I_\lambda(\tau_\lambda, y')p(\tau_\lambda, y', y)d\omega \tag{2.30}$$

where I_λ is the spectral radiation intensity at wavelength λ, μ is the cosine of the solar zenith angle, τ_λ is the atmospheric optical depth, $p(\tau_\lambda,\acute{y},y)$ is the scattering distribution or phase function from direction $\acute{y}$ into the direction y, ω_0 is the single scattering albedo, and ω is the solid angle.

When solved, the radiative transfer equation will give the total solar irradiance at the earth's surface after integration over azimuth and zenith angles, and then over the wavelengths of the solar spectrum. However, exact solutions are computationally intensive. The more usual approach is to simplify the radiative transfer equation and to separately account for cloudless and cloudy sky conditions (Hay, 1993a). Cloudy conditions often result in less accurate estimations than cloudless conditions due to the lack of data on the type, distribution, and properties of clouds.

For cloudless skies, Davies and Hay (1980) solve the radiative transfer equation for direct radiation where the spectral transmittance at normal incidence is expressed by Beer's law:

$$\frac{I_\lambda(\tau)}{I_\lambda(0)} = \exp\left(\frac{-\tau_\lambda}{\mu}\right) \tag{2.31}$$

The τ_λ term includes the principle scatter and absorption components. It is the aggregation of the optical depths due to absorption by ozone and water vapour, scattering by dry air molecules (Rayleigh), and absorption and scattering by aerosols. Numerical evaluation requires detailed knowledge of the spectral optical properties.

For cloudy conditions the approach given by Hay (1993a) as having the strongest physical basis is cloud layer models where the cloud is treated as occurring in distinctive layers, with each layer having its own characteristic transmissivity. In these models the cloud transmittances are usually calculated from:

$$t_i = a\exp(-bm) \tag{2.32}$$

where a and b are parameters that depend on cloud type (Davies & McKay, 1982; Hay, 1993a).

Davies and McKay (1982, 1989) give the general form of global radiation from layer models as:

$$G = G_{clear}\sum_{i=1}^{n}\Psi_i f(\alpha,\beta) \tag{2.33}$$

where G_{clear} is the cloudless sky irradiance, Ψ_i is the ith cloud layer transmittance, and $f(\alpha,\beta)$ is a function of surface albedo (α) and the atmospheric reflectivity for surface reflected irradiation (β) to calculate multiple reflections between the ground and atmosphere.

For cloud layer models using cloud amount the general form is:

$$G = G_0\prod_{i=1}^{n}(1-C_i+t_iC_i)(1-\alpha\beta)^{-1} \tag{2.34}$$

where C_i is the cloud amount and t_i is the transmissivity of an individual layer.

2.2.1.2 Empirical models

Due to the complexity and data requirements of the theoretical approach, many empirical methods for calculating global radiation have been developed. The empirical approach relates global, diffuse, and direct radiation to the ETR, and uses meteorological parameters such as SSH, relative humidity, and temperature. Empirical methods for calculating global radiation are simpler to use than theoretical models; however, the values of the empirical coefficients, usually determined by a regression analysis, tend to vary with location and season and thus are not easily transferred in time and space (Hay, 1993b). The values of the empirical coefficients can also change

depending on the averaging length of the data, i.e. different values are expected for daily versus monthly input data.

2.2.1.2.1 Angstrom-Prescott equation

From the many correlations that have been used for estimating global radiation, the most well-known is the Angstrom-Prescott equation (Angstrom, 1924), which estimates monthly mean daily global radiation from SSH data (*n*), scaled by the daylength (*N*) and the ETR. The SSH data is a measure of the amount of time the direct radiation from the sun is above a certain threshold.

The original model (Angstrom, 1924) is an empirical linear relationship between global radiation on a horizontal surface (*G*) (MJ m^{-2} d^{-1}) scaled by clear sky global radiation (G_{clear}) (MJ m^{-2} d^{-1}) and the mean daily sunshine fraction (*n/N*). The general form of the Angstrom equation is:

$$\frac{G}{G_{clear}} = a + (1-a)\frac{n}{N} \tag{2.35}$$

where *a* is a regression parameter specific to a location. It is generally recognised that *a* is equivalent to the mean proportion of radiation received on a completely overcast day (Mani & Rangarajan, 1983; Revfeim, 1997).

The original Angstrom equation used the ratio of the monthly average daily global radiation to the monthly average daily clear sky radiation. This considers the local effects on the atmospheric transmittance of solar radiation. In the modified form, these are considered with an additional constant.

It is difficult to obtain sufficient measurements of clear sky radiation for use in the Angstrom equation. Therefore, Prescott (1940) and Page (1961) modified the Angstrom equation to be based on ETR on a horizontal surface where ETR is easily calculated, rather than on clear sky radiation. A disadvantage of the Angstrom-Prescott equation is that it needs an additional parameter to account for the local effects on the atmospheric transmittance of solar radiation (e.g., due to water vapour) (Suehrcke, 2000).

The Angstrom-Prescott equation is suggested by the FAO-56 (Allen et al., 1998) for use in evaporation estimates. In this method global radiation *G* is given by:

$$\frac{G}{G_0} = a + b\left(\frac{n}{N}\right) \tag{2.36}$$

where G_0 is the daily total ETR on a horizontal surface, *a* and *b* are regression parameters, and *n/N* is the SSH fraction.

In equation (2.36), the coefficients are empirical; however, they have some physical explanation. The parameter *a* represents the fraction of ETR received during a completely cloudy day (when *n/N* =0). Conversely, the parameter combination (*a* + *b*) represents the overall mean transmission factor of global radiation under clear sky conditions (when *n/N* = 1) (Mani & Rangarajan, 1983).

Several factors influence the parameters *a* and *b*. Martinez-Lozano et al. (1984) suggested the factors include latitude, height of the station, reflection coefficient of the surface, mean solar altitude, water vapour concentration, and natural or artificial pollution concentration. In particular, Mani and Rangarajan (1983) showed that the magnitude of *a* is dependent on the type and thickness of the clouds, and *b* is dependent on the transmission characteristics of the cloud free atmosphere, particularly the total water vapour content and turbidity.

Gueymard et al. (1995) discussed some problems with the Angstrom-Prescott equation. The coefficients of the Angstrom-Prescott equation may change when different aggregating periods are considered. Cloudless days generally have a different turbidity and precipitable water to cloudy days, and cloud transmittance does not necessarily vary with total cloud cover. Martinez-Lozano et al. (1984) compared regression parameters between authors who used data from the same location and time period and they showed that the coefficients determined using one kind of data (e.g., monthly) are not interchangeable with those determined using a different set of data (e.g., daily or weekly).

2.2.1.3 Other empirical global radiation models

Since the introduction of the Angstrom-Prescott equation, many empirical estimates of monthly mean daily global radiation from daily SSH data have been developed. Bakirci (2009) presented a review of 60 models for global radiation calculated from SSH data. Many of the empirical models simply suggest parameter values for the Angstrom-Prescott equation and consequently parameter values have been calculated at many locations around the world (e.g., Black et al., 1954; Page, 1961; Rietveld, 1978).

Some authors have modified the Angstrom-Prescott equation to include various types of nonlinearities. For example, Akinoglu and Ecevit (1990) added a quadratic term:

$$\frac{G}{G_0} = 0.145 + 0.845\left(\frac{n}{N}\right) - 0.280\left(\frac{n}{N}\right)^2 \tag{2.37}$$

while Samuel (1991) and Ertekin and Yaldiz (2000) used a cubic model of the form:

$$\frac{G}{G_0} = a + b\left(\frac{n}{N}\right) + c\left(\frac{n}{N}\right)^2 + d\left(\frac{n}{N}\right)^3 \tag{2.38}$$

Almorox and Hontoria (2004) used an exponential model:

$$\frac{G}{G_0} = a + b.e^{\left(\frac{n}{N}\right)} \tag{2.39}$$

Newland (1989) and Ampratwum and Dorvlo (1999) added a logarithmic term:

$$\frac{G}{G_0} = a + b\left(\frac{n}{N}\right) + c\log\left(\frac{n}{N}\right) \tag{2.40}$$

Ogelman et al. (1984) derived an equation that used the monthly SSH fraction and its standard deviation ($\sigma_{n/N}$):

$$\frac{G}{G_0} = 0.204 + 0.758\left(\frac{n}{N}\right) - 0.250\left[\left(\frac{n}{N}\right)^2 + \sigma^2_{\frac{n}{N}}\right] \tag{2.41}$$

Rietveld (1978) examined published values for *a* and *b* and found that *a* is linearly related to the mean monthly value of *n/N*, while *b* is hyperbolically related to the mean monthly value of *n/N*:

$$a = 0.10 + 0.24\left(\frac{n}{N}\right) \tag{2.42}$$

$$b = 0.38 + 0.08\left(\frac{N}{n}\right) \tag{2.43}$$

This method was shown to achieve a greater accuracy than the use of constants for the coefficients when compared with the models of Black (1954) and Penman (1956), particularly for *n/N* values smaller than 0.40. However, Rietveld did not presume that the linear and hyperbolic functions had a general validity.

The Angstrom-Prescott equation can be further enhanced by using geographical and seasonal parameters to account for variations in latitude and season. Glover and McCulloch (1958) expressed *a* in terms of latitude (φ), while keeping *b* constant:

$$\frac{G}{G_0} = 2.09\cos\varphi + 0.52\left(\frac{n}{N}\right); \qquad \varphi < 60° \tag{2.44}$$

Gopinathan (1988a), using data from around the world, suggested that the coefficients were a function of the SSH fraction, altitude (*h*) and latitude:

$$a = -0.309 + 0.539\cos\varphi - 0.0693h + 0.290\left(\frac{n}{N}\right) \tag{2.45}$$

$$b = 1.527 - 1.027\cos\varphi + 0.0926h - 0.359\left(\frac{n}{N}\right) \tag{2.46}$$

Gopinathan (1988a) suggested that these coefficients could be used for any location around the world to estimate global radiation on a horizontal surface with an accuracy of about 10%.

Some authors have specified different coefficients based on the time of year. For example, Benson et al. (1984) provided a set of values for April to September and another set for the rest of the year. Similarly, Soler (1990a) derived coefficients for each month from Rietveld's model using data from 100 European locations.

Brooks and Brooks (1947) showed that the Campbell-Stokes SSH recorder, which measures the number of bright SSH in a day, usually only responds to sunshine when the sun is greater than 5° above the horizon. Accordingly, other authors such as Hay

(1979) have modified the Angstrom-Prescott equations to account for a reduced maximum bright daylight period.

Hay (1979) also accounted for multiple reflections between the land surface and the atmosphere for global radiation correlations. However, Jain (1986) incorporated these two effects into his study, both separately and together, and found that they did not offer any advantage over the Angstrom equation. In a further study, Jain and Jain (1988) noted that Jain (1986), due to lack of surface albedo data, assumed a common constant value of 0.2 for all seasons and locations. Jain and Jain (1988) then assessed the use of the equations incorporating the two effects using measured values of surface albedo. However, they still found that the inclusion of the Campbell-Stokes response and the multiple reflections did not significantly reduce the scatter of the parameter values. They did find that Hay's improvements slightly increased the correlation coefficients for all sites. They suggested that the effect of multiple reflections is only significant under some conditions, in regions where the surface albedo is high (>~0.3). The inclusion of the Campbell-Stokes response made no difference. It is worthy of note that Hay only studied both effects together.

2.2.1.4 Comparison of models and regional applicability

Many modifications have been made to the Angstrom-Prescott equation. However, the complex modified versions do not tend to offer any advantage due to the interdependency of the different variables. Many studies have been undertaken which compare the different methods for estimating monthly mean daily global radiation. The main conclusion is that the models generally perform equally well, although the linear models may perform slightly better.

Several authors examined the Angstrom-Prescott equation across various locations and proposed parameter values that may be applicable worldwide (e.g., Black et al., 1954; Penman, 1956). Other authors have incorporated latitude into the Angstrom-Prescott type equations to make the models more regionally applicable (e.g., Glover & McCulloch, 1958; Gopinathan, 1988c). Alternatively, Rietveld (1978) suggested that the coefficients could be derived from the relative sunshine duration of a location, and that this method was preferable to the use of worldwide constant coefficients. The

regression parameters have sometimes been suggested to be globally applicable, although many authors doubt their independence.

2.2.2 Direct and diffuse radiation

Knowledge of the amounts of direct and diffuse radiation is important for agriculture and ecosystem modelling and for modelling canopy photosynthesis. Diffuse and direct radiation differ in how they transfer through plant canopies, which affects the process of photosynthesis (Gu et al., 2002; Kanniah et al., 2012). Diffuse radiation can penetrate deeper into dense subcanopies and has been found to result in higher light use efficiencies by plant canopies (Roderick et al., 2001; Gu et al., 2002). Cloudiness can lead to increased amounts of diffuse radiation but this only leads to increased photosynthesis if the benefit of the increased diffuse radiation is not outweighed by the decrease in direct radiation (Alton, 2008).

The amounts of direct and diffuse radiation are functions of the factors that deplete the ETR as it travels through the atmosphere, such as solar altitude, water vapour, dust, and ozone. In a relatively clean atmosphere (nonindustrial location with small dust effects), the daily variation, with the sun at a fixed altitude, is primarily due to variation of the atmospheric water vapour (Liu & Jordan, 1960).

The intensity of direct radiation, unlike diffuse radiation, also varies according to the geometry of the terrain. Therefore, to calculate global radiation on a sloped surface, the amount of the direct and diffuse components needs to be explicitly known.

Direct and diffuse radiation measurements are limited; however, they can be calculated from theoretical and empirical models. The theoretical models account for absorption and scattering by various atmospheric constituents. These formulae require values of the concentration of ozone, water vapour, and particulate matter in the atmosphere. Empirical models, while not physically correct, are simpler, less data intensive, and hence are more commonly used.

2.2.2.1 Empirical models

Empirical models typically estimate direct and diffuse radiation from SSH, from the clearness index, or both. The clearness index k_t is given as:

$$k_t = \frac{G}{G_0} \tag{2.47}$$

where G is the global radiation and G_0 is the extraterrestrial radiation.

The diffuse fraction has a strong relationship with the clearness index and this relationship is commonly used to estimate diffuse radiation (e.g., Liu & Jordan, 1960; Page, 1961; Ruth & Chant, 1976; Erbs et al., 1982; Hollands & Crha, 1987; Jain 1990). Other authors have correlated direct and diffuse radiation with SSH measurements and ETR (Hay, 1976; Iqbal, 1979; Benson et al., 1984; Garg & Garg, 1985; Jain, 1990). A third type correlates direct and diffuse radiation with both SSH and global radiation (Benson et al., 1984; Gopinathan 1988b, 1988c; Al-Hamdani et al., 1989; Al-Riahi et al., 1992; Tiris et al., 1996). Some of the hourly k_t models have different equations for different clearness values (e.g., Orgill & Hollands, 1977; Erbs et al., 1982; Reindl et al., 1990).

Further models have been developed to estimate direct and diffuse radiation that use additional variables, such as solar altitude, humidity, cloudiness and temperature data (e.g., Collares-Pereira & Rabl, 1979; Skartveit & Olseth, 1987; Reindl et al., 1990; Coppolino, 1990, 1991; Munawwar & Muneer, 2007). Coppolino (1990, 1991) calculated monthly mean daily diffuse radiation from the clearness index and minimum air mass. Munawwar and Muneer (2007) developed a series of empirical models to calculate daily diffuse radiation from sunshine fraction, a cloudiness factor, and the daily clearness index.

Reindl et al. (1990) assessed twenty-eight potential variables using correlation analysis to predict hourly diffuse radiation. A stepwise regression found four significant predictors: (1) the clearness index, (2) solar altitude, (3) ambient temperature, and (4) relative humidity. Note that they did not assess SSH as a predictor. The clearness index was found to be the most important variable at low and mid clearness index intervals,

but decreased in significance at high intervals. Solar altitude was found to be more important for clear skies than cloudy skies and was found to be the dominant predictor variable for clear skies. The diffuse fraction, under clear skies, was found to increase with decreasing solar altitude angles due to the longer path length of the radiation. Iqbal (1980) and Skartveit and Olseth (1987) also suggested that the solar altitude is an important predictor variable for diffuse radiation.

While the global radiation models tend to give a monthly mean daily average, the diffuse radiation models related to global radiation have been developed for many timescales ranging from hourly (Orgill & Hollands, 1977; Iqbal, 1980; Erbs et al., 1982; Al-Riahi et al., 1992; Posadillo & Lopez Luque, 2009), to daily (Ruth & Chant, 1976; Collares-Pereira & Rabl, 1979), and monthly (Liu & Jordan, 1960; Al-Hamdani et al., 1989). The SSH based models tend to use a monthly mean daily timescale (e.g., Barbaro et al., 1981; Benson et al., 1984; Garg & Garg, 1985; Gopinathan 1988c), although Gopinathan (1992) used a monthly mean hourly estimation of global and diffuse radiation from hourly SSH measurements.

2.2.2.1.1 Liu and Jordan (1960) type model

The most well-known method for determining diffuse radiation, and the basis of many others, is that by Liu and Jordan (1960), which relates diffuse radiation to the clearness index. Liu and Jordan (1960), using data from one location (Blue Hill, Mass.) presented relationships for determining, on a horizontal surface, the instantaneous intensity of diffuse radiation on clear days along with long term hourly average and daily sums of diffuse radiation for days with differing amounts of cloud cover. These estimates required the global radiation on a horizontal surface to be known.

Their work showed that for average conditions, the daily diffuse radiation (G_d) could be determined from the daily global radiation (G) and the ETR (G_0) using linear regression:

$$\frac{G_d}{G} = c + d\left(\frac{G}{G_0}\right) \tag{2.48}$$

where c and d are regression parameters.

Subsequent investigations have used higher powers of G/G_0 to gain a greater accuracy (e.g., Barbaro et al., 1981). In a further study, Hay (1976) added a term to account for the multiple reflections between the ground and the atmosphere.

The disadvantage of using the clearness index is that global radiation measurements are needed. In contrast, SSH data is more readily available than global radiation data and has become the most dominant parameter for the estimation of diffuse as well as global radiation (Jain, 1990).

2.2.2.1.2 Models relating direct and diffuse radiation with sunshine hours

Several models have been developed that estimate monthly average daily diffuse and direct radiation from SSH and ETR. Different higher order equations have also been proposed.

For the diffuse radiation, Garg and Garg (1985), Gopinathan (1992) and Tiris et al. (1996) proposed a linear model:

$$\frac{G_d}{G_0} = a + b\left(\frac{n}{N}\right) \tag{2.49}$$

Iqbal (1979), Barbaro et al. (1981), Garg and Garg (1985) and Gopinathan (1988b) also used a quadratic model:

$$\frac{G_d}{G_0} = a + b\left(\frac{n}{N}\right) + c\left(\frac{n}{N}\right)^2 \tag{2.50}$$

For the direct radiation (G_b), Tiris et al. (1996) used a linear model:

$$\frac{G_b}{G_0} = a + b\left(\frac{n}{N}\right) \tag{2.51}$$

Iqbal (1979), Benson et al. (1984) and Garg and Garg (1985) used a quadratic model:

$$\frac{G_b}{G_0} = a + b\left(\frac{n}{N}\right) + c\left(\frac{n}{N}\right)^2 \tag{2.52}$$

While Benson et al. (1984) also used a cubic model.

The preferred diffuse and direct radiation models tend to be the quadratic versions (Iqbal, 1979; Barbaro et al., 1981; Bensen et al., 1984).

2.2.2.2 Comparison of models and regional applicability

Many authors have compared their Liu and Jordan type equations for estimating diffuse radiation from global radiation with those from other studies and found minimal difference. For example, Erbs et al. (1982) found their results compared very well with those of Orgill and Hollands (1977).

Other authors have compared the performance of the prediction of diffuse radiation calculated from global radiation with that calculated from ETR and SSH. Barbaro et al. (1981), using data from three Italian locations, compared the performance of the two methods for determining monthly mean diffuse radiation, and found both methods to perform similarly well and produce results very close to the experimental data. Garg and Garg (1985) also found both methods to be equally suitable for estimating diffuse radiation across eleven locations in India.

Benson et al. (1984) advocated using regressions with SSH duration to find the direct and diffuse component, rather than using regression with the global component, as there is more SSH data and less scatter in the predictions.

There is no consensus in the literature as to the worldwide applicability of the direct and diffuse coefficients. Ruth and Chant (1976) used a monthly Liu and Jordan type correlation to show that their correlations exhibited latitude dependence. In contrast, Srinivasan et al. (1986) used a seasonal (one parameter set per season) Liu and Jordan type correlation to compare their model curve to that of other authors, and showed that the diffuse fraction was not overly latitude dependent. However, this could have been influenced by the different seasonal parameter sets. Their correlations displayed a seasonal dependence: although spring, summer, and autumn were similar, winter was quite different. This was attributed to the cooler months having a lower diffuse fraction than the other months (drier air and less dusty).

Soler (1990b) examined the dependence of the coefficients of the Liu and Jordan type equation to latitude for European locations with latitudes in the range 36°N to 61°N. Although only latitude was examined, Soler suggested that the coefficients were complex functions of atmospheric conditions and relative SSH, as well as latitude. Higher latitudes are generally characterised by larger air mass.

Benson et al. (1984), using daily and monthly correlations, found no seasonal influence in the correlations of daily direct and diffuse radiation. This occurred despite winter being characterised by predominantly clear or very overcast days, while summer consisted of mostly partly cloudy conditions. In contrast, the monthly correlations showed a difference between the coefficients for summer and winter conditions.

Garg and Garg (1985) found that the direct radiation in India was highly dependent on local conditions. However, the diffuse radiation could have one equation applied to several locations collectively. The linear G_d/G_0 model correlated with SSH was found to perform better for regional regression in India than the G_d/G model.

2.2.2.3 Transmission of direct and diffuse radiation

The transmission of direct radiation through the atmosphere varies with latitude, altitude, and season, and also varies throughout the day. This is due to the changing optical air mass. The optical air mass is the length of the atmospheric path traversed by the sun's rays in reaching the earth, measured in terms of the length of this path when the sun is in the zenith. A longer path length results in less transmission of direct radiation. According to List (1968), for a zenith distance of the sun (z) less than 80°, the optical air mass is approximately equal to sec$z$.

List (1968) gives a basic formula for calculating the direct radiation on a horizontal surface in time (t) as:

$$\frac{dG_b}{dt} = \frac{J_0}{r^2} a^{\sec z} \cos z \tag{2.53}$$

where a is the transmission coefficient of the atmosphere, r is the radius vector of the earth, J_o is the solar constant and secz is equal to:

$$\sec z = \frac{1}{\sin\varphi \sin\delta + \cos\varphi \cos\delta \cos\omega} \tag{2.54}$$

where φ is the latitude, δ is the sun's declination and ω is the sun's hour angle.
For the period of sunrise to sunset, δ can be assumed constant for one day.

The J_o/r^2cos$z$ term gives the ETR (G_o). Therefore, the daily transmission of direct radiation can be written as:

$$G_b = G_0 a^{\sec z} \tag{2.55}$$

This method was also used by Garnier and Ohmura (1968, 1970) and Varley et al. (1993). Garnier and Ohmura (1968) cautioned that this approximation underestimates the solar energy at low sun altitudes. However, assuming that a maximum underestimation of 10% in daily totals is acceptable, this error is never exceeded on a horizontal surface within 35° of the equator. Williams et al. (1972) followed the procedure of Garnier and Ohmura (1968) for direct radiation. They suggested that the major contribution of direct radiation to global radiation was around solar noon, when any error in secz will be small. Revfeim (1976) also discussed the use of an optical air mass with secz exponent. They warned that the secz approximation is larger than the true optical air mass for z>60°.

Monteith (2007) likewise used a^{secz} for direct radiation transmission. Monteith suggested that for values of zenith angle less than 80°, the air mass (m) at a location could be given by:

$$m = \frac{p}{p_0} \sec z \tag{2.56}$$

where P is the location's atmospheric pressure, and P_0 is the standard atmospheric pressure at sea level.

Hottel (1976) gave the transmittance of direct radiation through the atmosphere (a) in clear conditions as:

$$a = a_0 + a_1 e^{k \sec z} \tag{2.57}$$

where a_0, a_1 and k are constant parameters. Secz is again used to approximate the air mass.

The diffuse radiation in List (1968; attributed to Fritz) under cloudless conditions is given by the assumption that, of the radiation that is scattered (i.e., not direct radiation), half is scattered forward and half scattered backwards. This is only strictly correct when the scattering particles are small compared with the wavelength of light.

Therefore, to calculate global radiation following the List method, the ETR is first calculated followed by the direct radiation, which is subtracted from the ETR. Half of the remainder is the diffuse radiation. The sum of the direct and diffuse radiation is the global radiation. This procedure was also used by Houghton (1954), Williams et al. (1972) and Varley et al. (1993).

2.2.3 The influence of clouds on radiation

The influence of clouds on the amounts of global, direct, and diffuse radiation is difficult to account for. Different cloud properties influence the global, direct, and diffuse radiation in different ways. In completely clear conditions, variations in the amount of global radiation occur with varying atmospheric turbidity and water vapour content. Under overcast conditions, additional variation occurs due to the type of the cloud cover (Benson et al., 1984). At a given level of sunshine, variation in the amount of global radiation can occur for partly cloudy conditions due to the varying cloud transmissivities for different types and thickness of clouds. Houghton (1954) discussed that the magnitude of absorption and scattering by clouds is dependent on cloud height, depth and density, the vertical distribution of the water vapour, and the suns zenith angle.

McCormick and Suehrcke (1991) found that their diffuse fraction – clearness index correlations had relatively wide scatter. McCormick and Suehrcke (1991) showed that two separate hours could have the same clearness index, but very different diffuse fractions depending on the type of cloud cover. Bugler (1977) suggested that a

significant source of scatter was the variety of cloudiness states possible for a given hourly clearness index value. Similarly, Erbs et al. (1982) suggested that the diffuse fraction was dependent on the type and distribution of clouds in the sky during the hour. Further to this, Benson et al. (1984) also stated that at zero sunshine, rainfall conditions significantly decreased the global radiation below what was experienced for cloudy conditions. Rain clouds are generally darker than non-precipitation clouds.

With increasing cloudiness, both direct and global radiation should decrease, while the additionally scattering should lead to an increase in the diffuse radiation. However, a heavier cloud presence will also decrease the diffuse radiation. The extent of the influence of the cloudiness effect should be smaller for the global radiation than the direct and diffuse radiation due to the partially compensating effect of the opposite trends in the direct and diffuse components.

2.3 Sunshine Hours and the Campbell-Stokes Recorder

Bright SSH are recorded at many locations around the world and can be used to estimate global, direct and diffuse radiation. Bright SSH can be measured using a variety of instruments. The most common in Australia and many parts of the world is the Campbell-Stokes (CS) recorder. This device responds to the direct radiation reaching the earth's surface. A sphere of glass focuses the sun's rays onto a strip of cardboard and burns a trace. The length of the burn trace is a measure of the number of bright SSH that occurred during the day (World Meteorological Organization, 2008).

One of the limitations of the CS recorder is that direct radiation needs to reach a threshold before the paper will begin to burn. This threshold is given as 120 Wm^{-2} by the WMO (2008). Painter (1981) gave the threshold range as 16–400 Wm^{-2}, with an average threshold of 170 Wm^{-2}. The threshold range can be attributed to differences in humidity. For example, when humidity is high, the card may become damp and require more intense radiation to burn. The threshold can also increase if dew or other water deposits are present on the glass sphere (Painter, 1981; Benson et al., 1984).

The threshold has also been shown to be dependent on sun angle and time of year (e.g., Brooks & Brooks, 1947; Painter, 1981; Kerr & Tabony, 2004). Brooks and Brooks

(1947) showed that the CS recorder responded later in the day in summer than in winter. In contrast, Painter (1981) showed that winter had a higher threshold of burning than summer due to the generally lower temperatures and damper conditions. Kerr and Tabony (2004) showed that a CS recorder overestimated sunshine amounts by approximately 20% in summer and 7% in winter. They attributed the seasonal difference to the influence of solar elevation.

There is also potential for inaccurate readings, quality of the paper, and maintenance issues. Benson et al. (1984) showed that CS recorders can underestimate the SSH at low sun angles. The length of the burn can also affect the daily reading during intermittent strong sunshine (Painter, 1981). Painter (1981) suggested that the burn will spread on days with intermittent strong sunshine. This can produce an overestimation of sunshine durations due to the actual width of burn mark. Overburn will be minimal on days with continuous sunshine. Therefore, the CS recorder is more accurate in completely clear or overcast conditions. It was also shown that the overburn of cards is less in winter than summer due to the lower irradiances that occur in winter.

A further limitation of the CS recorder is that it only records the period for which the direct radiation exceeds the threshold, and does not record the intensity of the radiation reaching the earth. Additionally, the CS recorder does not respond to diffuse radiation (Brooks & Brooks, 1947).

Sunshine duration is commonly recorded as a daily total. A primary disadvantage when using daily SSH estimates is that it is unknown when during the day the bright sunshine occurred. Bright sunshine at different parts of the day have different contributions to the daytime total radiation – an hour in the middle of the day will contribute more radiation than an hour at the start or end of the day. To counter this, common methods for estimating solar radiation calculate deterministic values of the radiation for a monthly timescale. These methods assume that the SSH measurement is averaged across the day (Revfeim, 1997). There is additional uncertainty due to the influence of clouds on the attenuation of the solar radiation. While these factors can be averaged out over long time periods (e.g., for monthly estimates), this is not useful for short term estimates.

Other authors have recognised that hourly SSH data is needed for more accurate results (e.g., Schulze, 1976; Revfeim, 1981; Yeboah-Amankwah & Agyeman, 1990). For example, Revfeim (1981) developed a model to calculate global radiation from hourly SSH fractions. This model gave improved estimates of global radiation. Although hourly data can lead to improved estimates of global radiation, hourly data is not always readily available. In recognition of this limitation, Revfeim (1997) presented a model to estimate hourly sunshine from daily data using a weighting factor, with a greater concentration around noon. This method replaces the hourly recorded sunshine fractions with a plausible pattern of sunshine for the daily fraction.

Despite the uncertainty associated with SSH measurements, the common methods for estimating solar radiation are purely deterministic – they estimate monthly values of the radiation based on average daily SSH measurements. A monthly estimate is used to average out errors and uncertainty due to the timing of bright hours and uncertainty of cloud effects on the attenuation of the radiation. This approach gives no indication of errors or uncertainty associated with daily radiation estimates.

2.4 Satellite Measurements of Global Radiation

The Bureau of Meteorology currently uses computer models to estimate global irradiance over a day from satellite data. These computer models use visible images from the geostationary meteorological satellites, taken every hour, to estimate daily global solar exposures at ground level (BoM, 2013). The procedure involves analysis of the brightness levels of each pixel, averaged over at least four pixels, and integrated over the entire day. The pixels contain 1024 different brightness levels and cover an area of 1.25 by 1.25 km at the equator, and a larger area at mid-latitudes.

The ground irradiance is calculated from the irradiance at the top of atmosphere, cloud albedo, surface albedo, and atmospheric absorption. The irradiance (*I*) at the ground is estimated from:

$$I_{\text{ground}} = I_{\text{Top of Atmosphere}} - I_{\text{Cloud Albedo}} - I_{\text{Surface Albedo}} - I_{\text{Atmospheric Absorption}} \tag{2.58}$$

The largest source of uncertainty in the estimate is associated with the reflectance from the clouds. As the top of the clouds are irregularly shaped, the reflectance from any cloud can vary with the relative positions of the sun and satellite. According to BoM (2013), this introduces an error of 5% into the model. The estimation of water vapour in the atmosphere also introduces an error of approximately 2%.

The computer models were calibrated against the ground-based measurements (BoM, 2013). A comparison of the satellite estimates with the ground-based pyranometer data led to the conclusion that the satellite model has an error of 7% or better in clear sky conditions and up to 20% in cloudy conditions. In terms of the accuracy of predictions in relation to the location of the pyranometer, the satellite method is given as more accurate than using the pyranometer at a distance typically 40 km from the pyranometer.

Weymouth and Le Marshall (2001) compared the satellite and ground-based estimates at twelve Australian locations from July 1997 to April 1998. The locations included Adelaide, Alice Springs, Broome, Darwin, Mildura, Mt. Gambier, Tennant Creek and Wagga Wagga. The overall difference between the observed and modelled estimates was 6.2%. The largest error over all conditions occurred at Cairns with 9.06% error, as Cairns experienced large cloud variations throughout the year. The smallest error was 4.71% at Wagga Wagga.

2.5 Summary

This chapter presents a summary of the available literature on ET modelling, global, direct and diffuse radiation modelling, and the use of SSH data for radiation modelling. It is evident that ET is important for many hydrological studies; however, the fundamentals of the relationship between temperature and ET are sometimes misunderstood and/or poorly represented in empirical models.

Whilst important for many hydrological applications, ET is difficult to measure. This has led to the formation of many empirical models for estimating ET. These models have different data requirements, although the more commonly used and most accepted models require an estimate of global radiation as an input. It is further shown that estimates of global radiation are also quite scarce; however, many empirical models have been formed to estimate global radiation and its components. Most of these models estimate the radiation from SSH data. These models are generally deterministic, do not account for the timing of the 'bright' hours during the day, and do not provide an estimate of the errors associated with the radiation predictions. Consequently, there exists a need for a stochastic model that estimates the radiation and its components from sunshine hours, and explicitly accounts for the variability in the estimate due to the timing of the bright hours, as well as any external influences on the radiation.

Chapter 3 - Stochastic Radiation Model Development

Overview

The previous chapter highlights a need for a stochastic model to estimate global radiation and its components and also provide a measure of the uncertainty in the estimates. This chapter develops several different stochastic models that use daily SSH data to produce probabilistic predictions of global, direct and diffuse radiation, including associated uncertainties. Five global models, three direct models and five diffuse radiation models are developed. The models differ in the parameterisation of the diffuse and direct portions of the global radiation, using either no scaling, linear or quadratic scaling of the radiation by the daily SSH fraction to account for the attenuation of radiation by clouds. Two sources of predictive uncertainty are considered: (i) the timing of the SSH during the day and (ii) external errors such as variability in cloud type and amount. The models are calibrated under different residual error assumptions, including constant, linear and quadratic variances related to SSH fraction and the simulated radiation.

This chapter also summarises the meteorological data used in the analysis of the radiation models. Nine main locations that have observations of global, direct and diffuse radiation for an extended number of years are used in the development of the stochastic radiation models. These locations cover a range of climate conditions. The observations from an additional eleven locations are also used in the development of the regional radiation models.

3.1 Data

The data used in the development of the stochastic radiation models comprises daily SSH measurements and ground-based measurements of half-hourly global, direct and diffuse radiation. All data was provided by the Bureau of Meteorology (BoM, 2013). The SSH data was measured with a CS recorder while the ground-based global radiation

was measured with a pyranometer. The measurement uncertainty for SSH duration is ±0.1 h with a resolution of 0.1 h (WMO, 2008). The ground radiation measurements are aggregated to give daily estimates. Only days with complete records of radiation and SSH are used. In addition, daily estimates of satellite-derived global radiation were obtained to compare against the modelled global radiation.

Only nine locations have global, direct and diffuse radiation data along with SSH data for the same time period covering at least seven years from 1999 to 2010. These locations are used for the development and assessment of the stochastic SSH models. The models are calibrated using data from 2003-2005. This period was selected as continuous daily data is available at each of the locations. Three years is chosen in an attempt to encompass a wide range of radiation and rainfall variability. The remaining data is used to validate the models.

Aside from the nine main study locations, eleven other locations have observed radiation measurements. The observations from these locations are used in the development of a regional version of the stochastic models.

3.2 Climatology

The climatology of the main nine locations and the additional eleven locations is detailed in this section.

3.2.1 Main nine study locations

The following nine locations are used in the development and analysis of the stochastic radiation models. The locations used and the SSH and rainfall statistics for these locations are listed in Table 3.1.

Table 3.1 Data for the nine main locations used.

Location	Station No.	Years	Latitude	SSH fraction	No. days n/N>0.8	No. days n/N<0.3	Rain days >0mm	Av.Ann Rainfall (mm)	Av. 9am Humidity (%)
Adelaide	23034	2003-2010	-34.95	0.631	144	64	108	394.7	61
Alice Springs	15590	1999-2010	-23.80	0.810	256	31	43	314.4	40
Broome	3003	1999-2010	-17.95	0.817	272	20	62	742.7	55
Darwin	14015	1999-2010	-12.42	0.720	202	40	125	1769.9	69
Melbourne	86282	1999-2010	-37.67	0.535	89	91	135	460.3	69
Mildura	76031	1999-2005	-34.24	0.725	204	41	66	242.7	63
Mt Gambier	26021	1999-2006	-37.75	0.536	88	93	190	692.7	75
Tennant Creek.	15135	1999-2006	-19.64	0.806	256	27	55	570.2	39
Wagga Wagga	72150	1999-2010	-35.16	0.686	192	62	97	504.7	66

Each of the locations has a different climate. According to BoM (2013):

- Adelaide, located in South Australia, has a temperate climate with warm dry summers and cold wet winters.
- Alice Springs, located in inland Northern Territory around central Australia, has a grassland climate and is arid with low rainfall.
- Broome, located on the coast of Western Australia, also has a grassland climate with a marked wet summer and dry winter.
- Darwin, located on the coast of the Northern Territory, has a tropical climate with a marked wet summer and dry winter.
- Melbourne, located on the coast of Victoria, has a temperate climate with uniform rainfall throughout the year and no dry season.
- Mildura, located in inland Victoria, has a grassland climate. It is warm and persistently dry with a wet winter and low summer rainfall.
- Mount Gambier, near the coast in the south of South Australia, has a temperate climate with a wet winter and low summer rainfall.
- Tennant Creek, located in inland Northern Territory, to the north of Alice Springs, has a grassland climate and is arid with low rainfall in winter.
- Wagga Wagga, located in inland New South Wales, has a temperate climate with no dry season.

3.2.2 Additional eleven locations

Along with the main study locations, the following eleven locations are used in the development of the regional stochastic models. The locations are listed in Table 3.2.

Table 3.2 Data for the additional eleven locations used.

Location	Station No.	Years	Latitude	SSH fraction	No. days n/N>0.8	No. days n/N<0.3	Rain days >0mm	Rainfall mm
Brisbane	40223	1983-1995	-27.42	0.664	173	60	124	1081.4
Cairns	31011	1999-2003	-16.87	0.641	152	60	156	1847.8
Canberra	70014	1983-1994	-35.30	0.621	131	62	107	636.1
Halls Creek	2012	1970-1980	-18.23	0.792	238	26	67	544.1
Hobart	94008	1968-1980	-42.83	0.496	64	98	146	514.8
Laverton	87031	1968-1980	-37.86	0.514	78	100	149	587.3
Oodnadatta	17043	1969-1980	-27.56	0.800	258	33	35	215.2
Perth	09021	1975-1980	-31.93	0.702	182	36	108	672.5
Sydney	66037	1983-1994	-33.95	0.600	153	79	130	1136.4
Williamtown	61078	1969-1979	-32.79	0.591	134	84	147	1145.4
Woomera	16001	1968-1979	-31.16	0.759	230	37	55	244.1

The climate of these locations is as follows:

- Brisbane, located on the coast in the south of Queensland, has a subtropical climate with a wet summer and low winter rainfall.
- Cairns, located on the coast in the north of Queensland, has a tropical climate with a marked wet, humid summer and dry winter.
- Canberra, located in inland New South Wales, has a temperate climate with uniform rainfall throughout the year.
- Halls Creek, located in inland Western Australia, has a grassland climate with a marked wet summer and dry winter.
- Hobart, located in Tasmania, has a temperate climate with uniform rainfall throughout the year.
- Laverton, located next to Melbourne, has a very similar climate to Melbourne.
- Oodnadatta, located in inland South Australia, has a desert climate and is arid, hot and persistently dry.
- Perth, located on the coast in the south of Western Australia, has a subtropical climate with a distinctly wet winter and dry summer.

- Sydney, located on the coast of NSW, has a temperate climate and has no dry season with uniform rainfall.
- Williamtown, also located on the coast of NSW, has a temperate climate and has no dry season with uniform rainfall.
- Woomera, located in inland South Australia, has a desert climate and is hot and persistently dry. It is arid with low rainfall.

3.3 Stochastic Radiation Model Overview

For any given day, the daytime ETR G_0 and the day length N can be calculated from the time of year and latitude. Also known is the number of bright SSH observed on that day, n. Since the ETR is the dominant control on the radiation reaching the top of the atmosphere and is readily calculated, all the radiation models use ETR as the upper bound on the estimate of daily radiation.

The ETR is depleted through absorption and scattering as it passes through the atmosphere. With a constant atmospheric consistency, all sunny, clear days should have the same transmittance of ETR in the form of direct radiation. This can be parameterised by a transmission coefficient A_{dir}. Following List (1968), Garnier and Ohmura (1968), Hottel (1976), Revfeim (1981) and Varley et al. (1993), the transmission coefficient is scaled by sec$z$, where z is the solar zenith angle, to account for changing air mass (path length through atmosphere) with season, time of day, altitude and latitude. A longer path length results in less transmission of direct radiation.

$$R_{direct} = A_{dir}^{\sec z} G_0 \tag{3.1}$$

where R_{direct} (MJ m^{-2} d^{-1}) is the direct radiation, G_0 is the extra-terrestrial radiation (MJ m^{-2} d^{-1}) and sec$z$ is the secant of the solar zenith angle z (rad).

The composition of the atmosphere ensures that there is always some diffuse radiation present (Sen, 2008). Even when no clouds are present, the gases, aerosols and dust ensure some of the ETR is scattered towards the earth. As the cloudiness increases, more ETR is scattered, increasing the amount of diffuse radiation. However, as the SSH fraction, n/N, drops below about 0.45, the diffuse radiation decreases as the clouds

prevent more of the scattered light from reaching the surface. On completely overcast days the clouds prevent essentially all direct radiation from reaching the land surface and only allow a minimal amount of diffuse radiation to reach the land surface.

The diffuse fraction is generally thought to be less than 0.5 if, following List (1968), it is assumed that all the attenuated radiation is scattered (no absorption) and half of that radiation is scattered to the ground. The diffuse fraction parameter A_{diff} gives the amount of ETR converted to diffuse radiation on a completely cloudy day.

$$R_{diffuse} = A_{diff} G_0 \tag{3.2}$$

The five models developed in this study differ in how they represent the influence of clouds and in the formulation of the direct and diffuse components. Clouds are difficult to incorporate into radiation estimates as they are highly variable in space and time (Hay 1993a). It is often very difficult to define the amount and properties of clouds. Two days could have the same SSH measure but have different types and amounts of clouds with different attenuation of the radiation – the bright hours could have direct radiation intensities just above the threshold or close to the maximum possible ETR.

As SSH is the only directly measured variable, the SSH fraction n/N is used as a scaling factor to reduce the amount of direct radiation on cloudy days and to scale the amount of diffuse radiation for different cloud conditions. Similar to Angstrom (1924) and Rietveld (1978), the models developed use the assumption that as SSH decreases, the cloudiness increases and so the density of the cloud may also increase, which results in a decrease in transmission of ETR. Each model uses a different scaling process to calculate the fraction of ETR transmitted.

The day length N is used to give the maximum number of bright hours possible on a given day. The ETR and day length calculations are as given in the FAO-56 (Allen et al., 1998) and are widely used for evaporation estimates.

The ETR, G_0, as given by the FAO-56 guide, for each time period h, is calculated using:

$$G_{0,h} = \frac{12(60)}{\pi} G_{sc} d_r \left[(\omega_2 - \omega_1) \sin(\varphi) \sin(\delta) + \cos(\varphi) \cos(\delta) \left(\sin(\omega_2) - \sin(\omega_1) \right) \right] \quad (3.3)$$

where G_{sc} is the solar constant (0.0820 MJ m^{-2} min^{-1}), d_r is the inverse relative sun-earth distance, ω_1 is the solar time angle at the beginning of the period (rad), ω_2 is the solar time angle at the end of the period (rad) φ is the latitude (rad) and δ is the solar declination (rad).

The inverse relative Earth-Sun distance, d_r, is calculated using the day of the year, J:

$$d_r = 1 + 0.033 \cos\left(\frac{2\pi}{365} J \right) \quad (3.4)$$

The solar time angles at the beginning and end of the period are given by:

$$\omega_1 = \omega - \frac{\pi p_1}{24} \quad (3.5)$$

$$\omega_2 = \omega - \frac{\pi p_1}{24} \quad (3.6)$$

where ω is the solar time at the midpoint of the time period (rad) and p_1 is the length of the calculation period (hours).

The solar time angle at the midpoint of the period is:

$$\omega = \frac{\pi}{12} \left[(ct + 0.06667(L_z - L_m) + S_c) - 12 \right] \quad (3.7)$$

where ct is the standard clock time at the midpoint of the period (hour), L_z is the longitude of the centre of the local time zone (degrees west of Greenwich), L_m is the longitude of the measurement site and S_c is the seasonal correction for solar time (hour), given by:

$$S_c = 0.1645 \sin(2b) - 0.1255 \cos(b) - 0.025 \sin(b) \quad (3.8)$$

where

$$b = \frac{2\pi(J - 81)}{364} \quad (3.9)$$

The solar decimation δ in radians, is:

$$\delta = 0.409 \sin\left(\frac{2\pi}{365} J - 1.39\right) \tag{3.10}$$

Day length N is calculated as:

$$N = \frac{24}{\pi} \omega_s \tag{3.11}$$

where ω_s is the sunset hour angle in radians, given by:

$$\omega_s = \arccos\left[-\tan(\varphi)\tan(\delta)\right] \tag{3.12}$$

For a bright hour to be recorded, the direct radiation needs to reach a threshold before the paper in the CS recorder will begin to burn. Each day is split into the potential sunshine hours, *N'*, which are the hours when the direct radiation is above the threshold, and the tails of the day, which are the interval when the direct radiation is below the threshold (see Figure 3.1). The bright hours can occur at any point during the potential sunshine hours. If the distribution of bright hours is known for a location, this can be used to help narrow the timing of the bright hours.

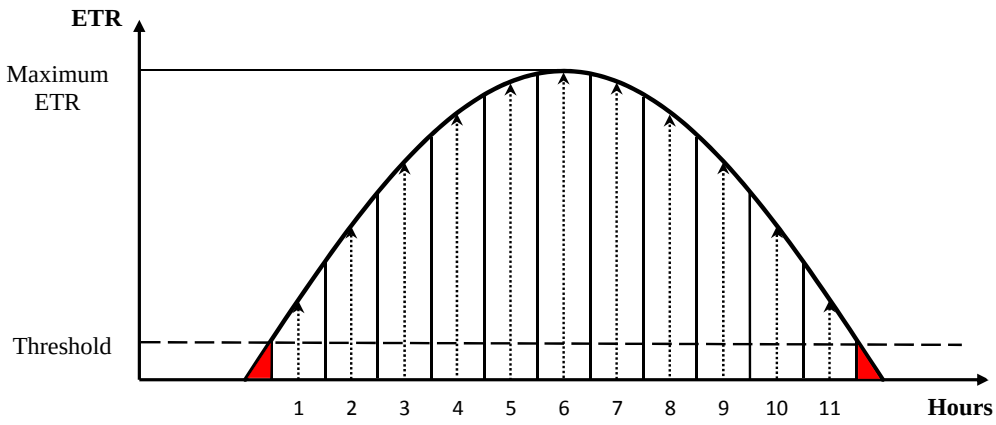

Figure 3.1 Calculation of ETR for each hour in a day that has 11 potential sunshine hours. The 'tails' of the day, when the direct radiation is below the threshold, are shaded red.

3.4 Modelling Process

Five global radiation models, three direct radiation models and five diffuse radiation models are proposed, designed, calibrated and evaluated. The specific equations for each of the models are given in Sections 3.5-3.8 below while a summary of the model parameters is given in Table 3.3. Each model is composed of a deterministic and a stochastic component. The deterministic component represents the long term average behaviour of the radiation and is given by the internal radiation model equations (given in Section 3.5). There are two stochastic components, namely the "internal" (calculated in the radiation model equations) and "external" variances, which both represent the short term variability. The internal model variance accounts for the uncertainty in the timing of the bright hours, which is directly related to the SSH measurement. The internal variance is determined from the radiation calculated using the radiation model equations, and associated with the random sampling of the bright hours. The external error variance accounts for the factors influencing the radiation which is not accounted for by the amount and timing of the bright hours, such as uncertainty in the atmospheric composition and additional uncertainty in the SSH measurement. The external variance is the difference between the total residual error variance (calculated from the residual error models given in Section 3.8) and the internal variance.

3.4.1 Calibration of global radiation models

To begin the modelling process, all radiation and residual error model parameters are assigned values sampled randomly from a uniform distribution (any value within parameter bounds is equally likely). For each day t where n is known, the ETR G_0 and day length N are calculated from latitude and Julian day using equations (3.3) and (3.11). This is then used to calculate the number of potential bright sunshine periods N' for each day (see Figure 3.1):

$$N' = \sum_{h=1}^{Nh} I\left(R_{direct}^{(h)} > R_T\right) \tag{3.13}$$

where $I()$ is the indicator function (1 if the Boolean argument is true, 0 otherwise), Nh = 24 is the number of hours per day, $R_{direct}^{(h)}$ is the direct radiation during hour h, and R_T is the threshold of direct radiation required for the CS recorder to record a bright period.

Given n, the corresponding number of bright periods (direct radiation above the threshold) and dull periods n_d (direct radiation below the threshold) are randomly selected for each day from a uniform distribution, where:

$$n_d = N' - n \tag{3.14}$$

For example, if N' = 9 hours (time periods h_1 to h_9) and n = 4 hours, then n_d = 5 hours. For the random sampling, h_3, h_4, h_7, h_9 may be bright and therefore h_1, h_2, h_5, h_6, h_8 will be dull.

The global radiation is then calculated as the sum of the direct and diffuse radiation for the selected bright periods, and the diffuse radiation from the remaining dull periods (equations for R_{direct} and $R_{diffuse}$ given in Section 3.5).

$$\text{e.g. } G_t = \sum_{h=3,4,7,9} R_{direct,h} + \sum_{h=3,4,7,9} R_{diffuse,h} + \sum_{h=1,2,5,6,8} R_{diffuse,h} \tag{3.15}$$

The random selection of bright periods is repeated i amount of times to obtain the daily mean $\mu_{G,t}$ and variance $\sigma^2_{G,t}$ of radiation (internal model variance) associated with the given SSH measurement , where:

$$\mu_{G,t} = \frac{1}{i}\sum_1^i G_{t,i} \tag{3.16}$$

$$\sigma^2_{G,t} = \frac{1}{i}\sum_1^i \left(G_{t,i} - \mu_{G,t}\right)^2 \tag{3.17}$$

Once the distribution of radiation is calculated for each day, the total error variance is calculated from the residual error models (see Section 3.8). The external variance is calculated as the total variance minus the internal model variance for each day. The entire process is then repeated with a new parameter set.

The WMO (2008) gives a standard threshold of the CS recorder as 120 Wm^{-2}. To test the applicability of a constant threshold, the models are recalibrated with the threshold in the models set equal to 120 Wm^{-2}. Thus each model is calibrated twice for each location.

3.4.2 Calibration of direct and diffuse radiation models

Separate to the calibration of the global radiation models, in the calibration of the direct radiation models (given in Section 3.6) and the diffuse radiation models (given in Section 3.7), a step wise process is used to calibrate the direct and diffuse parameters. The direct radiation model parameters are calibrated first. The direct radiation model parameters are calibrated using the same process as the global radiation (Section 3.4.1) but the diffuse radiation is not calculated. The best direct radiation model parameter values (found to be with Model 2) are then used in the calibration of the diffuse radiation model parameters. The diffuse radiation model parameters are also calibrated using the same process as the global radiation. The direct radiation is calculated first as it is only dependant on the daily ETR and the atmospheric composition. In contrast, the diffuse radiation requires the direct component to be already known. This is because, for a bright hour, once the amount of ETR reaching the land surface as direct radiation is known, the diffuse component can be calculated from the remaining scattered amount.

3.4.3 Model assessment

Once calibrated, the models are run in forward mode. The performance of the different global, direct and diffuse radiation models is assessed and compared using the RMSE and relative error between the mean of the predicted radiation (R_{sim}) and the observed radiation (R_{obs}) for each radiation type.

$$\text{RMSE} = \sqrt{\frac{\sum_1^t \left(R_{Sim,t} - R_{Obs,t}\right)^2}{t}} \tag{3.18}$$

$$\text{relative error} = \left| \frac{\overline{R_{Sim,t} - R_{Obs,t}}}{\overline{\mathrm{R}}_{\text{obs}}} \right| \times 100\% \tag{3.19}$$

The extent to which the probabilistic predictions are compatible with the observed data is investigated using Quantile-Quantile (QQ) plots, as outlined in Thyer et al. (2009). To construct the QQ plots, the cumulative distribution function (cdf) of observed p-values are plotted against the cdf of a theoretical uniform distribution. The cdf of observed p-values are determined by comparing the predictive distributions of radiation to the corresponding observed radiation. When producing the predictive distribution, relevant noise (constant, linear or quadratic, dependant on the residual error model used

in calibration, see Section 3.8), is added to the estimates to represent the external variance.

To assess the validity of the calibrated models, the models are run using the remaining available data not used for the calibration.

Table 3.3 Summary of parameters for the global, direct and diffuse radiation models and the residual error models. Note that each of the radiation models is calibrated separately using the five residual error models.

Radiation Model Parameters			
Model	Direct radiation component parameters	Diffuse radiation component parameters	
		Bright hours	Dull hours
Global Radiation			
1	A_{dir}	-	A_{diff}
2a	A_{dir}, B_{dir}	A_{diff}, B_{diff}	A_{diff}
2b	A_{dir}, B_{dir}	A_{diff}, B_{diff}	A_{diff}, B_{diff}
3a	A_{dir}, B_{dir}	A_{diff}, B_{diff}, C_{diff}	A_{diff}
3b	A_{dir}, B_{dir}	A_{diff}, B_{diff}, C_{diff}	A_{diff}, B_{diff}, C_{diff}
Direct Radiation			
1	A_{dir}	-	-
2	A_{dir}, B_{dir}	-	-
3	A_{dir}, B_{dir}, C_{dir}	-	-
Diffuse Radiation			
1	-	-	A_{diff}
2a	A_{dir}, B_{dir}	A_{diff}, B_{diff}	A_{diff}
2b	A_{dir}, B_{dir}	A_{diff}, B_{diff}	A_{diff}, B_{diff}
3a	A_{dir}, B_{dir}	A_{diff}, B_{diff}, C_{diff}	A_{diff}
3b	A_{dir}, B_{dir}	A_{diff}, B_{diff}, C_{diff}	A_{diff}, B_{diff}, C_{diff}

Residual Error Model Parameter	
Model	Parameters
Constant Variance	-
Variance dependent on SSH-linear	A_{var}, B_{var}
Variance dependent on SSH-quadratic	A_{var}, B_{var}, C_{var}
Variance dependent on simulated radiation-linear	A_{var}, B_{var}
Variance dependent on simulated radiation-quadratic	A_{var}, B_{var}, C_{var}

3.5 Global Radiation Model Equations

3.5.1 Global Model 1: No scaling by *n/N*

In this Model, all bright hours are assumed to be completely bright and are given the full amount of direct radiation available. Similarly, dull hours are assigned the maximum available diffuse radiation. During bright hours only direct radiation R_{direct} reaches the land surface and during dull hours only diffuse radiation $R_{diffuse}$ reaches the land surface.

For a bright hour:

$$R_{direct} = A_{dir}^{\sec(z)} \times G_{0,h} \tag{3.20}$$

$$R_{diffuse} = 0 \tag{3.21}$$

For a dull hour:

$$R_{direct} = 0 \tag{3.22}$$

$$R_{diffuse} = A_{diff} \times G_{0,h} \tag{3.23}$$

3.5.2 Global Model 2a and 2b: Linear scaling by *n/N*

This Model allows for diffuse radiation in the bright hours and introduces a factor that linearly scales the direct and diffuse radiation for bright hours, when there is some cloud present during the day. Similar to Model 1, in a dull hour only diffuse radiation reaches the land surface.

For a bright hour:

$$R_{direct} = \left[A_{dir} - B_{dir}\left(1 - \frac{n}{N}\right)\right]^{\sec(z)} G_{0,h} \tag{3.24}$$

$$R_{diffuse} = \left[A_{diff} - B_{diff}\left(\frac{n}{N}\right)\right]\left[G_{0,h} - R_{direct}\right] \tag{3.25}$$

For a dull hour, two different representations of the diffuse radiation behaviour are considered. Version A assumes that the diffuse radiation is a constant and therefore the

same for each dull hour. Version B assumes that the diffuse radiation varies in proportion to the amount of sunshine hours:

$$R_{direct} = 0 \tag{3.26}$$

a) $$R_{diffuse} = A_{diff} \times G_{0,h} \tag{3.27}$$

b) $$R_{diffuse} = \left[A_{diff} - B_{diff} \left(\frac{n}{N} \right) \right] G_{0,h} \tag{3.28}$$

3.5.3 Global Model 3a and 3b: Quadratic scaling by *n/N*

This Model is similar to Model 2 but uses a quadratic model of diffuse radiation.

For a bright hour:

$$R_{direct} = \left[A_{dir} - B_{dir} \left(1 - \frac{n}{N} \right) \right]^{\sec(z)} G_{0,h} \tag{3.29}$$

$$R_{diffuse} = \left[A_{diff} + B_{diff} \left(\frac{n}{N} \right) + C_{diff} \left(\frac{n}{N} \right)^2 \right] \left[G_{0,h} - R_{direct} \right] \tag{3.30}$$

For a dull hour, 2 variations of the model are again considered:

$$R_{direct} = 0 \tag{3.31}$$

a) $$R_{diffuse} = A_{diff} \times G_{0,h} \tag{3.32}$$

b) $$R_{diffuse} = \left[A_{diff} + B_{diff} \left(\frac{n}{N} \right) + C_{diff} \left(\frac{n}{N} \right)^2 \right] G_{0,h} \tag{3.33}$$

3.6 Direct Radiation Model Equations

The following direct radiation models are based on the direct radiation components of the global radiation models. For all models, the direct radiation only occurs during bright hours. For the dull hours the direct radiation equals zero.

3.6.1 Direct Model 1: No scaling by *n/N*

$$R_{direct} = A_{dir}^{\sec(z)} \times G_{0,h} \tag{3.34}$$

3.6.2 Direct Model 2: Linear scaling by *n/N*

$$R_{direct} = \left[A_{dir} - B_{dir}\left(1 - \frac{n}{N}\right)\right]^{\sec(z)} G_{0,h} \tag{3.35}$$

3.6.3 Direct Model 3: Quadratic scaling by *n/N*

$$R_{direct} = \left[A_{dir} + B_{dir}\left(\frac{n}{N}\right) + C_{dir}\left(\frac{n}{N}\right)^2\right]^{\sec(z)} G_{0,h} \tag{3.36}$$

3.7 Diffuse Radiation Model Equations

The following diffuse radiation models are based on the diffuse radiation components of the global radiation models.

3.7.1 Diffuse Model 1: No scaling by *n/N*

In this Model no diffuse radiation is calculated during the bright hours. For each dull hour:

$$R_{diffuse} = A_{diff} \times G_{0,h} \tag{3.37}$$

3.7.2 Diffuse Model 2: Linear scaling by *n/N*

This Model allows for diffuse radiation in the bright hours and introduces a factor that linearly scales the diffuse radiation for bright hours when there is some cloud present during the day.

For a bright hour:

$$R_{diffuse} = \left[A_{diff} - B_{diff}\left(\frac{n}{N}\right)\right]\left[G_{0,h} - R_{direct}\right] \tag{3.38}$$

For a dull hour, 2 variations of the diffuse radiation are considered:

a) $$R_{diffuse} = A_{diff} \times G_{0,h} \tag{3.39}$$

b) $$R_{diffuse} = \left[A_{diff} - B_{diff}\left(\frac{n}{N}\right)\right] G_{0,h} \tag{3.40}$$

3.7.3 Diffuse Model 3: Quadratic scaling by *n/N*

This Model is similar to Model 2 but uses a quadratic function to model the diffuse radiation.

For a bright hour:

$$R_{diffuse} = \left[A_{diff} + B_{diff}\left(\frac{n}{N}\right) + C_{diff}\left(\frac{n}{N}\right)^2 \right]\left[G_{0,h} - R_{direct}\right] \tag{3.41}$$

For a dull hour, 2 variations of the model are considered:

a) $$R_{diffuse} = A_{diff} \times G_{0,h} \tag{3.42}$$

b) $$R_{diffuse} = \left[A_{diff} + B_{diff}\left(\frac{n}{N}\right) + C_{diff}\left(\frac{n}{N}\right)^2 \right] G_{0,h} \tag{3.43}$$

3.8 Residual Error Models

For any day *t* the residual error e_t is given by:

$$e_t = R_{Sim,t} - R_{Obs,t} \tag{3.44}$$

where $R_{Sim,t}$ is the mean of the simulated radiation for each day and $R_{Obs,t}$ is the observed radiation. The residual errors are assumed to follow a Gaussian distribution.

Five different residual error models are considered, differing in their parameterisation of the variance of the residuals:

1: constant variance: $\sigma_t^2 = const$ (3.45)

2: variance dependant on the daily SSH fraction (*n/N*)

- linear dependence: $\sigma_t^{\,2} = A_{\text{var}} + B_{\text{var}}\left(\frac{n_t}{N_t}\right)$ (3.46)
- quadratic dependence: $\sigma_t^{\,2} = A_{\text{var}} + B_{\text{var}}\left(\frac{n_t}{N_t}\right) + C_{\text{var}}\left(\frac{n_t}{N_t}\right)^2$ (3.47)

3: variance dependent on the magnitude of the simulated radiation scaled by ETR

- linear dependence: $\sigma_t^{\,2} = A_{\text{var}} + B_{\text{var}}\left(\dfrac{R_{Sim,t}}{G_{0,t}}\right)$ (3.48)
- quadratic dependence: $\sigma_t^{\,2} = A_{\text{var}} + B_{\text{var}}\left(\dfrac{R_{Sim,t}}{G_{0,t}}\right) + C_{\text{var}}\left(\dfrac{R_{Sim,t}}{G_{0,t}}\right)^2$ (3.49)

The SSH is normalised by the day length and the simulated radiation by the ETR to be independent of month, season and location, as the maximum number of possible SSH and amount of radiation vary with time of year and latitude.

3.9 Objective Function

The parameters of all models were calibrated under the assumption that the total uncertainty is approximately Gaussian. This yields an objective function Φ derived from the Gaussian probability density function, containing the sum of squared residual errors:

$$\Phi(\theta_M, \theta_\varepsilon) = \log N\left(e_{1:t}(\theta_M) \mid \mu, \sigma_t(\theta_\varepsilon)^2\right) = -\sum_{t=1}^{m_{obs}} \log\left(\sigma_t\sqrt{2\pi}\right) - \frac{1}{2}\sum_{t=1}^{m_{obs}} \frac{e_t^2}{\sigma_t^2} \qquad (3.50)$$

where m_{obs} is the number of observations and the notation $N(x|\mu,\sigma^2)$ denotes the probability density of a Gaussian deviate x with mean μ and variance σ^2.

This objective function explicitly indicates the dependence of residuals on the model parameters θ_M (different for each radiation model) and the dependence of the Gaussian error variance on the error model parameters θ_ε (different for each error model).

The calibration approach consists of maximizing the objective function in equation (3.50) with respect to the model parameters θ_M and the error model parameters θ_ε. The optimisation method used is the shuffled complex evolution (SCE) algorithm (Duan et al., 1992).

3.10 Summary

In this chapter, the meteorological data used in the development and analysis of the radiation models is summarised. Nine main locations that have observations of global, direct and diffuse radiation for an extended number of years are used in the development of the stochastic radiation models. These locations cover a range of climate conditions.

This chapter also outlines the development of five stochastic global radiation models, three direct radiation models and five diffuse radiation models. The models differ in the parameterisation of the diffuse and direct portions of the global radiation, using either no scaling, linear or quadratic scaling of the radiation by the daily SSH fraction to account for the attenuation of ETR by clouds.

Also developed are five different residual error models which are used to calibrate the radiation models. These residual error models have different assumptions including constant, linear and quadratic variances related to SSH fraction and the simulated radiation. Two sources of predictive uncertainty are considered: (i) the timing of the bright SSH during the day and (ii) external uncertainty such as variability in cloud type and amount.

Chapter 4 - Performance of Radiation Models

Overview

Stochastic models for estimating global, direct and diffuse radiation were developed in Chapter 3. In this chapter the performance of the different global, direct and diffuse radiation models and the different residual error models are presented and compared for each radiation type. The results for the global radiation models are presented first, followed by the results for the direct models, and finally the results for the diffuse models.

4.1 Global Radiation

4.1.1 Global radiation distributions from observed data

In the developed models, the SSH data is used to estimate the daily global radiation. Therefore, the relationship between SSH and global radiation is first presented. To illustrate each relationship, Figure 4.1 shows scatter plots of the observed daily SSH and global radiation fraction. The global radiation model simulations are also shown to demonstrate how well they model the observed radiation. These scatter plots also give an indication of the cloudiness and by extension the rainfall regimes at each location.

The observed global radiation appears to follow a linear relationship with SSH. The direct and diffuse components of global radiation both follow nonlinear relationships with SSH (shown in Sections 4.2.1 and 4.3.1) but when summed together they make the global radiation follow an almost linear relationship. The linear relationship weakens around SSH=0.8, where there is a large amount of scatter. For all locations the scatter plots show that some global radiation exists regardless of SSH amount. The global radiation is approximately 20% of the ETR when there is no bright SSH (n/N=0). This increases to approximately 75% when the day is completely sunny (n/N=1).

For the locations studied, Adelaide, Mount Gambier, Melbourne, Mildura and Wagga Wagga have relatively uniform rainfall throughout the year. In Figure 4.1 Melbourne

and Mount Gambier have a more even spread across all SSH fractions. For Alice Springs, Tennant Creek, Darwin and Broome, most of the observations have a high SSH and radiation fraction (most days are predominantly sunny). These locations have distinct wet and dry seasons with minimal rainfall from April-November with the majority of the rainfall occurring in the December-March period (monsoon season). From the climate classifications, discussed in Chapter 3, Alice Springs and Tennant Creek are arid, Broome and Darwin have a marked wet summer and dry winter, Mildura, Wagga Wagga, Adelaide and Mount Gambier have wet winter and low summer rainfall while Melbourne has uniform rainfall.

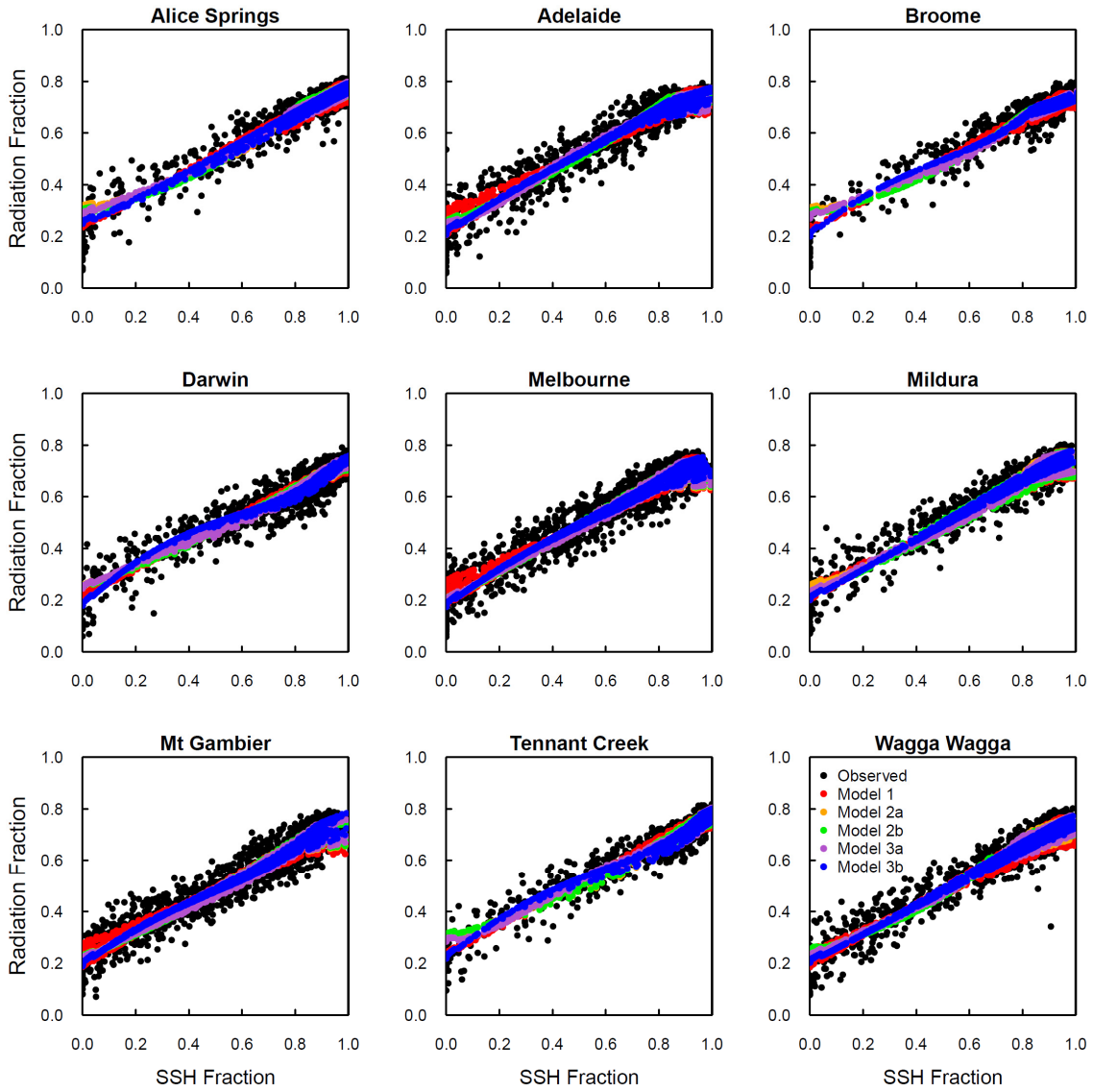

Figure 4.1 Scatter plots showing the relationship between global radiation and SSH for all locations. Figure constructed from the observed SSH fraction and global radiation as well as the modelled radiation.

4.1.2 Model calibration results

Figure 4.2 and Figure 4.3 show the time series of global radiation for Model 1, for Alice Springs and Melbourne respectively. Only Model 1 is shown as all the models perform similarly. The scatter plots in Figure 4.1 also compare all five models for each location. From Figure 4.1 it can be seen that all the models have similar predictions of global radiation with the change in SSH fraction.

For all locations, the calibrated threshold is quite low, generally less than 200 W m^{-2}, and varies between the models and locations. Alice Springs and Tennant Creek, located in central Australia, have the lowest value at approximately 10 W m^{-2} for Model 1. For all locations, Model 3a generally has a higher threshold than the other models. The threshold is influenced by early morning humidity as discussed previously. The 9am relative humidity for each of the locations is given in Table 3.1. Tennant Creek and Alice Springs have the lowest threshold and the lowest humidity.

The transmission coefficient gives an indication of the clearness of the atmosphere. A higher value corresponds to a clearer atmosphere. The transmission coefficient (parameter A_{dir}) is reasonably consistent between Models 1 and 2a at all locations. Values for Models 2b and 3a are consistently lower than the other models while those for Model 3a are higher. For Models 1 and 2a, all locations have a value equal to approximately 0.77 except for Alice Springs and Tennant Creek which have a slightly higher value at 0.80. This suggests that for a clear day, approximately 77% to 80% of the ETR is transmitted as direct radiation. This greater transmission is expected for Alice Springs and Tennant Creek as they are located in inland Australia and for most of the year (the dry season) have a relatively clear atmosphere with lower humidity.

Note that the model parameters can interact with each other. For example, if the transmission coefficient is reduced, global radiation can remain unchanged if the diffuse fraction is increased. Therefore, the parameters are correlated and need to be examined jointly.

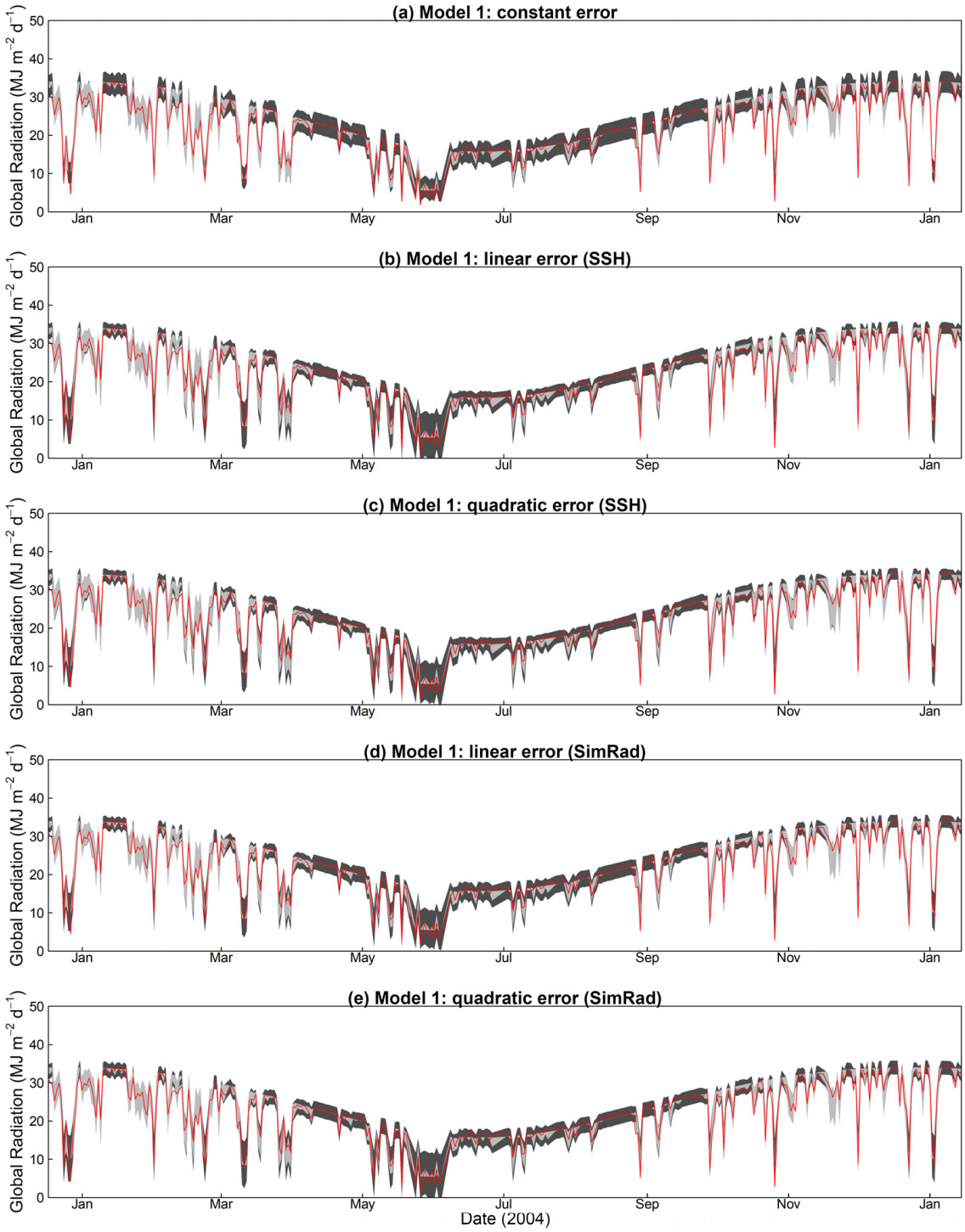

Figure 4.2 Time series of predicted radiation for the year 2004 (calibration period) for Alice Springs using Model 1. Panel (a) uses the constant residual error model, panels (b) and (c) use the *n/N* (SSH) residual error models while panels (d) and (e) use the simulated radiation (SimRad) residual error models. The red line is the observed radiation, the light grey shading is the internal variance of the modelled radiation, and the dark grey shading is the 95% predictive limit of the external ("residual error") variance. The total variance is the sum of the internal and external variance.

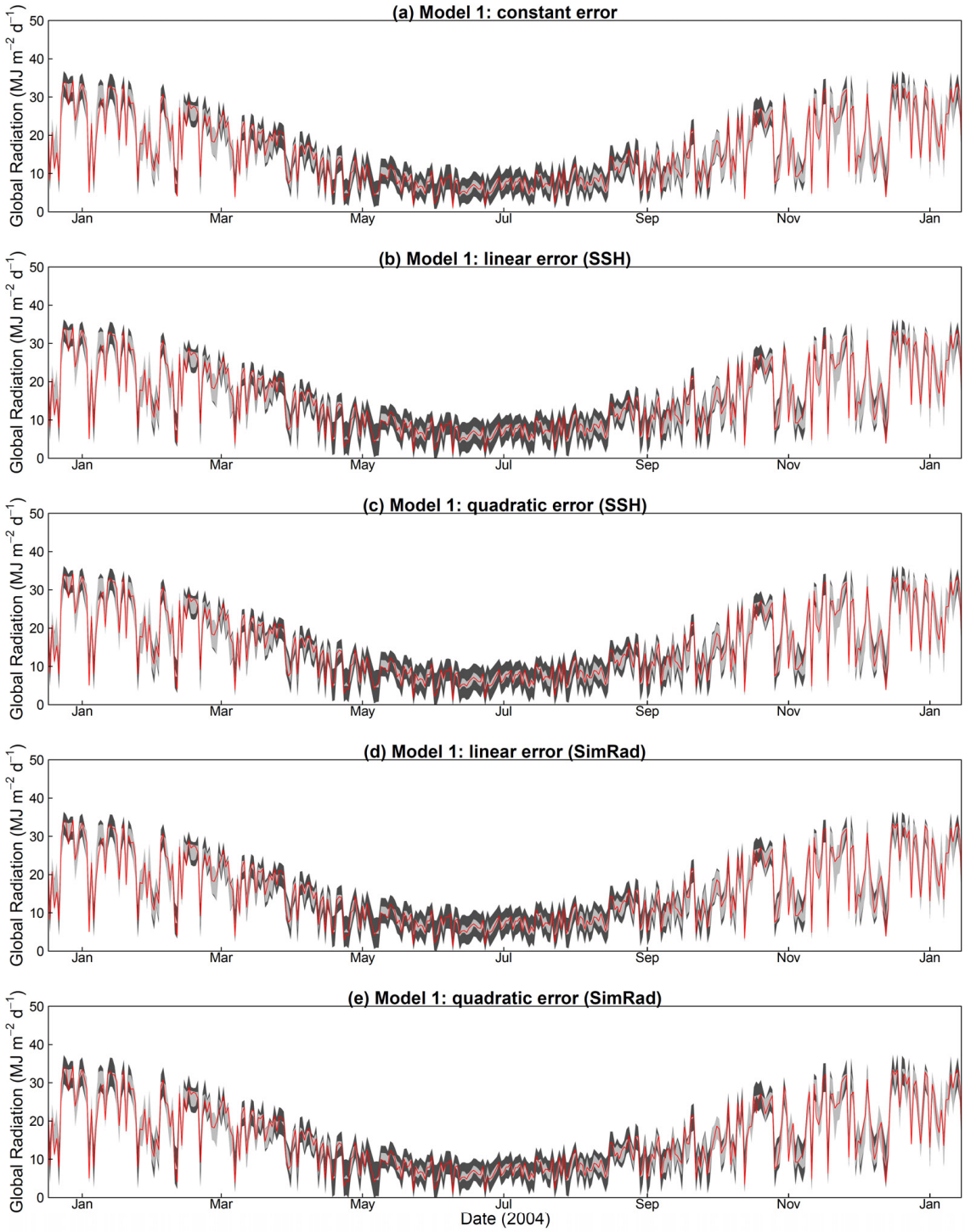

Figure 4.3 Time series of predicted radiation for the year 2004 (calibration period) for Melbourne using Model 1. Panel (a) uses the constant residual error model, panels (b) and (c) use the *n/N* (SSH) residual error models while panels (d) and (e) use the simulated radiation (SimRad) residual error models. The red line is the observed radiation, the light grey shading is the internal variance of the modelled radiation, and the dark grey shading is the 95% predictive limit of the external ("residual error") variance. The total variance is the sum of the internal and external variance.

At each location, varying the residual error model structure does not significantly influence the radiation model parameters (direct and diffuse parameters). Similarly, the residual error model parameters are reasonably consistent between the radiation models for each location. The residual error model parameters vary more between the locations. This suggests the errors are more dependent on local atmospheric conditions than the radiation model structure. The different residual error variances can be seen in the different time series in Figure 4.2 and Figure 4.3. Additionally Figure 4.4 shows the residual error variances for the range of SSH fractions and simulated radiations. Only the variance for Model 1 for Melbourne and Alice Springs is shown but is representative of all the locations and radiation models.

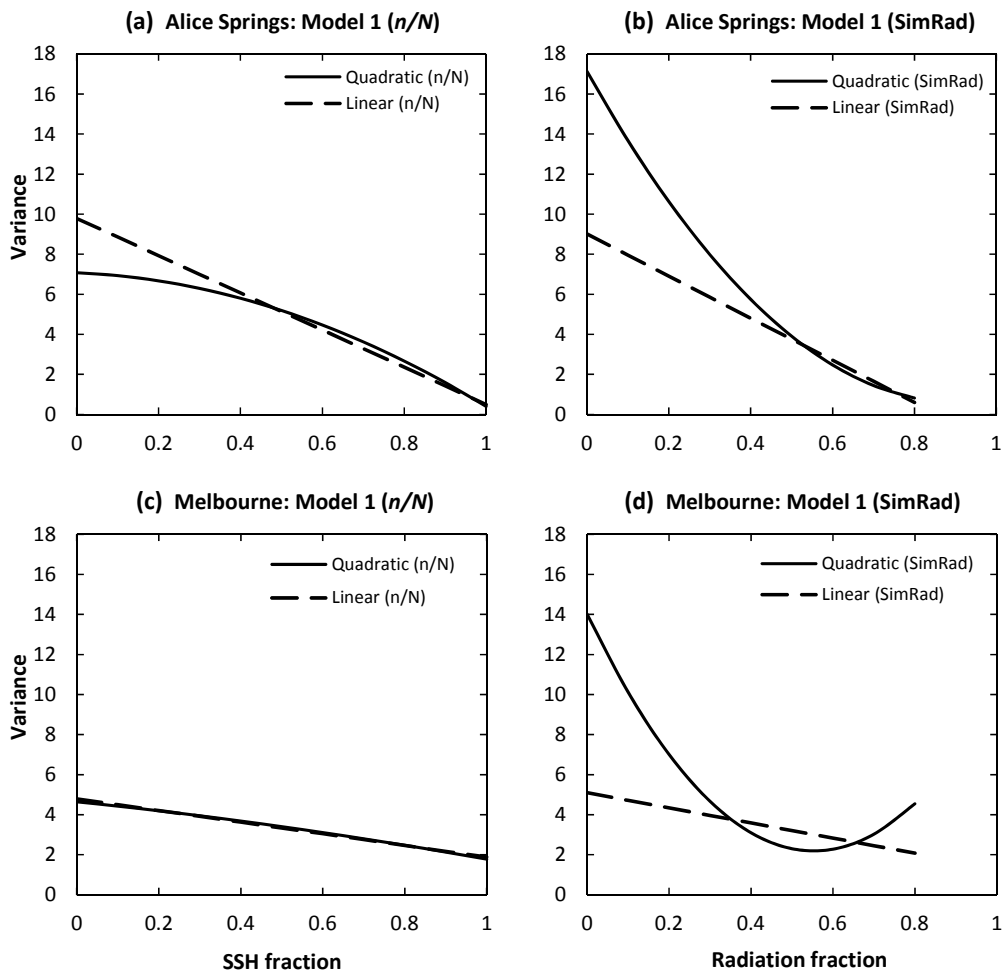

Figure 4.4 Linear and quadratic error variance ($MJ^2\ m^{-4}\ d^{-2}$) for Model 1 calibrated to Alice Springs (panels a and b) and Melbourne (panels c and d). The error variance is dependent on *n/N* (panels a and c) and the simulated radiation (SimRad) (panels b and d).

In order to compare the panels of Figure 4.4, note that when *n/N*=1 the predicted mean radiation fraction is approximately 0.8. For both locations, the four different error structures result in a higher variance for cloudy days (low SSH and radiation fractions) than sunny days. The error variance for all four error structures approaches zero for sunny days for both locations, however, for cloudy days the variance is much higher for Alice Springs than Melbourne. Alice Springs has two distinct rainfall seasons – wet and dry. Almost no rainfall occurs during the dry season with the majority falling within a few months of the wet season. In contrast, Melbourne has uniform rainfall throughout the year. This means that Alice Springs has a greater seasonal variation in cloudy days and relative humidity than Melbourne. As only one parameter set is used for the whole year, it is suggested that this results in a higher uncertainty for Alice Springs than Melbourne.

For cloudy days, the quadratic variance is much higher for the simulated radiation structure (Figure 4.4b and d) than the *n/N* structure (Figure 4.4a and c). This suggests that the *n/N* structure is more precise.

4.1.3 Model performance

Next, Figure 4.5 compares the models based on their maximum, minimum and average RMSE, internal and external variance.

By comparing the RMSE (Figure 4.5a) between the models for each location, it is clear that the models tend to perform similarly – there is only a very small difference between the models for each location. However, on average, Model 3b performs marginally better than the other models. The RMSE is more variable between the different locations, shown in Table 4.1.

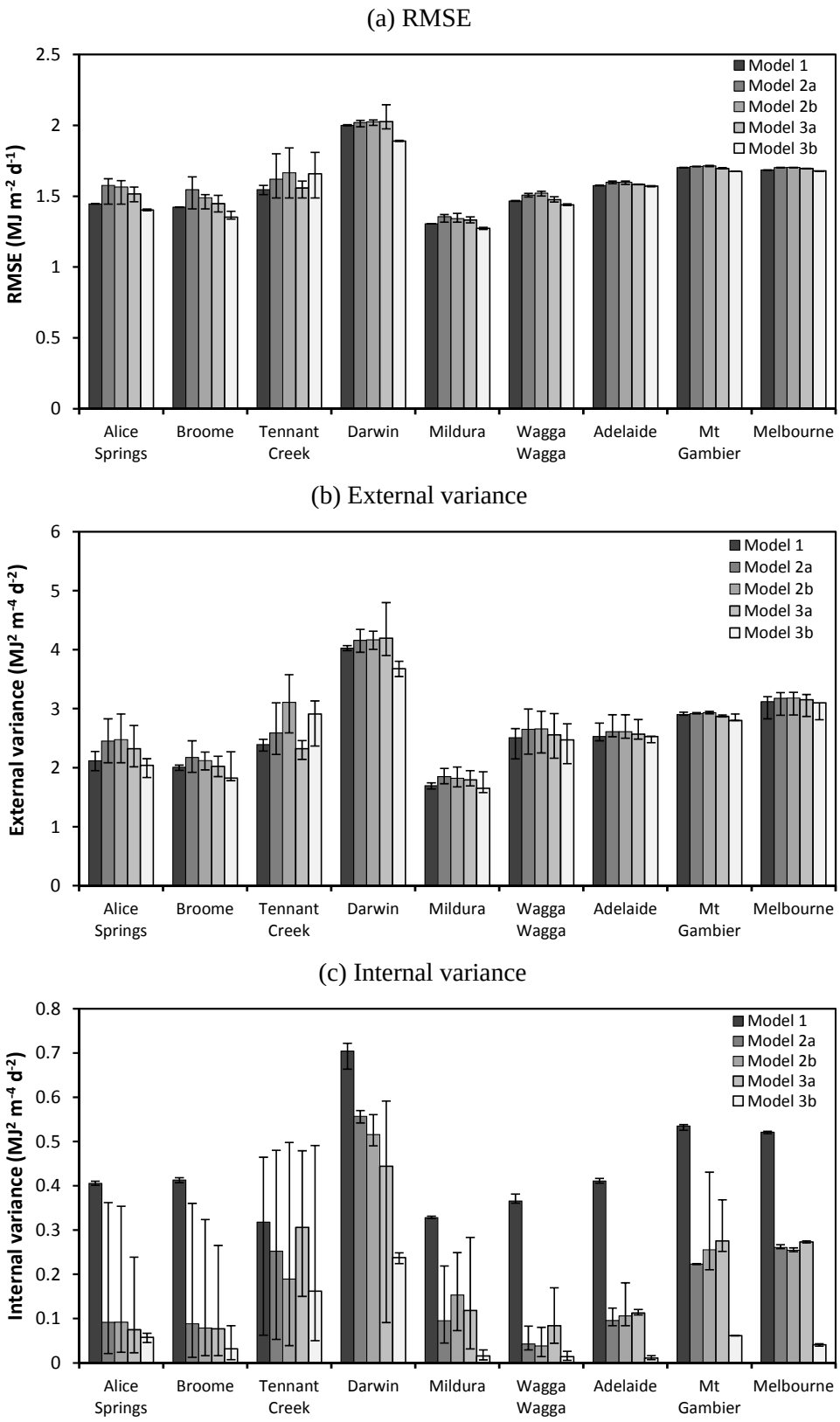

Figure 4.5 (a) RMSE, (b) external variance and (c) internal variance averaged individually for each of the models for all locations. The error bars indicate the maximum and minimum RMSE, internal and external variance for each location given by the different residual error models.

Table 4.1 Average RMSE and external variance of all models. The ranking for each location is given in the parenthesis where (1) is the best performance.

Location	**Av. RMSE** ($MJ\ m^{-2}\ d^{-1}$)	**Av. Ext. Var.** ($MJ^2\ m^{-4}\ d^{-2}$)
Adelaide	1.60 (6)	2.6 (5)
Alice Springs	1.50 (4)	2.3 (3)
Broome	1.46 (2)	2.0 (2)
Darwin	1.99 (9)	4.0 (9)
Melbourne	1.80 (8)	3.2 (8)
Mildura	1.32 (1)	1.8 (1)
Mt Gambier	1.71 (7)	2.9 (7)
Tennant Creek	1.60 (5)	2.7 (6)
Wagga Wagga	1.49 (3)	2.6 (4)

The difference in RMSE between the locations can be partially attributed to the different SSH amounts and rainfall regimes, which can be inferred from the scatter plots in Figure 4.1 and the annual rainfall and average sunshine hour fraction listed in Table 3.1. It is assumed that rainfall is a proxy for cloudiness, while the SSH fraction and radiation are closely related to cloudiness (Allen et al., 1998; Shuttleworth, 1992). Darwin has the highest rainfall with distinct wet and dry seasons. Given the highly variable nature of the rainfall and associated cloud amounts, it is reasonable that the models for Darwin have the poorest performance. Melbourne and Mount Gambier have the most variable SSH fractions (the scatter plots exhibit the most even spread across all SSH fractions), the lowest average SSH fraction and a relatively high amount of annual rainfall. For these locations, the models also perform comparatively poorly. The scatter plots for Melbourne, Mount Gambier and Adelaide also show more scatter in the relationship between the global radiation and SSH fraction than the plots for the other locations. In contrast, Mildura has the smallest amount of annual average rainfall, a higher average SSH fraction and the best model performances. This is expected as it is easier for the model to fit to sunny conditions as there is less uncertainty as to the composition of the atmosphere (type and amount of clouds etc.) which is reflected in the SSH fraction. Additionally, the CS recorder only responds to direct radiation which is greatest in sunny conditions. It does not give an indication of diffuse radiation which is greatest in cloudy conditions.

For the average external variance (Figure 4.5b), there is only a small difference between the models at each location, except for Alice Springs, Tennant Creek and Darwin. No

model performs consistently better than the other models. There is a greater difference in the external variance when the different locations are compared, as shown in Table 4.1. This is a similar order of performance as the RMSE, which is expected as a better performance is linked with smaller variability between the observed and simulated radiation.

The average internal variance (Figure 4.5c) shows a little more variability between the radiation and residual error models. Model 1 tends to have the highest average internal variance, ranging from 0.34 (Mildura) to 0.7 MJ^2 m^{-4} d^{-2} (Darwin), while Model 3b tends to have the least internal variance ranging from 0.01 (Wagga Wagga) to 0.24 MJ^2 m^{-4} d^{-2} (Darwin). It is interesting to note that Model 1 is the least complex while Model 3b is the most complex.

When n/N = 0 or 1 there is no internal variability in the predicted radiation as either no hours or all hours are selected as bright respectively. The internal model variance is greatest for mid values of SSH fractions (n/N~0.5). For a mid-range of hours, for example at Alice Springs on a summer day, the predicted global radiation varies from 17 to 22 MJ m^{-2}. A greater range of radiation can be sampled with a mid-range of bright hours compared with a small or a large amount. This can be seen in Figure 4.2 and Figure 4.3 where the internal variance for Model 1 accounts for most of the total variance in the mid SSH ranges. This is not as pronounced for the other models which have a smaller internal variance.

The linear residual error model and the quadratic residual error model both perform similarly well. Additionally, the residual error models based on SSH fraction and the residual error models based on simulated radiation perform similarly well. Therefore, the main difference between the residual error models is the amount of internal variance.

At a given location, the choice of radiation model and residual error model does not appear to significantly influence the average total variance. However, as shown in Figure 4.4, the residual error variance for each day shows a clear dependence on both the daily SSH fraction and the simulated radiation amount. So although the average

total variance is not improved by using either linear or quadratic variance over constant variance, it is suggested that the linear residual error structure be used.

Models 2a and 2b along with Models 3a and 3b vary in their structure of the radiation for the dull hours. The 'b' models allow for more variability in the radiation, which is dependent on the SSH fractions. There is no consistent difference in the performance of the models; however, Model 3b tends to have a lower internal variance than Model 3a.

To further demonstrate the performance of the models, Figure 4.6 shows the relative error of the modelled radiation compared with the observed radiation for Model 3b with the linear *n/N* residual error model. Only this model is shown as the relative errors are very similar for all the residual error models within each radiation model for each location. The relative errors are also very similar for all the radiation models for each location, although Model 3b tends to have a slightly lower relative error.

In Figure 4.6 the relative error is plotted against the percentage of data points. The relative error for all data points ranges from 6% at Broome and Alice Springs to 11% at Melbourne. The average relative error for all locations is 9%. The greatest amount of relative error occurs at low SSH fractions where the amount of radiation is at a minimum.

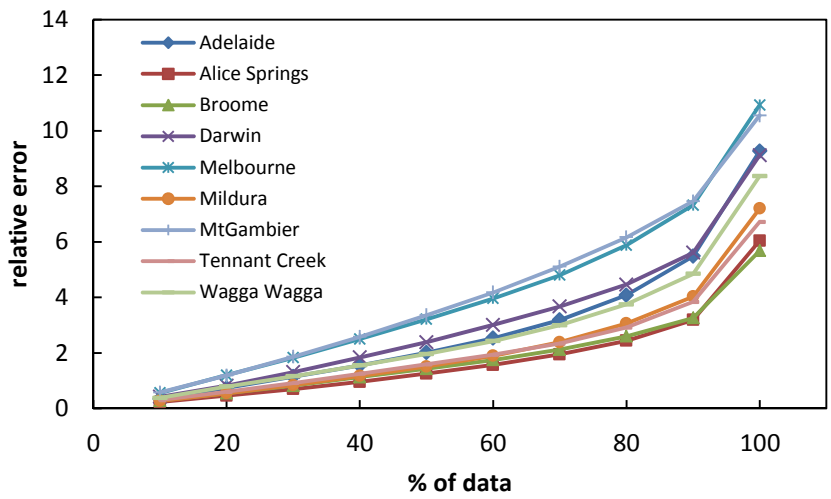

Figure 4.6 Change in relative error with the change in percentage of data for all locations using Model 3b with the linear *n/N* residual error model.

To examine this relationship further, Figure 4.7 shows the relative error between the observed and simulated global radiation plotted against the SSH fraction for Alice Springs and Melbourne. Melbourne has the highest relative error for most SSH fractions while Alice Springs has one of the lowest relative errors for all SSH fractions. In Figure 4.7 it can be seen that the relative error is the greatest for SSH fractions less than 0.2, which corresponds with minimum amounts of global radiation, and approaches zero as the SSH fraction increases. Therefore, the large relative error is in general the equivalent of less than 1 MJ m^{-2} d^{-1}.

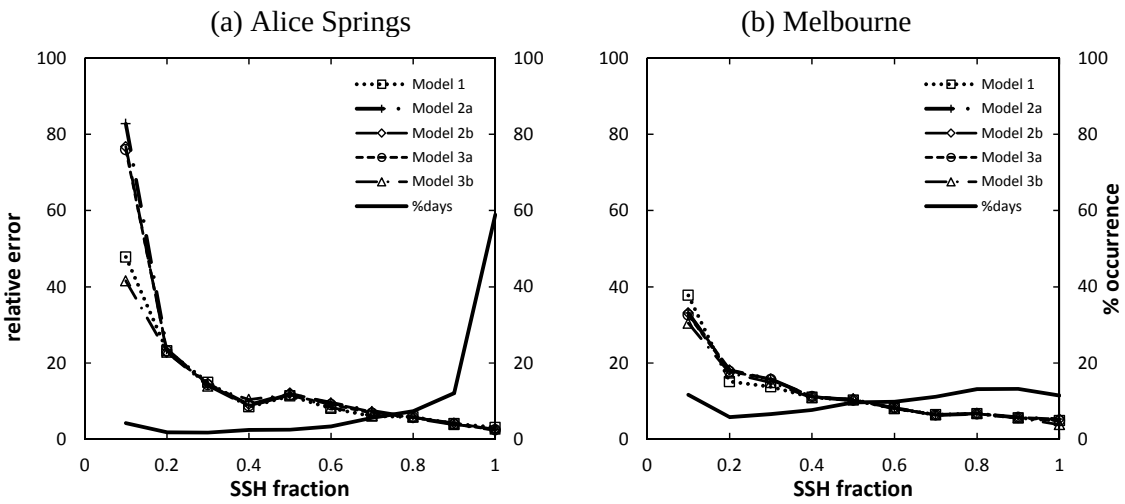

Figure 4.7 Relative error with the change in SSH fraction for (a) Alice Springs and (b) Melbourne. All five radiation models are shown with the linear *n/N* error structure. The percentage of days with each SSH fraction is shown by the thick solid line and corresponds to the % occurrence axis.

The relationship between the relative error and SSH fraction for all locations is shown in Figure 4.8. All locations follow very similar and consistent trends with the majority of the error occurring for SSH fractions less than 0.2, which corresponds to generally less than 10% of the data.

These results are comparable to the global radiation estimated from satellite images (BoM, 2013). The satellite model, as given by BoM, has an error of 7% or better in clear sky conditions and up to 20% in cloudy conditions.

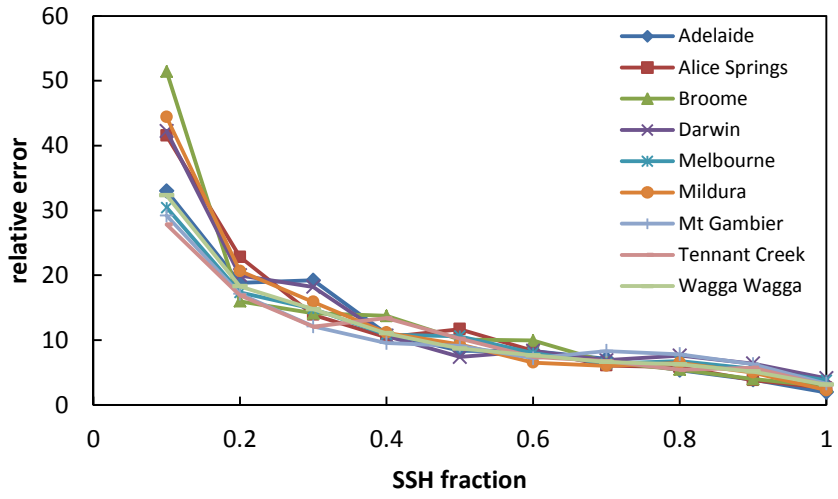

Figure 4.8 Relative error with the change in SSH fraction for all locations using Model 3b with the linear *n/N* residual error model.

4.1.4 Predictive reliability of the global models: QQ plots

QQ plots are developed to compare the predictive reliability of the different radiation models and residual error models. The QQ plots for Alice Springs and Melbourne are shown in Figure 4.9 and Figure 4.10 respectively. To the extent that the observations are statistically consistent with the predicted distribution, the p-values in the QQ plots fall approximately on the 1:1 line.

By examining the QQ plots with no external noise added (the only source of randomness is due to the sampling of the SSH hours within the day), the left column of Figure 4.9 and Figure 4.10, it is clear that all of the models under-estimate the predictive uncertainty. The under-estimation is particularly strong for Model 3b. This indicates that the uncertainty due to the timing of the bright hours does not account for all the variation between the observed and simulated radiation.

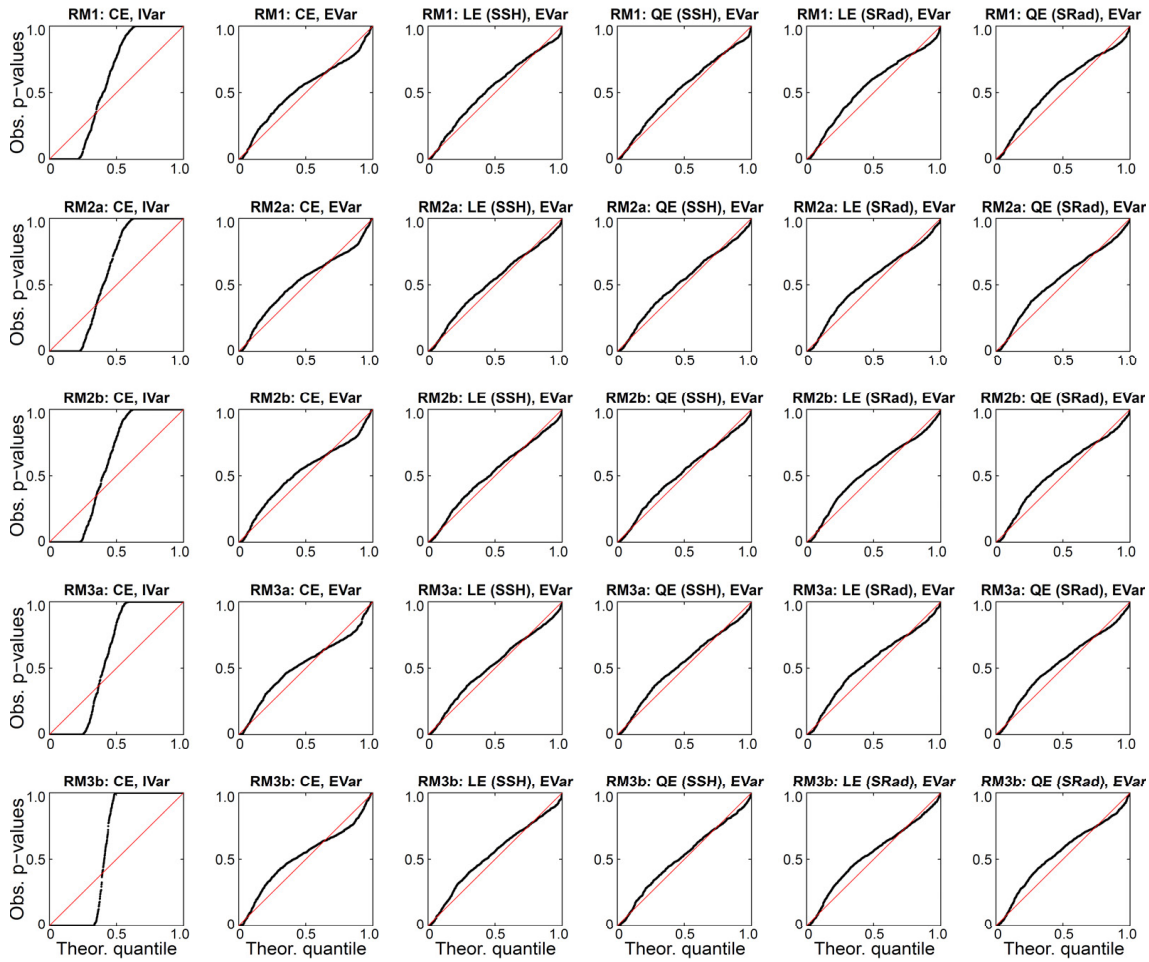

Figure 4.9 QQ plots for Alice Springs for all radiation models and residual error model structures. The left column is for the internal variance while the other columns show the external variance for the five error models. RM stands for radiation model, CE for constant error, LE for linear error, QE for quadratic error, SRad for simulated radiation, EVar for external variance and IVar for internal variance.

With noise added to the modelled radiation, all the radiation models and residual error models slightly over-estimate the predictive uncertainty. The constant residual error model has the greatest over-estimation of all the models. The linear and quadratic error variance dependent on SSH produce the best agreement between the predictions and the observations, particularly in the Alice Springs simulations (Figure 4.9). This indicates that the best residual error models are those with heteroscedasticity based on the SSH fraction. Both the linear and quadratic residual error models perform equally well. Given that the linear structure has one less parameter to be calibrated, it is suggested that the models are best calibrated with linear error variance based on SSH fraction.

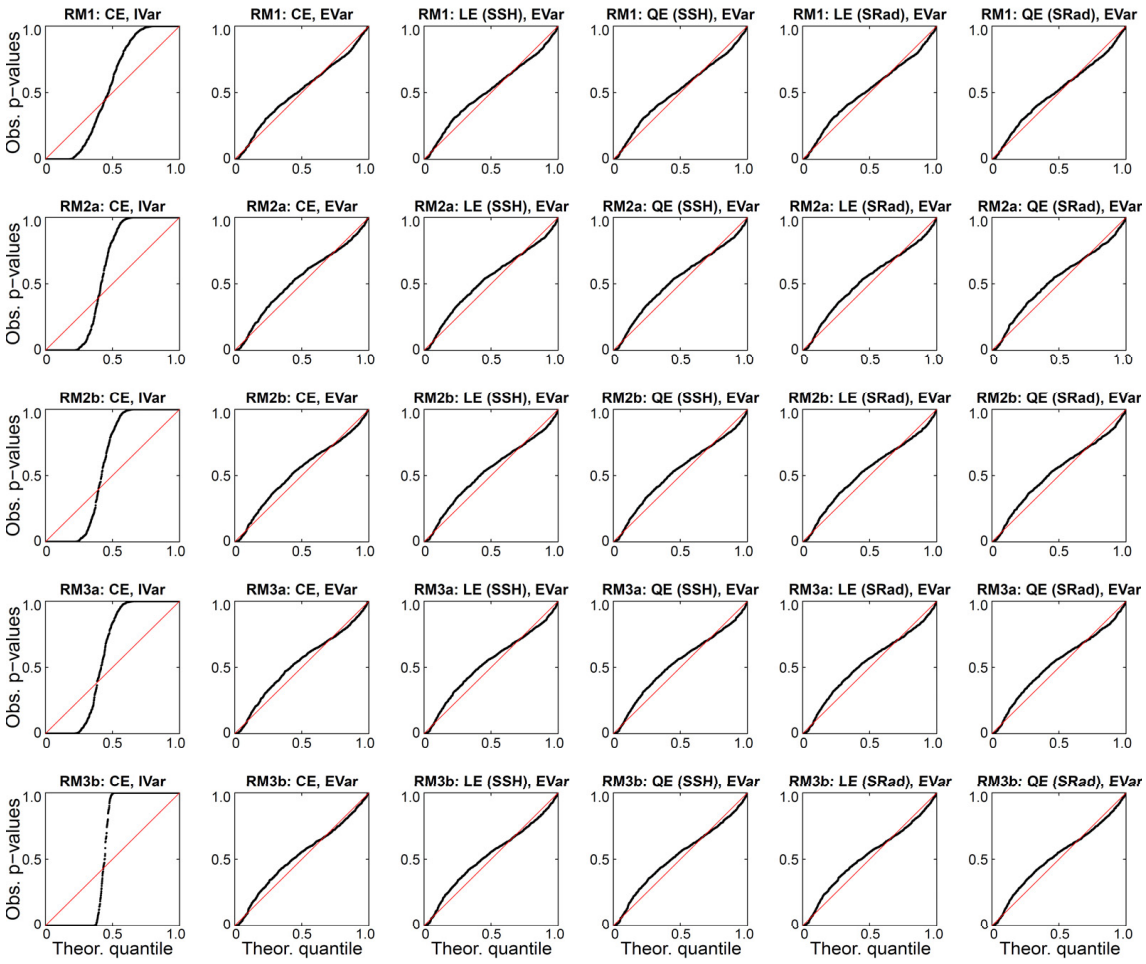

Figure 4.10 QQ plots for Melbourne for all radiation models and residual error model structures. The left column is for the internal variance while the other columns show the external variance for the five error models. RM stands for radiation model, CE for constant error, LE for linear error, QE for quadratic error, SRad for simulated radiation, EVar for external variance and IVar for internal variance.

4.1.5 Setting the threshold at 120 Wm^{-2}

The WMO (2008) gives a standard threshold of the CS recorder as 120 Wm^{-2}. The applicability of this constant threshold is tested by setting the threshold in the models equal to 120 Wm^{-2} and recalibrating the parameters. This also gives an indication of how sensitive the models are to the threshold value.

It is found that forcing the threshold only leads to a very minor change in the models internal and external variance for each location. The decrease in model performance (RMSE) is also only very minor suggesting that the models are relatively insensitive to the threshold.

4.1.6 Validation

As a validation, each of the calibrated radiation models and residual error models, with variable threshold, for each location were run using the remaining available data not used for the calibration. The time period used and the change in RMSE and the variances can be seen in Table 4.2.

For each location, the models perform similarly between the calibration and validation period. At four locations, the models show a slightly improved performance, in terms of RMSE and total and external variance, for the validation period. Melbourne has the greatest reduction in RMSE, reduced by an average of 0.1 MJ m^{-2} d^{-1}. Darwin has the best performance in terms of the change in average external variance. For Darwin, the average external variance is actually smaller in the validation period than in the calibration period with a difference of -0.115 MJ^2 m^{-4} d^{-2}. Tennant Creek has the greatest increase in RMSE by 0.220 MJ m^{-2} d^{-1}, while Mildura has the greatest increase in external variance by 0.171 MJ^2 m^{-4} d^{-2}. The average change in internal variance is only minor for each location.

The validation test was also repeated for the models with the threshold set at 120 Wm^{-2}. The validation results using this constant threshold are very similar to the validation results using a variable threshold.

The similar performance of the models in the calibration and validation periods suggests that the models are quite robust and that the period used for calibration contains a sufficiently wide range of atmospheric conditions e.g. a variety of cloudy and sunny days. As with the calibration, no model performs consistently better than the others for the validation period.

Table 4.2 Change in average model RMSE, internal and external variance for each location for the validation period compared with the calibration period with a variable threshold.

Location	**Years**	**RMSE** ($MJ\ m^{-2}\ d^{-1}$)	**Internal Variance** ($MJ^2\ m^{-4}\ d^{-2}$)	**External Variance** ($MJ^2\ m^{-4}\ d^{-2}$)
Adelaide	2006-2010	-0.090	-0.009	-0.155
Alice Springs	1999-2002, 2006-2010	+0.143	+0.002	+0.112
Broome	1999-2002, 2006-2010	+0.095	+0.004	+0.124
Darwin	1999-2002, 2006-2010	-0.027	-0.040	-0.115
Melbourne	1999-2002, 2006-2010	-0.100	+0.007	-0.043
Mildura	1999-2002	+0.173	+0.027	+0.171
Mount Gambier	1999-2002	-0.023	-0.006	-0.016
Tennant Creek	1999-2002	+0.220	+0.000	+0.083
Wagga Wagga	1999-2002, 2006-2010	+0.113	+0.009	+0.051

4.2 Direct Radiation

4.2.1 Direct radiation distributions from observed data

The relationship between SSH and the direct radiation can be seen in Figure 4.11 which shows scatter plots of the observed direct radiation plotted against the SSH fraction. The direct radiation model simulations are also shown.

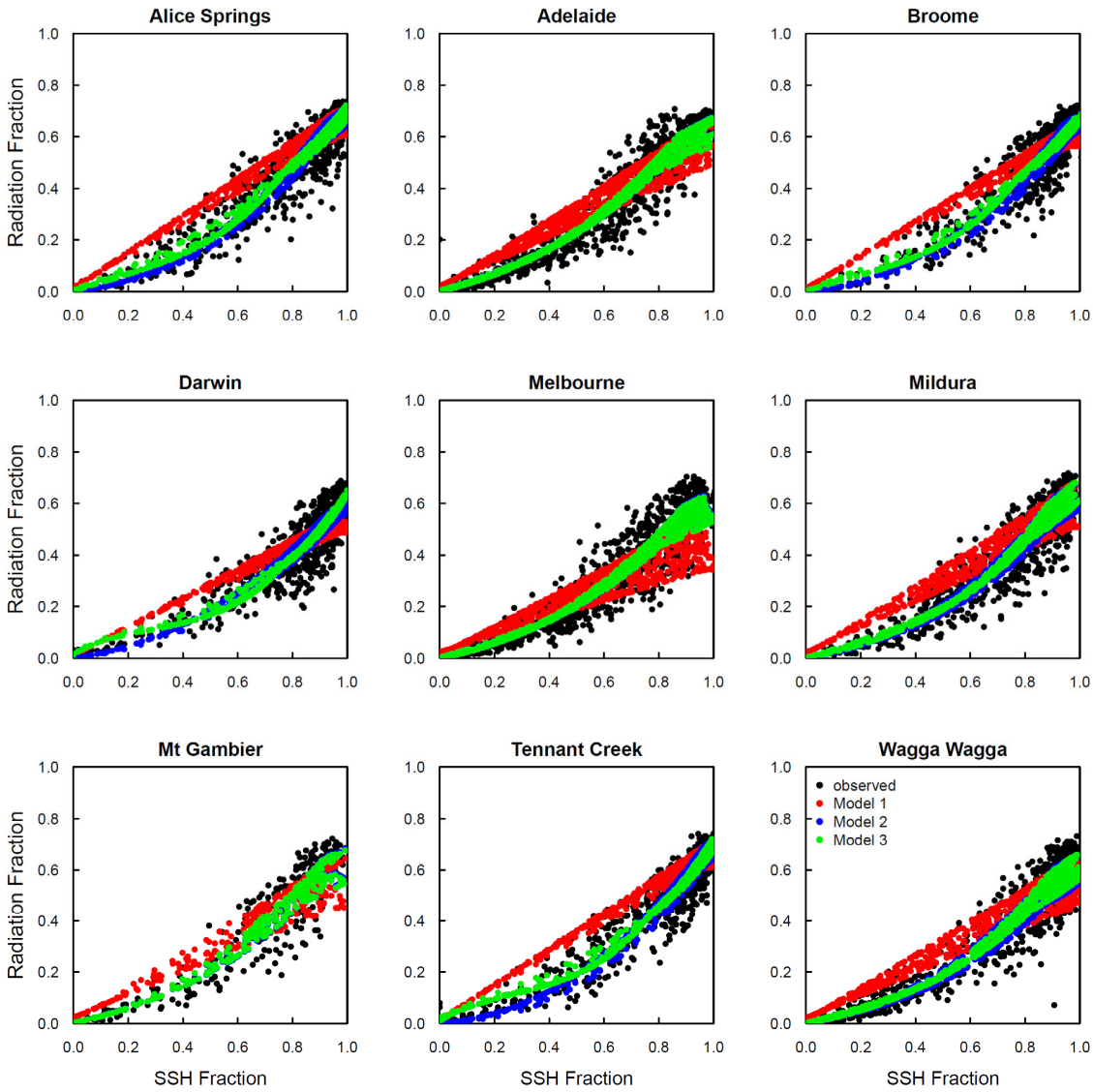

Figure 4.11 Direct radiation scatter plots showing the relationship between the observed and modelled direct radiation with SSH fraction.

The observed direct radiation data appears to follow a convex quadratic relationship with the SSH fraction. As the SSH increases so does the direct radiation, with a greater slope at higher SSH. When *n/N*=0 there is almost no direct radiation. In the mid ranges of the SSH, there is quite a lot of scatter. In comparison, the scatter at *n/N*~0 is much smaller. Alice Springs, Broome, Darwin and Tennant Creek also show little scatter at *n/N*~1 while Adelaide, Melbourne, Mount Gambier and Wagga Wagga have a greater amount of scatter.

4.2.2 Model calibration results

Comparison of the observed and simulated data in Figure 4.11 reveals that Models 2 and 3 perform similarly well for most locations while Model 1 does not perform as well. Models 2 and 3 follow the quadratic structure of the observed radiation with SSH fraction. In contrast, Model 1 is quite poor and follows a linear structure. Time series for Model 2 for the year 2004 are shown in Figure 4.12 for Alice Springs and Figure 4.13 for Melbourne.

It is found that varying the residual error model structure does not significantly influence the radiation model parameter values at each location. The residual error model values are also reasonably consistent between the radiation models for each location, with minimal difference between radiation Models 2 and 3. The parameters vary more between the locations. This suggests that the errors are more dependent on local atmospheric conditions than the radiation model structure. This is similar to what was found with the global radiation.

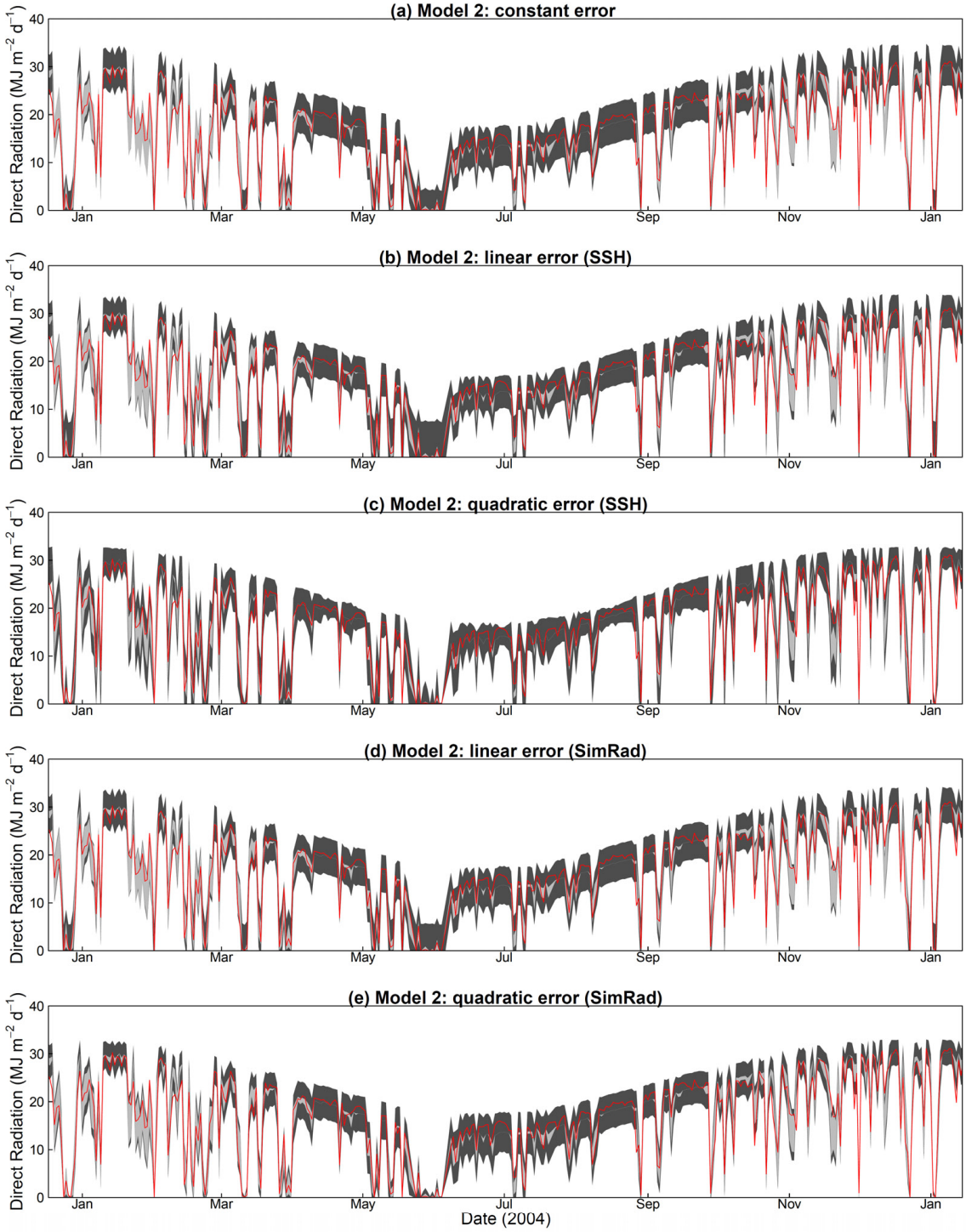

Figure 4.12 Time series of predicted radiation for the year 2004 (calibration period) for Alice Springs using Model 2. The red line is the observed radiation, the light grey shading is the internal variance of the modelled radiation, and the dark grey shading is the 95% predictive limit of the external ("residual error") variance. The total variance is the sum of the internal and external variance.

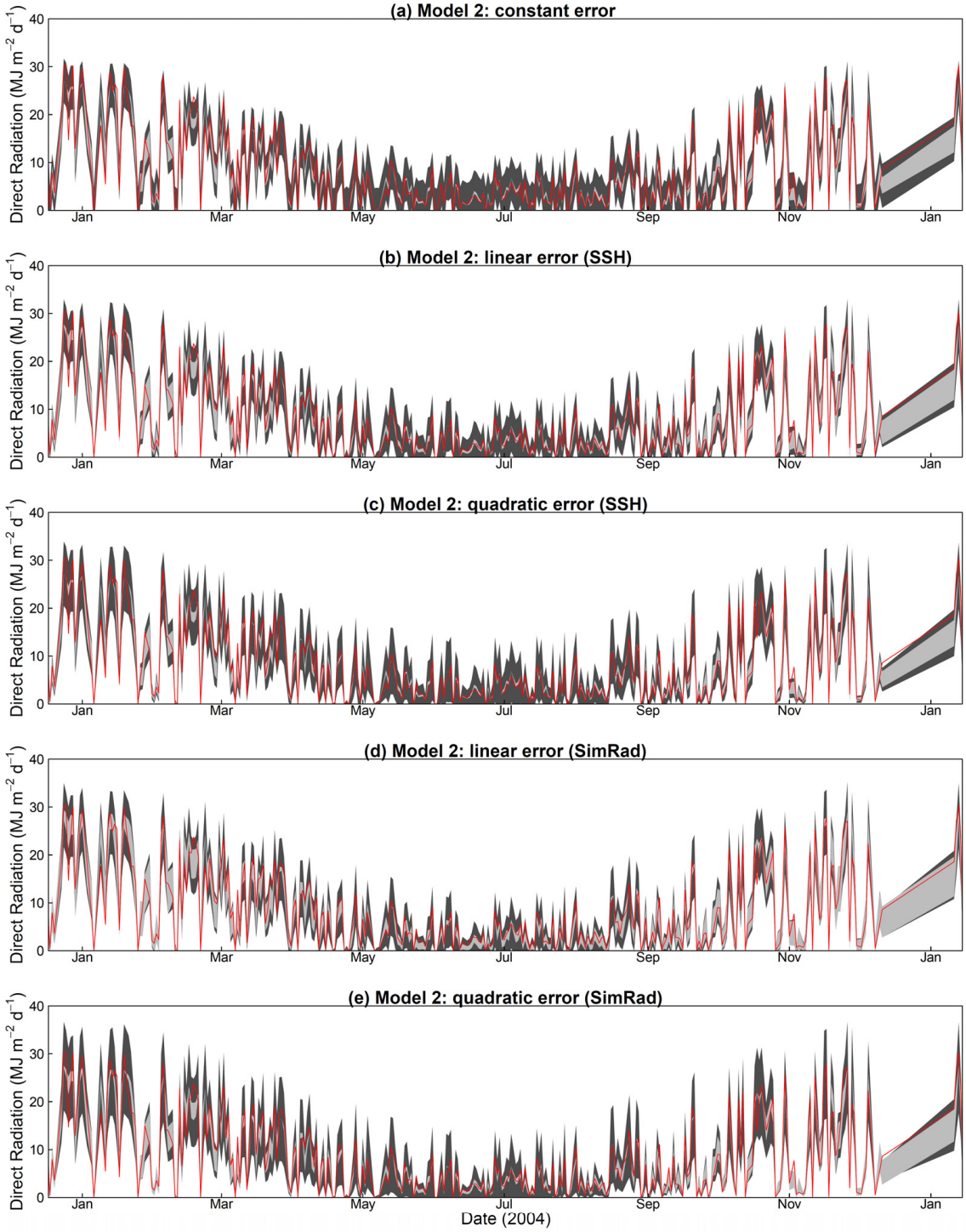

Figure 4.13 Time series of predicted radiation for the year 2004 (calibration period) for Melbourne using Model 2. The red line is the observed radiation, the light grey shading is the internal variance of the modelled radiation, and the dark grey shading is the 95% predictive limit of the external ("residual error") variance. The total variance is the sum of the internal and external variance.

The different error variances can be seen in the different time series for Model 2 in Figure 4.12 and Figure 4.13. Additionally, Figure 4.14 shows the error variances for the range of SSH fractions and simulated radiations for Model 2 for Alice Springs and Melbourne. The error variance is very similar for all the radiation models. Therefore, only the variance for Melbourne and Alice Springs is shown but is representative of all the locations and models. Alice Springs is representative of Broome, Darwin and Tennant Creek while Wagga Wagga, Melbourne, Mt Gambier, Mildura and Adelaide have similar error variances.

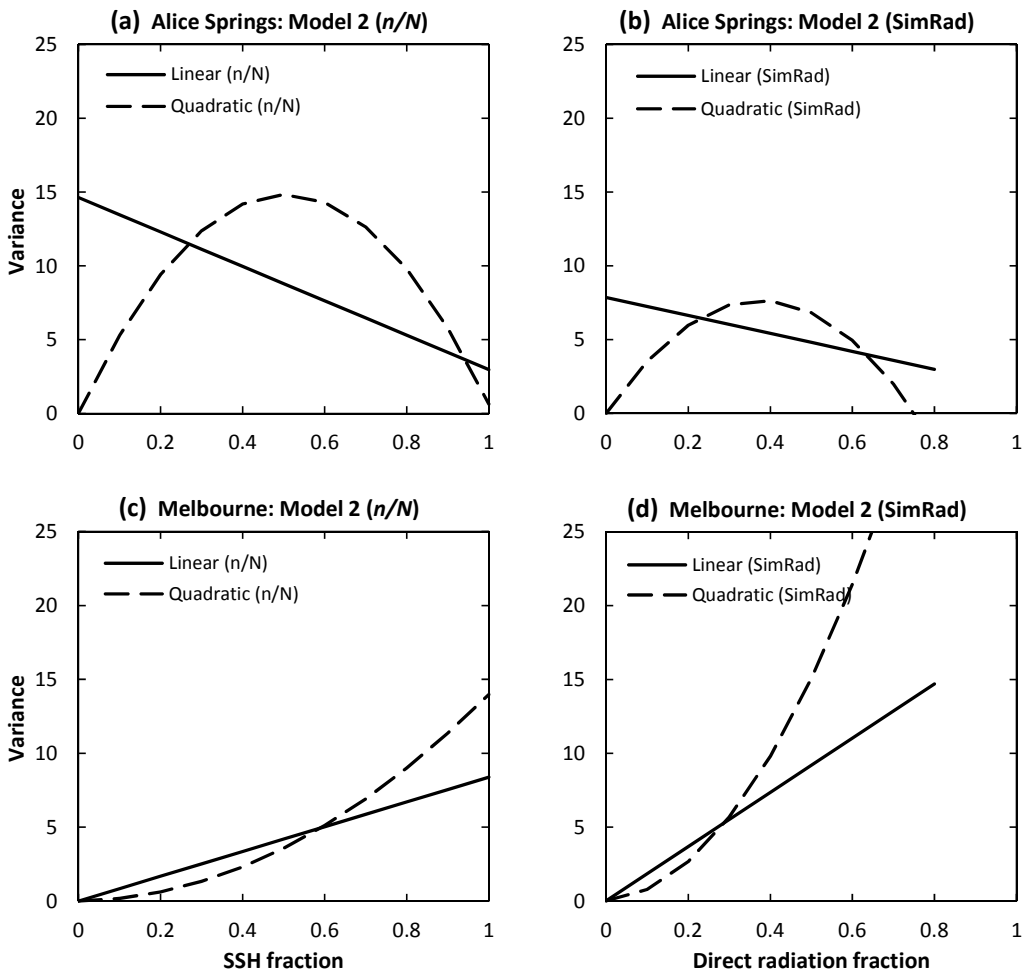

Figure 4.14 Linear and quadratic error variance ($MJ^2\ m^{-4}\ d^{-2}$) for Model 2 calibrated to Alice Springs (panels a and b) and Melbourne (panels c and d) data. The error variance is dependent on *n/N* (panels a and c) and the simulated radiation (SimRad) (panels b and d).

In order to compare the panels of Figure 4.14, note that when *n/N*=1 the predicted mean direct radiation fraction is approximately 0.7. For both locations, the quadratic structure has a higher variance for mid-range sunny days (*n/N* and direct radiation fraction ~0.5) than cloudy days (*n/N* and radiation fraction ~0). The error approaches zero on completely overcast days as minimal direct radiation occurs under these conditions. This can also be seen in the scatter plots in Figure 4.11. As the day becomes clearer (*n/N* increases), the amount of direct radiation increases and there is a corresponding increase in the variance of the error. For Alice Springs, both the *n/N* and SimRad structures have reduced scatter as the day becomes completely clear.

The linear error structure for both locations, but particularly Alice Springs, appears unable to adequately model the structure of the variance with changing SSH and radiation fraction. This is because there is not a constant change in variance with the change in SSH fraction.

The linear and quadratic structures tend to follow similar trends for the SSH and simulated radiation structures for all locations. For Alice Springs, the maximum variance tends to be higher for the *n/N* structure than the simulated radiation structure. However, for other locations, the *n/N* structure shows less variance. Therefore, no error structure has a consistently smaller maximum variance for all locations.

4.2.3 Model performance

Figure 4.15 compares the average, minimum and maximum RMSE, internal and external variance for each of the direct radiation models at all locations.

In terms of the RMSE (Figure 4.15a), it is clear that Model 1 has the poorest performance while Models 2 and 3 perform similarly well. Model 3 generally performs slightly better than Model 2. The residual error model structure only has a minor influence on the RMSE. As with the global radiation, Mildura and Alice Springs have the smallest RMSE while Darwin has the largest RMSE for Models 2 and 3.

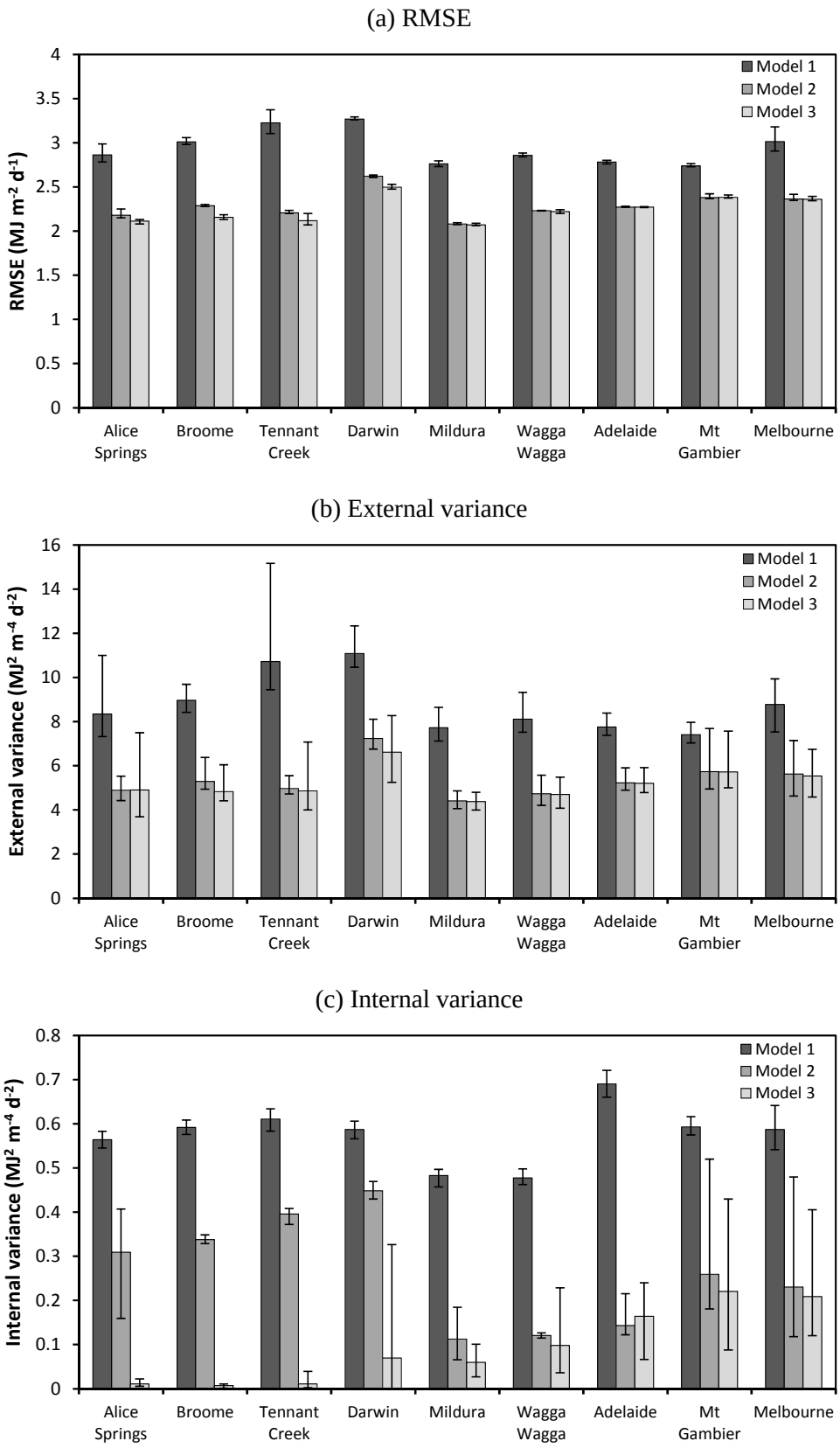

Figure 4.15 (a) RMSE, (b) external variance and (c) internal variance averaged individually for each of the models for all locations. The error bars indicate the maximum and minimum RMSE, internal and external variance for each location given by the different residual error models.

For the external variance (Figure 4.15b), following the same trend as the RMSE, Model 1 has the greatest amount of variance while Models 2 and 3 have similar amounts. The variance is greatest for Darwin and smallest for Mildura. The residual error model structure has a larger role in the amount of external variance. This could be due to the external variance being calculated as the total variance minus the internal variance, where the internal variance is shown to be influenced by the error model structure. There is no consistency as to which residual error model has the smallest external error variance.

For the internal model variance (Figure 4.15c), Model 1 has the greatest amount of variance for all locations followed by Model 2 and then Model 3. The residual error model structure has a larger influence on the internal variance particularly at Mount Gambier and Melbourne. There is no consistency between the models and locations as to which residual error model has the greatest amount of internal variance. However, compared to the external variance, on average the internal variance is relatively small for all the models. Nevertheless, as shown in Figure 4.12 and Figure 4.13, on days with mid values of the SSH fraction, the internal variance accounts for most of the total variance for all the error models.

The difference in RMSE and external variance between the locations is similar to the global radiation. The performance of the models at each location can be attributed to the climate of each location, as discussed for the global radiation in Section 4.1.3 above.

To further demonstrate the performance of the models, Figure 4.16 shows the relative error of the modelled radiation, compared with the observed radiation, for Model 2 with the quadratic *n/N* residual error model. Only this model is shown as the relative errors are very similar for all the residual error models, within each radiation model, for each location. The relative errors are also similar for Models 2 and 3, and these are lower than those for Model 1 for all locations.

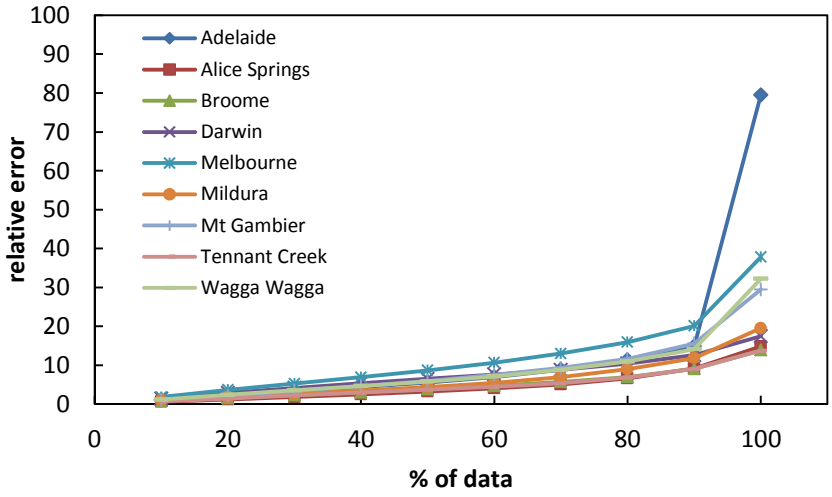

Figure 4.16 Relative error with percentage of data for all locations for Model 2 with the quadratic *n/N* error structure.

In Figure 4.16, the relative error is plotted against the percentage of data points. The relative error for all data points ranges from 14% at Tennant Creek and Alice Springs to 80% at Adelaide, with an average of 23% for all locations. This relative error is quite large for Adelaide; however, the greatest amount of error occurs at low SSH fractions where the amount of radiation is at a minimum.

To examine this relationship further, Figure 4.17 shows the relative error plotted against the SSH fraction for Alice Springs and Melbourne. Melbourne has the highest relative error for most SSH fractions while Alice Springs has one of the lowest relative errors for all SSH fractions. In Figure 4.17, it can be seen that the relative error is greatest for SSH fractions less than 0.2, which corresponds with minimum amounts of direct radiation, and approaches zero as the SSH fraction increases. Therefore, the large relative error is in general the equivalent of less than 1 MJ m^{-2} d^{-1}. All locations follow similar trends with the majority of the relative error occurring for SSH fractions less than 0.2, which corresponds to generally less than 10% of the data.

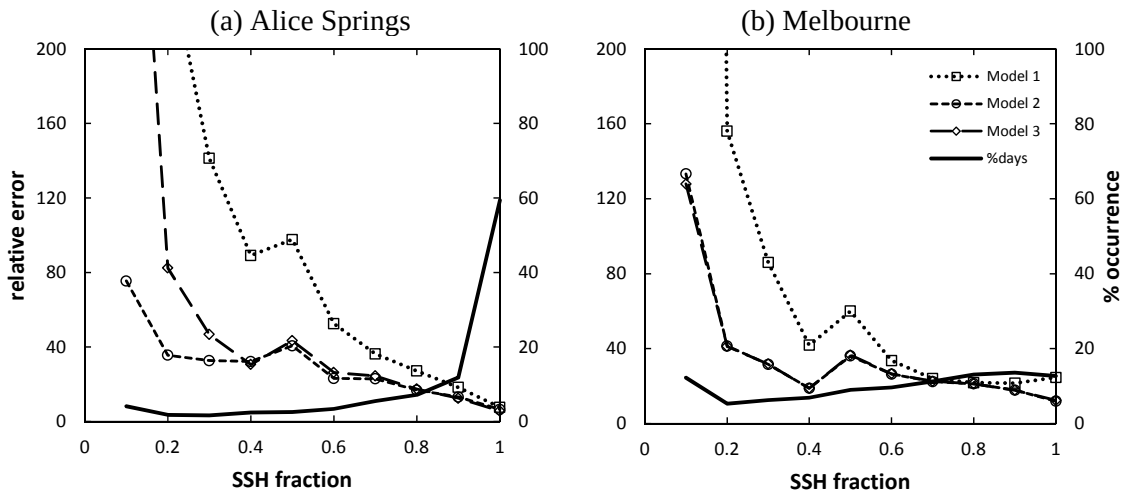

Figure 4.17 Relative error with the change in SSH fraction for (a) Alice Springs and (b) Melbourne. All three models are shown with the quadratic *n/N* error structure. The percentage of days with each SSH fraction is shown by the thick solid line.

4.2.4 Predictive reliability of the direct models: QQ plots

QQ plots are formed to check the extent to which the probabilistic predictions of the different radiation and residual error models are compatible with the observed data. These can be seen in Figure 4.18 for Alice Springs and Figure 4.19 for Melbourne.

By examining the QQ plots with no external noise added (the only source of randomness is due to the sampling of the bright SSH hours within the day), the left column of Figure 4.18 and Figure 4.19, it is clear that all of the models under-estimate the predictive uncertainty, particularly Model 3. This indicates that the uncertainty due to the timing of the bright hours does not account for all the variation between the observed and simulated direct radiation.

With noise added, Models 2 and 3 slightly over-estimate the predictive uncertainty. The constant error variance has the greatest over-estimation for all the models. Model 1 also tends to result in an over-prediction. For Alice Springs the quadratic *n/N* error model is closest to the 1:1 line for Models 2 and 3. For Melbourne the quadratic *n/N* error model also has the smallest overestimation (closest to the 1:1 line).

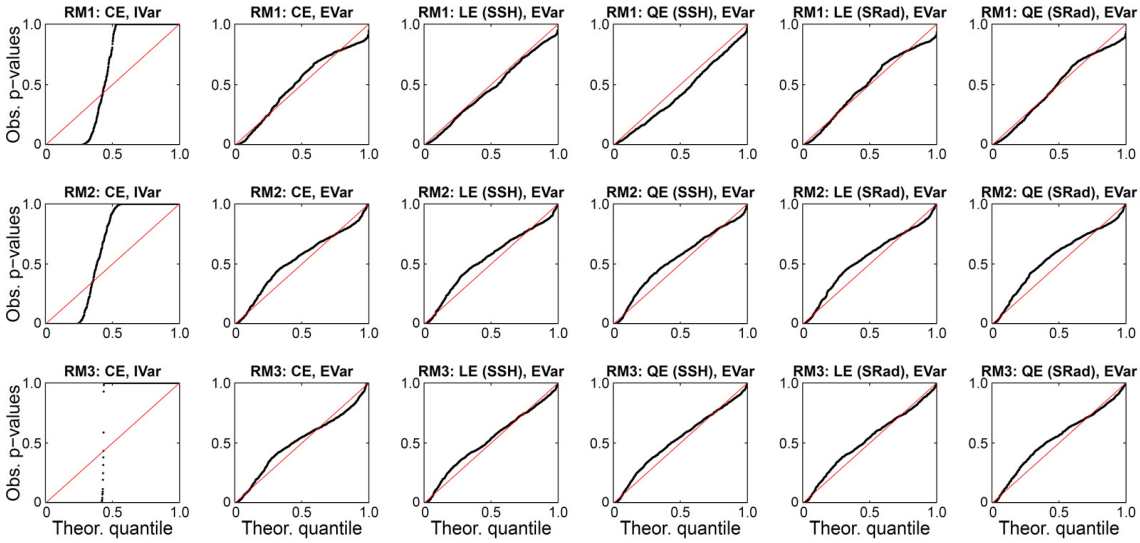

Figure 4.18 QQ plots for Alice Springs for all radiation models and residual error model structures for the calibration period. The left column is the internal variance while the other columns show the external variance for the five error structures. RM stands for radiation model, CE for constant error, LE for linear error, QE for quadratic error, SRad for simulated radiation, EVar for external variance and IVar for internal variance.

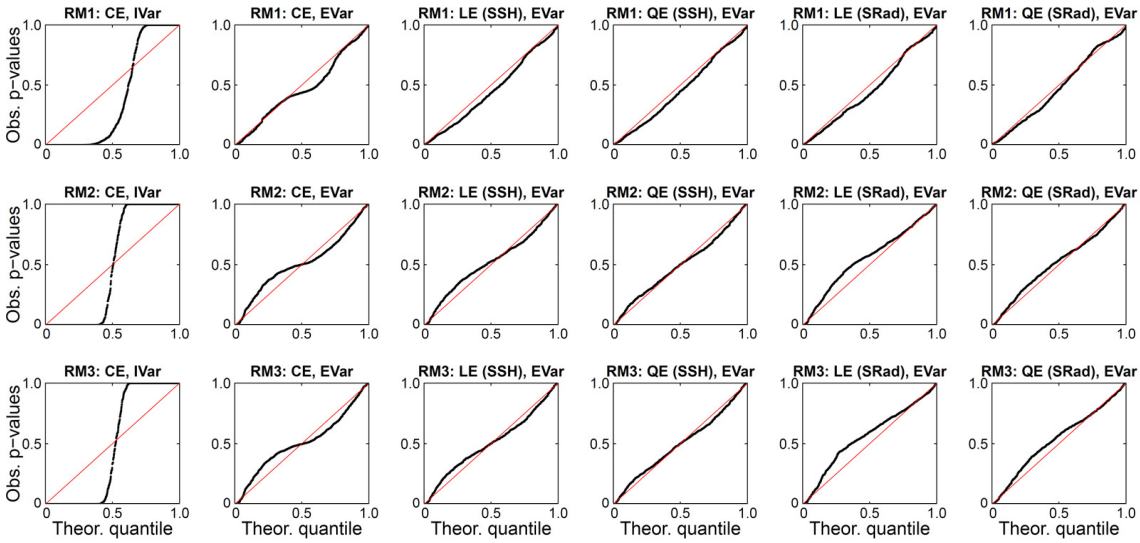

Figure 4.19 QQ plots for Melbourne for all radiation models and residual error model structures for the calibration period. The left column is the internal variance while the other columns show the external variance for the five error structures. RM stands for radiation model, CE for constant error, LE for linear error, QE for quadratic error, SRad for simulated radiation, EVar for external variance and IVar for internal variance.

The predictive reliability is shown to be similar for all the models. This could be because the majority of data at all locations have a SSH fraction greater than 0.8 and the variance amount for this fraction is similar for all the models. Similarly, for the simulated radiation residual error model structures, the majority of data falls in the 0.5-0.7 radiation fraction range, and the residual error model structures have an error variance of similar magnitude in this range. Further, Models 2 and 3 produce very similar mean direct radiation values for all residual error model structures. As this is what is used to determine the total and external variance, it is expected that they would have similar predictive distributions.

For all locations it is clear that Model 1 does not perform as well as Models 2 and 3 in terms of RMSE, external variance and relative error. Models 2 and 3 perform similarly well. It is therefore suggested that Model 2 is the preferred model as it has one less parameter. It is clear that a single parameter, as used in Model 1, describing the amount of direct radiation as a fixed fraction of the ETR, is not sufficient to model the direct radiation. The diminution of the ETR with changes in the SSH fraction needs to be accounted for. A linear decrease in the radiation with the SSH fraction is sufficient.

4.2.5 Setting the threshold at 120 Wm^{-2}

The applicability of the constant threshold for the CS recorder is tested by setting the threshold in the models equal to 120 Wm^{-2} and recalibrating the parameters. This also gives an indication of how sensitive the models are to the threshold value.

The forced threshold only leads to a minor change in the radiation model parameter values. The error structures are also very similar between the variable threshold and the forced threshold for all locations for Models 2 and 3. However, Model 1 has much greater error variance terms.

Changing the threshold to 120 Wm^{-2} only leads to a small increase in the RMSE for Models 2 and 3. For Model 1 the increase is much greater for all the locations. For Model 2 and 3 the greatest increase is 0.12 MJ m^{-2} d^{-1} for Darwin while for Model 1 the greatest increase is 1.28 MJ m^{-2} d^{-1} at Adelaide. The smallest increase for Models 2 and

3 is at Mildura where the increase is 0.004 MJ m^{-2} d^{-1}. For Model 1 the smallest increase is 0.81 MJ m^{-2} d^{-1} at Darwin.

The trend in external variance is similar to that in the RMSE. Model 1 has a much greater increase than Models 2 and 3, with the difference ranging from 5.77 (Broome) to 8.56 MJ^2 m^{-4} d^{-2} (Adelaide). For Model 2, the difference ranges from -0.01 (Mildura) to 0.62 MJ^2 m^{-4} d^{-2} (Darwin) and for Model 3 the difference ranges from -0.07 (Melbourne) to 0.64 MJ^2 m^{-4} d^{-2} (Broome).

There is no consistent change to the internal variance. Different locations and different models exhibit either an increase or a decrease. The change ranges from -0.43 (Adelaide) to -0.31 MJ^2 m^{-4} d^{-2} (Wagga Wagga) for Model 1, -0.34 (Darwin) to 0.03 MJ^2 m^{-4} d^{-2} (Adelaide) for Model 2, and -0.09 (Mt Gambier) to 0.12 MJ^2 m^{-4} d^{-2} (Alice Springs) for Model 3.

It is therefore suggested that a threshold of 120 Wm^{-2} can be used for Models 2 and 3 but not Model 1.

4.2.6 Validation

The change in RMSE and the variances between the calibration and validation periods can be seen in Table 4.3. For each location, the models perform similarly well between the validation and calibration periods. Models 2 and 3 show a slightly improved performance, in terms of RMSE and total and external variance, for the validation period at six locations while Model 1 shows an improved performance at four locations. The average change in internal variance is only minor for each location and model.

For Models 2 and 3, Mt Gambier exhibits the greatest improvement in performance with the RMSE reduced by an average of 0.21 MJ m^{-2} d^{-1} and the external variance reduced by 0.36 MJ^2 m^{-4} d^{-2}. The greatest increase in RMSE is by 1.15 MJ m^{-2} d^{-1} at Mildura followed by Tennant Creek with an increase of 0.32 MJ m^{-2} d^{-1}. Similarly, the greatest increase in external variance is at Mildura (0.83 MJ^2 m^{-4} d^{-2}) followed by Broome (0.37 MJ^2 m^{-4} d^{-2}). For Model 1, Mt Gambier also has the greatest improvement with the RMSE reduced by an average of 0.22 MJ m^{-2} d^{-1} and the greatest reduction in

external variance by 0.42 MJ^2 m^{-4} d^{-2}. Mildura has the greatest increase in RMSE by 1.00 MJ m^{-2} d^{-1} and external variance by 0.91 MJ^2 m^{-4} d^{-2}.

With the threshold set at 120 Wm^{-2}, the validation results are very similar to the variable threshold results.

The similar performance of the models in the calibration and validation periods suggests that the models are quite robust and that the period used for calibration contained a sufficiently wide range of atmospheric conditions. Models 2 and 3 perform consistently well between the validation and calibration periods for all locations while Model 1 tends to have a slightly reduced performance.

Table 4.3 Change in average direct radiation model (M) performance for each location for the validation period compared with the calibration period with a variable threshold.

	RMSE ($MJ\ m^{-2}\ d^{-1}$)			**Internal Variance ($MJ^2\ m^{-4}\ d^{-2}$)**			**External Variance ($MJ^2\ m^{-4}\ d^{-2}$)**		
Location	**M1**	**M2**	**M3**	**M1**	**M2**	**M3**	**M1**	**M2**	**M3**
Adelaide	-0.128	-0.101	-0.100	-0.025	-0.009	-0.010	-0.048	-0.003	-0.003
Alice Springs	0.054	-0.019	-0.053	-0.053	-0.026	-0.002	-0.229	-0.127	-0.261
Broome	0.205	0.296	0.261	0.039	0.010	0.001	0.468	0.315	0.444
Darwin	-0.097	-0.070	-0.113	0.011	-0.015	-0.002	-0.394	-0.292	-0.056
Melbourne	0.002	-0.066	-0.062	0.012	0.006	0.006	-0.108	-0.126	-0.128
Mildura	1.007	1.149	1.147	0.048	0.014	0.006	0.906	0.853	0.827
Mt Gambier	-0.217	-0.208	-0.209	0.000	-0.009	-0.008	-0.417	-0.358	-0.356
Tennant Creek	0.540	0.349	0.302	0.035	0.024	0.000	0.237	0.169	0.052
Wagga Wagga	-0.077	-0.130	-0.129	0.025	0.008	0.007	0.017	-0.102	-0.088

4.3 Diffuse Radiation

4.3.1 Diffuse radiation distributions from observed data

The SSH data is next used to estimate the daily diffuse radiation. The relationship between SSH and the diffuse radiation can be seen in Figure 4.20 which shows scatter plots of the observed diffuse radiation plotted against the SSH fraction. The diffuse radiation model simulations are also shown.

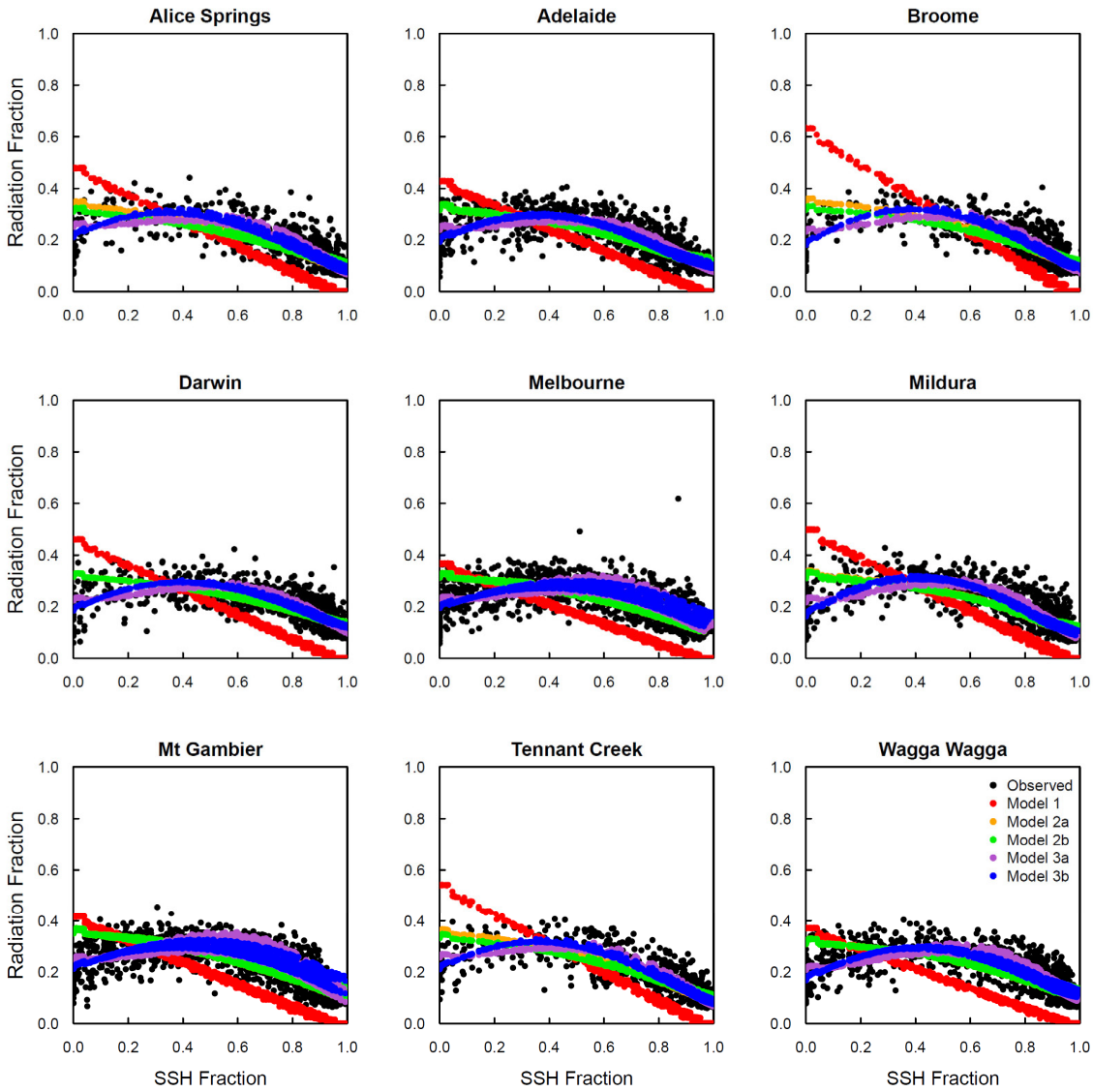

Figure 4.20 Diffuse radiation scatter plots showing the relationship between the observed and modelled diffuse radiation with SSH fraction for all locations.

The observed diffuse radiation data appears to follow a concave quadratic relationship with the SSH fraction. Unlike the direct radiation, the diffuse radiation is greatest at mid values of SSH (n/N~0.45) and decreases towards the upper and lower SSH limits. Diffuse radiation is present for all SSH fractions. The scatter in the data is fairly uniform across all SSH values, with a slight increase at the lower SSH bound.

Diffuse radiation is higher on cloudy days than clear or completely overcast days due to the scattering effect of clouds (Liu and Jordan, 1960; Choudhury 1963). Unlike the direct radiation, which does not occur on completely overcast days, the composition of the atmosphere ensures that there is always some diffuse radiation present. Even when no clouds are present, gases, aerosols and dust ensures some of the ETR is scattered towards the earth. As the cloudiness increases, more ETR is scattered, becoming diffuse radiation. However, as the SSH fraction drops below about 0.45 the diffuse radiation decreases as the clouds prevent more of the scattered light from reaching the surface. On completely overcast days, the clouds only allow a minimal amount of diffuse radiation to reach the land surface.

4.3.2 Model calibration results

The five diffuse radiation models are calibrated using the Model 2 direct radiation parameters. For the diffuse radiation, Models 2a and 2b perform similarly well, as do Models 3a and 3b for most locations; however, Model 3b shows a slightly better performance than the other models. The time series for Model 3b for the year 2004 are shown in Figure 4.21 for Alice Springs and Figure 4.22 for Melbourne. The scatter plots in Figure 4.20 also compare the models for each location. From Figure 4.20 it is clear that Models 2a and 2b have similar predictions of diffuse radiation, as do Models 3a and 3b. However, only Models 3a and 3b follow the curved structure of the observed diffuse radiation with SSH fraction. Model 1 is linear and does not follow the curved structure of the observed radiation, while Models 2a and 2b only follow part of the curved structure.

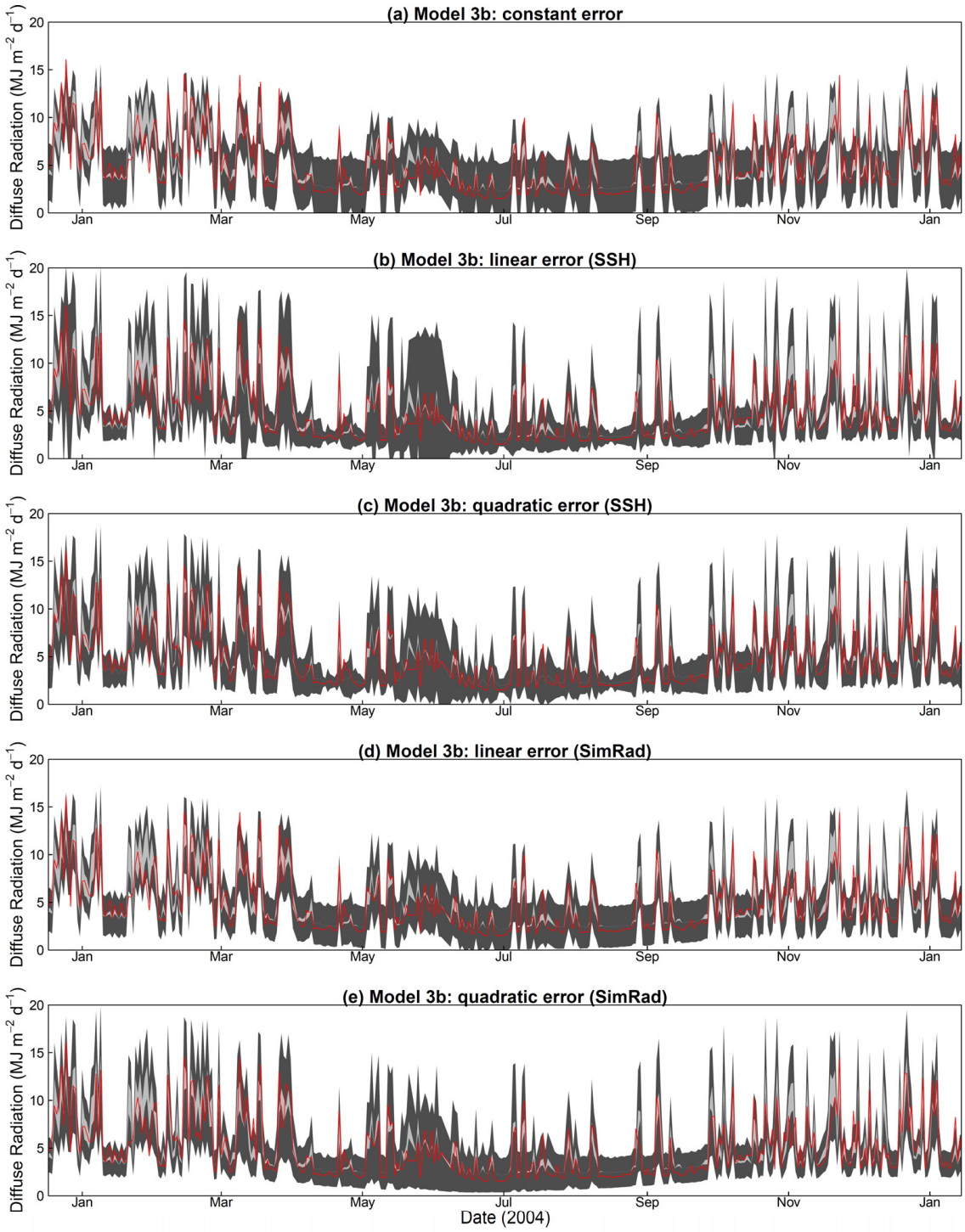

Figure 4.21 Time series of predicted diffuse radiation for the year 2004 (calibration period) for Alice Springs using Model 3b. The red line is the observed radiation, the light grey shading is the internal variance of the modelled radiation while the dark grey shading is the 95% limit of the external variance of the modelled radiation. The total variance is the sum of the internal and external variance.

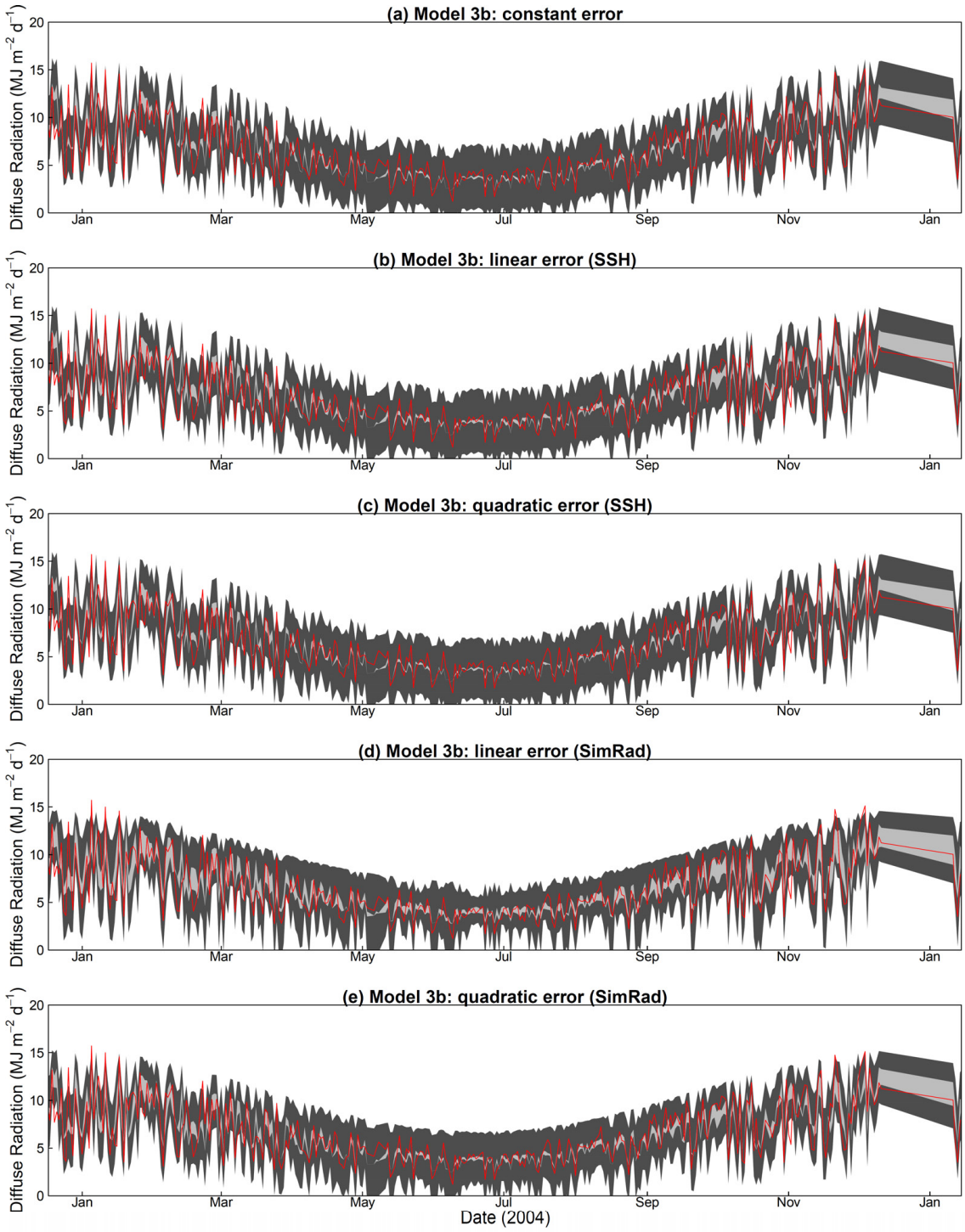

Figure 4.22 Time series of predicted diffuse radiation for the year 2004 (calibration period) for Melbourne using Model 3b. The red line is the observed radiation, the light grey shading is the internal variance of the modelled radiation while the dark grey shading is the 95% limit of the external variance of the modelled radiation. The total variance is the sum of the internal and external variance.

At each individual location, the radiation model parameter values are consistent between the different residual error model structures. The residual error model values are also reasonably consistent between the radiation models for each location, with minimal difference between Models 2a and 2b and between Models 3a and 3b. The error values tend to be greater for Model 1. As was found with the global and direct radiation, the diffuse radiation model parameters vary more between the locations.

The different error variances can be seen in the different time series for Model 3b in Figure 4.21 and Figure 4.22. Additionally, the error variances for the range of SSH fractions and simulated radiations can be seen for Model 3b in Figure 4.23 for Alice Springs and Melbourne. Note that the error variance for all the models is very similar, however, the smallest variance occurs for Model 3b. As with the direct radiation, only the variance for Melbourne and Alice Springs is shown but is representative of all the locations.

Unlike the direct radiation, the SSH and simulated radiation structures in Figure 4.23 are not directly comparable. From the scatter plots in Figure 4.20, it is clear that the same simulated radiation fraction can occur for both high and low SSH fractions. The diffuse radiation fraction tends to range between 0.1 and 0.4.

From the scatter plots in Figure 4.20, it can be seen that the observed diffuse radiation is reasonably scattered for all SSH fractions for all locations. This is reflected for Melbourne in the almost horizontal error variance for the SSH structure in Figure 4.23c. Each of the SSH error structures has a slightly higher variance for cloudy days (low SSH fraction) than sunny days, approaching zero as the SSH fraction approaches 1.

The simulated radiation (SimRad) error variance structures are not as consistent between models or locations. For Alice Springs the simulated radiation variance is greater at higher diffuse radiation fractions (~0.4) while at Melbourne the error variance is greater at mid radiation fractions (~0.2). However, for all locations the error variance is generally smaller for Models 3a and 3b than for Models 2a and 2b.

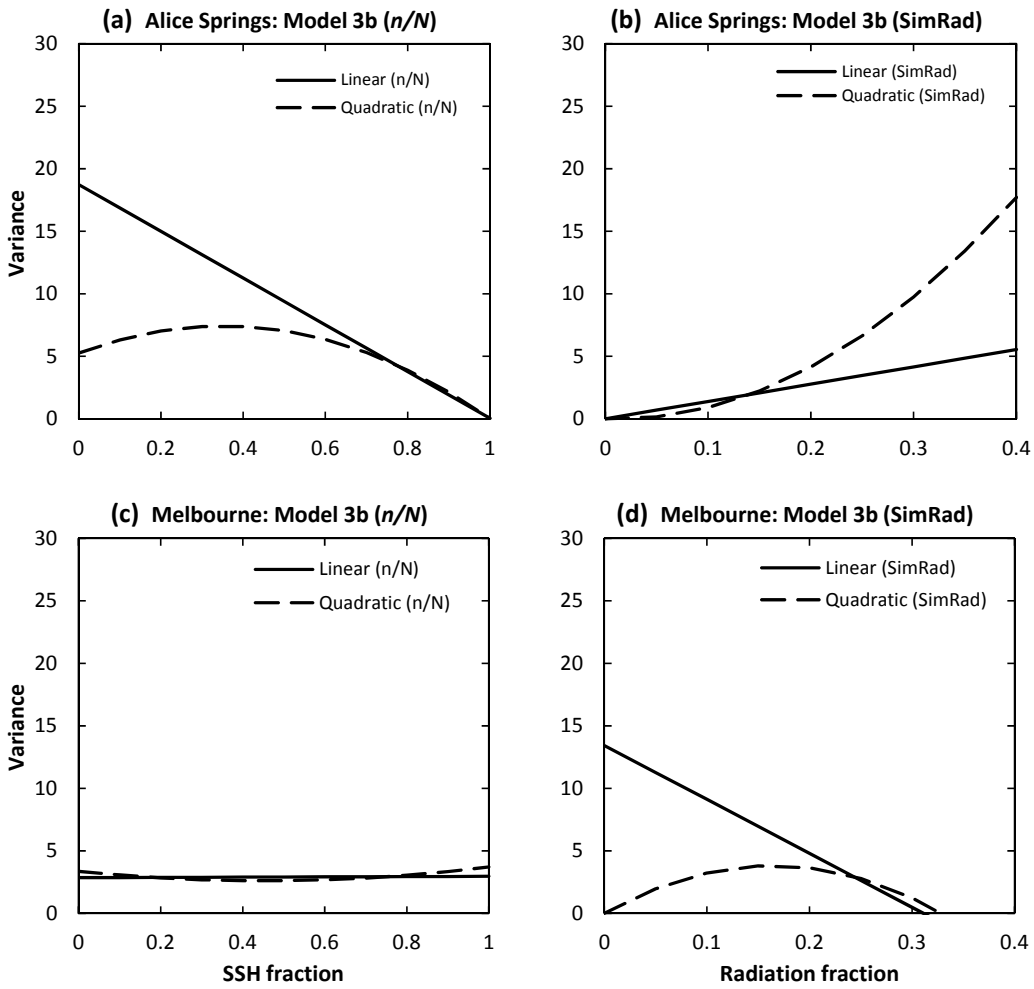

Figure 4.23 Linear and quadratic error variance for Model 3b calibrated to Alice Springs (panels a and b) and Melbourne (panels c and d) data. The error variance is dependent on *n/N* (panels a and c) and the simulated radiation (SimRad) (panels b and d).

4.3.3 Model performance

Next, Figure 4.24 compares the diffuse radiation models based on their RMSE values, as well as the internal and external variance.

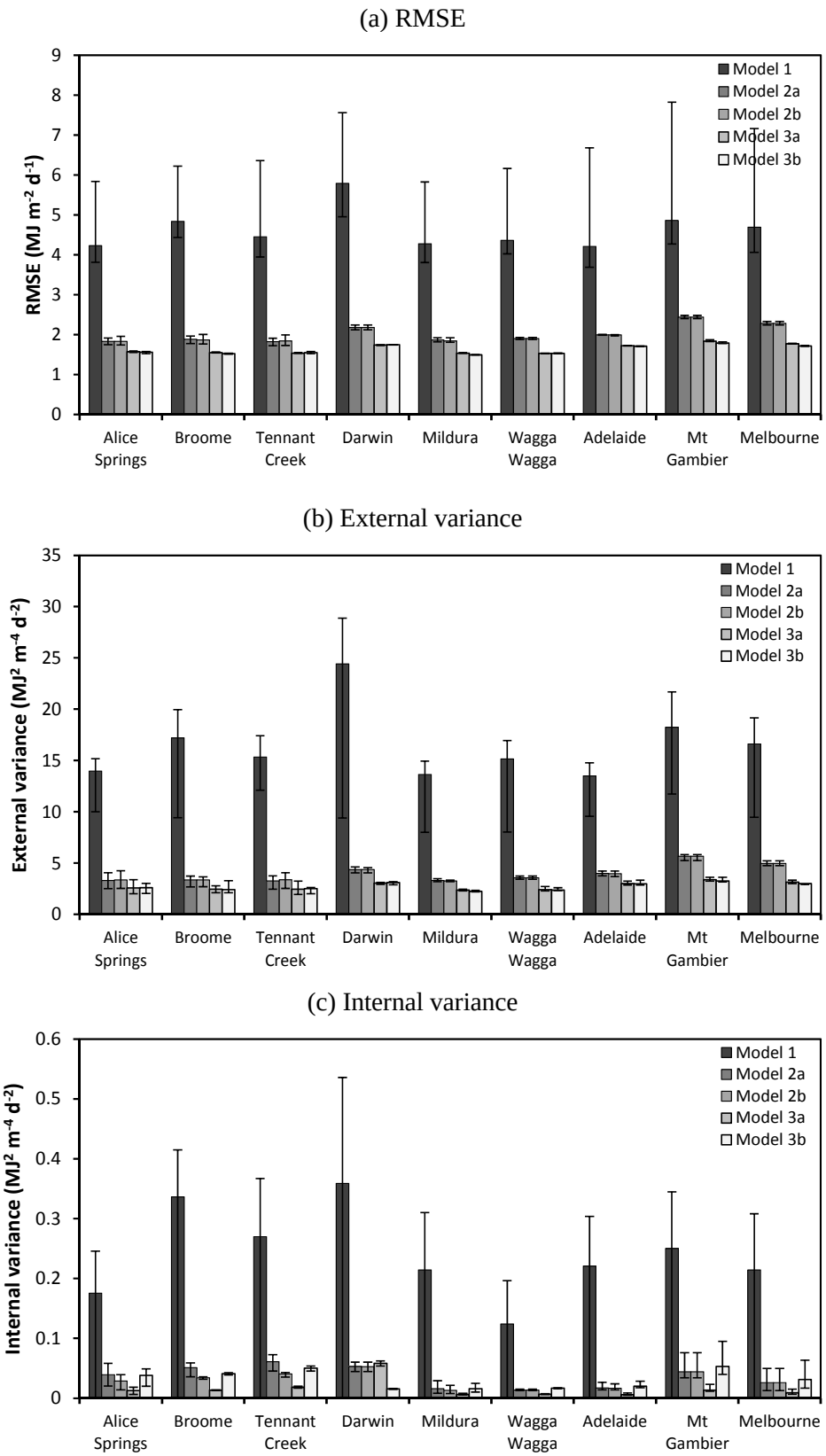

Figure 4.24 (a) RMSE, (b) external variance and (c) internal variance averaged individually for each of the models for all locations. The error bars indicate the maximum and minimum RMSE, internal and external variance for each location given by the different residual error models.

The RMSE values (Figure 4.24a) show that Model 1 has the poorest performance. Models 3a and 3b have the best performance, followed closely by Models 2a and 2b. With the exception of Model 1, the range of RMSE for each model shows that the residual error models only have a minor influence on the RMSE. The RMSE values are reasonably similar for all locations, except for Model 1. For Model 1, Darwin has the greatest RMSE value while Adelaide has the smallest value. For Models 2a and 2b, Mt Gambier, Melbourne and Darwin have the greatest values while Alice Springs, Tennant Creek and Mildura have the lowest values. For Models 3a and 3b, the RMSE is more consistent for all locations.

For the external variance (Figure 4.24b), following the same trend as the RMSE, Model 1 has the greatest amount of variance while Models 3a and 3b have the smallest variance. Model 3b tends to have a slightly better performance than Model 3a. For Model 1, the variance is greatest at Darwin and smallest at Adelaide. For the remaining models, the external variance is greatest at Mt Gambier and smallest at Mildura. This follows a trend similar to the RMSE, as expected. With the exception of Model 1, the different error models only have a reasonably small influence on the external variance. Again there is no consistency as to which error model has the smallest error variance.

For the internal model variance (Figure 4.24c), Model 1 shows the greatest amount of variance for all locations while the remaining models show a much smaller internal variance. The different residual error model structures have a slightly larger influence on the internal variance at Mt Gambier and Melbourne. There is no consistency between the models and locations as to which error model has the greatest amount of internal variance. As was found with the global and direct radiation, on average the internal variance only accounts for a small amount of the total variance. However, as shown in Figure 4.21 and Figure 4.22, on days with the mid values of the SSH fraction, the internal variance accounts for a larger portion of the total variance.

The model performances can again be linked with the annual rainfall at each location. Mildura generally has the best performance and the smallest annual rainfall while Darwin and Mt Gambier have relatively high annual rainfall totals and comparatively poor performances.

To further demonstrate the performance of the models, Figure 4.25 shows the relative error of the modelled radiation, compared with the observed radiation, for Model 3b with the quadratic *n/N* residual error model. Only this model is shown as the relative errors are very similar for all the residual error models within each radiation model for each location. The relative errors are also similar for radiation Models 3a and 3b and for Models 2a and 2b. The average relative errors for Models 3a and 3b are lower than those for Models 1, 2a and 2b for all locations.

The relative error for all data points ranges from 21% at Tennant Creek and Broome to 23% at Mt Gambier, with an average error of 22% for all locations. This again suggests that the models perform similarly well at all locations.

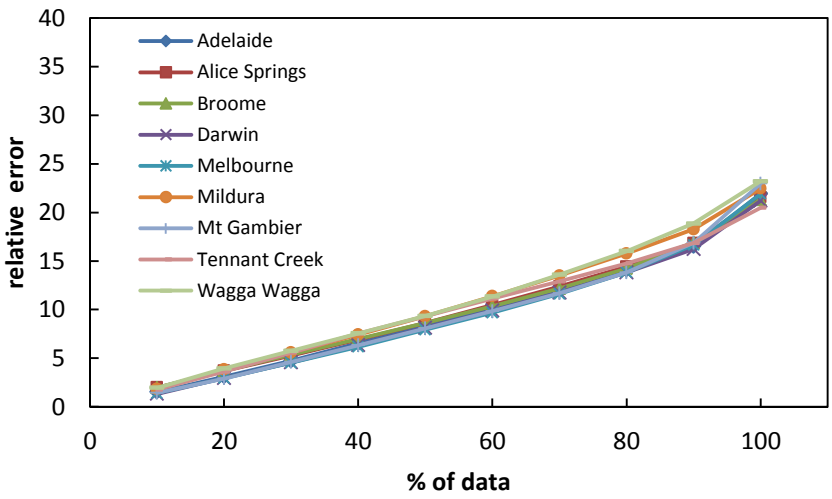

Figure 4.25 Relative error with percentage of data for all locations for Model 3b with the quadratic *n/N* error structure.

Figure 4.26 shows the relative error plotted against the SSH fraction for all radiation models, using the quadratic *n/N* residual error model, for Alice Springs and Melbourne. It is clear that Model 1 has the greatest relative error. For the remaining models, for SSH fractions greater than 0.2, the relative error is generally around 20%. As was found with the direct radiation, the relative error is greatest for SSH fractions less than 0.2 which corresponds with minimum amounts of diffuse radiation. Therefore, the large relative error is in general the equivalent of less than 3 MJ m^{-2} d^{-1}. All locations follow

similar trends with the majority of the error occurring for SSH fractions less than 0.2, which corresponds to generally less than 10% of the data.

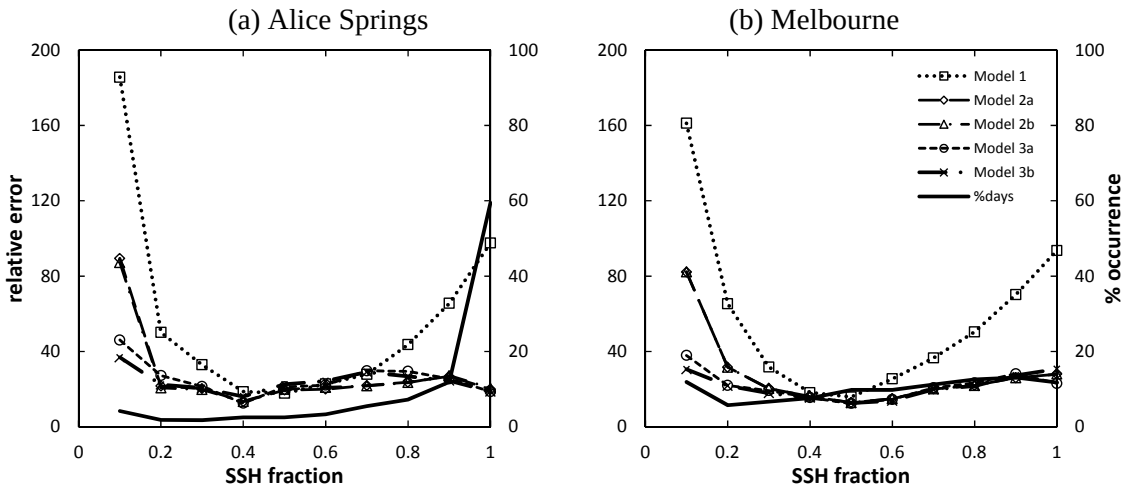

Figure 4.26 Relative error with the change in SSH fraction. All five models are shown with the quadratic *n/N* error structure. The percentage of days with each SSH fraction is shown by the thick solid line.

4.3.4 Predictive reliability of the diffuse models: QQ plots

QQ plots are formed to check the extent to which the probabilistic predictions are compatible with the observed data. These can be seen in Figure 4.27 for Alice Springs and Figure 4.28 for Melbourne. The predictive reliability is consistent for Models 2a, 2b, 3a and 3b. In contrast, Model 1 has a large under-prediction. Similar to the direct radiation, the internal variance shows significant under-estimation of the predictive uncertainty. This indicates that the uncertainty due to the timing of the bright hours does not account for all the variation between the observed and simulated diffuse radiation. For the external variance, the *n/N* (SSH) error models are closest to the 1:1 line.

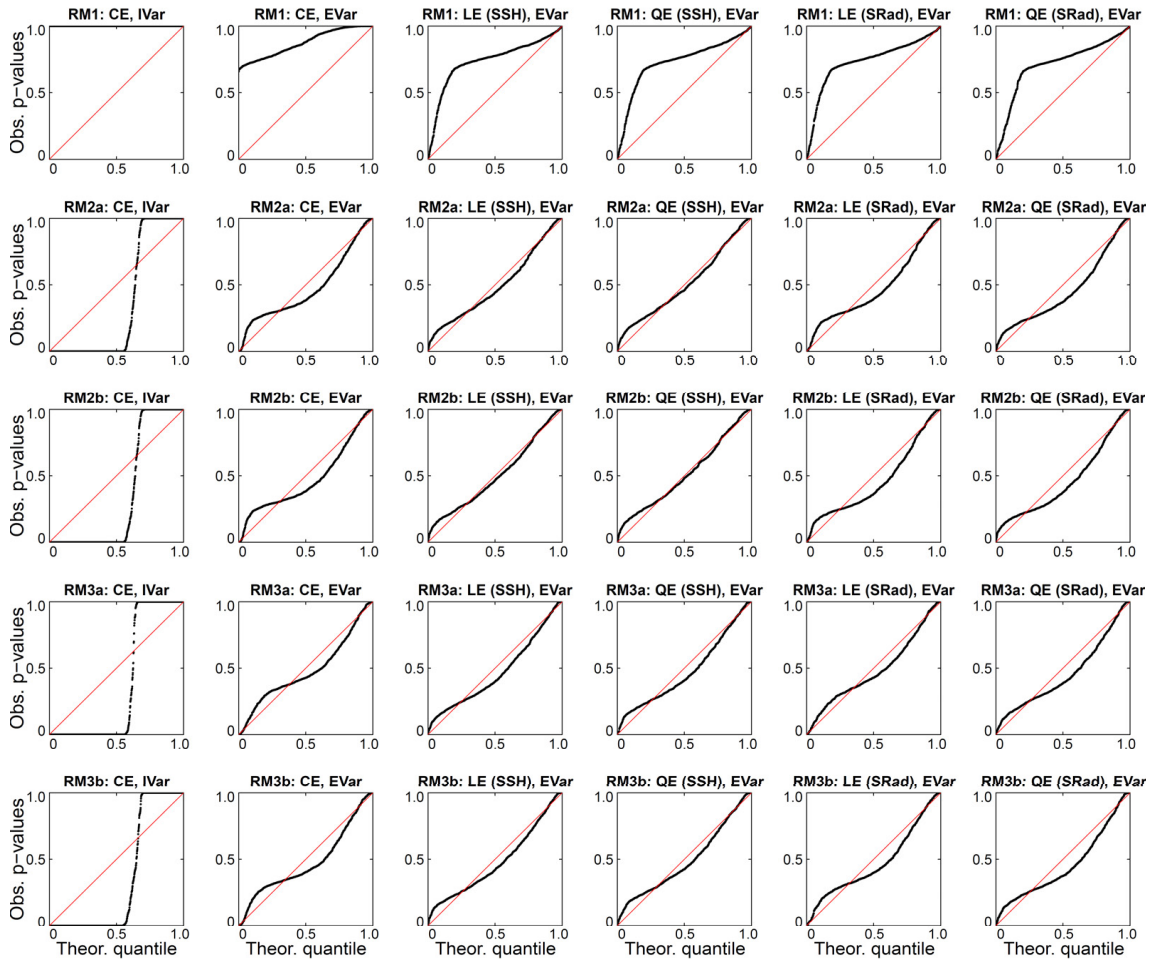

Figure 4.27 QQ plots for Alice Springs for all radiation models and residual error model structures for the calibration period. The left column is the internal variance while the other columns show the external variance for the five error structures. RM stands for radiation model, CE for constant error, LE for linear error, QE for quadratic error, SRad for simulated radiation, EVar for external variance and IVar for internal variance.

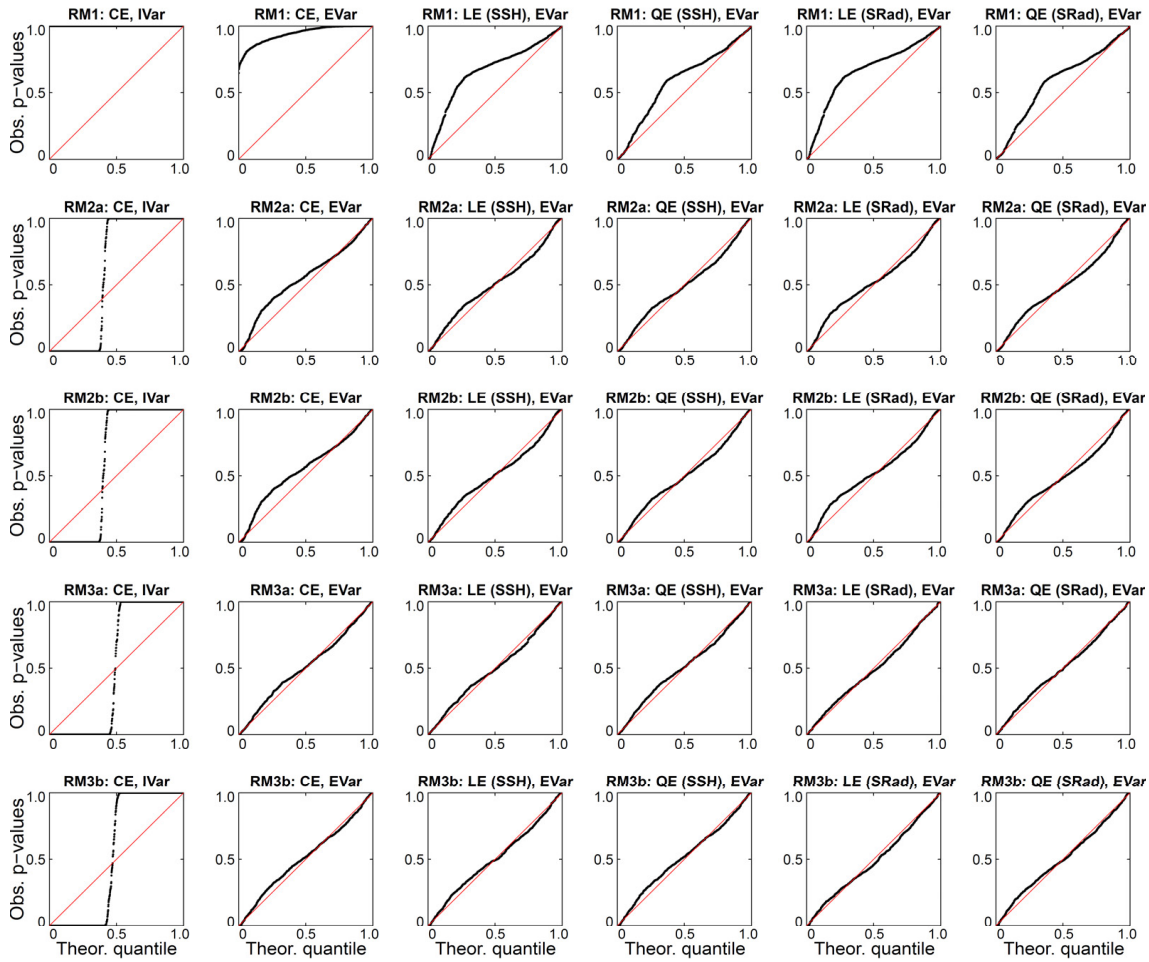

Figure 4.28 QQ plots for Melbourne for all radiation models and residual error model structures for the calibration period. The left column is the internal variance while the other columns show the external variance for the five error structures. RM stands for radiation model, CE for constant error, LE for linear error, QE for quadratic error, SRad for simulated radiation, EVar for external variance and IVar for internal variance.

4.3.5 Setting the threshold at 120 Wm^{-2}

The radiation model and residual error model parameter values are reasonably similar between the forced and variable threshold calibrations for all models and locations. In terms of model performance, the forced threshold results in a small increase in RMSE for all models, with the greatest increase in Model 1. For Model 1, the greatest increase is at Mildura (0.19 MJ m^{-2} d^{-1}) and the smallest increase is at Darwin (<0.01 MJ $m^{-2}d^{-1}$). For Models 2a and 2b, the greatest increase is at Darwin (0.05 MJ m^{-2} d^{-1}) and the smallest increase at Alice Springs (<0.01 MJ m^{-2} d^{-1}). For Models 3a and 3b the greatest increase is at Tennant Creek (0.04 MJ m^{-2} d^{-1}) and the smallest increase at Mt Gambier (<0.01 MJ m^{-2} d^{-1}).

The trend in external variance is similar to that in the RMSE. Model 1 has a greater increase than the other models, ranging from 2.4 (Alice Springs) to 6.6 $MJ^2m^{-4}d^{-2}$ (Mt Gambier). For Model 2a the range is from -0.008 (Mt Gambier) to 0.19 $MJ^2m^{-4}d^{-2}$ (Tennant Creek) while for Model 2b the range is -0.009 (Mt Gambier) to 0.21 $MJ^2m^{-4}d^{-2}$ (Broome). For Model 3a the range is -0.04 (Mt Gambier) to 0.09 $MJ^2m^{-4}d^{-2}$ (Alice Springs) and for Model 3b the range is -0.06 (Mt Gambier) to 0.16 $MJ^2m^{-4}d^{-2}$ (Tennant Creek).

For all locations, except Adelaide, the forced threshold leads to a slight reduction in the internal variance (~0.02 $MJ^2m^{-4}d^{-2}$). The increase at Adelaide is approximately 0.003 $MJ^2\ m^{-4}\ d^{-2}$.

From these results, it is suggested that a set threshold of 120 Wm^{-2} can be used for Models 2a, 2b, 3a and 3b but not Model 1.

4.3.6 Validation

The change in RMSE and variance between the calibration and validation periods can be seen in Table 4.4.

Table 4.4 Change in average diffuse radiation model performance for each location for the validation period compared with the calibration period with a variable threshold.

	RMSE ($MJ\ m^{-2}\ d^{-1}$)			**Internal Variance ($MJ^2\ m^{-4}\ d^{-2}$)**			**External Variance ($MJ^2\ m^{-4}\ d^{-2}$)**		
Location	**M1**	**M2**	**M3**	**M1**	**M2**	**M3**	**M1**	**M2**	**M3**
Adelaide	-0.054	-0.116	-0.147	-0.018	-0.002	-0.002	-0.498	-0.134	-0.107
Alice Springs	0.081	0.093	-0.044	-0.004	-0.001	-0.001	-0.046	0.011	-0.046
Broome	0.175	0.141	0.070	0.013	0.000	0.000	1.268	0.341	0.177
Darwin	-0.178	-0.097	-0.040	0.021	0.001	0.001	-0.085	0.057	0.068
Melbourne	-0.051	-0.052	-0.063	0.006	0.001	0.001	0.183	0.061	-0.016
Mildura	0.425	0.263	0.254	0.025	0.002	0.001	0.630	0.315	0.189
Mt Gambier	-0.141	-0.140	-0.034	-0.004	-0.002	-0.001	0.018	-0.045	-0.038
Tennant Creek	0.080	0.075	-0.009	0.001	0.001	0.000	-0.761	-0.128	-0.084
Wagga Wagga	-0.087	-0.004	-0.023	0.001	0.000	0.000	0.101	-0.023	-0.002

For each location, the models perform similarly well between the calibration and validation period. For the validation period, Models 1, 2a and 2b show a slightly smaller RMSE at five locations while Models 3a and 3b show a slightly smaller RMSE at six locations. For all models, Mildura has the greatest increase in RMSE. Broome has a greater external variance for Models 1 and 2 while Mildura has the greatest external variance for Model 3.

For Model 1, Darwin shows the greatest improvement in RMSE, which is reduced by an average of 0.18 MJ m^{-2} d^{-1}, while Tennant Creek has the greatest reduction in external variance by 0.76 MJ^2 m^{-4} d^{-2}. For Models 2a and 2b, Mt Gambier has the greatest reduction in RMSE by 0.14 MJ m^{-2} d^{-1}, while Adelaide has the greatest reduction in external variance by 0.13 MJ^2 m^{-4} d^{-2}. For Models 3a and 3b, Adelaide has the greatest reduction in RMSE by 0.15 MJ m^{-2} d^{-1} and the greatest reduction in external variance, by 0.11 MJ^2 m^{-4} d^{-2}.

The average change in internal variance is only minor for each location and model.

With the threshold set at 120 Wm^{-2}, the validation results are very similar to the variable threshold results.

The similar performance of the models in the calibration and validation periods suggests that the models are quite robust and that the period used for calibration contains a sufficiently wide range of atmospheric conditions.

4.4 Conclusions

This chapter examines the performance of each of the stochastic global, direct and diffuse radiation models. Each of the five global radiation models performs reasonably well for all locations. The performance of the global radiation models appears to be influenced by the rainfall regime at each of the locations. Mildura is the driest location and has the best performance, with an average RMSE of 1.32 MJ m^{-2} d^{-1}. Darwin has the highest amount of rainfall and the poorest performance, with an average RMSE of 1.99 MJ m^{-2} d^{-1}. The relative error for all data points ranges from 6% at Broome and

Alice Springs, to 11% at Melbourne, with an average relative error of 9% for all locations.

When the residual error models are compared, the constant residual error model over-estimates the predictive uncertainty. The linear and quadratic residual error models perform equally well. Given that the linear error model has one less parameter to be calibrated, it is concluded that the global radiation models are best calibrated with linear error variance based on SSH fraction.

The five global radiation models perform equally well for all individual locations in terms of the RMSE. This could be because the models estimate the direct and diffuse components which are then summed to give the global radiation, which has a linear relationship with SSH. The components may interact and offset each other to give similar global estimates. The magnitude of the error variance is also very similar between the models for each location, although Model 1 has the greatest internal variance. Therefore, in the interest of parsimony, the simplest model (Model 1) is sufficient for giving estimates of global radiation.

In contrast to the global radiation models, the more complex models are better at predicting the individual direct and diffuse radiation components. The linear model (Model 2) is sufficient for modelling the direct radiation. These model parameters are then used to model the diffuse radiation component. The quadratic model (Model 3b) best models the diffuse radiation. The linear model for the direct radiation has RMSE values between 2.1 MJ m^{-2} d^{-1} for Mildura and 2.6 MJ m^{-2} d^{-1} for Darwin with an average relative error of approximately 23% for all locations. The quadratic model for the diffuse radiation has an RMSE between 1.5 MJ m^{-2} d^{-1} at Mildura and 1.8 MJ m^{-2} d^{-1} at Mt Gambier with an average relative error of approximately 22% for all locations. As with the global radiation, the models perform better at locations with smaller annual rainfall totals than those with much higher annual totals. For both the direct and diffuse radiation, the residual errors are best (and most efficiently) described using the quadratic SSH residual error model. This results in a greater error variance for sunny days for the direct radiation, and a greater error variance for cloudy days for the diffuse radiation.

For the global, direct and diffuse radiation, the uncertainty due to the timing of the bright hours during the day, (the average internal error variance), only accounts for a small amount of the average total error variance. On average, the external error variance, due to the external influences not accounted for by the SSH timing, accounts for a larger amount of the total error variance. However, the internal variance is greatest for days which have mid values of the SSH fraction. On these days, the internal error variance accounts for a large portion of the total error variance.

Knowledge of the amounts of global radiation, and the direct and diffuse radiation components, are important for a variety of applications including ecosystem modelling and the solar energy industry. The results of this study indicate that reasonable estimates of global, direct and diffuse radiation can be determined from SSH data. The accuracy can be determined with an error of approximately 9% for the global radiation, 23% for the direct component, and 22% for the diffuse component.

Chapter 5 - Development of Regional Radiation Models

Overview

Models for estimating global, direct and diffuse radiation are developed and assessed in Chapters 3 and 4. These models are calibrated to observed data from individual locations, and each location has a separate parameter set. In this chapter, two different types of regional model are developed and assessed; a bulk-regional and a latitude-dependant model. These regional models allow the global, direct and diffuse radiation to be determined at any location in Australia that has SSH data.

The development of the regional models is first outlined. The performance of the global, direct and diffuse regional models is then compared with the performance of the locally calibrated models. For the global radiation, the radiation estimated using the regional and local models are also compared to the BoM satellite-derived estimates of global radiation.

5.1 Motivation

Chapter 4 shows that global, direct and diffuse radiation can be well modelled using SSH data. However, to calibrate the developed stochastic models, observed local radiation data is required. This data is relatively scarce. Only 21 locations in Australia have both SSH data and global radiation data. In contrast, there are over 200 locations that have measured SSH data (BoM, 2013). To enable estimation of the global, direct and diffuse radiation at these sites, an Australian-wide or regional model is required.

Previous authors have developed global radiation models with regional parameter sets (e.g., Black et al., 1954; Penman, 1956). These models have one parameter set that can be used for a wide range of locations. Other authors have derived relationships between the parameters of the global radiation models and latitude (e.g., Glover and McCulloch, 1958; Gopinathan, 1988c).

The Bureau of Meteorology has also derived estimates of global radiation from satellite data. These radiation estimates are calculated using computer models which estimate the radiation at ground level from the reflectance from cloud tops. These estimates are recognised to have an error of 7% or better in clear sky conditions, and up to 20% in cloudy conditions. However, this data is generally only available from 1990 onwards.

5.2 Data and Methodology

5.2.1 Bulk-regional model

The bulk-regional models are developed by calibrating each of the radiation models, outlined in Chapter 3, to a lumped data set. This data set contains observed data from nine locations across Australia. The locations chosen cover a range of latitudes and climate regimes, and have measured data for the global, direct and diffuse radiation. For each location, three years of calibration data are chosen that include both relatively cloudy and sunny years, based on the annual total of sunshine hours. The bulk-regional models are validated using data from eleven other locations. The locations used and the years of available data are presented in Table 5.1 and Figure 5.1. Note that of all the available locations, four locations only have measurements of global radiation. A further six locations only have measurements of diffuse radiation. For these six locations, the direct radiation is calculated as the difference between the global and diffuse radiation.

As the locations in the north of Australia generally have a different climate to those in the south, the bulk-regional models are also formed separately using the northern and southern locations. The northern locations tend to have a marked wet and dry season while the southern locations tend to have more uniform rainfall throughout the year.

In Chapter 4, it was shown that the global radiation models are best calibrated for all locations using a linear SSH error structure. It was also shown that using a fixed threshold of 120 Wm^{-2} does not diminish the performance of the models. Therefore, the

five global radiation bulk-regional models are developed using the linear SSH error structure with a fixed threshold of 120 Wm^{-2}.

For the direct and diffuse radiation, the local models are best calibrated with a quadratic SSH error structure. As with the global radiation, a fixed threshold of 120Wm^{-2} does not diminish the performance of the direct and diffuse radiation models (except Model 1, which has a poor performance anyway). Therefore, bulk-regional models for the direct and diffuse radiation are developed using the same approach as the global radiation, using the quadratic SSH error model.

Table 5.1 Locations used in the regional model development. The locations used for the bulk-regional model calibration are in bold. The * indicates locations which only have measurements of global radiation. The ^ indicates locations which only have measurements of global and diffuse radiation.

ID	Location	Latitude	Years of data	North/ South
1	**Adelaide**	-34.9524	2003-2010	S
2	**Alice Springs**	-23.7951	1999-2010	N
3	**Brisbane^**	-27.4178	1983-1995	M
4	**Broome**	-17.9475	1999-2010	N
5	**Cairns**	-16.8736	1999-2003	N
6	**Canberra^**	-35.3049	1983-1994	S
7	**Darwin**	-12.4239	1999-2010	N
8	Halls Creek*	-18.2292	1970-1980	N
9	**Hobart^**	-42.8339	1968-1980	S
10	Laverton^	-37.8565	1968-1980	S
11	Melbourne	-37.6655	1999-2010	S
12	Mildura	-34.2358	1999-2005	S
13	Mt Gambier	-37.7473	1999-2006	S
14	Ooodnadatta*	-27.5553	1969-1980	M
15	**Perth^**	-31.9275	1975-1980	S
16	Sydney^	-33.9465	1983-1994	S
17	Tennant Creek	-19.6423	1999-2006	N
18	Wagga Wagga	-35.1583	1999-2010	S
19	Williamtown*	-32.7932	1969-1979	S
20	Woomera*	-31.1558	1968-1979	S

M = Middle, N = North, S = South

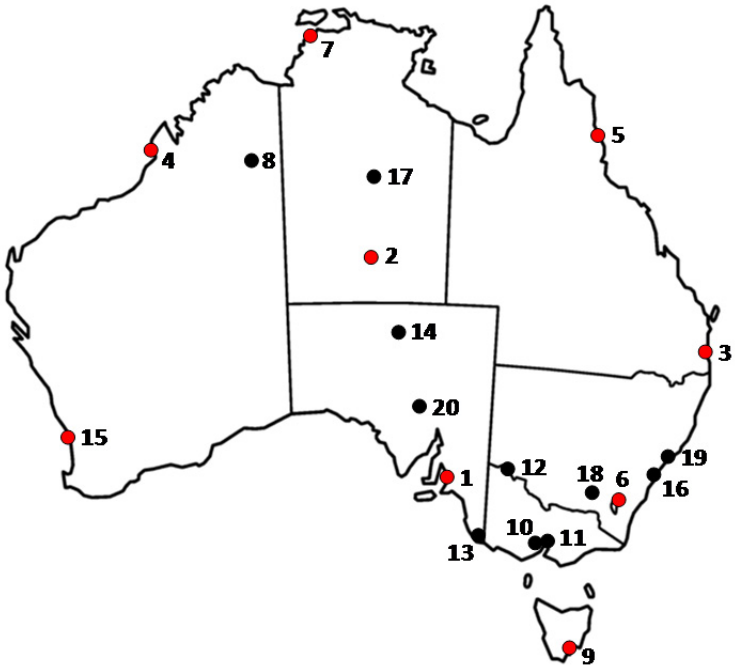

Figure 5.1 Location of stations. Stations in red are used for the bulk-regional calibration.

5.2.2 Latitude-dependant model

The latitude-dependent regional models are developed using the relationship between latitude and the locally calibrated global, direct and diffuse radiation model parameter values. For each radiation type, the locally calibrated parameter values for all individual locations are aggregated. For the global radiation, the linear SSH residual error model is used, while for the direct and diffuse radiation, the quadratic SSH residual error model is used. The parameter sets from the nine main locations as well as the additional eleven locations are used. For each model, and for each individual parameter, the values from the different locations are linearly regressed against the latitude of the locations, with latitude as the independent variable. The resulting linear regression equations are then used to calculate a new parameter set at each location.

5.2.3 Model assessment

The bulk-regional and latitude-dependent models are used to calculate the global, direct and diffuse radiation at all locations. The performance of the regional models at each location is determined by calculating the RMSE and relative error. QQ plots are also formed to check the extent to which the probabilistic predictions from the regional

models are compatible with the observed data. At each location, the performance of the regional models is compared with the performance of the locally calibrated models.

For the global radiation, the radiation estimates using the local and regional models are also compared with the global radiation derived from satellite data. The satellite radiation estimates are obtained from the Bureau of Meteorology (BoM, 2013).

5.3 Performance of the Global Radiation Regional Models

5.3.1 Bulk-regional model

All five bulk-regional global radiation models only have a slightly reduced performance compared to the locally calibrated models at all locations. In general, bulk-regional radiation Model 3b tends to perform slightly better than the other bulk-regional models. The RMSE for the bulk-regional and local Model 3b is shown in Figure 5.2 for all locations.

The greatest increase in RMSE for the bulk-regional Model 3b, compared with the local Model 3b, is at Williamtown. The RMSE is increased by 0.38 MJ m^{-2} d^{-1} (22%). This poor performance may be because the data for Williamtown is not used in the calibration of the bulk-regional model. If the data were incorporated, the performance may be improved at Williamtown. However, the data for Adelaide is used in the calibration, yet Adelaide has the second highest increase in RMSE by 19%.

The average difference in RMSE for all locations is an increase of 0.08 MJ m^{-2} d^{-1} (5%). The average relative error of local Model 3b for the nine main locations is 8.7%. For the bulk-regional Model 3b, the average relative error is 9.3%. Therefore, the bulk-regional model only results in a minor loss of performance.

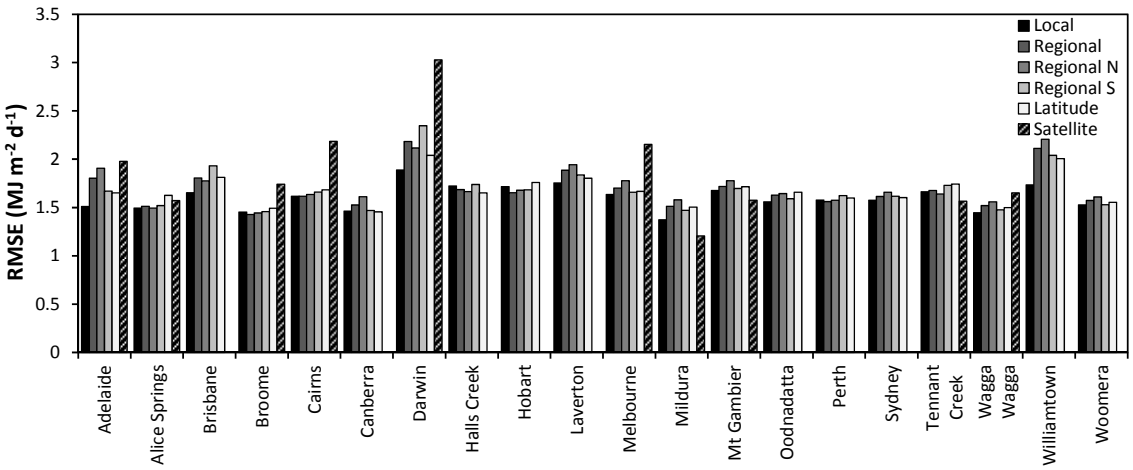

Figure 5.2 Comparison of the RMSE for the local, bulk-regional and latitude-dependent regional models at all locations using Model 3b. The satellite-derived global radiation is also shown.

For the separate southern bulk-regional calibration, in general, the RMSE is slightly improved for the southern locations when using the southern bulk-regional Model 3b. For Williamtown, the increase in RMSE is reduced to 17%. A similar result is seen for the northern locations using the northern models. However, the increase in performance compared with the Australia-wide bulk-regional Model 3b is only minor.

QQ plots for the Australia wide bulk-regional Model 3b can be seen in Figure 5.3 for each location. These plots show the extent to which the probabilistic predictions from the bulk-regional model are compatible with the observed data. The agreement between the predictions and observed data is very close at Brisbane, Broome, Cairns, Halls Creek, Hobart, Melbourne, Mt Gambier, Perth and Sydney. It can be observed that the bulk-regional Model 3b tends to slightly under-predict the radiation at half of the locations, with Adelaide displaying the greatest levels of under-prediction. At Brisbane and Darwin, the bulk-regional model slightly over-predicts the radiation.

These results suggest that despite that range of climates seen in Australia, a regionally calibrated single parameter set can be applied across Australia, with minimal loss of accuracy compared with the local calibration of the radiation models.

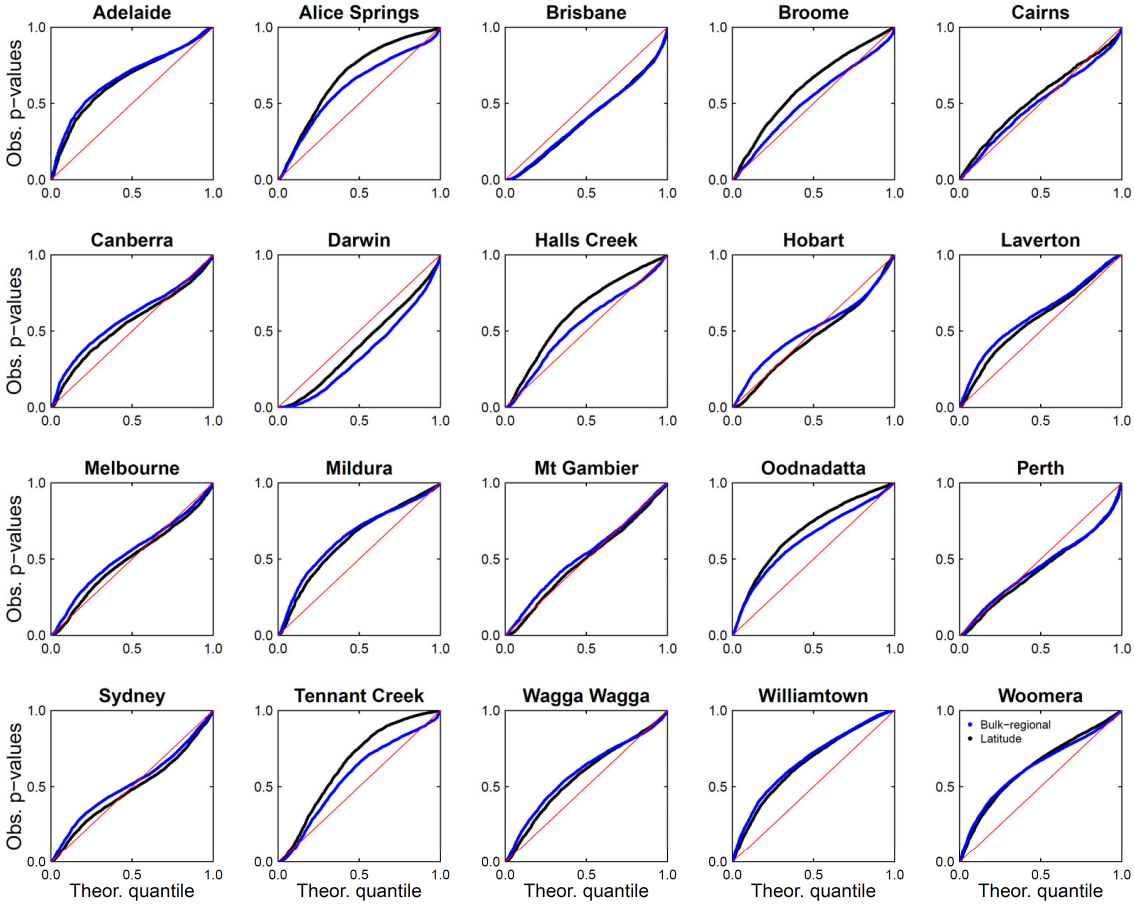

Figure 5.3 Global radiation regional QQ plots using Model 3b. The black line is the latitude-dependant model and the blue line is the bulk-regional model. The red line is the 1:1 line.

5.3.2 Latitude-dependent regional model

The relationship between latitude and each of the locally calibrated model parameters can be seen in Figure 5.4. The R^2 and p-value of the regressions can be seen in Table 5.2. As shown, a significant relationship with latitude occurs for most parameters, particularly for Models 2a, 2b and 3a.

Also of interest, for all models, except Model 1, the error parameters show a significant trend with a higher error at the higher latitudes (northern Australia), as shown in Figure 5.5. The locations in the north of Australia tend to have a greater variability in the SSH fractions, with distinct wet and dry seasons. This may cause the greater error variance at these latitudes.

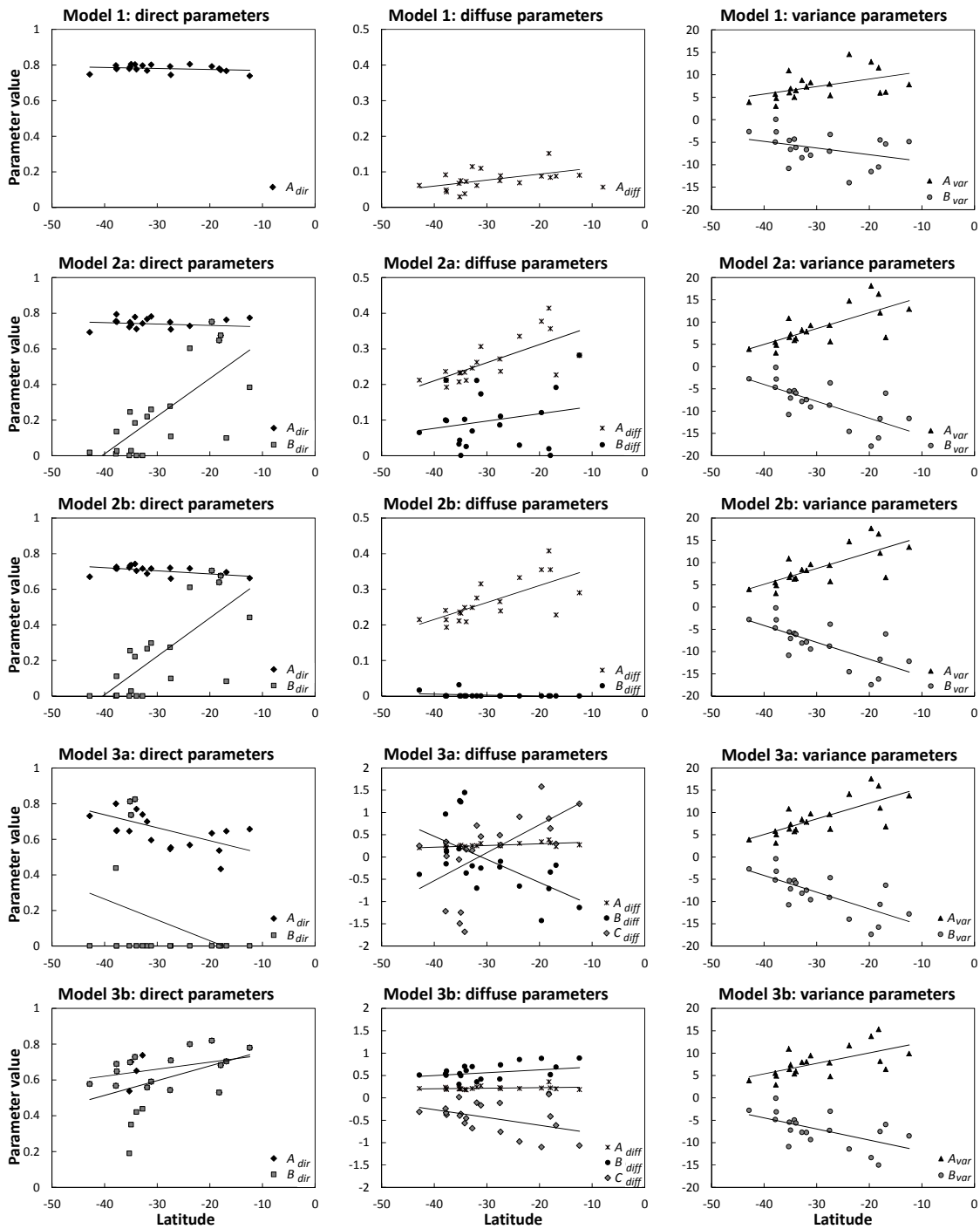

Figure 5.4 Linear regression of the locally calibrated global parameters against latitude using the linear *n/N* residual error model.

Table 5.2 Results of the regression between the local parameter values and latitude for the global radiation models.

parameter	model	gradient	intercept	R^2	*p*-value
A_{dir}		-0.001	0.764	0.060	0.297
B_{dir}		-	-	-	-
A_{diff}	1	0.002	0.127	0.262	0.021**
B_{diff}		-	-	-	-
C_{diff}		-	-	-	-
A_{var}		0.166	12.371	0.224	0.035**
B_{var}		-0.147	-10.704	0.135	0.112
A_{dir}		-0.001	0.716	0.031	0.456
B_{dir}		0.021	0.856	0.523	0.001***
A_{diff}	2a	0.005	0.414	0.486	0.001***
B_{diff}		0.002	0.159	0.049	0.349
C_{diff}		-	-	-	-
A_{var}		0.356	19.249	0.529	0.001***
B_{var}		-0.379	-19.182	0.489	0.001***
A_{dir}		-0.002	0.652	0.277	0.017
B_{dir}		0.022	0.870	0.538	0.001***
A_{diff}	2b	0.005	0.406	0.481	0.001***
B_{diff}		0.000	-0.006	0.101	0.171
C_{diff}		-	-	-	-
A_{var}		0.357	19.400	0.543	0.001***
B_{var}		-0.379	-19.310	0.498	0.001***
A_{dir}		-0.007	0.446	0.358	0.005***
B_{dir}		-0.012	-0.204	0.113	0.147
A_{diff}	3a	0.004	0.373	0.453	0.001***
B_{diff}		-0.052	-1.610	0.326	0.009***
C_{diff}		0.063	1.982	0.365	0.005***
A_{var}		0.350	19.085	0.554	0.001***
B_{var}		-0.376	-19.179	0.521	0.001***
A_{dir}		0.004	0.778	0.138	0.107
B_{dir}		0.008	0.844	0.193	0.053*
A_{diff}	3b	0.001	0.253	0.067	0.272
B_{diff}		0.006	0.754	0.073	0.249
C_{diff}		-0.017	-0.963	0.195	0.051*
A_{var}		0.235	14.740	0.382	0.004***
B_{var}		-0.248	-14.430	0.331	0.008***

*result significant at <10%
**result significant at <5%
***result significant at <1%

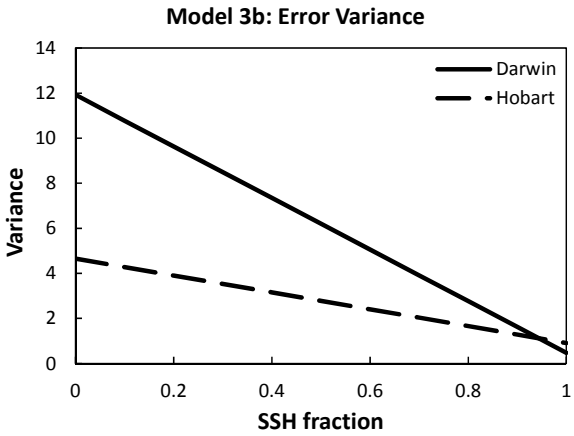

Figure 5.5 Global radiation error variance ($MJ^2\ m^{-4}\ d^{-1}$) for radiation Model 3b with the linear *n/N* error model. Darwin is the most northern location while Hobart is the most southern.

The new latitude-dependent models, derived from the linear regression equations, perform quite well for all of the radiation models. In particular, latitude-dependent Model 3b has the lowest RMSE and highest R^2 value at 17 of the 20 locations. The remaining latitude-dependent models do not show any consistency as to which has the best performance. For latitude-dependent Model 3b, the greatest increase in RMSE compared with the local model, is again at Williamtown. The RMSE is increased by 0.27 MJ $m^{-2}\ d^{-1}$ (16%).

For all locations, the average increase in RMSE is 0.07 MJ $m^{-2}\ d^{-1}$ (4.5%) for latitude-dependent Model 3b. The average relative error for the nine main locations is 8.94%. The latitude-dependent Model 3b performs better than the bulk-regional Model 3b at 11 of the 20 locations. The average relative error is also slightly smaller for the latitude-dependent Model 3b. However, for the bulk-regional Model 3b, only nine locations were used to calculate the parameter values. If different locations were used, the new parameters may result in an improved performance.

QQ plots for latitude-dependent Model 3b can also be seen in Figure 5.3. The reliability of the latitude-dependent model predictions is very similar to those of the bulk-regional model. Neither regional model performs better than the other at all locations.

5.3.3 Comparison with satellite data

Figure 5.2 also compares the performance of satellite-derived global radiation with the performance of the local and regional Model 3b. Note that only ten locations have concurrent measured and satellite-derived global radiation data. As shown in Figure 5.2, the satellite-derived global radiation has a lower RMSE than the simulated locally calibrated global radiation at three of the ten locations (Mildura, Mt Gambier and Tennant Creek). The RMSE is reduced by approximately 8% at these locations. At these three locations, the satellite-derived global radiation also performs better than the bulk-regional and latitude-dependent models. However, at the seven other locations, the satellite data performs significantly worse than the local and regional models, particularly at Cairns, Darwin and Melbourne, which have a large amount of rainy days. This is consistent with the results of Weymouth and Le Marshall (2001) who, in their comparison of the satellite estimates and ground-based observations, found that the largest error occurred at Cairns. This was attributed to the fact that Cairns experiences large cloud variations throughout the year.

5.4 Performance of the Direct Radiation Regional Models

5.4.1 Bulk-regional model

The direct radiation bulk-regional Models 2 and 3 only have a slightly reduced performance compared to the local Models 2 and 3. The performance for bulk-regional Model 1 is comparatively poor. Bulk-regional Models 2 and 3 perform similarly well, although bulk-regional Model 3 tends to perform marginally better. However, bulk-regional Model 3 has an extra parameter. The RMSE for the local and regional Model 2 is shown in Figure 5.6.

For bulk-regional Model 2, the greatest increase in RMSE, compared with the local Model 2, is at Adelaide. The RMSE is increased by 0.20 MJ m^{-2} d^{-1} (9%). The average increase in the RMSE for all locations is 0.11 MJ m^{-2} d^{-1} (5%).

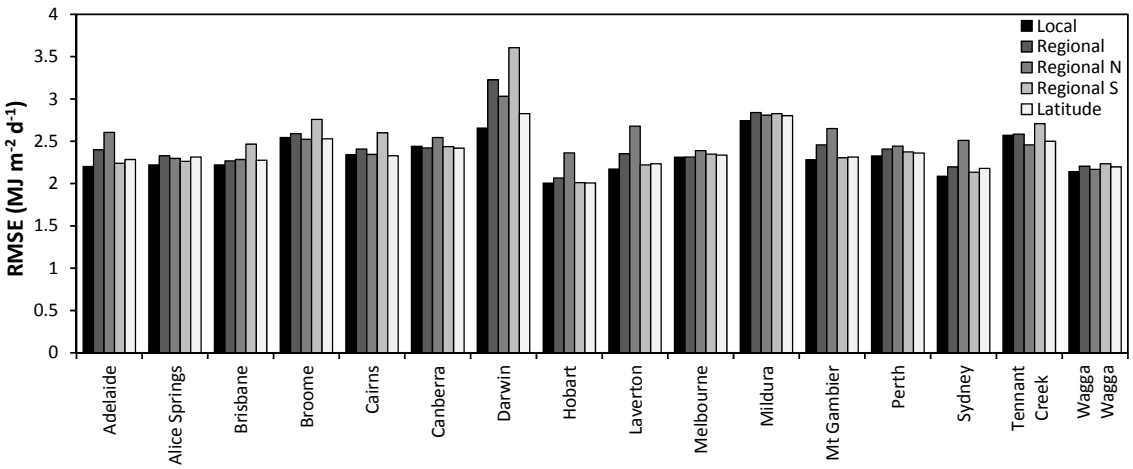

Figure 5.6 Comparison of the RMSE for the local, bulk-regional and latitude-dependent regional models at all locations using Model 2.

The average relative error of local Model 2 for the nine main locations is 22.4%. For bulk-regional Model 2, the average relative error is 30.2%. Therefore, the bulk-regional calibration leads to a noticeable increase in the relative error.

For the separate southern bulk-regional calibration, similar to the global radiation, in general the RMSE is slightly reduced for the southern locations when using the southern bulk-regional Model 2. For Adelaide, the increase in RMSE is reduced to 2%. The average increase in RMSE for the southern locations compared with the local Model 2 is 0.04 MJ m^{-2} d^{-1} (2%). A similar result is seen for the northern locations using the northern Model 2. The average increase in RMSE for the northern locations is 0.10 MJ m^{-2} d^{-1} (4%). However, this is only a minor increase in performance compared with the Australia-wide bulk-regional Model 2.

QQ plots for the Australia wide bulk-regional Model 2 can be seen in Figure 5.7. The agreement between the predictions and observed data is very close at Brisbane, Broome, Cairns, Canberra, Melbourne, Perth, Tennant Creek and Wagga Wagga. It can be observed that the bulk-regional Model 2 tends to slightly under-predict the radiation at about half of the locations, particularly at Adelaide, Laverton and Sydney. At Darwin the model slightly over-predicts the radiation.

These results suggest that a regionally calibrated model, using only one parameter set, can be applicable for calculating direct radiation across Australia.

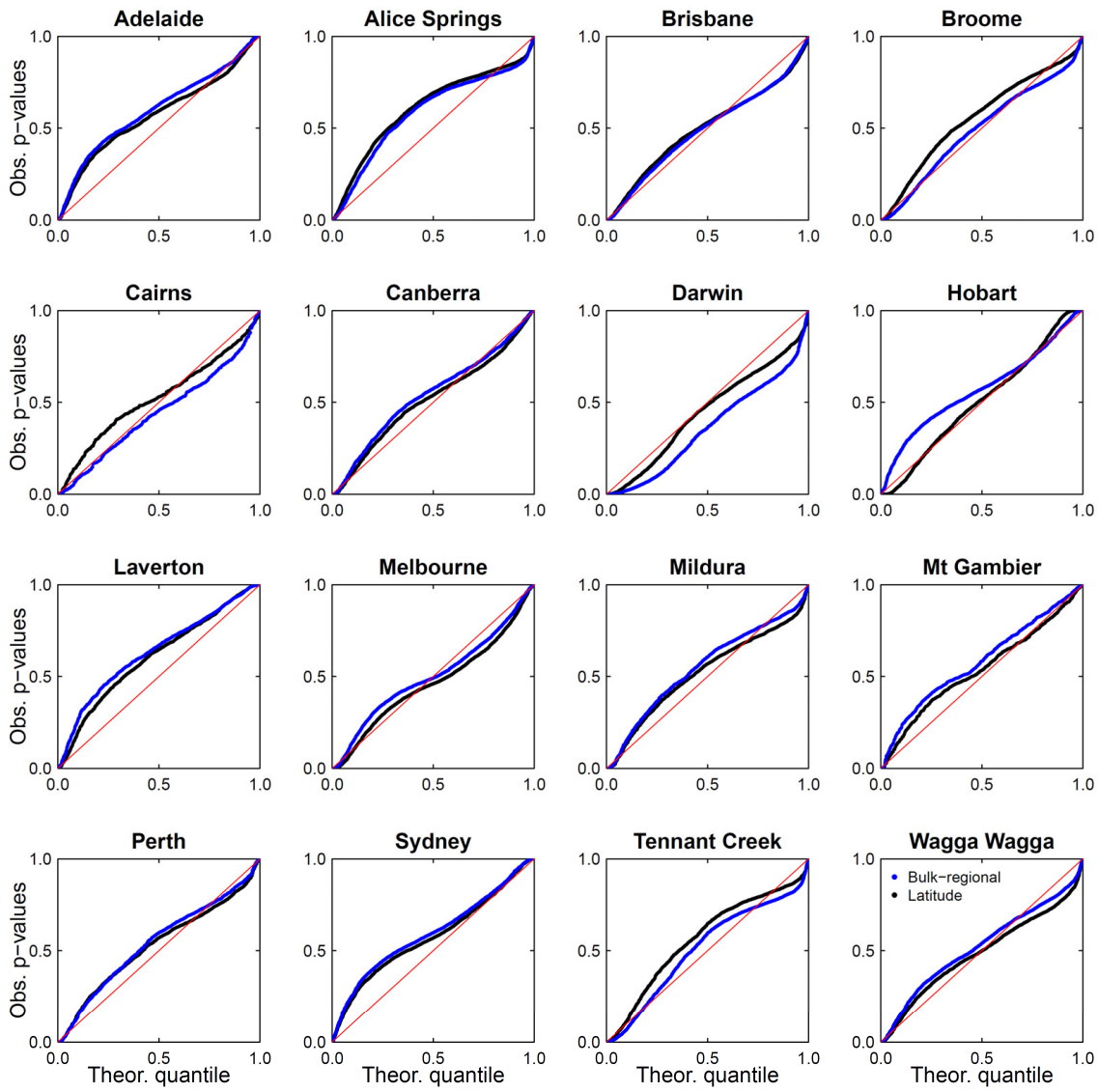

Figure 5.7 Direct radiation regional QQ plots using Model 2. The black line is the latitude-dependant model and the blue line is the bulk-regional model. The red line is the 1:1 line.

5.4.2 Latitude-dependent regional model

The relationship between latitude and each of the locally calibrated model parameters can be seen in Figure 5.8. The R^2 and p-value of the regressions can be seen in Table 5.3. As shown, a statistically significant relationship between the parameters and latitude occurs for most parameters in Model 3.

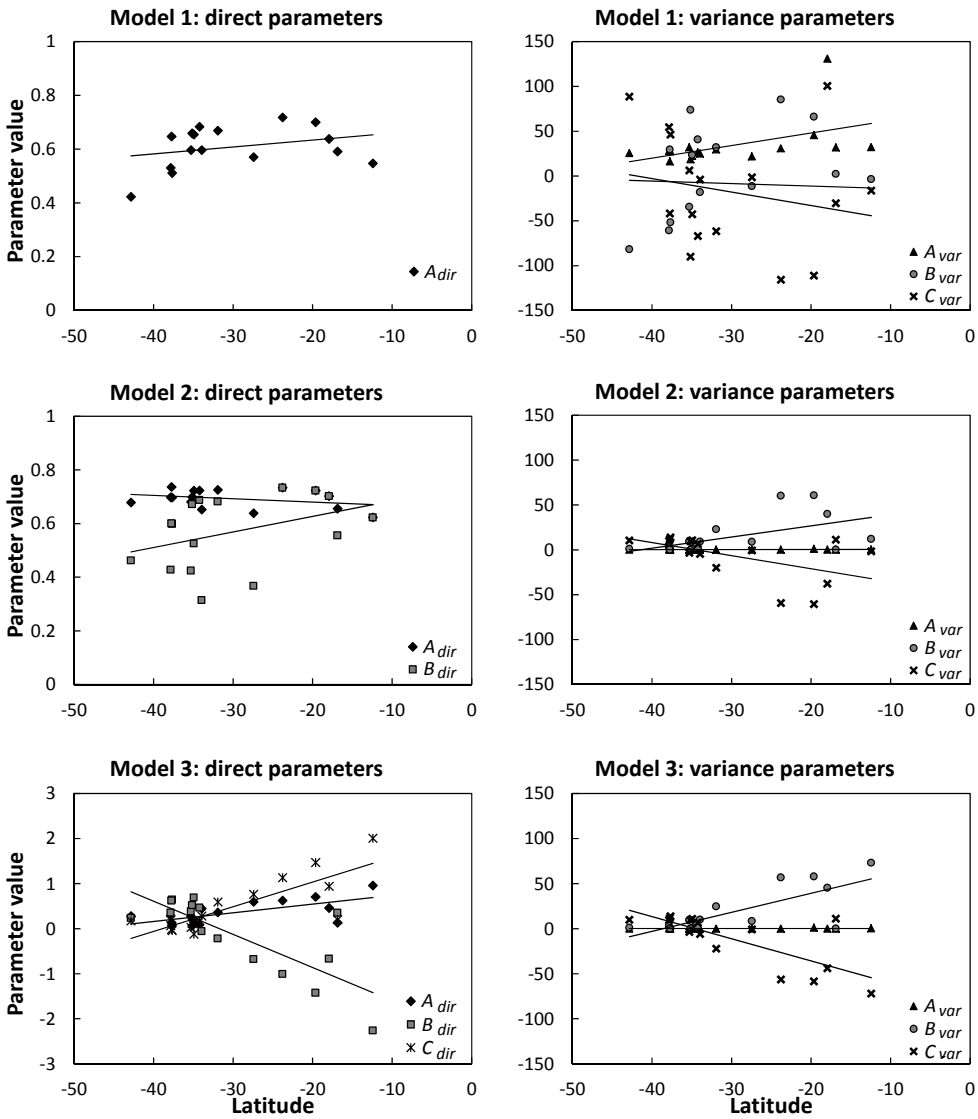

Figure 5.8 Linear regression of the locally calibrated direct parameters against latitude using the quadratic *n/N* residual error model.

The latitude-dependent Models 2 and 3, derived from the linear regression equations, perform well, while Model 1 does not. For latitude-dependent Model 2, the greatest increase in RMSE compared with local Model 2, is at Darwin. The RMSE is increased by 0.17 MJ m^{-2} d^{-1} (6%). The average increase in RMSE for all the locations is 0.04 MJ m^{-2} d^{-1} (2%). The average relative error for the nine main locations is 28.9%.

The latitude-dependent models perform better than the bulk-regional models at all locations except Melbourne. The relative error is also smaller for the latitude-dependent models than the bulk-regional models.

Table 5.3 Results of the regression between the local parameter values and latitude for the direct radiation models.

parameter	model	gradient	intercept	R^2	*p*-value
A_{dir}		0.003	0.686	0.090	0.258
B_{dir}		-	-	-	-
C_{dir}	1	-	-	-	-
A_{var}		1.404	76.190	0.228	0.061*
B_{var}		-0.286	-16.961	0.001	0.900
C_{var}		-1.506	-63.015	0.043	0.439
A_{dir}		-0.001	0.655	0.103	0.225
B_{dir}		0.006	0.743	0.155	0.132
C_{dir}	2	-	-	-	-
A_{var}		0.007	0.361	0.066	0.335
B_{var}		1.241	51.489	0.292	0.031**
C_{var}		-1.451	-50.070	0.280	0.035**
A_{dir}		0.019	0.930	0.449	0.005***
B_{dir}		-0.073	-2.330	0.602	0.001***
C_{dir}	3	0.055	2.128	0.648	0.001***
A_{var}		0.007	0.345	0.060	0.359
B_{var}		2.110	81.470	0.580	0.001***
C_{var}		-2.463	-85.140	0.572	0.001***

*result significant at <10%
**result significant at <5%
***result significant at <1%

QQ plots for latitude-dependent Model 2 can be seen in Figure 5.7. The latitude-dependent Model 2 performs similarly to the bulk-regional Model 2. At Broome, Tennant Creek and Wagga Wagga, the bulk-regional Model 2 is closer to the 1:1 line than the latitude-dependent Model 2; however, at the remaining thirteen locations, the latitude-dependent Model 2 is closer to the 1:1 line.

5.5 Performance of the Diffuse Radiation Regional Models

5.5.1 Bulk-regional model

The bulk-regional Models 2a, 2b, 3a and 3b for the diffuse radiation only have a slightly reduced performance compared to the local Models 2a, 2b, 3a and 3b, particularly bulk-regional Model 3b. The performance for bulk-regional Model 1 is comparatively very poor. The RMSE for the local and bulk-regional Model 3b are shown in Figure 5.9.

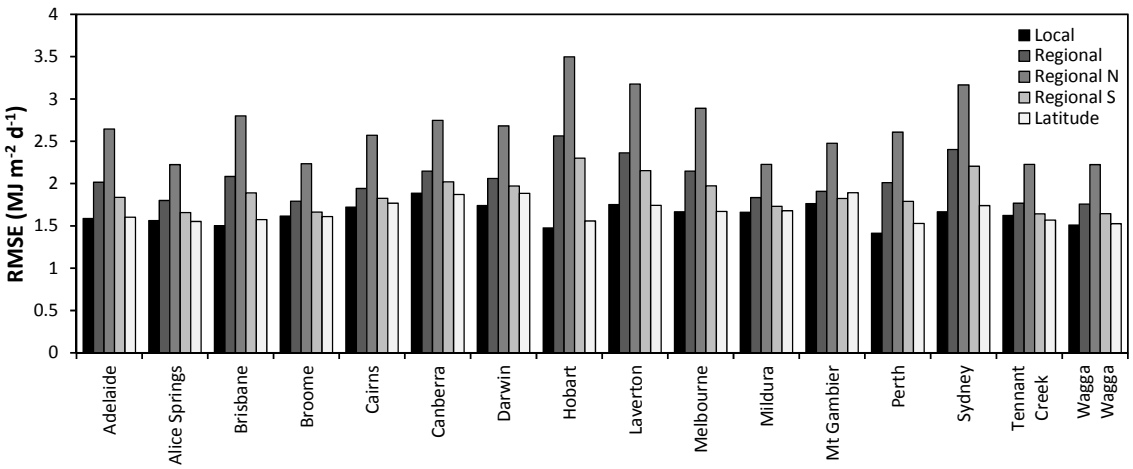

Figure 5.9 Comparison of the RMSE for the local, bulk-regional and latitude-dependent regional models at all locations using Model 3b.

For bulk-regional Model 3b, the greatest increase in RMSE compared with the local Model 3b, is at Hobart. The RMSE is increased by 1.1 MJ m^{-2} d^{-1} (76%). The average increase in RMSE for all locations is 0.42 MJ m^{-2} d^{-1} (26%).

The average relative error of local Model 3b for the nine main locations is 21.9%. For the bulk-regional Model 3b, the average relative error is 29.7% for the nine main locations. Therefore, the bulk-regional model results in a noticeable increase in the relative error.

For the separate southern bulk-regional calibration, for all locations the southern bulk-regional Model 3b performs better than both the Australia-wide bulk-regional Model 3b and the northern bulk-regional Model 3b. Using the southern Model 3b, the average increase in RMSE, compared with the local Model 3b, is 0.25 MJ m^{-2} d^{-1} (16%). For Hobart, the increase in RMSE is reduced to 0.83 MJ m^{-2} d^{-1} (56%). It is clear that the southern Model 3b is preferable for all locations across Australia. For the global radiation, the northern locations have a greater amount of uncertainty in the estimates. Therefore, it is expected that northern Model 3b would not perform as well as the southern Model 3b. However, it is unexpected that the northern Model 3b performs so poorly for the northern locations. The use of the direct radiation parameters in the development of the diffuse radiation parameters may have contributed to this poor performance.

QQ plots for the Australia wide bulk-regional Model 3b can be seen in Figure 5.10. The agreement between the predictions and observed data is very close at Cairns, Darwin and Mt Gambier. However, it can be observed that the bulk-regional Model 3b tends to over-predict the diffuse radiation at all locations, particularly Perth and Hobart.

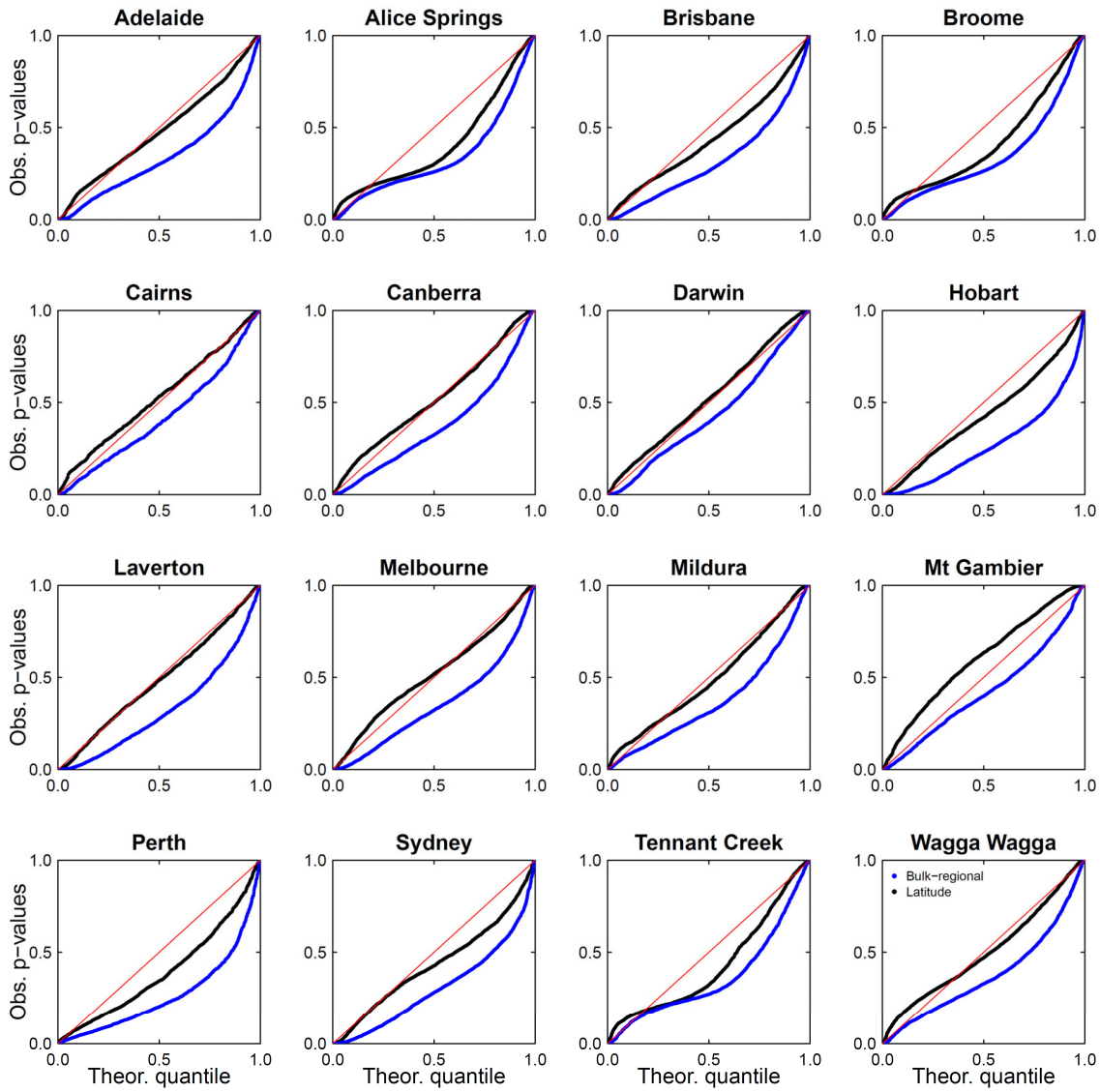

Figure 5.10 Diffuse radiation regional QQ plots using Model 3b. The black line is the latitude-dependant model and the blue line is the bulk-regional model. The red line is the 1:1 line.

5.5.2 Latitude-dependent regional model

The relationship between latitude and each of the locally calibrated diffuse model parameters can be seen in Figure 5.11. The R^2 and p-value of the regressions can be seen in Table 5.4. As shown, a significant relationship between the parameters and latitude occurs for most parameters in Model 3b as well as Model 2b.

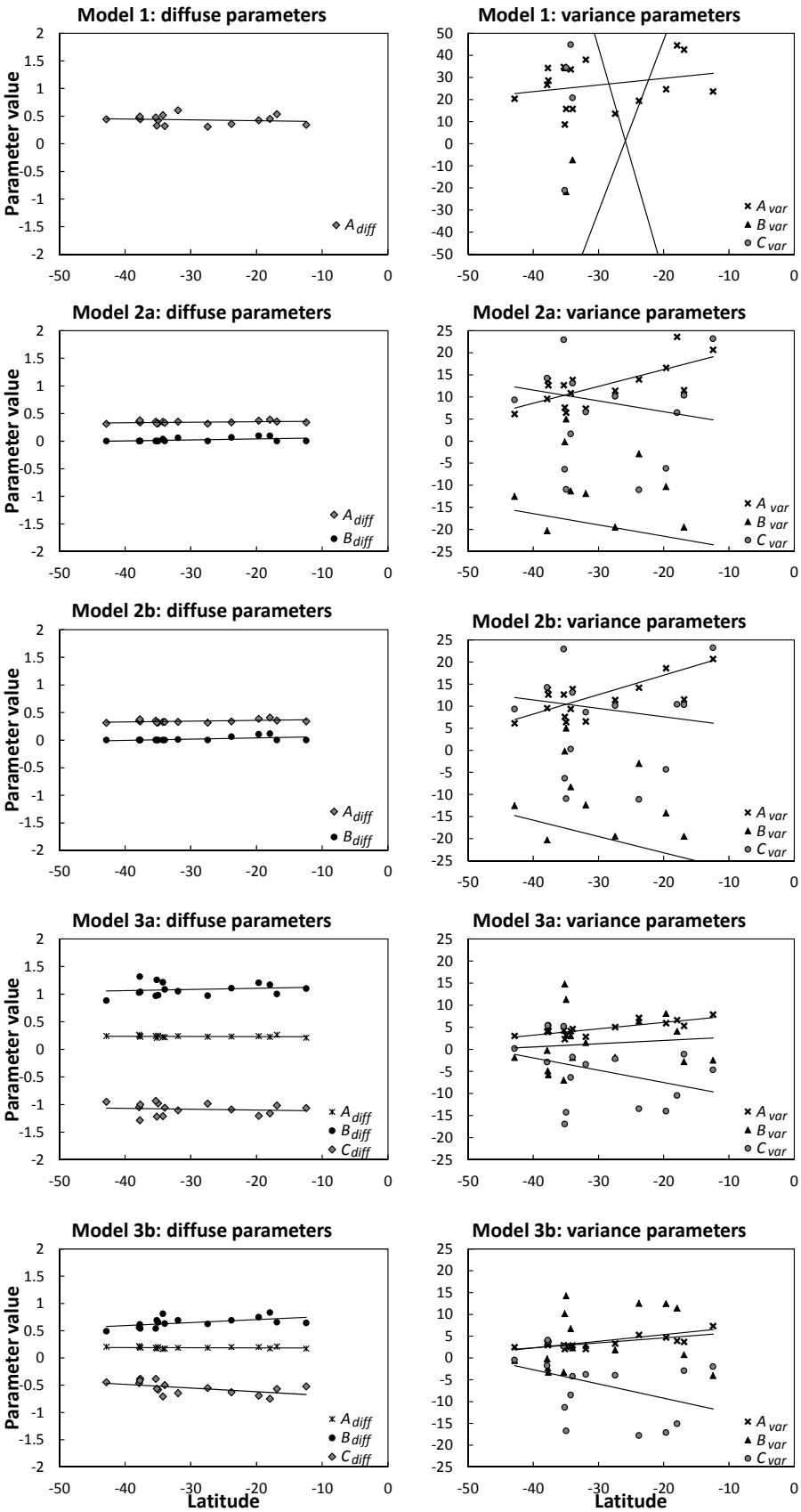

Figure 5.11 Linear regression of the locally calibrated diffuse parameters against latitude using the quadratic *n/N* residual error model.

Table 5.4 Results of the regression between the local parameter values and latitude for the diffuse radiation models.

parameter	model	gradient	intercept	R^2	*p*-value
A_{diff}	1	-0.001	0.389	0.025	0.562
B_{diff}		-	-	-	-
C_{diff}		-	-	-	-
A_{var}		0.301	35.600	0.066	0.338
B_{var}		7.769	202.473	0.413	0.007**
C_{var}		-10.269	-264.505	0.482	0.003**
A_{diff}	2a	0.001	0.372	0.147	0.143
B_{diff}		0.002	0.077	0.215	0.071*
C_{diff}		-	-	-	-
A_{var}		0.382	23.868	0.511	0.002***
B_{var}		-0.256	-26.659	0.029	0.530
C_{var}		-0.246	1.717	0.027	0.543
A_{diff}	2b	0.001	0.383	0.205	0.078*
B_{diff}		0.002	0.086	0.283	0.034**
C_{diff}		-	-	-	-
A_{var}		0.440	25.796	0.499	0.002***
B_{var}		-0.370	-30.617	0.056	0.378
C_{var}		-0.191	3.763	0.017	0.635
A_{diff}	3a	0.000	0.226	0.022	0.580
B_{diff}		0.002	1.151	0.028	0.539
C_{diff}		-0.002	-1.129	0.017	0.630
A_{var}		0.144	8.980	0.694	0.001***
B_{var}		0.073	3.468	0.011	0.693
C_{var}		-0.280	-13.106	0.121	0.186
A_{diff}	3b	0.000	0.181	0.021	0.590
B_{diff}		0.006	0.817	0.289	0.032**
C_{diff}		-0.007	-0.754	0.286	0.033**
A_{var}		0.114	6.888	0.585	0.001***
B_{var}		0.154	8.438	0.047	0.418
C_{var}		-0.326	-15.748	0.155	0.132

*result significant at <10%
**result significant at <5%
***result significant at <1%

The new latitude-dependent Models 2 and 3, derived from the linear regression equations, perform quite well, but latitude-dependent Model 1 does not. Latitude-dependent Model 3b has the best performance at all locations. For latitude-dependent Model 3b, the greatest increase in RMSE, compared with local Model 3b, is at Darwin. The RMSE is increased by 0.15 MJ m^{-2} d^{-1} (8%). The average increase in RMSE for all locations is 0.04 MJ m^{-2} d^{-1} (2%). The average relative error of the nine main locations is 22.9%, which is only slightly larger than that for the local Model 3b.

The latitude-dependent Model 3b performs better than the bulk-regional Model 3b at all locations. The latitude-dependent Model 3b also performs better than the southern bulk-regional Model 3b at all locations except for Mt Gambier. The average relative error for the latitude-dependent Model 3b is also much smaller than that for the bulk-regional Model 3b.

QQ plots for latitude-dependent Model 3b can be seen in Figure 5.10. The agreement between the predictions and observed data is very close at most of the locations. However, it can be observed that the latitude-dependent Model 3b tends to either slightly over-predict the radiation or under-estimate the predictive uncertainty. In comparison to the bulk-regional Model 3b, the latitude-dependent Model 3b is closer to the 1:1 line at all locations.

5.6 Conclusions

In this chapter a bulk-regional and a latitude-dependent regional model are developed. These models enable the global, direct and diffuse radiation to be calculated at any location where data does not exist for local calibration.

For the global radiation, the bulk-regional models perform well at all locations. The latitude-dependent models also perform well, particularly latitude-dependent Model 3b. The latitude-dependent Model 3b performs better than the bulk-regional Model 3b at 11 of the 20 locations studied.

The performance of the regional and local global radiation models is also compared to the satellite-derived global radiation at ten locations. At three of the locations, the satellite-derived global radiation performs slightly better than the global radiation calculated using the local and regional models. At the other seven locations, the satellite-derived radiation performs significantly worse than the radiation calculated from the local and regional models.

For the direct radiation, the bulk-regional and latitude-dependent Models 2 and 3 perform well for all locations, while the bulk-regional and latitude-dependent Model 1 do not. The latitude-dependent models perform better than the bulk-regional models at all but one location.

For the diffuse radiation, the bulk-regional and latitude-dependent Models 2a, 2b, 3a and 3b perform well, with Model 3b having the best performance. The latitude-dependent models perform better than the bulk-regional models at all locations.

From the results of this study, it is clear that a regional model can be used to estimate the global, direct and diffuse radiation at all locations studied, with minimal loss of accuracy compared with the local models. For the global radiation, the bulk-regional and latitude-dependent models both perform well. Either model can therefore be used to determine the radiation at any location in Australia that has SSH data. For the direct and diffuse radiation, the latitude-dependent models perform better than the bulk-regional models, and are therefore recommended for use when local calibration is not possible.

At seven of the ten locations studied, the global radiation estimated from the regional models is also closer to the observed measurements than the satellite-derived global radiation. The disadvantage of the regional models is that SSH data is needed as a model input. For locations where there is no measured SSH data, the SSH will need to be estimated from nearby measurements. At these locations, the radiation predicted by the regional models may not be as accurate as the satellite-derived estimates. However, the disadvantage of the satellite estimates is that they have only recently begun, and therefore cannot be used for historical analyses.

Chapter 6 - Influence of Uncertainty in the Global Radiation Estimate on Evapotranspiration Rates

Overview

In this chapter, a selection of radiation-based ET models, along with the FAO-56 Penman-Monteith model, are used to determine the influence of the uncertainty in the global radiation estimate on ET rates. The chosen ET models are commonly used in agricultural and climate studies. The ET is first estimated for all models using the average modelled radiation for each day. The upper and lower 95% limits of the radiation are then used to estimate the uncertainty in the ET. Following this, the associated amount of uncertainty in the ET estimates for the different ET models are compared.

6.1 Data and Method

The radiation-based ET models used are the Priestley-Taylor (PT), Hargreaves, Turc, Makkink, Doorenbos-Pruitt (DP), modified Jensen-Haise (mod-JH) and Abtew models. These models are outlined in Chapter 2. Along with the radiation-based ET models, the FAO-56-PM model is also used. The FAO-56-PM model and the radiation-based models all estimate ET for a reference crop. The ET models are used to calculate the ET at the nine main locations; Adelaide, Alice Springs, Broome, Darwin, Melbourne, Mildura, Mt Gambier, Tennant Creek and Wagga Wagga.

Daily values of maximum temperature, minimum temperature, wind speed, vapour pressure and relative humidity, for use in the ET models, were obtained from the Bureau of Meteorology. The SSH data, as given in Chapter 3, is used to estimate the global radiation for each day following the procedure in Chapter 3.

The FAO-56-PM and PT models use net radiation rather than global radiation. The net radiation R_n (MJ m^{-2} d^{-1}) is calculated using:

$$R_n = R_{ns} - R_{nl} \tag{6.1}$$

where R_{ns} is the net shortwave radiation (MJ m^{-2} d^{-1}) and R_{nl} is the net longwave radiation (MJ m^{-2} d^{-1}). The net shortwave radiation is calculated using:

$$R_{ns} = (1-\alpha)R_s \tag{6.2}$$

where R_s is the global radiation and α is the albedo. Following Allen et al. (1998), α is equal to 0.23 for the hypothetical grass reference crop (dimensionless). The net longwave radiation is calculated using:

$$R_{nl} = \sigma\left[\frac{T_{\max,K}{}^4 + T_{\min,K}{}^4}{2}\right]\left(0.34 - 0.14\sqrt{e_a}\right)\left(1.35\frac{R_s}{R_{so}} - 0.35\right) \tag{6.3}$$

where σ is the Stefan-Boltzmann constant (4.903 10^{-9} MJ K^{-4} m^{-2} d^{-1}), $T_{\max,K}$ is the maximum absolute temperature during the 24-hour period, $T_{\min,K}$ is the minimum absolute temperature during the 24-hour period, e_a is the actual vapour pressure (kPa) and R_{so} is the clear-sky radiation (MJ m^{-2} d^{-1}), calculated using:

$$R_{so} = (0.75 + 2\times10^{-5}z)R_a \tag{6.4}$$

where z is the station elevation above sea level (m) and R_a is the ETR (MJ m^{-2} d^{-1}).

Following the FAO-56 guide (Allen et al., 1998), in the PM model the ground heat flux is ignored.

The FAO (Allen et al., 1998) have proposed using the FAO-56-PM model as the standard equation for estimating reference ET. The FAO-56-PM model is commonly used for evaluating and calibrating ET models when local ET measurements do not exist (Jensen et al., 1990; Amatya et al., 1995; Trajkovic and Kolakovic, 2009; Tabari et al., 2011). Following Jensen et al. (1990), Amatya et al. (1995) and Xu and Singh (2000; 2001) the ET models are calibrated to the FAO-56-PM estimates using linear regression. The linear regression produces a constant which is used to adjust the

estimates for each location. This allows for the ET estimates, and the influence of the radiation uncertainty, to be directly comparable at the different locations.

The length of period for which the ET estimates are applicable is different for each of the models. The FAO-56-PM model can be used on a daily basis, while the PT, Hargreaves, Turc, Makkink, DP and mod-JH models generally require a ten-day or longer averaging period. Therefore, each of the ET estimates are calculated using a daily, ten-day and monthly averaging period.

To determine the influence of the uncertainty of the global radiation on the ET estimate, each ET model is calculated using the average global radiation estimate, along with the 95% predictive limits of the global radiation amounts derived from the daily SSH values. The global radiation estimates are developed using the locally calibrated radiation models. All five global radiation models with a linear SSH error variance are used. In addition, the global radiation derived using the bulk-regional and latitude-dependent regional models are also used to calculate the ET amounts. This allows for the uncertainty of the global radiation estimate on the ET to be determined and compared for the different local and regional global radiation models and ET models.

To compare the uncertainty in the ET estimated by the different methods, the percent uncertainty of the estimates is calculated using;

$$\text{percent uncertainty} = \pm \frac{0.5\left(ET_{\max} - ET_{\min}\right)}{ET_{ave}} \times 100\% \tag{6.5}$$

where ET_{max} is the ET calculated using the upper radiation limit, ET_{min} is the ET calculated using the lower radiation limit and ET_{ave} is the ET calculated using the average global radiation estimate.

6.2 Uncertainty in the Evapotranspiration Estimate from the Local Radiation Models

The uncertainty in the ET estimate varies between the ET models and between the locations. Figure 6.1 shows the range of ET estimated from the different ET and radiation models for Alice Springs and Melbourne. Of the locations considered, Alice Springs generally has the smallest uncertainty in the ET estimate while Melbourne generally has the largest uncertainty. Of the ET models, the FAO-56-PM model generally has the smallest uncertainty in the ET amount, while the Makkink and DP models have the greatest uncertainty.

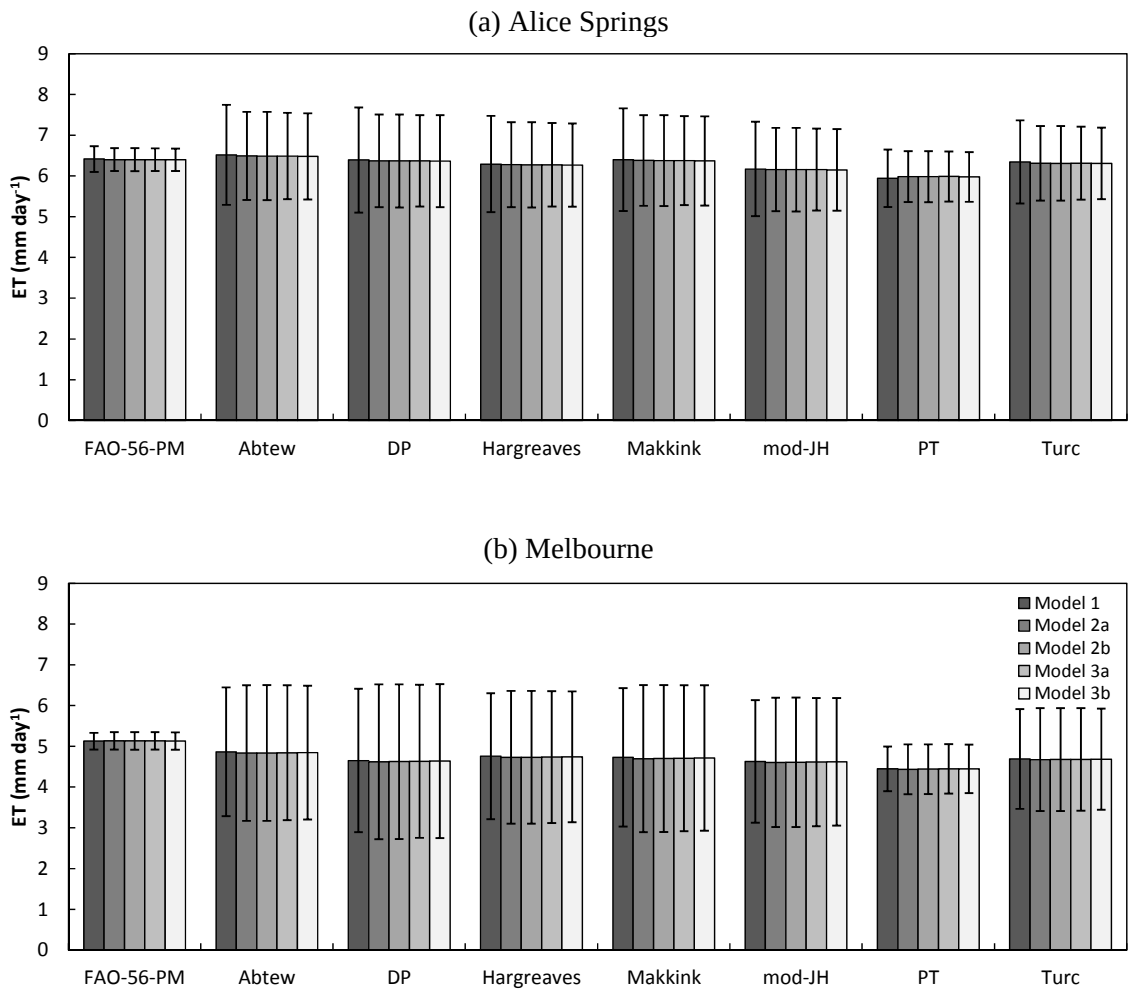

Figure 6.1 Average ET and average range of daily ET predicted by the eight ET models and the five global radiation models for (a) Alice Springs and (b) Melbourne. The global radiation is estimated using the locally calibrated parameters. The different global radiation models are given by the different grey shades. The error bars indicate the range of ET for each day.

As shown in Figure 6.1, the choice of global radiation model does not significantly influence the average, or range, of ET produced by each ET model. In general, global radiation Model 3b leads to a slightly smaller uncertainty in each ET estimate. This is because the uncertainty in the radiation estimate is slightly smaller for Model 3b than the other four models, as shown and discussed in Chapter 4.

Figure 6.2 shows the average daily percentage uncertainty in the ET estimates for all locations using radiation Model 3b. This gives the uncertainty in the range of ET, due to the range in estimated radiation, compared to the average ET estimated for each day (see equation 6.5). From Figure 6.2 it is clear that the uncertainty is dependent on both location and ET model. The extent of the uncertainty is dependent on both the local atmospheric variables, such as the temperature and wind speed, as well as the estimated uncertainty in the radiation estimates.

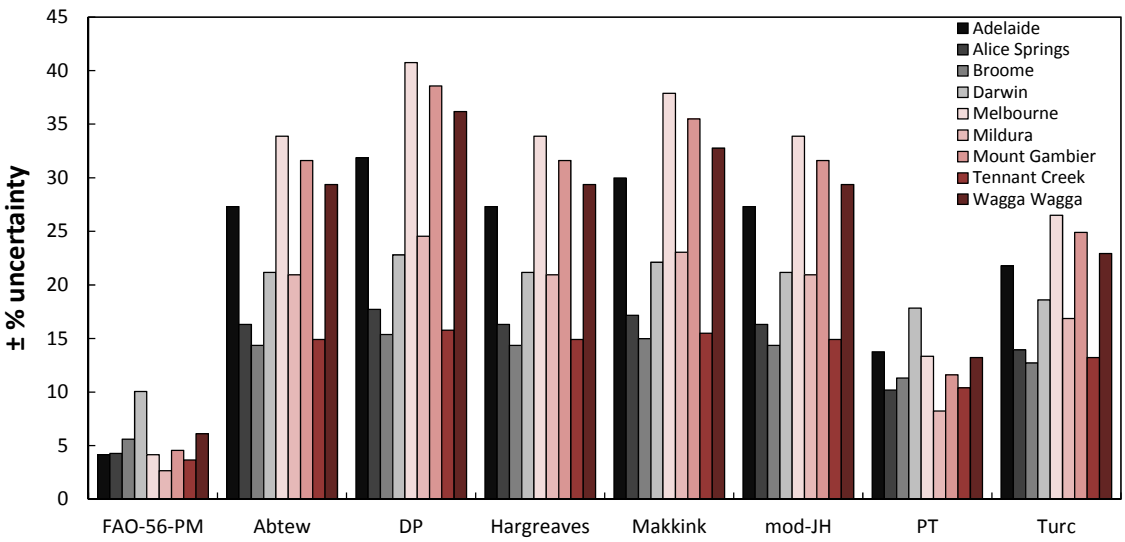

Figure 6.2 Average uncertainty in the daily ET estimates for all locations and ET models using global radiation Model 3b.

Box plots of the distribution of the daily percentage uncertainty in the ET estimates can be seen in Figure 6.3 for Alice Springs and Melbourne. From these plots, it can be seen that the range of uncertainty in the ET estimates is much larger for Melbourne than Alice Springs. Of the ET models, it is clear that the DP model has the greatest maximum uncertainty, although the upper and lower quartiles reveal that the majority of the data has a much smaller amount of uncertainty. For all the ET models, the greatest

percentage uncertainty generally occurs on cloudy days when the average ET amount is reduced. Therefore, the high percentage uncertainty is only equivalent to a small range of ET.

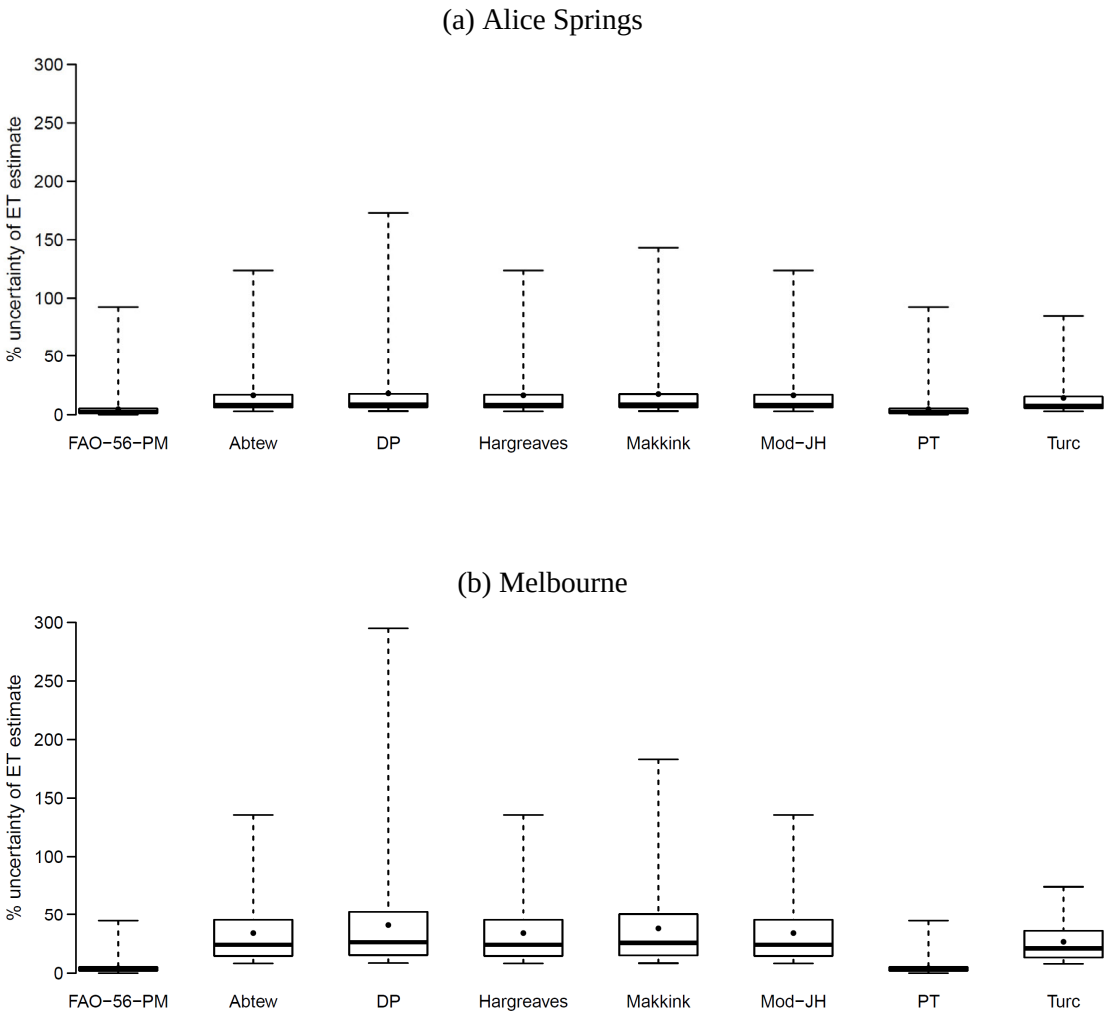

Figure 6.3 Box plots of the daily percentage uncertainty of the ET estimates for (a) Alice Springs and (b) Melbourne. The whiskers cover the entire range of percentage uncertainty. The dot is the mean percentage uncertainty.

The amount of ET variability is generally less for the FAO-56-PM model than the radiation-based ET models. For Alice Springs, the average uncertainty in the radiation-based ET estimate ranges from ±10% of the average ET for the PT model, to ±17% of the average ET for the DP model. The average uncertainty of all the radiation-based models is ±15%. For Melbourne, the uncertainty in the ET estimate ranges from ±13%

of the average ET for the PT model, to ±39% of the average ET for the DP model. The average uncertainty of all the radiation-based models is ±31%.

The PM model is recommended by many authors as the best performing method for estimating ET (e.g., Jensen et al., 1990; McKenney and Rosenberg, 1993; Allen et al., 1998) The PM model is physically derived, incorporates all the driving variables and has been shown to perform well in a variety of climates. The FAO-56-PM model is considered the standard method for estimating ET. For both Alice Springs and Melbourne, the uncertainty in the FAO-56-PM model is ±4% while for all locations the average uncertainty is ±5%. The maximum average uncertainty in the FAO-56-PM method is at Darwin, and is ±10%. It is clear that the uncertainty in the ET estimate due to the radiation uncertainty is much smaller for the FAO-56-PM model than the radiation-based models.

The FAO-56-PM and PT models both show the smallest uncertainty in the ET estimate at all locations. These models both use net radiation rather than just global radiation. The net radiation estimate adds additional uncertainty, as the longwave radiation estimate is calculated using the global radiation estimate. However, a higher global radiation amount (such as the upper limit of the radiation estimate) leads to a higher net longwave radiation estimate. As the net radiation is calculated as the difference between the net global and net longwave radiation, this leads to a smaller uncertainty in the net radiation amount. Therefore, the FAO-56-PM and PT models have a much smaller uncertainty in the ET estimate than the models which only use the global radiation. Note, however, that the calculated longwave radiation amount is only an estimate. Therefore, there is uncertainty in the longwave radiation estimate, and hence the net radiation estimate, which is not considered in the error bars of Figure 6.1.

6.3 Influence of the Averaging Period

While the FAO-56-PM model can be used on a daily timescale, the radiation-based ET models usually require an averaging period of at least ten days. Therefore, the above analysis is repeated using a ten-day and a monthly averaging period.

Using a ten-day and monthly averaging period does not greatly influence the average uncertainty in the ET estimates. For the FAO-56-PM model, the uncertainty is reduced from ±4% to ±3% in Melbourne and Alice Springs, for both the ten-day and monthly averaging period. For the DP model, which shows the greatest uncertainty, the uncertainty is reduced from ±17% to ±14% for the ten-day period, and to 13% for the monthly averaging period for Alice Springs. For Melbourne, the uncertainty in the DP model is reduced from ±39% to ±35% and ±31% for the ten-day and monthly averaging period respectively.

The main influence of using a ten-day or monthly averaging period is a reduction in the maximum range, and an increase in the minimum range, of ET estimated for each day. This leads to a reduction in the maximum uncertainty and an increase in the minimum uncertainty of the ET estimates. Box plots of the percentage uncertainty in the ET for the ten-day averaging period can be seen in Figure 6.4. From this figure, it can be seen that there is a much smaller range of uncertainty in the ET estimates for all models, with a reduced maximum and a slightly increased minimum uncertainty, compared with the daily estimate (Figure 6.3).

As an example of how the averaging period changes the range and uncertainty of the estimated ET, individual days from December 2005 for Alice Springs are analysed. Using the daily estimate, the greatest range in ET for the FAO-56-PM model is 2.2mm/day, while the smallest range is 0.0 mm/day. For the ten-day averaging period, the greatest range is 1.1 mm/day, while the smallest range is 0.04mm/day. For the monthly averaging period, the range is 0.8 mm/day. It can therefore be seen that increasing the averaging period reduces the maximum uncertainty and range of ET estimated for each day, and increases the minimum uncertainty and range of ET for each day.

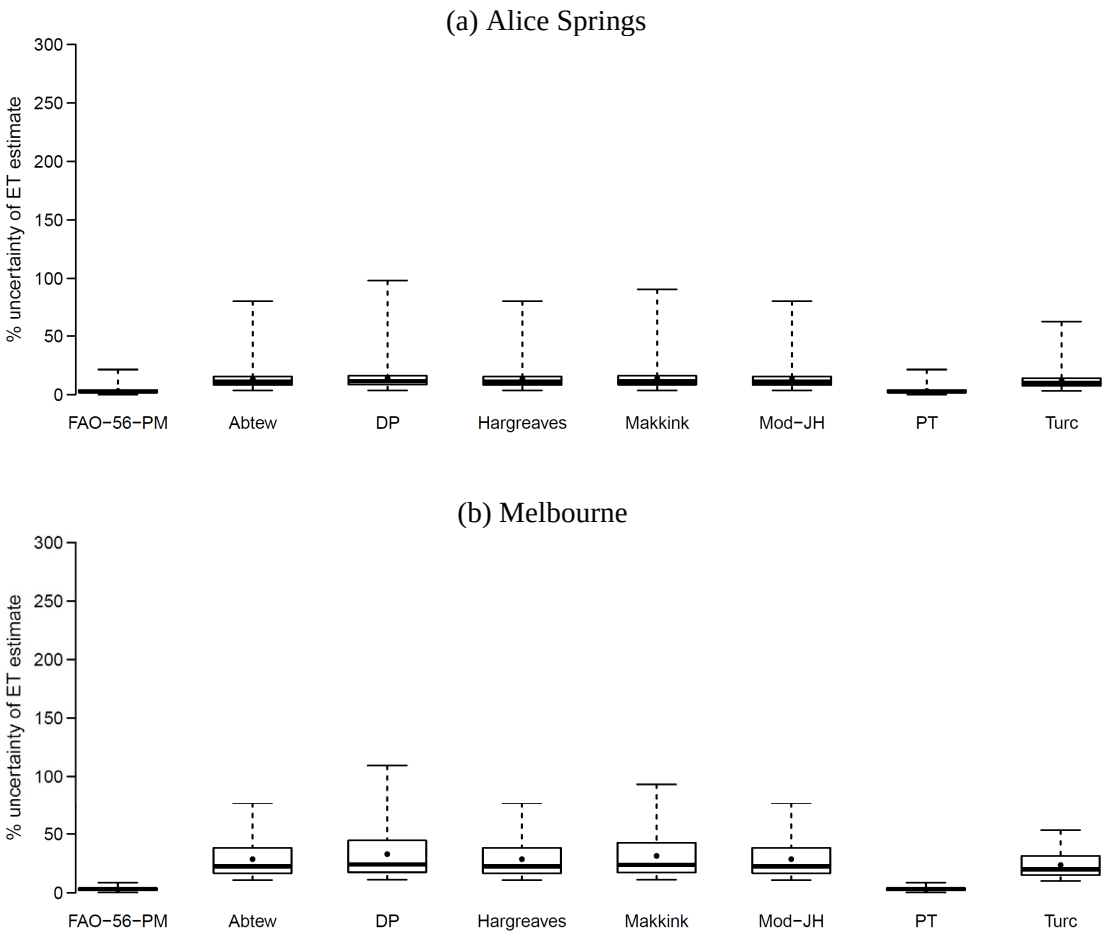

Figure 6.4 Box plots of the percentage uncertainty of the ET estimates using a ten-day averaging period for (a) Alice Springs and (b) Melbourne. The whiskers cover the entire range of percentage uncertainty. The dot is the mean percentage uncertainty.

6.4 Uncertainty in the Evapotranspiration Estimate from the Regional Radiation Models

The use of the radiation estimated from both the bulk-regional and latitude-dependent regional models only leads to a very minor change in the mean ET estimated by all of the ET models. The change in the percentage uncertainty of the ET estimate is also minor. For both Alice Springs and Melbourne, the increase in the uncertainty for the FAO-56-PM model is <1% for both regional models. For the radiation-based ET models, the latitude-dependent regional radiation models show a slight decrease in the ET uncertainty, while the bulk-regional models show an average increase of approximately 1% for Alice Springs and 2% for Melbourne. Therefore, using the

regional global radiation models only leads to a minor loss in accuracy of the mean ET estimate, and a minor change in the uncertainty for all the ET models.

6.5 Conclusions

In this chapter, the influence of the uncertainty in the global radiation estimates on ET rates is determined. The uncertainty in the ET estimate is shown to be dependent on location, the type of ET model used, and the initial uncertainty in the radiation estimate. The locations with a greater uncertainty in the radiation estimate have a greater uncertainty in the ET estimate. The choice of global radiation model does not significantly influence the average, or range, of ET produced by each ET model.

The amount of ET uncertainty is generally less for the FAO-56-PM model than the radiation-based ET models. The average uncertainty in the FAO-56-PM model is ±4% for Alice Springs and Melbourne, and ±5% for all locations. For the radiation-based ET models, the average uncertainty is ±15% for Alice Springs, and ±31% for Melbourne. The FAO-56-PM model has a much lower uncertainty as it accounts for the influence of wind speed and humidity, and this reduces the influence of the radiation component on the ET estimates. The FAO-56-PM model also uses net radiation instead of just the global radiation. The estimate of the longwave radiation in the net radiation calculation reduces the uncertainty of the radiation estimate.

The use of a ten-day and monthly averaging period does not greatly influence the average uncertainty in the ET estimates. However, the averaging period does reduce the maximum uncertainty, and increase the minimum uncertainty, in the ET for an individual daily estimate.

The ET is also estimated using the regional radiation models. For all ET methods and regional radiation models, the use of the regional models only leads to a minor loss in the accuracy of the ET estimate.

Of all the ET models, the combination-type FAO-56-PM model gives the smallest amount of uncertainty. Of the radiation-based ET models, the PT model gives the smallest uncertainty. It is therefore recommended that the FAO-56-PM model be used to estimate ET. In addition to having the smallest uncertainty, the FAO-56-PM model also incorporates all the driving variables of ET. When sufficient data is not available for using the FAO-56-PM model, the radiation-based PT method is recommended, as it gives the next smallest uncertainty in the ET estimate.

Chapter 7 - Influence of Increased Temperature on Evapotranspiration Rates

Overview

In the Murray-Darling Basin, the air temperatures during the 2002 drought were about 2°C warmer than the long-term average. Investigations into this drought led previous authors to incorrectly speculate that increased temperatures lead to a marked increase in ET rates. Other authors have estimated the influence of increased temperatures from climate change on ET rates, estimated by empirical equations, using GCM output such as temperature, global radiation, humidity and wind speed. A main conclusion of these studies is that the different ET models can produce vastly different responses to climate change, even of opposite sign. This chapter investigates the influence of a 2°C increase in temperature on ET rates, calculated by combination, radiation and temperature-based ET models. The change in ET due to the increased temperature is compared with the uncertainty in the ET estimate due to the uncertainty in the radiation input.

7.1 Data and Method

The radiation-based ET models, and data used in Chapter 6, are used here to simulate the influence of a 2°C increase in temperature on ET rates. Only the average of the modelled radiation is used in this analysis. In addition to the radiation-based ET models, the six temperature-based models outlined in Chapter 2 are also used. These are the Thornthwaite, FAO-24 Blaney-Criddle (FAO-24-BC), Hamon, Romanenko, Hargreaves-Samani (HS), and Kharrufa models.

The ET rates are first calculated using the observed temperatures. This establishes a baseline of ET which is used as a comparison for the temperature enhanced output from the different ET models. Using the method outlined in Chapter 6, the ET models are calibrated to the FAO-56-PM estimates using linear regression. This allows for the ET estimates to be directly comparable at the different locations.

The vapour pressure deficit (VPD), which is the difference between the saturated vapour pressure e_s and the actual vapour pressure e_a, is also calculated for each day:

$$e_s = 0.611e^{\left(\frac{17.27T}{T+237.3}\right)} \tag{7.1}$$

where T is the air temperature.

$$e_a = 0.611e^{\left(\frac{17.27T_w}{T_w+237.3}\right)} - 0.00066P(T_d - T_w)(1 + 0.00115T_w) \tag{7.2}$$

where P is the station pressure (kPa), T_d is the dry bulb temperature (°C) and T_w is the wet bulb temperature (°C). The e_a can also be calculated from the dew point temperature, but the results are essentially the same.

To simulate the influence of an increase in temperature, 2°C is added to the observed minimum temperature and maximum temperature for each day. The FAO-56-PM model requires the VPD. The saturated vapour pressure is calculated at the increased temperature. The actual vapour pressure is calculated using the VPD from the unenhanced temperatures.

The VPD is kept constant between the two scenarios as it is not known how an increase in temperature will influence the VPD. However, Roderick and Farquhar (2004) suggest that although temperatures have been observed to be increasing, the VPD has remained relatively constant in Australia. Roderick et al. (2007) also assessed the trend in VPD at 41 sites from 1975-2004 and only found a small trend of -0.2Pa a^{-1} compared to a background average of 1205Pa (less than 1% over the 30 years). As an alternative, in a third scenario, the e_a is calculated keeping the relative humidity constant between the baseline simulations and the simulations with the increased temperature.

The average daily ET amounts for each ET model are determined using a daily, ten-day, and monthly averaging period.

This method is relatively simple as the purpose of this investigation is only to see how the increase in temperature affects the output from the ET models. An increase in temperature may affect other driving variables of ET; however, this is beyond the scope.

7.2 Results and Discussion

The average daily ET from the baseline scenario and the two enhanced temperature scenarios, using a ten-day averaging period, can be seen in Figure 7.1 for Alice Springs and Melbourne.

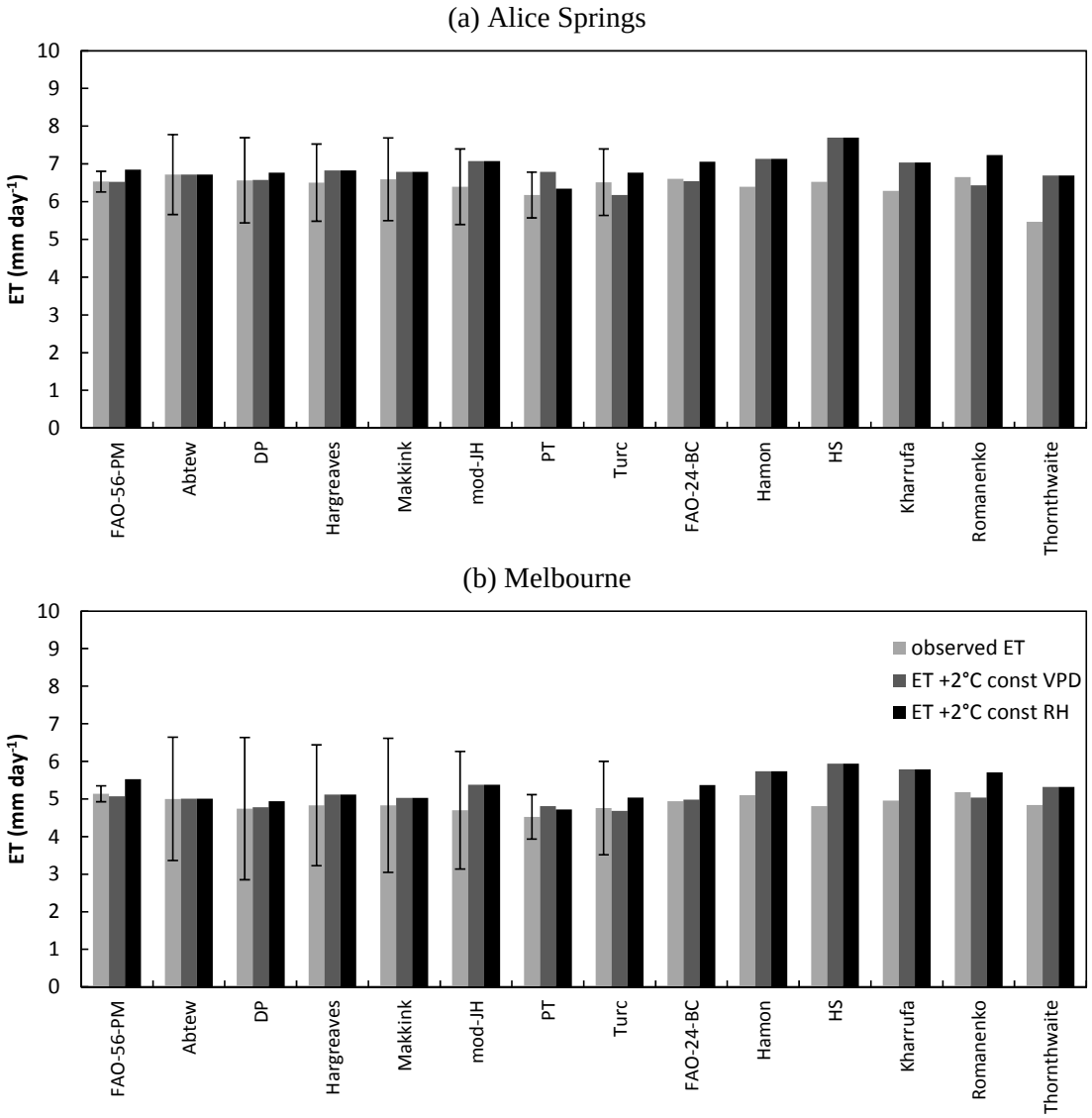

Figure 7.1 Average daily ET using a ten-day averaging period, for each ET model, for (a) Alice Springs and (b) Melbourne. The error bars give the uncertainty in the ET estimate due to the uncertainty in the radiation input.

From Figure 7.1, it can be seen that an increase in temperature using a constant VPD leads to a range of changes in ET, even of differing sign. Table 7.1 compares the percentage change in the temperature enhanced ET with the base-line ET for Melbourne and Alice Springs using the ten-day and monthly averaging periods. The monthly and ten-day averaging periods produce results very similar to the daily estimates.

Table 7.1 Average daily ET from the observed data and the percentage increase in ET resulting from the addition of 2°C, using a constant VPD and constant relative humidity (RH).

ET model	Alice Springs					Melbourne				
	Obs. ET (mm d^{-1})	% increase in ET				Obs. ET (mm d^{-1})	% increase in ET			
		10 day		month			10 day		month	
		VPD	RH	VPD	RH		VPD	RH	VPD	RH
FAO-56-PM	6.5	-0.1	4.8	0.0	4.9	5.1	-1.2	7.6	-1.2	7.6
Abtew	6.7	0.0	0.0	0.0	0.0	5.0	0.1	0.1	0.0	0.0
DP	6.6	0.2	3.0	0.2	3.0	4.7	0.7	4.2	0.7	4.2
Hargreaves	6.5	5.0	5.0	5.0	5.0	4.8	5.9	5.9	5.9	5.9
Makkink	6.6	3.0	3.0	3.0	3.0	4.8	4.1	4.1	4.1	4.1
Mod JH	6.4	10.7	10.7	10.7	10.7	4.7	14.5	14.5	14.6	14.6
PT	6.2	10.0	2.7	10.5	2.8	4.5	6.3	4.3	7.9	4.4
Turc	6.5	-5.2	3.9	-5.2	3.9	4.8	-1.6	5.8	-2.0	5.8
FAO-24-BC*	6.6	-1.0	6.8	-0.9	6.8	4.9	0.9	8.7	0.9	8.6
Hamon*	6.4	11.6	11.6	11.7	11.7	5.1	12.6	12.6	12.5	12.5
HS*	6.5	17.9	17.9	17.9	17.9	4.8	23.5	23.5	23.5	23.5
Kharrufa*	6.3	11.9	11.9	11.9	11.9	5.0	16.8	16.8	16.7	16.7
Romanenko*	6.6	-3.3	8.8	-3.3	8.7	5.2	-2.8	10.1	-2.9	10.1
Thornthwaite*	5.5	22.4	22.4	22.1	22.1	4.8	9.9	9.9	9.8	9.8

*Temperature-based ET models

Using a constant VPD, the temperature enhanced ET rate remains almost unchanged for the FAO-56-PM and Abtew models. This is expected of the Abtew model as the ET is calculated as a fraction of the global radiation only, which remains constant. The FAO-56-PM model is physically derived and incorporates all the driving variables of ET. With the increased temperature, keeping the VPD constant results in a corresponding increase in relative humidity. This increased relative humidity counteracts the effect of the increased temperature, leading to a minimal change in ET.

The ET rate is decreased for the Turc and Romanenko models by 5% and 3% respectively at Alice Springs, and 2% and 3% respectively at Melbourne. The FAO-24-BC model also shows a slight decrease of 1% at Alice Springs, but a slight increase of 1% at Melbourne. The ET rate is increased for the remaining models. The Turc, Romanenko and FAO-24-BC models all include a humidity term along with a temperature term. It is this increase in humidity which leads to the decrease in the ET rate.

The increased relative humidity plays a large role in the influence of the increased temperature on the ET rates. This effect can be further illustrated by recalculating the ET rates while keeping a constant relative humidity between the baseline and enhanced temperature scenarios. With the relative humidity held constant, as shown in Figure 7.1, the ET is slightly enhanced for the FAO-56-PM, DP, Turc, FAO-24-BC and Romanenko models. The ET is enhanced for the FAO-56-PM model because keeping the relative humidity constant results in an increase in the VPD. For the DP, Turc, FAO-24-BC and Romanenko models, which only use the relative humidity term rather than the VPD term, the relative humidity is lower in the constant relative humidity scenario, which allows for greater ET rates. The remaining models, which do not include a humidity term, are unaffected.

Of the radiation-based models, the greatest increase in ET is seen for the mod-JH model, which is increased by 11% and 15% at Alice Springs and Melbourne respectively. In comparison, for the temperature-based models, the greatest increase for Alice Springs is seen with the Thornthwaite model, which has an increase of 22%. For Melbourne, the HS model has the greatest increase, by 23%.

The Thornthwaite model gives the greatest increase in ET at Alice Springs; however, Alice Springs is an arid location and therefore the Thornthwaite model is not strictly valid. Shaw (1994) has shown that compared to the Penman model, the Thornthwaite model tends to exaggerate ET in arid climates. For Melbourne, which has a temperate climate, the increase in ET is much smaller. The other ET models do not display a large difference in the ET between the different climate states.

Table 7.1 shows the average daily percentage change in ET due to the increased temperature; however, the change in ET is much more variable on a day-to-day basis. The response of the ET to the increased temperatures is generally greater in summer than in winter. A time series of the daily ET for Alice Springs can be seen in Figure 7.2. These figures reveal that the increase in ET from the higher temperatures is much more prominent in the summer months for the temperature-based models, particularly for the Thornthwaite model.

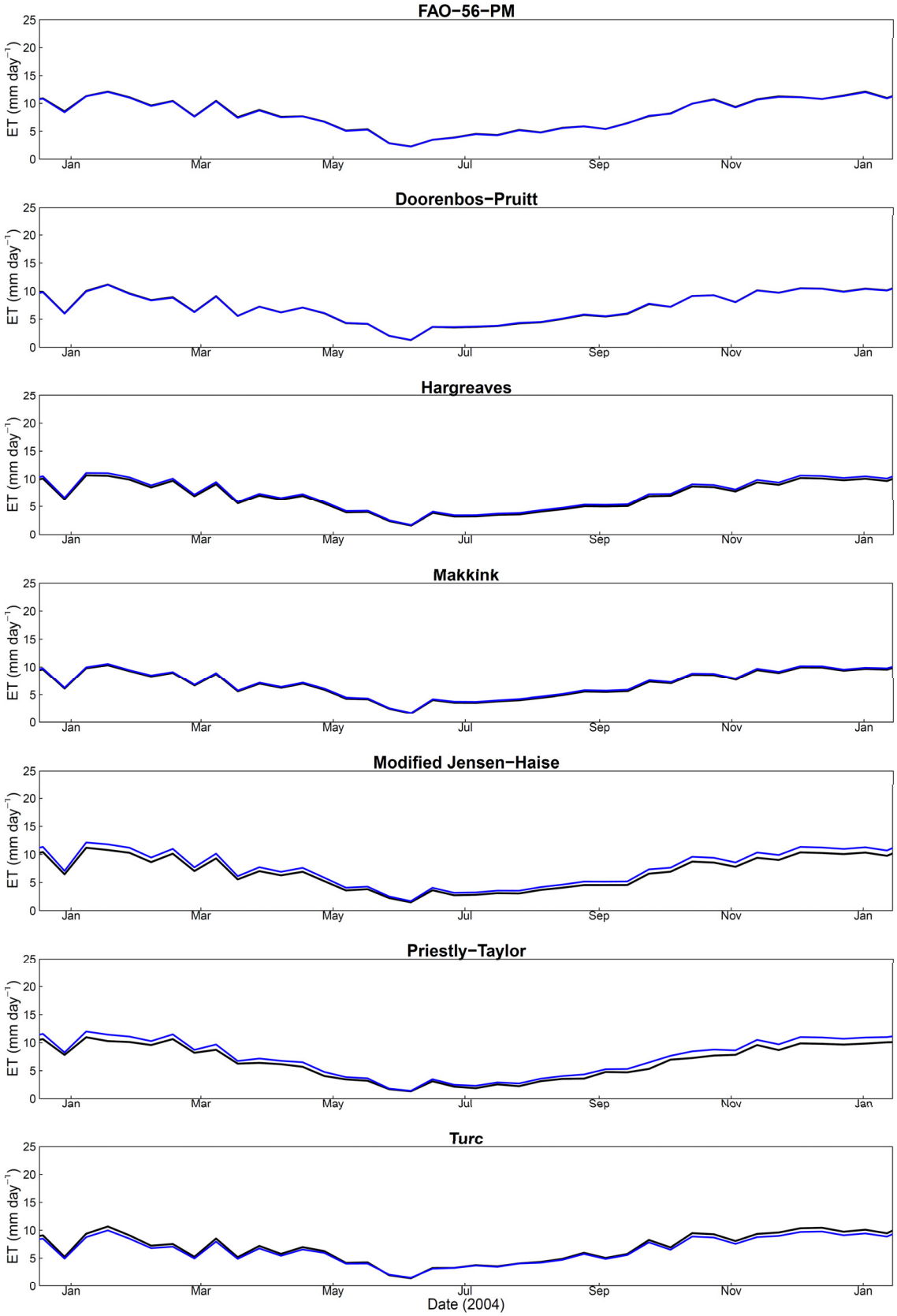

(a) Radiation-based ET models

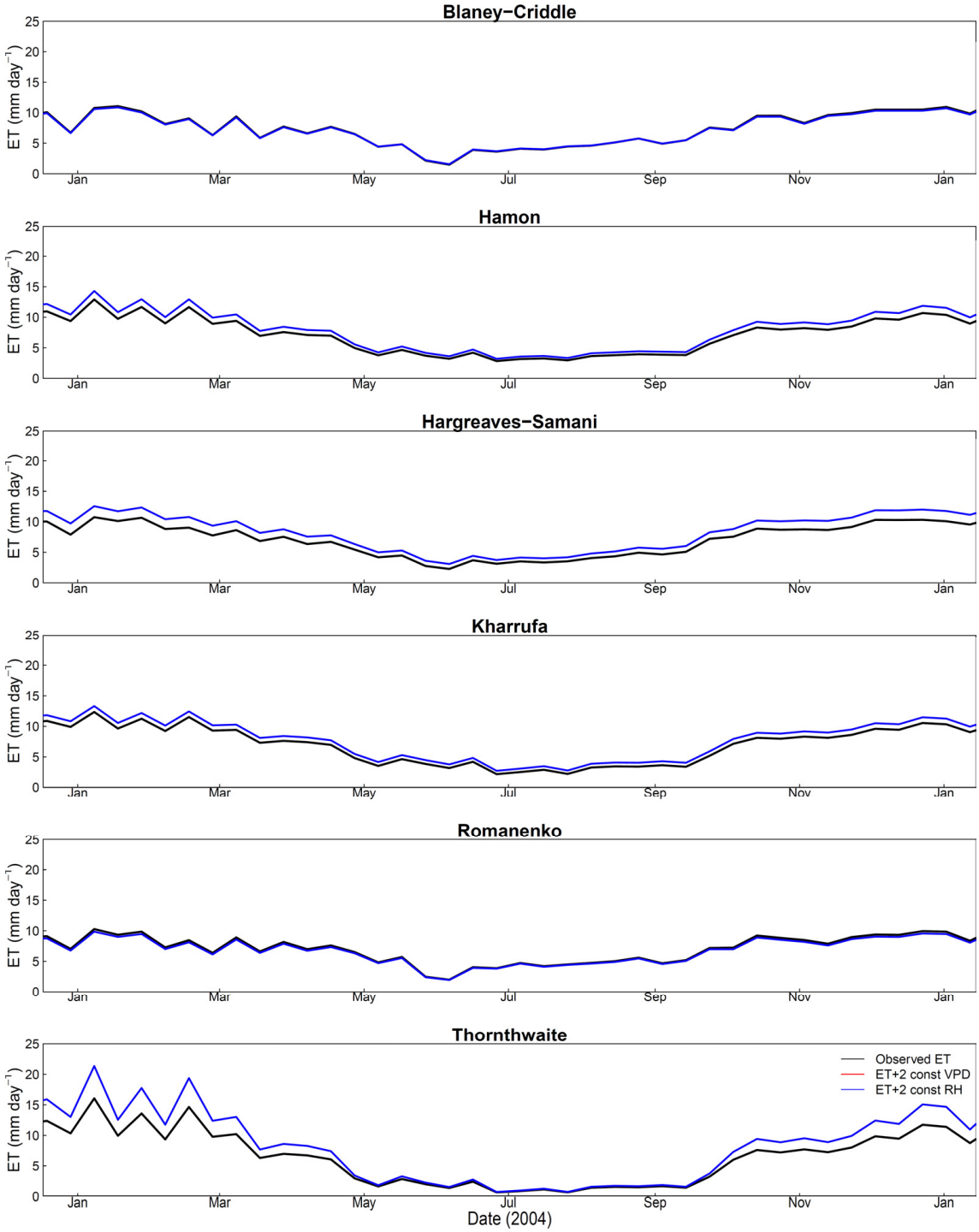

(b) Temperature-based ET models

Figure 7.2 Time series of daily ET estimated using a ten-day averaging period for Alice Springs for (a) the radiation-based ET models and (b) the temperature-based ET models. The baseline observed ET is shown in black. The ET resulting from the increased temperature using a constant VPD is shown in red and the ET using a constant relative humidity is shown in blue.

The temperature-based models, with the exception of the Romanenko and FAO-24-BC models with constant VPD, generally have a much greater increase in ET than the FAO-56-PM model. The greatest increase is seen with the HS, Kharrufa and Thornthwaite models. This is because the Thornthwaite model only has inputs of the average daily temperature and a heat index term. Similarly, the HS model uses the difference between the maximum and minimum daily temperature, and the ETR. The Kharrufa model uses temperature and a daylength term. In contrast, the other models all include some measure of humidity along with the temperature term. Only the FAO-24-BC model, which uses wind speed, relative humidity and the SSH fraction, gives similar results to the FAO-56-PM model.

Of the radiation-based ET models, the mod-JH model has the greatest increase in ET. This model does include a saturated vapour pressure term rather than a humidity term, but temperature is still a key input. Of the remaining models, only the DP model, which has terms for humidity and windspeed, gives similar results to the FAO-56-PM method. However, on average the radiation models tend to produce results more similar to the FAO-56-PM model than the temperature-based models. This is consistent with the studies of Jensen et al. (1990) and Trajkovic and Kolakovic (2009).

The influence of temperature on the ET derived by the Thornthwaite model is particularly important. The Thornthwaite model is commonly used in the calculation of the PDSI, which gives a measure of dryness of the land surface. The results of this study suggest that an increase in temperature will result in enhanced ET rates, using the Thornthwaite model, leading to greater drying of the land surface and drought conditions. However, these ET rates are exaggerated compared with the other ET estimates. This suggests that PDSI estimates may be more extreme than reality would suggest, particularly for arid environments.

The uncertainty in the ET amount due to the uncertainty in the radiation amount is shown in Figure 7.1 along with the average ET for the FAO-56-PM and radiation-based ET models. For both Melbourne and Alice Springs, it is clear that the uncertainty in the radiation-based ET estimates is greater than the change in ET resulting from the increase in temperature. This suggests that the uncertainty in the radiation estimate has a

greater influence on possible ET amounts than the influence of increased temperatures. The FAO-56-PM model has a much smaller uncertainty associated with the radiation estimate. For this model, the uncertainty in the ET due to the radiation is comparable with the change in ET from increased temperatures with constant relative humidity.

7.3 Conclusions

This chapter demonstrates the influence of a 2°C increase in temperature on ET rates, using a variety of well-known ET models. The increased temperature leads to a range of responses in ET rates. This is consistent with the studies of McKenney and Rosenberg (1993), Kay and Davies (2008) and Hobbins et al. (2008). The response of the models differs depending on the climatic factors each model considers. It is also shown that the effect of the increasing temperature on humidity also influences the amount of ET calculated. Whether or not the relative humidity or VPD is held constant affects how the increased temperature influences the ET rates.

When the VPD is kept constant between the baseline and enhanced temperature scenarios, the ET rate for the FAO-56-PM and Abtew models remains almost constant, and decreases for the temperature-based Romanenko model and the radiation-based Turc model. This is consistent with the work of Roderick et al., (2009) who noted that pan ET rates have decreased over the last several decades while the VPD has remained almost constant. The decrease in pan ET was attributed mainly to decreasing wind speed with some regional contributions from decreasing solar irradiance. Air temperature, as well as the VPD, was found to play only a minor role in the changes in pan ET. The remaining models calculate an increase in ET of up to 23% of the average baseline ET. The ET models that include a relative humidity term lead to either a decrease, or a very minor increase, in ET rate.

When the ET is recalculated keeping the relative humidity constant between the baseline and enhanced temperature scenarios, the ET rate increases for all the models. The ET models that only use temperature as an input have the greatest increase in ET with the increase in temperature. The models that have ET rates most similar to the FAO-56-PM model all include humidity terms.

Given the range of responses of the ET models to the increase in temperature, it is clear that not all empirical models can be used to estimate the influence of increased temperatures on ET. The FAO-56-PM model, the standard for estimating ET, suggests that the ET response to an increase in temperature will only be very minor. In contrast, the radiation and temperature-based models can lead to overly high, as well as negative estimates of ET. The Thornthwaite model, based solely on air temperature, leads to a large increase in ET, which has important implications for the application of the PDSI.

In an environment where the temperatures are increasing, simple temperature-based ET models cannot be relied on to give accurate estimates of ET. ET is influenced by more than just temperature. With an increase in temperature, it is unknown how humidity, radiation amounts and wind speed may be influenced. Donohue et al. (2010) suggested that under conditions of climate change, the driving variables may have different, even opposing, trends on ET. As shown in this study, with a constant VPD, the FAO-56-PM model suggests there will be a very slight decrease in the average daily ET rates. In contrast, with a constant relative humidity, the FAO-56-PM model suggests there will be a slight increase in the average daily ET rates.

This study also shows that for the radiation-based ET models, the uncertainty in the radiation amount can lead to large differences in the predicted ET. Of all the ET models, only the DP model has estimates close to that of the FAO-56-PM model, suggesting it is the most reliable method; however, in Chapter 6 it was shown that this model has the largest uncertainty due to the radiation input.

Temperature-based models are clearly erroneous when compared to the FAO-56-PM model, which is physically-based. From this analysis, we do not advocate the use of temperature-based empirical models for determining the influence of enhanced temperatures on ET rates. Models such as the PM model, which include radiation and humidity terms, can be expected to give more physically realistic results. However, the PM model itself has limitations as it is one-dimensional, and has what is known as a big leaf canopy assumption (Calder, 1990). In addition, the FAO-56-PM model is a simplified version of the PM model and represents a hypothetical crop, similar to grass, and is not representative of all vegetation types.

Chapter 8 - The Role of Soil Moisture in Daytime Evolution of Temperatures

Overview

The previous chapter presents a simple analysis of the influence of a 2°C increase in temperature on potential ET rates, as estimated by simple empirical equations at a daily, ten-day and monthly timescale. In this chapter, the relationship between temperature, evaporation and soil moisture is explored in more detail using a planetary boundary layer (PBL) model. It focuses on illustrating and quantifying the effect of soil moisture on the evolution of daytime temperatures, and the interaction between potential and actual evaporation and temperatures under drought conditions. This chapter also reiterates the known fundamental processes associated with temperature and soil moisture, with the aim of providing a very simple demonstration of cause and effect. A coupled PBL/Penman-Monteith model is used to simulate the evolution of the PBL and evaporation over the course of a day in order to quantify the effect of soil moisture content on the evolution of daytime air temperature.

8.1 Motivation

Investigations into the recent drought in the MDB have brought to light confusion surrounding the cause and effect of temperatures and evaporation. These studies have noted that during the recent drought, low rainfall totals were accompanied by anomalously high air temperatures. In particular, Karoly et al. (2003) noted that whilst monthly rainfall totals were at extreme lows during the 2002 drought, the monthly average maximum temperatures were much higher than in previous droughts. This led the authors to state that "…the higher temperatures caused a marked increase in evaporation rates, which sped up the loss of soil moisture and the drying of vegetation and watercourses. This is the first drought in Australia where the impact of human-induced global warming can be clearly observed…" (p. 1).

Similarly, Nicholls (2004) investigated the anomalously high air temperatures that occurred during the 2002 cool season (May–October) in the MDB. This was achieved through a comparison to an identified negative correlation between average monthly temperature and average monthly rainfall, between 1952 and 2002. Nicholls (2004) then examined the residual time series of the correlation which demonstrated a statistically significant monotonic increase toward higher air temperatures over the period of the regression data. It was then speculated that this was due to the increasing trend in atmospheric carbon dioxide and other greenhouse gases, and that "the warming has meant that the severity and impacts of the most recent drought have been exacerbated by enhanced evaporation and evapotranspiration" (p. 334).

In a more recent study, Cai and Cowan (2008) suggested that increased temperatures are the cause of reduced inflows into the MDB since 1950. They showed that a rise of 1°C leads to an approximate 15% reduction in annual inflows. Similarly, Cai et al. (2009) speculated that increased temperatures have led to decreased soil moisture, and that annually a rise of 1°C leads to a 9% reduction in soil moisture over the southern MDB.

The actual relationship between temperatures and evaporation is driven by interactions between the land surface and the lowest part of the atmosphere, known as the PBL. The land surface and PBL are a tightly coupled system (Santanello et al., 2005; Shuttleworth et al., 2009). The characteristics of the landscape (predominantly soil moisture) influence the atmosphere by controlling the division of net radiation into latent and sensible heat fluxes (Stensrud, 2007). Conversely the atmosphere forces the land surface through precipitation, momentum and radiative fluxes, due to the moving atmospheric fluid (Trier et al., 2008).

Shuttleworth et al. (2009) also examined the role of large scale changes in the atmosphere, which are then reflected in near-surface values, on the interactions between pan ET and atmospheric drivers in Australia. They found evidence for landscape-scale coupling between the surface and PBL via surface radiation, wind speed, and VPD as well as changes in pan ET that are associated primarily with large-scale changes in wind speed and to a lesser extent surface radiation. They recognise that changes in area-average ET are controlled by changes in atmospheric demand, as well as changes in

area-average surface resistance, which reflect changes in available moisture at the surface.

8.2 Planetary Boundary Layer

The PBL can be conceptualized to comprise three layers as seen in Figure 8.1. These are the surface layer, where potential temperature increases towards the warmer ground surface, the uniformly mixed layer, which has constant profiles with height of potential temperature, θ, and specific humidity, q, and the inversion layer ($\Delta\theta$, Δq), above the mixed layer, where potential temperature increases with height. The inversion layer separates the turbulent boundary layer from the free atmosphere and is where entrainment occurs.

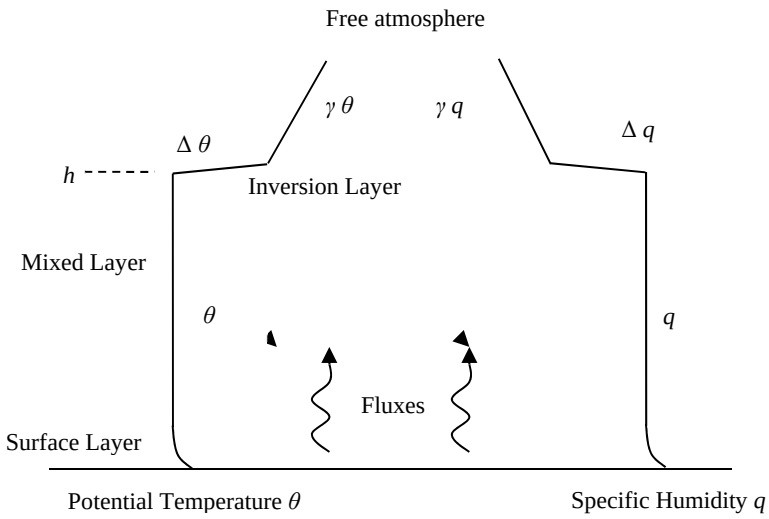

Figure 8.1 Boundary layer profiles of potential temperature and specific humidity. Figure based on the schematics presented by Quinn et al. (1995) and Margulis and Entekhabi (2001).

The PBL can be as shallow as tens of meters and as deep as several kilometres. Generally the PBL height is between 100 and 300m in the early morning and can reach 1-3km by the afternoon (Margulis & Entekhabi, 2001). Evolution of the boundary layer begins at sunrise when solar radiation reaches the land surface and begins to warm the ground (Stensrud, 2007). Consequently heat and moisture fluxes from the ground to the atmosphere become larger. In response the boundary layer slowly deepens as thermals reach the top of the layer and overshoot their level of neutral buoyancy, causing

entrainment. The depth of the mixed layer is controlled by the rate of entrainment of fluid across the inversion and by advective effects (Stull, 1976). Along with sensible heat flux from the ground surface, wind shear also plays a role in boundary layer development by generating turbulence (Stensrud, 2007). The PBL typically reaches its maximum depth by the middle of the day, often approaching a well-mixed structure when turbulence is vigorous. At the end of the day the heat flux vanishes and the turbulence quickly dissipates causing the PBL to collapse to a residual level which is maintained through forced convection.

Figure 8.2 shows an example of the evolution of the PBL temperature profile through a day. Each line shows the profile of the PBL at a given time determined from radiosonde data. As can be seen, the potential temperature is predominantly uniform with height in the mixed layer due to the entrainment and surface sensible heat flux, which help support the well mixed structure of the boundary layer. The boundary layer warms and increases in height through the day.

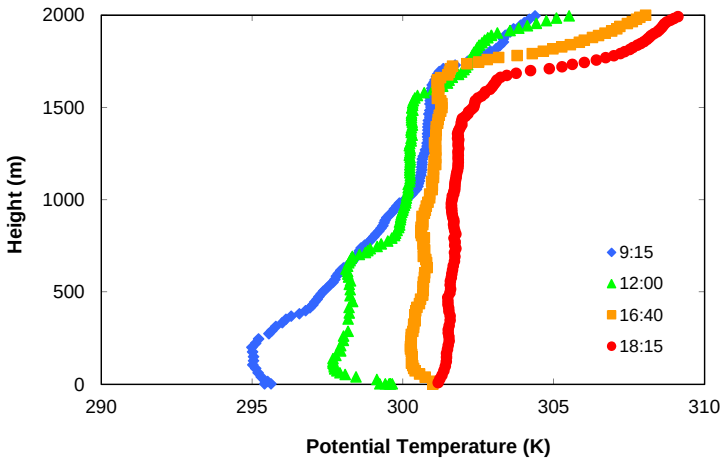

Figure 8.2 The development of the boundary layer temperature profile for 5 June 1987.

8.3 Methodology

8.3.1 Planetary Boundary Layer model

This investigation uses a simple PBL model coupled to the Penman-Monteith equation to model the interaction between the atmosphere and the land surface. This methodology is similar to that of van Heerwaarden et al. (2010) and has been

successfully used in previous studies to model the dynamics of the daytime PBL coupled to the land surface (e.g. Shuttleworth et al., 2009). PBL models have been used for many purposes and many investigations into the dynamics of the PBL have been reported (e.g. Tennekes, 1973; Betts et al., 1992; Quinn et al., 1995; Margulis & Entekhabi, 2001, 2004; Courault et al., 2007; Trier et al., 2008).

A simple convective model of the PBL is used to assess the evolution of daytime temperature under different soil moisture scenarios. In this model, the PBL is represented by a slab of air of height h (m) with uniform potential temperature and uniform specific humidity. A step inversion caps the slab which is in turn overlain by drier stably stratified air, as shown in Figure 8.1. The inversion is idealised as a step discontinuity in temperature and humidity. The governing equations below are as given in Quinn et al. (1995) and are based on the model first presented by Tennekes (1973) and Carson (1973). The reader is referred to Raupach (2000, 2001) and Culf (1994) for more detailed analysis of the physics of the coupled system.

The temperature of the slab (θ), is described using the differential equation:

$$\frac{d\theta}{dt} = \frac{H_S + H_i}{h\rho c_P} \tag{8.1}$$

where ρ is the density of air (kg m^{-3}), c_P is the specific heat capacity (J kg^{-1} K^{-1}) of the air at constant pressure and t is time (s).

The water vapour budget is similar and controlled by the fluxes of water vapour at the surface, E_S (kg m^{-2} s^{-1}), and at the inversion, E_i (kg m^{-2} s^{-1}). For the specific humidity, q:

$$\frac{dq}{dt} = \frac{E_S + E_i}{h\rho} \tag{8.2}$$

The sensible heat flux at the inversion, H_i (W m^{-2}), is given by:

$$H_i = \rho c_P \Delta\theta \frac{dh}{dt} \tag{8.3}$$

and the water mass flux at the inversion, E_i, is given by:

$$E_i = \rho \Delta q \frac{dh}{dt} \tag{8.4}$$

The sensible heat flux at the inversion is proportional to the sensible heat flux at the surface, H_S (W m^{-2}), where the constant of proportionality (the entrainment coefficient c_e) takes values in the range 0–1. This yields the rate of change of height, h, of the slab as follows:

$$\frac{dh}{dt} = \frac{c_e H_S}{\rho c_P \Delta \theta} \tag{8.5}$$

The inversion strength ($\Delta\theta$) tends to decrease as the boundary layer warms. Additionally the inversion strength tends to increase as entrainment into the stable air above the inversion base increases (Tennekes, 1973). Following Quinn et al. (1995) the entrainment increases the inversion strength by an amount $\gamma dh/dt$ giving a net rate of change of Δ as:

$$\frac{d\Delta\theta}{dt} = \gamma_\theta \frac{dh}{dt} - \frac{d\theta}{dt} \tag{8.6}$$

for temperature, and:

$$\frac{d\Delta q}{dt} = \gamma_q \frac{dh}{dt} - \frac{dq_m}{dt} \tag{8.7}$$

for humidity. In equations (8.6) and (8.7), γ_θ and γ_q are the gradients (lapse rates) of potential temperature (K m^{-1}) and specific humidity (kg kg^{-1} m^{-1}) in the overlying air.

To avoid numerical instabilities and solution errors that can corrupt the behaviour of the simple PBL model, the system of equations (8.1)-(8.7) is discretized in time using the implicit Euler scheme and solved using Newton-Raphson iteration (e.g., Kavetski & Clark, 2011).

Equations (8.1)-(8.7) are limited to simulating the PBL only throughout daylight hours, until the PBL begins to decay. There is no simple model available to run continuously throughout the night due to the complex nature of the nocturnal boundary layer.

The physical boundary layer is a complex system and as such is only roughly approximated by the simplified PBL model used in this study. For example, equations (8.1)-(8.7) ignore lateral advection, which, along with sensible heat flux from the ground surface, also plays a large role in boundary layer development (Stensrud, 2007). Using a model that neglects lateral advection may bias individual daily estimates (Margulis & Entekhabi, 2004), but building a 3D model allowing for lateral advection is beyond the scope of this work.

The evolution of the PBL potential temperature and specific humidity is principally driven by the balance between the surface sensible and latent heat fluxes and the entrainment fluxes at the top of the mixed layer.

Boundary layer models based on the work of Tennekes (1973) require a parameterisation of the entrainment coefficient c_e. However, entrainment is difficult to measure directly and there is much discussion of values and how to determine them in the literature. Santanello et al. (2005) suggest that the entrainment coefficient can be estimated using gradients of temperature and moisture at or near the top of the PBL, but recognise that such methods require numerous assumptions. Quinn et al. (1995) used a simple entrainment estimate based on the jump in temperature from the mixed layer to the free atmosphere and the rate of PBL growth, from the work of Tennekes (1973). However this estimate ignores advection, subsidence and radiation and is sensitive to small errors in height and to uncertainty in inversion-level temperature and humidity (Santanello et al., 2005).

A range of entrainment coefficient values are suggested in the literature. The traditional value for thermally driven dry convective boundary layers has been $c_e \approx 0.2$ (Quinn et al., 1995; Stensrud, 2007). Encompassing studies from 1960 to 1975 most of the published values for c_e lie between 0.1 and 0.3 although values ranging from zero to one have been used (Stull, 1976). These values are mostly based on early studies (e.g. Tennekes, 1973) that tried to quantify PBL growth and entrainment using simple models for PBL growth where the downward entrainment of virtual heat flux was parameterised as a fraction of the surface virtual heat flux (Margulis & Entekhabi, 2004).

Later studies have found larger values of the entrainment coefficient. A larger entrainment value means that the PBL grows, warms and entrains dry air more rapidly (Betts et al., 1992) which will impact on the PBL moisture budget. Santanello et al. (2005) found a mean value of the entrainment parameter as 0.48. Margulis and Entekhabi (2004), using FIFE data, estimated the entrainment parameter by combining radiosonde and micrometeorological observations with a simple coupled boundary-layer and land surface model. They calculated a range of values from 0.22 (for June FIFE observations) to 0.54 (for August FIFE observations) with an average of 0.40. Also using FIFE data, Betts et al., (1992) found c_e to be 0.38 ± 0.16 and even for low wind cases found $c_e \approx 0.4$. Large values of c_e estimated from field experiments have been linked to high wind speeds in the PBL as wind enhances entrainment at the base of the inversion layer (Betts et al., 1992; Margulis & Entekhabi, 2004; Santanello et al., 2005).

Santanello et al. (2005) advise caution when using common parameterisations for c_e when c_e is proportional to the surface sensible heat flux. Substantial errors in the estimated entrainment fluxes can be introduced when setting c_e equal to a constant as the magnitude of the sensible heat flux varies diurnally from day to day. The value of the entrainment coefficient parameter is highly dependent on weather conditions (Margulis & Entekhabi, 2004) requiring calibration for each day.

8.3.2 Penman-Monteith equation

The Penman-Monteith model is used to estimate the latent heat flux (Monteith, 1965, 1981). This model is given in Section 2.1.2.1.1 of Chapter 2.

The aerodynamic resistance term in the PM model is calculated using:

$$r_a = \frac{\left(\log\left(\frac{z_a - d_z}{z_0}\right)\right)^2}{k^2 u} \tag{8.8}$$

where u is the mean wind speed (m s^{-1}), z_a is the reference height of the anemometer (m), d_z is the zero plane displacement (m), z_0 the roughness length (m) and k is the dimensionless von Karman's constant equal to 0.41.

The specific humidity deficit terms can be calculated using:

$$e_s = 0.611e^{\left(\frac{17.27T_d}{T_d+237.3}\right)} \tag{8.9}$$

$$e_a = 0.611e^{\left(\frac{17.27T_w}{T_w+237.3}\right)} - 0.00066P(T_d - T_w)(1+0.00115T_w) \tag{8.10}$$

where P is the station pressure (kPa), T_d is the dry bulb temperature (°C) and T_w is the wet bulb temperature (°C).

8.3.3 Data

Data required by the model was obtained from observations made during the First ISLSCP (International Satellite Land Surface Climatology Project) Field Experiment (FIFE). This was a land-surface-atmosphere experiment, conducted from May 1987 to late 1989, centred on a 15 × 15km grassland site near Manhattan, Kansas. During the Intensive Field Campaigns the fluxes of heat, moisture, carbon dioxide, and radiation were measured. The primary source of data used to calibrate and run the model comes from the spatially-averaged FIFE surface measurements and the PBL radiosonde observations (Betts & Ball, 1998). The surface measurements were collected from numerous stations and are given at 30-min resolution, while radiosondes were launched most days at roughly 90-min intervals with zero to eight launches occurring each day between sunrise and sunset.

The initial conditions required by the model are determined using the radiosonde data. The initial conditions consist of mixed-layer height (h), potential temperature (θ), specific humidity (q), temperature step size ($\Delta\theta$) and humidity step size (Δq). The inversion strength (Δ), or the size of the step, is the potential temperature and specific humidity difference across the inversion layer. It is difficult to determine the inversion strength from many of the profiles as the step is not clearly defined.

The model also requires parameter values of the lapse rates (gradients) in potential temperature (γ_θ) and specific humidity (γ_q) above the mixed layer which represent the general characteristics of the free atmosphere. For each day an early morning radiosonde is used to estimate these lapse rates.

In addition to the initial conditions and parameters, the model also requires the latent and sensible heat flux as forcing variables. The latent heat flux (W m^{-2}) through the day is determined using the Penman-Monteith equation. The sensible heat flux is then calculated as the difference between the net radiation (minus the ground heat flux) and the latent heat flux.

Data from both a dry and a wet day are used to calibrate the model. Given several important assumptions in the PBL model, the days chosen from the FIFE database are selected to most closely adhere to the assumptions in the model. In particular, days are chosen that are relatively cloud free with no precipitation and have relatively light winds. Cloudless days are desirable to ensure no outside influence on turbulence and a strong surface buoyancy flux to stabilise the model. Days with minimal lateral advection are chosen as lateral advection is not modelled. The magnitude of lateral advection is inferred from the wind speed as the advection terms are proportional to mean horizontal wind speed (Margulis & Entekhabi, 2004).

The days chosen are 12 August 1989 which is a relatively dry day and 5 June 1987 which is relatively wet. 5 June 1987 is considered a silver day with no clouds present while 12 August 1989 does have some clouds present. Both days have no precipitation. For 5 June the temperature increases from 20.5°C to 27.1°C and the maximum net radiation is 691 Wm^{-2}. For 12 August the temperature increases from 23.7°C to 28.3°C with a maximum net radiation of 481Wm^{-2}. 5 June, although a relatively wet day, has a greater maximum net radiation which results in the greater increase in temperature.

8.3.4 Calibration and sensitivity analysis

The PBL parameters for a given site are not known a priori and require calibration. The range of the parameter values can be seen in Table 8.1. Since the PBL model predicts the evolution of three state variables (temperature, latent heat and PBL height), a multi-response objective function is defined, based on scaled RMSE's for individual state variables. The "optimal" parameter set is obtained as the parameter set that minimizes the multi-response objective function, thus providing a tradeoff between fitting the multiple time series.

Table 8.1 The range of parameter values used in this study.

Parameter	Range
r_s (s m^{-1})	50 - 1000
z_0 (m)	0.02 - 0.12
d_z (m)	0.15 - 0.35
c_e (-)	0 - 1

The multi-response objective function is based on standardized sums-of-squared errors:

$$\Phi(\theta) = \frac{1}{\mathrm{var}\left[\varepsilon^{(T)}\right]}\sum_{j=1}^{n}\left(\varepsilon_j^{(T)}\right)^2 + \frac{1}{\mathrm{var}\left[\varepsilon^{(LE)}\right]}\sum_{j=1}^{n}\left(\varepsilon_j^{(LE)}\right)^2 + \frac{1}{\mathrm{var}\left[\varepsilon^{(Ht)}\right]}\sum_{j=1}^{nH}\left(\varepsilon_j^{(Ht)}\right)^2 \quad (8.11)$$

where ε is the error in the temperature (T), latent energy (LE) and height (Ht), n is the number of observations for the temperature and latent energy and nH is the number of observations of the PBL height. The error variances are pre-estimated based on single-objective optimization of the fit to the individual time series of temperature, latent energy and height. This is similar to previous multi-response applications (e.g., Franks et al., 1999).

In addition to parameter optimization, a simple sensitivity analysis is carried out to explore the performance of the PBL model as quantified by the multi-response objective function.

Both parameter optimization and sensitivity analysis are carried out using a simple Monte Carlo approach as follows. 10000 model simulations are generated, with parameter sets randomly sampled from a uniform distribution spanning the parameter range. Each simulation begins at the time the first PBL height was measured and finishes at the warmest part of each day as the PBL model does not simulate the decay of the PBL.

8.4 Influence of Wet and Dry Soil Moisture on Temperature

The PBL model is calibrated to the three state variables individually (temperature, latent heat and PBL height) as well as using the multi-response objective function. The sensitivity plots for the single-objective calibrations can be seen in Figure 8.3. The r_s parameter is found to have the greatest influence on the ability of the model to

reproduce the observations for all three variables, with the strongest influence on the LE. This is also seen using the multi-response objective function. The r_s parameter is a measure of the soil moisture. It therefore controls the division of net radiation into latent and sensible heat (temperatures). This in turn influences the growth of the boundary layer. The optimum r_s value is similar for each of the individual calibrations for both days. Using the multi-response objective function, 5 June 1987 has a calibrated r_s value of 97 s m^{-1}, while 12 August 1989 has a value of 339 s m^{-1}. This shows that 5 June 1987 was a relatively wet day while 12 August 1989 was relatively dry.

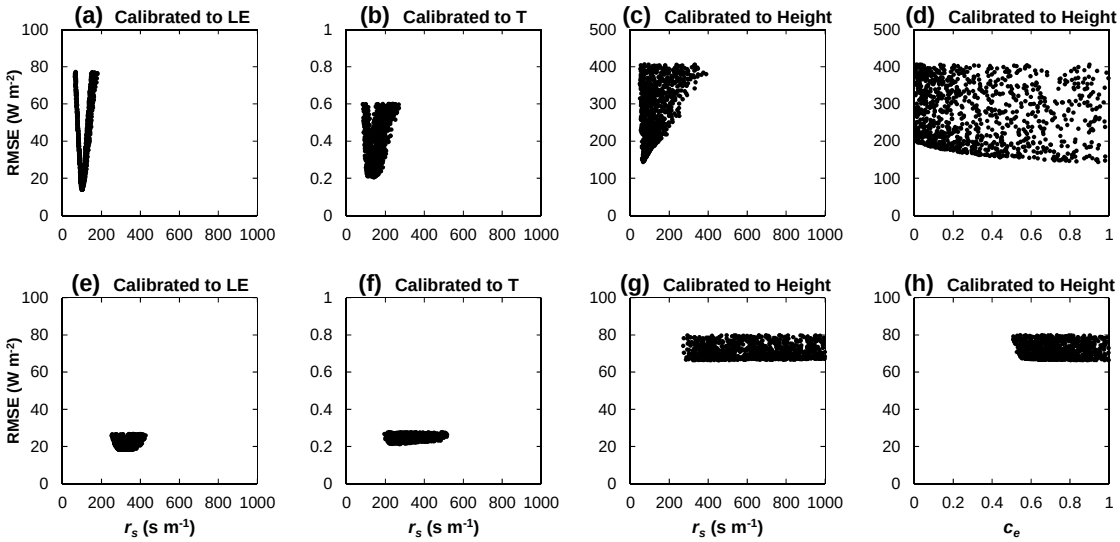

Figure 8.3 Sensitivity analysis of the PBL model for 5 June 1987 (top row) and 12 August 1989 (bottom row). The plot panels show the sensitivity of the RMSE criterion to changes in the surface resistance r_s and the entrainment coefficient c_e for individual calibration to latent energy (panels a and e), temperature (panels b and f) and height (panels c, d, g, h). For visual display purposes, only the top 1000 simulations are shown.

Additionally, it is found that the coefficient of entrainment does not have a strong influence on the temperature or latent energy but does have a small influence on the height of the PBL. The other parameters are insensitive.

The calibrated model is used to determine the influence of soil moisture on the evolution of day time temperatures. The surface resistance parameter, which is a measure of moisture availability, is used to simulate varying soil moisture conditions. A value of r_s = 50 s m^{-1} is used to simulate high soil moisture while a value of r_s = 5000 s m^{-1} is used to simulate very low soil moisture. For consistency, the atmospheric and

meteorological forcing is kept the same for each day. The temperature evolution resulting from wet and dry soil moisture can be seen in Figure 8.4.

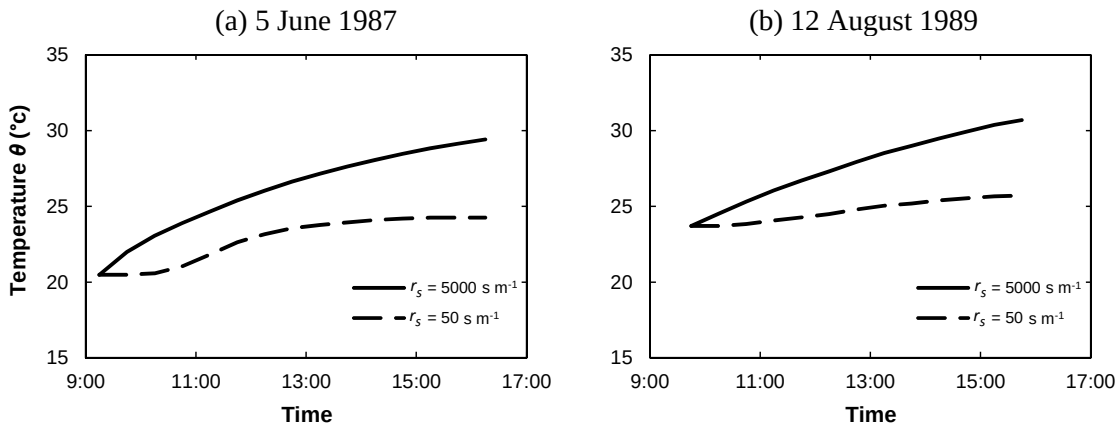

Figure 8.4 PBL-based simulation of temperature evolution under wet and dry soil moisture conditions.

Using the identified optimum parameter set, for the wet day, 5 June 1987, the wet soil moisture conditions yield a temperature increase of 3.8°C with a maximum temperature of 24.3°C. The dry soil moisture conditions yield a temperature increase of 8.9°C with a maximum temperature of 29.4°C. For the dry day, 12 August 1989, the wet soil moisture conditions lead to a temperature increase of 2.0°C with a maximum temperature of 25.7°C. Under the dry soil moisture conditions the temperature increases by 7.0°C with a maximum temperature of 30.7°C.

To gauge the sensitivity of the results to the optimised model parameter values, the experiments are repeated using the best 100 parameter sets. As seen in Table 8.2 for 5 June 1987 the temperature increase range under wet conditions is 2.9 to 3.8°C and under dry conditions 9.1 to 9.4°C. For 12 August 1989 the range of temperature increase under wet conditions is 1.7 to 2.1°C and under dry conditions 7.2 to 7.6°C.

Table 8.2 Daytime temperature increase (°C) from best 100 simulations for wet and dry soil moisture conditions.

	Wet	**Dry**
5 June 1987	2.9 - 3.8 (°C)	9.1 - 9.4 (°C)
12 August 1989	1.7 - 2.1 (°C)	7.2 - 7.6 (°C)

From these results it is clear that soil moisture influences the maximum temperature that can be reached during the daytime. Soil moisture controls the division of net radiation into latent and sensible heat. Dry soil moisture conditions lead to higher temperatures as there is less actual evaporation and therefore more net radiation is partitioned into sensible heat allowing for increased temperature.

The different ranges that occurred over the two days demonstrate that net radiation also influences the evolution of temperature over a day. 12 August 1989, with a maximum net radiation of 481 Wm^{-2}, has a smaller temperature increase under both dry and wet conditions than 5 June 1987 which has a maximum net radiation of 691 Wm^{-2}.

These results demonstrate that daytime temperatures are influenced by both net radiation and soil moisture. Given the model limitations previously discussed, the temperature increase found is only applicable to the conditions of the two days of FIFE data used. However, it is clear that the general trend is that dry soil moisture conditions result in considerably higher maximum temperatures than wet conditions.

8.5 Influence of Soil Moisture and 2°C Temperature Increase on Evaporation

The studies by Nicholls (2004) and Karoly et al. (2003) both proposed that the increased temperatures of the 2002 drought led to enhanced evaporation. This represents a confusion of cause and effect of temperature and evaporation. Here, the calibrated PBL model is used to test this proposition. Note that the 2002 drought was about 2°C warmer than the long term average. As before, the dry day and the wet FIFE day are used along with extreme dry and wet soil moisture conditions to determine the influence of a 2°C temperature increase on actual ET.

The model is first run using the observed temperature data for both days, under wet and dry soil moisture conditions. The ET at each time step is recorded. To determine the influence of a temperature increase, the temperature at each time step is increased by 2°C. This is investigated under two different scenarios. In Scenario A, the dry bulb temperature T_d is increased by 2°C and the wet bulb temperature T_w is increased by an

amount that keeps the same VPD as the original simulation. This is to ensure that any change to the ET is due only to the temperature increase and wet/dry scenarios and not due to an increased atmospheric vapour demand. In Scenario B, 2°C is added to both the observed wet and dry bulb temperatures. This allows for an enhanced VPD which effectively adds additional evaporative demand to the atmosphere. These results can be seen in Figure 8.5.

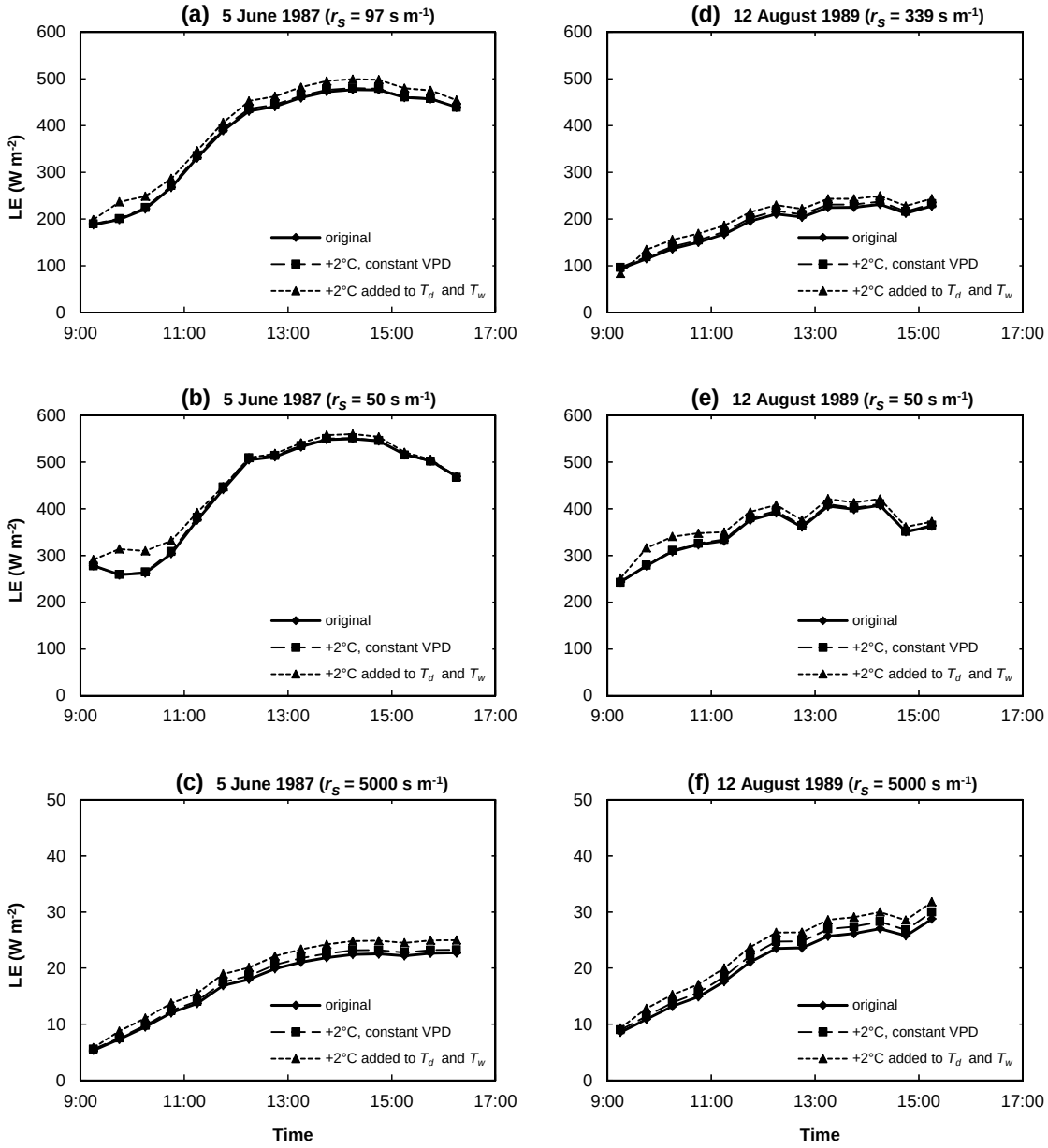

Figure 8.5 Simulation of evaporation for 5 June 1987 (left column) and 12 August 1989 (right column). Each plot shows the original modelled ET along with: (i) the effect of increasing the temperature by 2°C with the vapour pressure deficit preserved (keeping constant VPD) and (ii) the effect of adding 2°C to both the dry and wet bulb temperatures (T_d and T_w).

As expected, the evaporation is greater with wet soil moisture conditions than dry. Importantly it can be seen that only a minor increase in evaporation with an increase in temperature is apparent in each of the simulations. A simple calculation gives the additional evaporation resulting from a 2°C increase for both scenarios, shown in Table 8.3.

For the wet day, Scenario A leads to an increase of at most 0.004 mm/hr while Scenario B leads to an increase of at most 0.03 mm/hr. For the dry day, Scenario A leads to an increase of at most 0.007 mm/hr while Scenario B leads to an increase of at most 0.026 mm/hr.

The influence of a 2°C increase in temperature on evaporation is most pronounced, in terms of percentage increase, under dry soil moisture conditions (r_s = 5000 s m^{-1}). However, due to the lack of evaporation occurring under dry conditions, this is only an increase of at most 0.001 mm/hr in Scenario A and 0.004 mm/hr in Scenario B. The percentage increase under wet conditions (r_s = 50 s m^{-1}) is much smaller. However, due to the increased evaporation with wet conditions, this is a corresponding increase of at most 0.004 mm/hr in Scenario A and at most 0.026 mm/hr in Scenario B.

These simulations reveal that adding 2°C to both the wet and dry bulb temperatures leads to the greater increase in evaporation. This is because the VPD is enhanced, which effectively adds atmospheric evaporative demand, and hence allows for a greater increase in evaporation.

Table 8.3 Additional evaporation resulting from a 2°C increase in temperature. The percentage increase is given in the parentheses.

		Increase in evaporation (mm/hr)	
	r_s, s m^{-1}	**Scenario A** +2°C, **keeping constant VPD**	**Scenario B** +2°C **added to T_d and T_w**
5 June 1987	97	0.004 (0.76%)	0.030 (5.48%)
	50	0.003 (0.39%)	0.022 (3.34%)
	5000	0.001 (3.04%)	0.003 (11.45%)
12 August 1989	339	0.007 (2.74%)	0.023 (8.67%)
	50	0.004 (0.69%)	0.026 (5.15%)
	5000	0.001 (4.77%)	0.004 (12.09%)

A question arises as to which simulation is more likely to occur. Maximum temperatures have been observed to be increasing, however, Roderick and Farquhar (2004) report that in Australia the VPD has remained near constant. This suggests that Scenario A (which uses a constant VPD) is more realistic and that a 2°C increase in temperature will only lead to a hydrologically insignificant increase in evaporation.

8.6 Conclusions

This chapter uses a simple convective PBL model, coupled with the Penman-Monteith equation, to estimate ET, to examine the relative impact of dry and wet soil moisture conditions on daytime temperatures and to examine the interaction between temperature and evaporation. Using this model it is illustrated that soil moisture, along with the available net radiation, influences the maximum temperature that can be reached during the day. Soil moisture controls the partition of net radiation into latent and sensible heat. Dry soil moisture conditions lead to higher temperatures as there is less evaporation and therefore more net radiation is partitioned into sensible heat. For the days examined, daily maximum temperatures can be up to 5°C higher under extreme dry conditions compared with wet conditions.

Some recent literature has suggested that rising temperatures are the cause of reduced soil moisture and inflows in the MDB, implying that increased temperatures lead to increased evaporation. However, in this study it is shown that an increase in temperature only has a minor influence on evaporation. Soil moisture is the dominant control on evaporation and it is shown that the amount of evaporation has a controlling influence on the temperatures reached in the daytime. The findings highlight an important weakness of climatological studies and climatological projections based on the assumption that increased temperatures are responsible for increased evaporation, and lend more weight to the use of more physically realistic energy-balance models.

Chapter 9 - Conclusions

Overview

The primary objective of this thesis was to develop a new stochastic SSH based model for estimating global, direct and diffuse radiation, explicitly accounting for the uncertainty in the radiation estimates. The model output was to be applied to ET models to determine the influence of the uncertainty in the global radiation amounts on the ET estimates. The secondary objective was to examine the relationship and interaction between evaporation, temperature and soil moisture. This final chapter summarises how these objectives were achieved, the major conclusions and findings of this thesis, and future directions of this research.

9.1 Stochastic Radiation Model Development and Performance

The review of available literature on the modelling of ET and global radiation concluded that the more commonly used and most accepted ET models require global radiation as an input. However, measured radiation data are not very common. Consequently, a variety of empirical models have been developed for estimating global radiation. These empirical models are deterministic and give no indication of the uncertainty in the radiation estimates. This provided the motivation for the development of a stochastic model for estimating global radiation and its components.

The development of the stochastic radiation models was outlined in Chapter 3. Five new stochastic models were developed for estimating daily global radiation distributions which use SSH as the main input. Each of the five models developed had a different complexity- a constant, linear or quadratic structure, scaled by SSH to account for the influence of clouds on the attenuation of the radiation. The five models were calibrated using five different statistical residual error models, including assumptions of constant residual error variance, linear and quadratic residual error variance dependent on SSH

fraction, and linear and quadratic error variance dependant on the simulated global radiation.

For any day, the models developed provide estimates of the mean global radiation, a probability distribution of the radiation based on the timing of the bright hours, and an estimate of the errors from the external influences on radiation not accounted for by the SSH input.

At each location, the different global radiation models and residual error models were all found to perform well. Therefore, in the interests of parsimony, it was concluded that Model 1, calibrated with linear error variance based on SSH fraction, was sufficient for modelling global radiation. The performance of the radiation models at each location was found to be influenced by the rainfall regime of the location. Mildura was the driest station and had the best performance, with an RMSE of 1.32 MJ m^{-2} d^{-1}. In contrast, Darwin had the highest amount of rainfall and consequently the poorest performance, with an RMSE 1.99 MJ m^{-2} d^{-1}. The average error of the global radiation predictions was approximately 9% for all locations.

The calibration of the global radiation models did not account for the ability of the individual simulated direct and diffuse radiation components to model the observed direct and diffuse radiation. These individual estimates are important when applying the estimates to uneven terrain, photosynthesis calculations and forest ecosystem studies. Therefore, three direct and five diffuse radiation models, based on the components of the global radiation models, were separately calibrated to the individual direct and diffuse radiation components. The three direct and five diffuse radiation models consisted of a constant, linear and quadratic structure. It was found that these stochastic models could be used to reliably estimate the individual direct and diffuse radiation components.

Unlike the global radiation, the direct and diffuse radiation had an optimal model. The linear model (Model 2) was found to be sufficient for modelling the direct radiation. These model parameters were then used to model the diffuse radiation component. It was found that the quadratic model (Model 3b) best modelled the diffuse radiation. For

both the direct and diffuse radiation, the residual errors were best (and most efficiently) described using the quadratic SSH estimate. This resulted in greater error variance for sunny days for the direct radiation, and greater variance for cloudy days for the diffuse radiation. As with the global radiation, the models performed better at stations with smaller annual rainfall totals than those with much higher annual totals. For all locations, the average error of the direct radiation predictions was approximately 23%, while the average error of the diffuse radiation predictions was approximately 22%.

For the global, direct and diffuse radiation, the uncertainty due to the timing of the bright hours during the day, (the internal variance), only accounted for a small amount of the total error variance. On average, the external variance, which was due to the external influences not accounted for by the SSH timing, accounted for a larger amount of the total error variance. However, the internal variance was greatest for mid values of the SSH fraction. On these occasions, the internal variance accounted for a large portion of the total variance.

While all five radiation models performed equally well at estimating global radiation amounts, there was a preferred model for estimating the direct and diffuse radiation. Therefore, to model the global radiation with the direct and diffuse components being accurately accounted for, Model 3b is the preferred model.

The models in Chapter 4 were calibrated to each location individually using observed radiation data. However, observed radiation data is relatively scarce. To enable estimation of the radiation at all sites that have SSH data, a regional model is required. Therefore, in Chapter 5 two different types of regional models were developed and assessed for the global, direct and diffuse radiation. These were a bulk-regional model and a latitude-dependent model. The bulk-regional models were formed by calibrating the radiation models to a lumped input, comprising data from a range of locations across Australia. This provided one parameter set that can be used for all locations. The latitude-dependent models were developed using the relationship between latitude and the locally calibrated global, direct and diffuse radiation model parameter values. At each location, the radiation estimates from the different regional models was compared with the radiation estimates from the local models. The regional models for global

radiation were also compared to the BoM satellite-derived estimates of global radiation at ten locations.

For the global radiation, all five bulk-regional and latitude-dependent models performed reasonably well at all locations, particularly latitude-dependent and bulk-regional Model 3b. The latitude-dependent Model 3b performed better than the bulk-regional Model 3b at eleven of the twenty locations. At three locations, the BoM satellite-derived global radiation performed slightly better than the regional and local models. However, at the other seven locations, the satellite-derived global radiation performed significantly worse than the local and regional models.

For the direct radiation, the bulk-regional and latitude-dependent models, with the exception of Model 1, were found to perform well. The latitude-dependent Model 2 performed better than the bulk-regional Model 2 at all locations except Melbourne. For the diffuse radiation, the bulk-regional and latitude-dependent Models 2a, 2b, 3a and 3b were found to perform well, with Model 3b having the best performance. The latitude-dependent Model 3b performed better than the bulk-regional Model 3b at all locations.

From these results, it is clear that the global, direct and diffuse radiation are well modelled using the developed stochastic models, particularly Model 2 for the direct radiation and Model 3b for the diffuse radiation. It is also clear that a regional model can be used to estimate the global, direct and diffuse radiation at all locations studied, with minimal loss of accuracy compared with the local models. For the global radiation, the bulk-regional and latitude-dependent models both performed well and either model can be used when local calibration is not possible. These models also performed well when compared with the BoM satellite-derived global radiation. For the direct and diffuse radiation, the latitude-dependent regional models are recommended for use when local calibration is not possible.

9.2 Influence of Uncertainty in the Radiation Estimate on Evapotranspiration Rates

Global radiation is an important input for many models which estimate ET. The maximum, minimum and average global radiation, simulated for each location, was therefore used in Chapter 6 to determine the influence of the uncertainty of the radiation estimate on ET amounts. The FAO-56-PM combination model was used in addition to seven radiation-based models.

It was found that the uncertainty in the ET estimate was dependent on the type of model used, the location of the estimates, and the initial uncertainty in the radiation estimates. The locations with a greater uncertainty in the radiation estimate produced a greater uncertainty in the ET estimate. The amount of uncertainty was generally less for the combination FAO-56-PM ET model than the radiation-based ET models. For the radiation-based ET models, the average uncertainty was ±15% of the average for Alice Springs, and ±31% for Melbourne. For the FAO-56-PM model, the uncertainty was ±4% for both Alice Springs and Melbourne. The FAO-56-PM model had a much lower uncertainty as it used net radiation rather than just global radiation, and also accounted for the influence of wind speed and humidity, which reduced the influence of the radiation component. The FAO-56-PM model is considered the standard model for estimating ET.

The ET was also estimated using the regional global radiation models. It was found that the use of the radiation from the regional models only led to a minor loss in accuracy in the ET estimate for all ET models and radiation models. Therefore, although the uncertainty in the radiation amount is location dependent, this uncertainty can be well estimated using the regional models, and there is only a minor loss of accuracy in the resulting ET estimates.

Of all the ET models, the FAO-56-PM model gave the smallest amount of uncertainty. Of the radiation models, the Priestley-Taylor model gave the smallest uncertainty, while the Doorenbos-Pruitt model gave the largest. It is therefore recommended that the FAO-56-PM model be used to estimate ET. When data is not available for using the FAO-56-

PM model, the radiation-based Priestley-Taylor model is recommended as it gives the next smallest uncertainty in the ET estimate. The global radiation, for input into the ET models, can also be estimated using the regional radiation models.

9.3 Interaction of Temperature and Evapotranspiration

In the context of climate change, there is uncertainty as to how increased temperatures may influence ET rates. The second focus of this thesis was therefore to examine the relationship between evaporation, soil moisture and temperature.

In Chapter 7, the influence of a 2°C increase in temperature on ET estimates, derived from combination, radiation- and temperature-based models, was investigated. The increased temperature was found to lead to a range of responses in ET. The response of the models differed depending on the climatic factors each model considered. It was also shown that the effect of the increasing temperature on humidity also influenced how much ET was calculated. Whether or not the relative humidity or VPD was held constant affected how the increased temperature influenced the ET rates.

When the VPD was kept constant between the baseline and enhanced temperature scenarios, the ET rate for the FAO-56-PM model and Abtew models remained constant, and decreased for the temperature-based Romanenko model and the radiation-based Turc model. The remaining models calculated an increase in ET of up to 23% of the average baseline ET. The ET models that included a relative humidity term led to either a decrease, or a very minor increase, in ET rate. When the ET was recalculated keeping the relative humidity constant between the baseline and enhanced temperature scenarios, the ET rate increased for all the models. The ET models that only use temperature as an input had the greatest increase in ET. The models that gave ET rates most similar to the FAO-56-PM model all included humidity terms.

It was shown that the influence of increased temperature on ET rates is model dependent and therefore not all models can be used in climate response studies. In particular, the Thornthwaite model, which is based solely on air temperature, led to a large increase in ET. This was particularly seen at the arid locations; however, the

Thornthwaite model has been shown to be unreliable in arid climates. This has important implications for the application of the PDSI. The ET rates from the Thornthwaite model were overinflated compared with the other model estimates. Therefore, in a warming climate, PDSI estimates may be more extreme than reality would suggest.

Chapter 6 showed that for the radiation-based models, the uncertainty in the radiation amount can lead to large differences in the predicted ET. For the enhanced temperature scenarios, only the Doorenbos-Pruitt model had estimates close to that of the FAO-56-PM model, suggesting it is the most reliable method; however, in Chapter 6 it was shown that this model has the largest uncertainty due to the radiation input. In studies of future climate states, the uncertainty in the radiation estimate may overshadow the change in ET due to the enhanced temperature.

The increased temperatures can also affect other meteorological components, which can be unaccounted for in the empirical models. In particular, it was shown that the effect of the increased temperature on humidity also influenced how much ET was calculated. With a constant VPD, the FAO-56-PM model led to a very slight decrease in the average daily ET rates. In contrast, with a constant relative humidity, there was a slight increase in the average daily ET rates.

For climate change studies, temperature-based ET models have been shown to be unreliable when compared to the FAO-56-PM model, which is physically-based and considered the standard for estimating ET. Models such as the PM model which include radiation and humidity terms can be expected to give more physically realistic results. However, it was also discussed that the PM model and the FAO-56-PM model have limitations.

It was also recognised that the temperature-ET relationship is driven by complex interactions between the land surface and atmosphere. In particular, soil moisture controls the division of net radiation into latent and sensible heat. Therefore, following the simple analysis of the influence of increased temperature on ET, Chapter 8 provided

a more in-depth study of the interaction between temperature, ET and soil moisture, using a PBL model.

It was illustrated that soil moisture, along with the available net radiation, influences the maximum temperature that can be reached during the day. Dry soil moisture conditions lead to higher temperatures as there is less evaporation and therefore more net radiation is partitioned into sensible heat. For the days examined, it was found that daily maximum temperatures can be up to 5°C higher under extreme dry conditions compared with wet conditions. It was also shown that, contrary to speculation in previous studies, an increase in temperature only has a minor influence on evaporation. Rather, soil moisture is the dominant control on evaporation.

The results of Chapters 7 and 8 highlight an important weakness of climatological studies and climatological projections based on the assumption that increased temperatures are responsible for increased evaporation, and lend more weight to the use of more physically realistic energy-balance models.

ET is influenced by more than just temperature. In an environment where the temperatures are increasing, simple temperature-based models cannot be relied on to give accurate estimates of ET. With an increase in temperature, it is unknown how humidity, radiation amounts and wind speed may be influenced. These variables may have different, even opposing trends on ET. As shown in Chapters 6, 7 and 8, the uncertainty in the humidity and radiation amounts can lead to large differences in the predicted ET.

9.4 Future Work

The stochastic radiation model developed in this thesis has applications beyond modelling evaporation rates. The global radiation and its components can, for example, be utilised by the solar energy industry for use in energy efficient building design, and for further agricultural applications.

The radiation distributions provided in this thesis were only for a horizontal surface. By knowing the direct and diffuse components, the radiation distributions can be calculated for a sloped surface. This is useful for the agricultural sector for applications such as determining the energy input for crops on a hill side. The influence of any obstructions on the radiation, such as nearby buildings or trees, can also be accounted for.

The radiation distributions were also only estimated using SSH as the input. However, previous authors have also estimated the radiation components from other variables such as the maximum and minimum daily temperature. These variables could be incorporated into the models. This may reduce the variance of the distributions. The temperature measurements may also help determine the timing of bright SSH within the day.

The regionalisation method used was highly simplified. More sophisticated regionalisation methods could be used to give better estimates at locations where measured data does not exist for calibration.

The temperature, evaporation, soil moisture relationship was also only examined using two days of data. It is known that the role of soil moisture on potential ET is different for energy limited and water limited environments. The relationship could be further studied using data from different climates and for multiple days. In this way, the influence of the change in soil moisture and atmospheric conditions on ET rates and temperature could be more fully explored.

Climate change may affect more than just temperatures. The change in humidity, wind speed and radiation will also influence ET rates. These influences can be further examined, both individually and together, using GCM output.

9.5 Concluding Remarks

This thesis has developed a novel stochastic sunshine hour based model for estimating distributions of global, direct and diffuse radiation. This model accounts for the uncertainty in the radiation estimate due to the timing of the bright sunshine hours during the day, and the external influences on the radiation such as the unknown properties of clouds. The global radiation distributions were used to determine the influence of the uncertainty in the radiation on evapotranspiration estimates. The resulting uncertainty in the evapotranspiration estimates was found to range from ±4% for the FAO-56-Penman-Monteith model to ±31% for the radiation-based models. This thesis then examined the relationship between evapotranspiration and temperature. It was illustrated that soil moisture, along with the available net radiation, influences the maximum temperature that can be reached during the day. Importantly, temperature increases were shown to have minor influences on evaporation rates. Consequently, temperature-based models were shown to lead to unreasonable estimates of evaporation when temperatures are increased.

References

Abtew, W. (1996), Evapotranspiration measurements and modeling for three wetland systems in south florida, *JAWRA Journal of the American Water Resources Association*, *32*(3), 465-473.

Akinoğlu, B. G., and A. Ecevit (1990), Construction of a quadratic model using modified Ångstrom coefficients to estimate global solar radiation, *Solar Energy*, *45*(2), 85-92.

Al-Hamdani, N., M. Al-Riahi, and K. Tahir (1989), Estimation of the diffuse fraction of daily and monthly average global radiation for Fudhaliyah, Baghdad (Iraq), *Solar Energy*, *42*(1), 81-85.

Al-Riahi, M., N. Al-Hamdani, and K. Tahir (1992), An empirical method for estimation of hourly diffuse fraction of global radiation, *Renewable Energy*, *2*(4–5), 451-456.

Alexander, L. (2011), Climate science: Extreme heat rooted in dry soils, *Nature Geoscience*, *4*(1), 12-13.

Allen, R., L. S. Pereira, D. Raes, and M. Smith (1998), Crop evapotranspiration - Guidelines for computing crop water requirements, *Irrigation and Drainage Paper No. 56*, Food and Agric. Org., U.N., Rome, 300 pp.

Almorox, J., and C. Hontoria (2004), Global solar radiation estimation using sunshine duration in Spain, *Energy Conversion and Management*, *45*(9–10), 1529-1535.

Alton, P. B. (2008), Reduced carbon sequestration in terrestrial ecosystems under overcast skies compared to clear skies, *Agricultural and Forest Meteorology*, *148*(10), 1641-1653.

Amatya, D., R. Skaggs, and J. Gregory (1995), Comparison of Methods for Estimating REF-ET, *Journal of Irrigation and Drainage Engineering*, *121*(6), 427-435.

Ampratwum, D. B., and A. S. S. Dorvlo (1999), Estimation of solar radiation from the number of sunshine hours, *Applied Energy*, *63*(3), 161-167.

Angstrom, A. (1924), Solar and terrestrial radiation, *Quarterly Journal of the Royal Meteorological Society*, *50*, 121-125.

Bakirci, K. (2009), Models of solar radiation with hours of bright sunshine: A review, *Renewable and Sustainable Energy Reviews*, *13*(9), 2580-2588.

Barbaro, S., G. Cannata, S. Coppolino, C. Leone, and E. Sinagra (1981), Diffuse solar radiation statistics for Italy, *Solar Energy*, *26*(5), 429-435.

Benson, R. B., M. V. Paris, J. E. Sherry, and C. G. Justus (1984), Estimation of daily and monthly direct, diffuse and global solar radiation from sunshine duration measurements, *Solar Energy*, *32*(4), 523-535.

Betts, A. K., and J. H. Ball (1998), FIFE Surface Climate and Site-Average Dataset 1987–89, *Journal of the Atmospheric Sciences*, *55*(7), 1091-1108.

Betts, A. K., R. L. Desjardins, and J. I. MacPherson (1992), Budget analysis of the boundary layer grid flights during FIFE 1987, *Journal of Geophysical Research: Atmospheres*, *97*(D17), 18533-18546.

Black, J. N., C. W. Bonython, and J. A. Prescott (1954), Solar radiation and the duration of sunshine, *Quarterly Journal of the Royal Meteorological Society*, *80*(344), 231-235.

Blaney, H. F., and W. D. Criddle (1950), Determining Water Requirements in Irrigated Areas from Climatological Irrigation Data, *Technical Paper No. 96, US Department of Agriculture, Soil Conservation Service, Washington, D.C.*, 48.

BoM (2013) Climate classifications: *http://www.bom.gov.au/jsp/ncc/climate_averages/climate-classifications/index.jsp*
Climate data: *http://www.bom.gov.au/climate/data/stations/*
Solar Exposure: *http://www.bom.gov.au/climate/austmaps/solar-radiation-glossary.shtml#globalexposure*

Bristow, K. L., and G. S. Campbell (1984), On the relationship between incoming solar radiation and daily maximum and minimum temperature, *Agricultural and Forest Meteorology*, *31*(2), 159-166.

Brooks, C. F., and E. S. Brooks (1947), Sunshine recorders: a comparative study of the burning-glass and thermometric systems, *Journal of Meteorology*, *4*(4), 105-115.

Bugler, J. W. (1977), The determination of hourly insolation on an inclined plane using a diffuse irradiance model based on hourly measured global horizontal insolation, *Solar Energy*, *19*(5), 477-491.

Cai, W., and T. Cowan (2008), Evidence of impacts from rising temperature on inflows to the Murray-Darling Basin, *Geophysical Research Letters*, *35*(7), L07701.

Cai, W., T. Cowan, P. Briggs, and M. Raupach (2009), Rising temperature depletes soil moisture and exacerbates severe drought conditions across southeast Australia, *Geophysical Research Letters*, *36*(21), L21709.

Calder, I. R. (1990). *Evaporation in the Uplands*. John Wiley & Sons Ltd., Chichester, 166 p.

Carson, D. J. (1973), The development of a dry inversion-capped convectively unstable boundary layer, *Quarterly Journal of the Royal Meteorological Society*, *99*(421), 450-467.

Choudhury, N. K. D. (1963), Solar radiation at New Delhi, *Solar Energy*, *7*(2), 44-52.

Collares-Pereira, M., and A. Rabl (1979), The average distribution of solar radiation-correlations between diffuse and hemispherical and between daily and hourly insolation values, *Solar Energy*, *22*(2), 155-164.

Coppolino, S. (1990), A new model for estimating diffuse solar radiation in Italy from clearness index and minimum air mass, *Solar & Wind Technology*, *7*(5), 549-553.

Coppolino, S. (1991), Extensive applicability of a new model for estimating diffuse solar radiation from clearness index and minimum air mass, *Renewable Energy*, *1*(2), 293-297.

Courault, D., P. Drobinski, Y. Brunet, P. Lacarrere, and C. Talbot (2007), Impact of surface heterogeneity on a buoyancy-driven convective boundary layer in light winds, *Boundary-Layer Meteorology*, *124*(3), 383-403.

Culf, A. (1994), Equilibrium evaporation beneath a growing convective boundary layer, *Boundary-Layer Meteorology*, *70*(1-2), 37-49.

D'Andrea, F., A. Provenzale, R. Vautard, and N. De Noblet-Decoudré (2006), Hot and cool summers: Multiple equilibria of the continental water cycle, *Geophysical Research Letters*, *33*(24), L24807.

Dai, A., K. E. Trenberth, and T. R. Karl (1999), Effects of clouds, soil moisture, precipitation, and water vapor on diurnal temperature range, *Journal of Climate*, *12*(8), 2451-2473.

Davies, J. A., and J. E. Hay (1980), Calculation of the solar radiation incident on a horizontal surface. In Proceedings First Canadian Solar Radiation Data Workshop (Edited by J. E. Hay and T. K. Won), *Canadian Atmospheric Environment Service, Downsview, Canada*, 32-58.

Davies, J. A., and D. C. McKay (1982), Estimating solar irradiance and components, *Solar Energy*, *29*(1), 55-64.

Davies, J. A., and D. C. McKay (1989), Evaluation of selected models for estimating solar radiation on horizontal surfaces, *Solar Energy*, *43*(3), 153-168.

Donohue, R. J., T. R. McVicar, and M. L. Roderick (2010), Assessing the ability of potential evaporation formulations to capture the dynamics in evaporative demand within a changing climate, *Journal of Hydrology*, *386*(1–4), 186-197.

Doorenbos, J., and W. O. Pruitt (1977), Crop Water Requirements, FAO Irrigation and Drainage Paper 24, *FAO*, Rome, 144 pp.

Duan, Q., S. Sorooshian, and V. K.,Gupta (1992), Effective and Efficient Global Optimization for Conceptual Rainfall-Runoff Models, *Water Resources Research*, *28*, 1015–1031.

Durre, I., J. M. Wallace, and D. P. Lettenmaier (2000), Dependence of Extreme Daily Maximum Temperatures on Antecedent Soil Moisture in the Contiguous United States during Summer, *Journal of Climate*, *13*(14), 2641-2651.

Erbs, D. G., S. A. Klein, and J. A. Duffie (1982), Estimation of the diffuse radiation fraction for hourly, daily and monthly-average global radiation, *Solar Energy*, *28*(4), 293-302.

Ertekin, C., and O. Yaldiz (2000), Comparison of some existing models for estimating global solar radiation for Antalya (Turkey), *Energy Conversion and Management*, *41*(4), 311-330.

Federer, C. A., C. Vorosmarty, and B. Fekete (1996), Intercomparison of methods for calculating potential evaporation in regional and global water balance models, *Water Resources Research*, *32*(7), 2315-2321.

Franks, S. W., K. J. Beven, and J. H. C. Gash (1999), Multi-objective conditioning of a simple SVAT model, *Hydrology and Earth System Sciences*, *3*(4), 477-489.

Garg, H. P., and S. N. Garg (1985), Correlation of monthly-average daily global, diffuse and beam radiation with bright sunshine hours, *Energy Conversion and Management*, *25*(4), 409-417.

Garnier, B. J., and A. Ohmura (1968), A Method of Calculating the Direct Shortwave Radiation Income of Slopes, *Journal of Applied Meteorology*, *7*(5), 796-800.

Garnier, B. J., and A. Ohmura (1970), The evaluation of surface variations in solar radiation income, *Solar Energy*, *13*(1), 21-34.

Glover, J., and J. S. G. McCulloch (1958), The empirical relation between solar radiation and hours of sunshine, *Quarterly Journal of the Royal Meteorological Society*, *84*(360), 172-175.

Gopinathan, K. K. (1988a), A general formula for computing the coefficients of the correlation connecting global solar radiation to sunshine duration, *Solar Energy*, *41*(6), 499-502.

Gopinathan, K. K. (1988b), Computing the monthly mean daily diffuse radiation from clearness index and percent possible sunshine, *Solar Energy*, *41*(4), 379-385.

Gopinathan, K. K. (1988c), Empirical correlations for diffuse solar irradiation, *Solar Energy*, *40*(4), 369-370.

Gopinathan, K. K. (1992), Estimation of hourly global and diffuse solar radiation from hourly sunshine duration, *Solar Energy*, *48*(1), 3-5.

Gu, L., D. Baldocchi, S. B. Verma, T. A. Black, T. Vesala, E. M. Falge, and P. R. Dowty (2002), Advantages of diffuse radiation for terrestrial ecosystem productivity, *Journal of Geophysical Research*, *107*(D6), 4050.

Gueymard, C., P. Jindra, and V. Estrada-Cajigal (1995), A critical look at recent interpretations of the Ångström approach and its future in global solar radiation prediction, *Solar Energy*, *54*(5), 357-363.

Hamon, W. (1961), Estimating potential evapotranspiration, *Journal of Hydraulics Division, Proceedings of the American Society of Civil Engineers*, *871*, 107–120.

Hargreaves, G. (1975), Moisture availability and crop production, *Transactions of the ASAE*, *18*, 980-984.

Hargreaves, G., and R. Allen (2003), History and Evaluation of Hargreaves Evapotranspiration Equation, *Journal of Irrigation and Drainage Engineering*, *129*(1), 53-63.

Hargreaves, G. H. (1974), Estimation of potential and crop evapotranspiration, *Transactions of the American Society of Agricultural Engineers*, *17*(4), 701-704.

Hargreaves, G. H., and Z. A. Samani (1982), Estimating potential evapotranspiration, *Journal of Irrigation and Drainage Division, Proceedings of the American Society of Civil Engineers*, *108*(3), 225-230.

Hargreaves, G. H., and Z. A. Samni (1985), Reference crop evapotranspiration from temperature, *Transactions of the American Society of Agricultural Engineers.*

Hay, J. E. (1976), A revised method for determining the direct and diffuse components of the total short-wave radiation, *Atmosphere*, *14*(4), 278-287.

Hay, J. E. (1979), Calculation of monthly mean solar radiation for horizontal and inclined surfaces, *Solar Energy*, *23*(4), 301-307.

Hay, J. E. (1993a), Calculating solar radiation for horizontal surfaces—I. Theoretically based approaches, *Renewable Energy*, *3*(4–5), 357-364.

Hay, J. E. (1993b), Calculating solar radiation for horizontal surfaces—II. Empirically based approaches, *Renewable Energy*, *3*(4–5), 365-372.

Hirschi, M., S. I. Seneviratne, V. Alexandrov, F. Boberg, C. Boroneant, O. B. Christensen, H. Formayer, B. Orlowsky, and P. Stepanek (2011), Observational evidence for soil-moisture impact on hot extremes in southeastern Europe, *Nature Geoscience*, *4*(1), 17-21.

Hobbins, M. T., A. G. Dai, M. L. Roderick, and G. D. Farquhar (2008), Revisiting the parameterization of potential evaporation as a driver of long-term water balance trends, *Geophysical Research Letters*, *35*(12).

Hollands, K. G. T., and S. J. Crha (1987), A probability density function for the diffuse fraction, with applications, *Solar Energy*, *38*(4), 237-245.

Hottel, H. C. (1976), A simple model for estimating the transmittance of direct solar radiation through clear atmospheres, *Solar Energy*, *18*(2), 129-134.

Houghton, H. G. (1954), On the annual heat balance of the northern hemisphere, *Journal of Meteorology*, *11*(1), 1-9.

Iqbal, M. (1979), Correlation of average diffuse and beam radiation with hours of bright sunshine, *Solar Energy*, *23*(2), 169-173.

Iqbal, M. (1980), Prediction of hourly diffuse solar radiation from measured hourly global radiation on a horizontal surface, *Solar Energy*, *24*(5), 491-503.

Jain, P. C. (1986), Global irradiation estimation for Italian locations, *Solar & Wind Technology*, *3*(4), 323-328.

Jain, P. C. (1990), A model for diffuse and global irradiation on horizontal surfaces, *Solar Energy*, *45*(5), 301-308.

Jain, S., and P. C. Jain (1988), A comparison of the Angstrom-type correlations and the estimation of monthly average daily global irradiation, *Solar Energy*, *40*(2), 93-98.

Jensen, M. E. (1966), Empirical methods of estimating or predicting evapotranspiration using radiation, *Proceedings, Evapotranspiration and its Role in Water Resources Management, the American Society of Civil Engineers*. Chicago, 49-53, 64.

Jensen, M. E., and H. R. Haise (1963), Estimating Evapotranspiration from Solar Radiation, *Proceedings of the American Society of Civil Engineers, Journal of the Irrigation and Drainage Division*, *89*, 15-41.

Jensen, M. E., D. C. N. Robb, and C. E. Franzoy (1970), Scheduling irrigations using climate-crop-soil data, *Journal of Irrigation and Drainage Engineering*, *96*(IR1), 25-38.

Jensen, M. E., R. D. Burman, and R. G. Allen (1990), Evapotranspiration and Irrigation Water Requirements. *American Society of Civil Engineers*, New York, New York, 332 pp.

Kanniah, K. D., J. Beringer, P. North, and L. Hutley (2012), Control of atmospheric particles on diffuse radiation and terrestrial plant productivity: A review, *Progress in Physical Geography*, *36*(2), 209-237.

Karoly, D. J., J. Risbey, and A. Reynolds (2003), Global warming contributes to Australia's worst drought, research report, *World Wildlife Fund Australia*, Sydney, N.S.W., Australia.

Kavetski, D., and M. P. Clark (2011), Numerical troubles in conceptual hydrology: Approximations, absurdities and impact on hypothesis testing, *Hydrological Processes*, *25*(4), 661-670.

Kay, A. L., and H. N. Davies (2008), Calculating potential evaporation from climate model data: A source of uncertainty for hydrological climate change impacts, *Journal of Hydrology*, *358*(3–4), 221-239.

Kerr, A., and R. Tabony (2004), Comparison of sunshine recorded by Campbell–Stokes and automatic sensors, *Weather*, *59*(4), 90-95.

Kharrufa, N. S. (1985), Simplified equation for evapotranspiration in arid regions, *Beiträge zur Hydrologie Sonderheft 5.1*, 39-47.

Kingston, D. G., M. C. Todd, R. G. Taylor, J. R. Thompson, and N. W. Arnell (2009), Uncertainty in the estimation of potential evapotranspiration under climate change, *Geophysical Research Letters*, *36*(20).

List, R. (1968), *Smithsonian Meteorological Tables*, 6 ed., Smithsonian Institute, Washington, DC.

Liu, B. Y. H., and R. C. Jordan (1960), The interrelationship and characteristic distribution of direct, diffuse and total solar radiation, *Solar Energy*, *4*(3), 1-19.

Liu, Q., and T. R. McVicar (2012), Assessing climate change induced modification of Penman potential evaporation and runoff sensitivity in a large water-limited basin, *Journal of Hydrology*, *464–465*(0), 352-362.

Lockart, N., D. Kavetski, and S. W. Franks (2009), On the recent warming in the Murray-Darling Basin: Land surface interactions misunderstood, *Geophysical Research Letters*, *36*(24), L24405.

Lu, J. B., G. Sun, S. G. McNulty, and D. M. Amatya (2005), A comparison of six potential evapotranspiration methods for regional use in the southeastern United States, *Journal of the American Water Resources Association*, *41*(3), 621-633.

Makkink, G. F. (1957), Testing the Penman formula by means of lysimeters, *Journal of the Institution of Water Engineers*, *11*, 277-288.

Manabe, S. (1969), Climate and the ocean circulation, *Monthly Weather Review*, *97*(11), 739-774.

Mani, A., and S. Rangarajan (1983), Techniques for the precise estimation of hourly values of global, diffuse and direct solar radiation, *Solar Energy*, *31*(6), 577-595.

Margulis, S. A., and D. Entekhabi (2001), A coupled land surface-boundary layer model and its adjoint, *Journal of Hydrometeorology*, *2*(3), 274-296.

Margulis, S. A., and D. Entekhabi (2004), Boundary-layer entrainment estimation through assimilation of radiosonde and micrometeorological data into a mixed-layer model, *Boundary-Layer Meteorology*, *110*(3), 405-433.

Martínez-Lozano, J. A., F. Tena, J. E. Onrubia, and J. De La Rubia (1984), The historical evolution of the Ångström formula and its modifications: Review and bibliography, *Agricultural and Forest Meteorology*, *33*(2-3), 109-128.

McCormick, P. G., and H. Suehrcke (1991), Diffuse fraction correlations, *Solar Energy*, *47*(4), 311-312.

McKenney, M. S., and N. J. Rosenberg (1993), Sensitivity of some potential evapotranspiration estimation methods to climate change, *Agricultural and Forest Meteorology*, *64*(1–2), 81-110.

McMahon, T. A., M. C. Peel, L. Lowe, R. Srikanthan and T. R. McVicar (2013), Estimating actual, potential, reference crop and pan evaporation using standard meteorological data: a pragmatic synthesis, *Hydrology and Earth System Sciences*, *17*(4), 1331-1363.

Milly, P. C. D., and K. A. Dunne (2011), On the Hydrologic Adjustment of Climate-Model Projections: The Potential Pitfall of Potential Evapotranspiration, *Earth Interactions*, *15*(1), 1-14.

Monteith, J. L. (1965), Evaporation and the environment. In, *The state and movement of water in living organisms. XIXth Symposium of the Society for Experimental Biology*, *19*, 205-234.

Monteith, J. L. (1981), Evaporation and surface temperature, *Quarterly Journal of the Royal Meteorological Society*, *107*(451), 1-27.

Monteith, J. L. (2007), *Principles of Environmental Physics*, 3rd edition ed., 440 pp., Academic Press Saint Louis, MO, USA

Munawwar, S., and T. Muneer (2007), Statistical approach to the proposition and validation of daily diffuse irradiation models, *Applied Energy*, *84*(4), 455-475.

Newland, F. J. (1989), A study of solar radiation models for the coastal region of South China, *Solar Energy*, *43*(4), 227-235.

Nicholls, N. (2004), The Changing Nature of Australian Droughts, *Climatic Change*, *63*(3), 323-336.

Ögelman, H., A. Ecevit, and E. Tasdemiroğlu (1984), A new method for estimating solar radiation from bright sunshine data, *Solar Energy*, *33*(6), 619-625.

Orgill, J. F., and K. G. T. Hollands (1977), Correlation equation for hourly diffuse radiation on a horizontal surface, *Solar Energy*, *19*(4), 357-359.

Page, J. K. (1961), The estimation of monthly mean values of daily total short wave radiation on vertical and inclined surfaces from sunshine records for latitudes 40°N-40°S, *Proceedings of UN Conference on new sources of energy, Rome*, *4*, 378-390.

Painter, H. E. (1981), The performance of a Campbell–Stokes sunshine recorder compared with a simultaneous record of the normal incidence irradiance, *Meteorological Magazine*, *110*, 102-109.

Palmer, W. C. (1965), Meteorological drought, Res. Pap. 45, 58 pp., U. S. Dep. of Comm., Washington, D. C.

Penman, H. L. (1948), Natural Evaporation from Open Water, Bare Soil and Grass, *Proceedings of the Royal Society of London. Series A, Mathematical and Physical Sciences*, *193*(1032), 120-145.

Penman, H. L. (1956), Evaporation: An introductory survey, *Netherlands Journal of Agricultural Science*, *4*, 9-29.

Posadillo, R., and R. López Luque (2009), Hourly distributions of the diffuse fraction of global solar irradiation in Córdoba (Spain), *Energy Conversion and Management*, *50*(2), 223-231.

Prescott, J. A. (1940), Evaporation from water surface in relation to solar radiation, *Transactions of the Royal Society of Australia*, *46*, 114-118.

Priestley, C. H. B., and R. J. Taylor (1972), On the assessment of the surface heat flux and evaporation using large-scale parameters., *Monthly Weather Review*, *100*, 81-92.

Quinn, P., K. Beven, and A. Culf (1995), The introduction of macroscale hydrological complexity into land surface-atmosphere transfer models and the effect on planetary boundary-layer development, *Journal of Hydrology*, *166*(3-4), 421-444.

Raupach, M. R. (2000), Equilibrium Evaporation and the Convective Boundary Layer, *Boundary-Layer Meteorology*, *96*(1), 107-142.

Raupach, M. R. (2001), Combination theory and equilibrium evaporation, *Quarterly Journal of the Royal Meteorological Society*, *127*(574), 1149-1181.

Reindl, D. T., W. A. Beckman, and J. A. Duffie (1990), Diffuse fraction correlations, *Solar Energy*, *45*(1), 1-7.

Revfeim, K. J. A. (1976), Solar Radiation at a Site of Known Orientation on the Earth's Surface, *Journal of Applied Meteorology*, *15*(6), 651-656.

Revfeim, K. J. A. (1981), Estimating solar radiation income from ‘bright’ sunshine records, *Quarterly Journal of the Royal Meteorological Society*, *107*(452), 427-435.

Revfeim, K. J. A. (1997), On the relationship between radiation and mean daily sunshine, *Agricultural and Forest Meteorology*, *86*(3–4), 183-191.

Rietveld, M. R. (1978), A new method for estimating the regression coefficients in the formula relating solar radiation to sunshine, *Agricultural Meteorology*, *19*(2–3), 243-252.

Roderick, M., G. Farquhar, S. Berry, and I. Noble (2001), On the direct effect of clouds and atmospheric particles on the productivity and structure of vegetation, *Oecologia*, *129*(1), 21-30.

Roderick, M. L., and G. D. Farquhar (2004), Changes in Australian pan evaporation from 1970 to 2002, *International Journal of Climatology*, *24*(9), 1077-1090.

Roderick, M. L., L. D. Rotstayn, G. D. Farquhar and M. T. Hobbins (2007), On the attribution of changing pan evaporation, *Geophysical Research Letters*, *34*, L17403, doi:10.1029/2007GLO31166

Romanenko, V. (1961), Computation of the autumn soil moisture using a universal relationship for a large area, *Proceedings Ukrainian Hydrometeorological Research Institute (Kiev)*, *3*.

Ruth, D. W., and R. E. Chant (1976), The relationship of diffuse radiation to total radiation in Canada, *Solar Energy*, *18*(2), 153-154.

Samani, Z. (2000), Estimating Solar Radiation and Evapotranspiration Using Minimum Climatological Data, *Journal of Irrigation and Drainage Engineering*, *126*(4), 265-267.

Samuel, T. D. M. A. (1991), Estimation of global radiation for Sri Lanka, *Solar Energy*, *47*(5), 333-337.

Santanello, J. A., M. A. Friedl, and W. P. Kustas (2005), An Empirical Investigation of Convective Planetary Boundary Layer Evolution and Its Relationship with the Land Surface, *Journal of Applied Meteorology*, *44*(6), 917-932.

Schulze, R. E. (1976), A physically based method of estimating solar radiation from suncards, *Agricultural Meteorology*, *16*(1), 85-101.

Sen, Z. (2008), Solar Energy Fundamentals and Modeling Techniques, edited, Springer London.

Seneviratne, S. I., T. Corti, E. L. Davin, M. Hirschi, E. B. Jaeger, I. Lehner, B. Orlowsky, and A. J. Teuling (2010), Investigating soil moisture–climate interactions in a changing climate: A review, *Earth-Science Reviews*, *99*(3–4), 125-161.

Shaw, E. M. (1994), *Hydrology in practice*, Third ed., Chapman and Hall, London.

Shuttleworth, W. J. (1992), Evaporation, in *Handbook of Hydrology*, edited by D. R. Maidment, McGraw Hill, New York, pp. 4.1-4.53.

Shuttleworth, W. J., A. Serrat-Capdevila, M. L. Roderick and R. L. Scott (2009), On the theory relating changes in area-average and pan evaporation, *Quarterly Journal of the Royal Meteorological Society*, *135*(642), 1230-1247.

Shuttleworth, W.J. (2012), *Terrestrial Hydrometeorology*, John Wiley & Sons, 448pp.

Skartveit, A., and J. A. Olseth (1987), A model for the diffuse fraction of hourly global radiation, *Solar Energy*, *38*(4), 271-274.

Soler, A. (1990a), Statistical comparison for 77 European stations of 7 sunshine-based models, *Solar Energy*, *45*(6), 365-370.

Soler, A. (1990b), Dependence on latitude of the relation between the diffuse fraction of solar radiation and the ratio of global-to-extraterrestrial radiation for monthly average daily values, *Solar Energy*, *44*(5), 297-302.

Srinivasan, R., V. Bahel, and H. Bakhsh (1986), Correlation for estimation of diffuse fraction of daily global radiation, *Energy*, *11*(7), 697-701.

Stensrud, D. J. (2007), *Parameterization schemes: keys to understanding numerical weather prediction models*, Cambridge University Press, Cambridge.

Stull, R. B. (1976), The Energetics of Entrainment Across a Density Interface, *Journal of the Atmospheric Sciences*, *33*(7), 1260-1267.

Suehrcke, H. (2000), On the relationship between duration of sunshine and solar radiation on the earth's surface: Ångström's equation revisited, *Solar Energy*, *68*(5), 417-425.

Tabari, H., M. Grismer, and S. Trajkovic (2011), Comparative analysis of 31 reference evapotranspiration methods under humid conditions, *Irrigation Science*, *31*(2), 107-117.

Tennekes, H. (1973), A Model for the Dynamics of the Inversion Above a Convective Boundary Layer, *Journal of the Atmospheric Sciences*, *30*(4), 558-567.

Thornthwaite, C. W. (1948), An Approach toward a Rational Classification of Climate, *Geographical Review*, *38*(1), 55-94.

Thyer, M., B. Renard, D. Kavetski, G. Kuczera, S. Franks, and S. Srikanthan (2009), Critical evaluation of parameter consistency and predictive uncertainty in hydrological modelling: A case study using bayesian total error analysis, *Water Resources Research*, *45*, W00B14, doi:10.1029/2008WR006825.

Tiris, M., Ç. Tiris, and İ. E. Türe (1996), Correlations of monthly-average daily global, diffuse and beam radiations with hours of bright sunshine in Gebze, Turkey, *Energy Conversion and Management*, *37*(9), 1417-1421.

Trajkovic, S., and S. Kolakovic (2009), Evaluation of Reference Evapotranspiration Equations Under Humid Conditions, *Water Resources Management*, *23*(14), 3057-3067.

Trier, S. B., F. Chen, K. W. Manning, M. A. LeMone, and C. A. Davis (2008), Sensitivity of the PBL and precipitation in 12-day simulations of warm-season convection using different land surface models and soil wetness conditions, *Monthly Weather Review*, *136*(7), 2321-2343.

Turc, L. (1961), Estimation of irrigation water requirements, potential evapotranspiration: a simple climatic formula evolved up to date, *Annals of Agronomy*, *12*, 13-49.

van Heerwaarden, C. C., J. Vilà-Guerau de Arellano, and A. J. Teuling (2010), Land-atmosphere coupling explains the link between pan evaporation and actual evapotranspiration trends in a changing climate, *Geophysical Research Letters*, *37*(21), L21401.

Varley, M. J., K. J. Beven, and H. R. Oliver (1993), A method for predicting spatial distribution of evaporation using simple meteorological data, in *Exchange Processes at the Land Surface for a Range of Space & Time Scales*, edited by H. J. Bolle, R. A. Feddes and J. D. Kalma, pp. 619-626, IAHS Pubn. No. 212. IAHS,, Wallingford.

Vautard, R., P. Yiou, F. D'Andrea, N. de Noblet, N. Viovy, C. Cassou, J. Polcher, P. Ciais, M. Kageyama, and Y. Fan (2007), Summertime European heat and drought waves induced by wintertime Mediterranean rainfall deficit, *Geophysical Research Letters*, *34*(7), L07711.

Vörösmarty, C. J., C. A. Federer, and A. L. Schloss (1998), Potential evaporation functions compared on US watersheds: Possible implications for global-scale water balance and terrestrial ecosystem modeling, *Journal of Hydrology*, *207*(3–4), 147-169.

Wang, K. and R. E. Dickinson (2012), A review of global terrestrial evapotranspiration: Observation, modeling, climatology, and climatic variability, *Reviews of Geophysics*, *50*(2), RG2005.

Weymouth, G. T., and J. F. Le Marshall (2001), Estimation of daily surface solar exposure using GMS-5 stretched-VISSR observations: The system and basic results, *Australian Meteorological Magazine*, *50*, 263-278.

Williams, L. D., R. G. Barry, and J. T. Andrews (1972), Application of Computed Global Radiation for Areas of High Relief, *Journal of Applied Meteorology*, *11*(3), 526-533.

Wong, L. T., and W. K. Chow (2001), Solar radiation model, *Applied Energy*, *69*(3), 191-224.

World Meteorological Organization (2008). *Guide to Meteorological Instruments and Methods of Observation, WMO-No. 8 (7th edition), Part 1: Measurement of meteorological variables, Chapter 8: Measurement of sunshine duration.*

Xu, C. Y., and V. P. Singh (1998), Dependence of evaporation on meteorological variables at different time-scales and intercomparison of estimation methods, *Hydrological Processes*, *12*(3), 429-442.

Xu, C. Y., and V. P. Singh (2000), Evaluation and generalization of radiation-based methods for calculating evaporation, *Hydrological Processes*, *14*(2), 339-349.

Xu, C. Y., and V. P. Singh (2001), Evaluation and generalization of temperature-based methods for calculating evaporation, *Hydrological Processes*, *15*(2), 305-319.

Yeboah-Amankwah, D., and K. Agyeman (1990), Differential Ãngstrom model for predicting insolation from hours of sunshine, *Solar Energy*, *45*(6), 371-377.

Zhang, J., W.-C. Wang, and L. Wu (2009), Land-atmosphere coupling and diurnal temperature range over the contiguous United States, *Geophysical Research Letters*, *36*(6), L06706.